Selective Mineralisation by Hydrothermal Methods

A thesis presented to the University of Dublin, Trinity College
for the degree of
Doctor of Philosophy in Chemistry
by

Adrián Sanz Arjona

Trinity College Dublin
Coláiste na Tríonóide, Baile Átha Cliath
The University of Dublin

Under the supervision of Prof. Peter W. Dunne
School of Chemistry

Date: 16/03/2022

Trinity College Dublin

Declaration

This thesis is submitted for the degree of Doctor of Philosophy to the University of Dublin, Trinity College and has not been submitted before for any degree or examination to this or any other university. Other than where acknowledged, all work described herein is original and carried out by the author alone.

I agree to deposit this thesis in the University's open access institutional repository or allow the Library to do so on my behalf, subject to Irish Copyright Legislation and Trinity College Library conditions of use and acknowledgement.

I consent to the examiner retaining a copy of the thesis beyond the examining period, should they so wish (EU GDPR May 2018).

Permission is granted so that the Library may lend or copy this thesis upon request. This permission covers only single copies made for study purposes, subject to normal conditions of acknowledgement.

Adrián Sanz Arjona

Acknowledgements

Most importantly, I would like to thank my supervisor Prof. Peter W. Dunne. He has been a great support during all the Ph.D. process not only sharing all his knowledge but his time regardless. Peter has always been a helping hand any time it was required being a model example as a supervisor and as a person. I'm pretty glad to say that I will follow his steps in these incoming adventures and hopefully someday being as good a PI as he is. As well, to my co-supervisor Juan Diego Rodriguez-Blanco for his guidance and help when it was required.

The Dunne Group has been my house for the last four years, and the people that have been part of it, my family. Firstly, I would like to thank Andrew S. Bathe for being as welcoming when I arrived as an undergrad and for his partnership during my first 2 years of Ph.D. The knowledge that he left behind after finishing has been essential for this work. Secondly, I would like to thank my two lab partners, Annie Regan and Karlijn Hertsig, for their undoubtable support, especially during this final period before submission. I wish them the best for their careers and projects that, as such talented women, will achieve, no doubt. You have me here whenever you need.

I must also acknowledge for his role in the phosphate work Francis Dilworth. Additionally, to the list of past members of the group which have been a valuable asset for the group and for me personally: Eve Kearney, Niamh O'Donoghue, Aoife Kavanagh, Matthew Priestley, Conor Hughes, Christian Heinekamp, Luke E. Fehily, Sarah Egan, Lauren Ellis and Charlie Daly. They've been an essential part of this journey bringing joy to the group. They will be missed.

I would like to extend my regards to the technical staff in the School of Chemistry, in particular to Brendan Twamley, whose help and guidance has been key for this work. The large number of hours spent in the XRD room would not have been feasible without him.

I would like to thank my family and friends. In particular to my parents who are the guidance of my life. They have supported me in every decision that I have made that has brought me to this point in my career. They are my biggest support.

Finally, thanks to Trinity College Dublin for the funding of this project.

"Look, your worship," said Sancho; "what we see there are not giants but windmills, and what seem to be their arms are the sails that turned by the wind make the millstone go." – *Don Quixote de la Mancha* by Miguel de Cervantes

Abbreviations

ACC	Amorphous Calcium Carbonate
ACP	Amorphous Calcium Phosphate
ATR	Attenuated Total Reflection
CNT	Classic Nucleation Theory
DCPA	Dicalcium Phosphate Anhydrous (Monetite)
DCPD	Dicalcium Phosphate Dehydrate (Brushite)
ff	Filling Fraction
FTIR	Fourier Transformed Infrared
FWHM	Full Width at Half Maximum
HA	Hemagglutinin
HAP	Hydroxyapatite
HPLC	High-Performance Liquid Chromatography
HRPD	High-Resolution Powder Diffraction
MD	March-Dollase
MTHM	Metric Tonnes of Heavy Metals
NA	Neuraminidase
NIST	National Institute of Science and Technology
OA	Oriented Attachment
PCA	Principal Component Analysis
PC	Principal Component
PDF	Pair Distribution Function
PID	Proportional-Integral-Derivate
PNC	Prenucleation Cluster
PTFE	Polytetrafluoroethylene
QDs	Quantum Dots
RDF	Radial Distribution Function
SARS	Severe Acute Respiratory Syndrome
SBCW	Subcritical Water
SEM	Scanning Electron Microscopy
SNF	Spent Nuclear Fuels
TEM	Transmission Electron Microscopy
TGA	Thermogravimetric Analysis
TOPO	Tri-n-octylphosphine Oxide
XRD	X-Ray Diffraction

Summary

Chapter 1. Contains a literature review focusing on the evolution and properties of hydrothermal synthesis. It includes a description of the nucleation of materials, classical and non-classical processes, as well as the growth pathways followed by them. Additionally, it illustrates the properties of water at hydrothermal conditions. Finally, it encompasses a comparison of different synthetic techniques, including the newly-designed injection reactor.

Chapter 2. Contains the description of the experimental methodologies followed in this thesis. It describes the standard operational procedure for standard "batch" hydrothermal synthesis and the hydrothermal injection reactor. A full description of the design and safety features for the hydrothermal injection reactor is included. Also presented the theory of the most relevant characterisation and analysis techniques carried out for describing the samples.

Chapter 3. Contains the hydrothermal reactions carried for obtaining the optimal conditions to synthesise zircon-type silicates ($MSiO_4$). First zircon ($ZrSiO_4$) and stetindite ($CeSiO_4$) syntheses are reported using them as surrogates for the synthesis of thorite ($ThSiO_4$) and coffinite ($USiO_4$).

Chapter 4. Contains the reactions carried for the synthesis of calcium orthophosphate minerals. Brushite, monetite and hydroxyapatite were obtained at different conditions. This chapter assesses the capability of the statistical approach called Principal Component Analysis (PCA) to simplify the data obtained from X-Ray diffraction and obtain trends from the correlation of synthetic variables and the compounds obtained.

Chapter 5. In this chapter the hydrothermal synthesis of calcium carbonate carried in the hydrothermal injection reactor is reported. It shows the optimisation of the Principal Component Analysis representation when it is carried out on the Pair Distribution Function of the X-Ray diffraction patterns. It is compared with the analysis of other techniques such as FTIR and Raman. The polymorph selection at different synthetic conditions is reported in this chapter.

Chapter 6. The final remarks and the future work that can be potentially carried for the projects is proposed in this chapter.

Table of Contents

Table of Figures

Table of Tables

Chapter 1. Introduction

1.1 Hydrothermal Synthesis

Hydrothermal synthesis is historically one of the most studied and important synthetic techniques with a high impact in materials chemistry due to its suitability for manufacturing materials intended for catalysis,[1,2] optoelectronics,[3,4] biomedical applications,[5] *etc.*. The term *hydrothermal synthesis* was first postulated by the British geologist Sir Roderick Murchinson (1792 – 1871). He described the role of water in the formation of rocks and minerals at extreme temperature and pressure conditions. Hydrothermal synthesis is described as the reaction of two or more precursors in the presence of an aqueous solvent in a sealed vessel, at high temperatures and pressures (typically autogenous). These conditions help to dissolve materials that are non- or partially soluble at standard conditions. Although etymologically the phrase hydrothermal is composed by the Greek words "hydro" that means water and "thermos" that means heat, there's still some conflict on the definition of hydrothermal synthesis. In more recent reports it is defined as any heterogeneous chemical reaction in the presence of a solvent, independently if it is aqueous, at temperatures and pressures higher than standard conditions.[6]

Although hydrothermal processes occur naturally, the use of hydrothermal synthesis as a common synthetic technique is somewhat recent. It is thought to have entered use around 1845, by the synthesis of sub-microscopic quartz particles from silicic acid in a Papin's digestor by Schafthaul.[7] Most of the products of early hydrothermal experiments developed around the second half of the 1800s and the early 1900s were nanosized. Due to the lack of the electron microscopic techniques these experiments were archived as failures due to the impossibility to observe or quantify the final product. After the standardisation of X-ray diffraction as an analysis technique for materials around the 1920s an idea of the implications of hydrothermal conditions for material synthesis was achieved by the study of the diffraction patterns of hydrothermally produced materials. During the 1950s and 1960s researchers started to show some interest in the deep understanding of hydrothermal synthesis, particularly its solution chemistry and kinetics during the reaction.[8,9] In the 1970s some attempts at observing the reactions were carried out by introducing sapphire windows to the reactor body. They were discarded because under the extreme conditions required for the reactions, they could jeopardise the integrity of the container. The next milestone that promoted the use of hydrothermal

synthesis was around 1980s when scanning electron microscopy (SEM) allowed researchers to observe the resultant product, completely beyond reach in the past. This progress caused the burst of material research during the 1990s in science and technology of nano-sized materials or nanotechnology.[10] Nowadays the research in this field is on a continuous advance gaining a high level of sophistication, not only being capable of analysing even smaller particles by electron transmission microscopes (TEM)[11–14] but unveiling previously non-observable processes, *in situ*, by neutron and X-ray diffraction coupled systems in synchrotron facilities.[15] An additional topic that has grown in recent times is green chemistry and sustainable technologies where hydrothermal methods have shown great potential.[16,17] Hydrothermal processing requires very low energy for reaction completion, simplifies the optimum conditions by using aqueous solvents, no gas production, *etc.*

The growing scope of hydrothermal synthesis has attracted the attention of researchers in a wide variety of fields. In 2021 more than 12000 publications were related to "hydrothermal" in Scopus®. From all the publications related to hydrothermal, from 1940 to 2021 (177438), 18.9% (a total number of 65870) were related to material science and 18.2% (a number of 63508) to chemistry. The large number of publications in different fields shows the broadness of impact of this technique.

Table 1.1.Table of Hydrothermal-related publications in Scopus® by topic to 2021 (until November).

Subject Area	Number of Publications	Percentage (%)
Materials Science	65870	18.93
Chemistry	63508	18.25
Earth and Planetary Sciences	43554	12.51
Physics and Astronomy	40942	11.76
Engineering	39652	11.39
Chemical Engineering	34573	9.93
Environmental Science	17813	5.12
Energy	15786	4.54
Agricultural and Biological Sciences	7394	2.12
Biochemistry, Genetics and Molecular Biology	6606	1.90
Multidisciplinary	2266	0.65
Other	10057	2.89

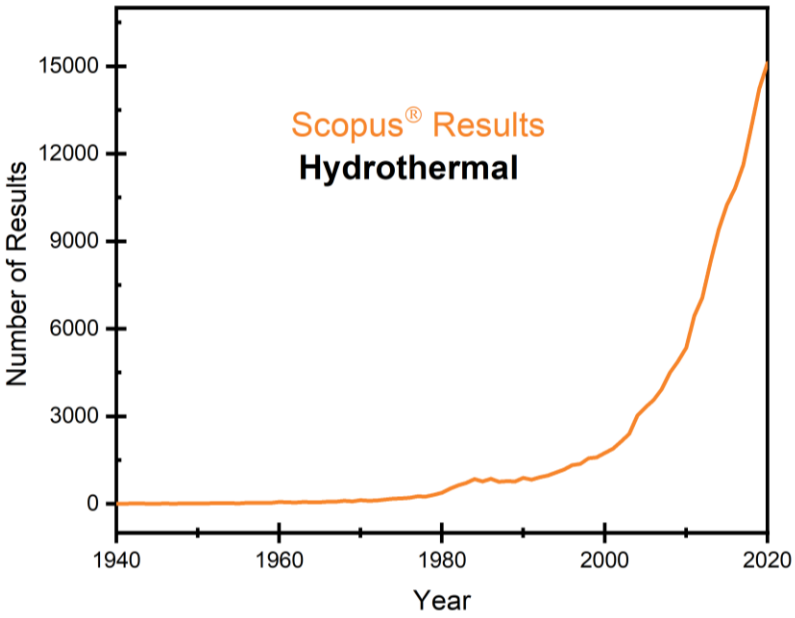

Figure 1.1. Number of results in Scopus® for "Hydrothermal" from 1940 to 2020 (November)

As already mentioned, hydrothermal synthesis was conceived from the very beginning as a way to replicate processes that occur in nature, playing a huge role on its most important events, as in the origin of life.[18–20] This relevance led to an increased interest for industrial processes, due to its huge control of the synthesis of materials coupled with an easy scalability. As an example, it has been used as a post treatment for semiconductor nanorods for transistors, enhancing the connectivity and improving the performance.[21,22]

Industrial hydrothermal processes can be demarcated in crystal synthesis, digestion of raw materials, hydrothermal treatment for improving building supplies' specifications or as general chemical processes.[23] In reference to crystal growth *via* hydrothermal synthesis, one of the milestones reached was the growth of hydrothermal quartz. It was just after World War II when the research lead by Western Electric Company (1946), based on information obtained from the Germans, proposed the use of this method for the growth of quartz on an industrial scale by the dissolution of silica in strong basic conditions inside a vertical reactor.[24] The container is not homogenously heated, so that, at the bottom of the container the temperature is higher where the heating systems are placed. The solution gets saturated with silicic acid at that fraction of the reactor, which migrates and nucleates at the higher colder part, transported by convection.

This process helped to overcome the need for natural quartz in various essential applications, most commonly as a piezoelectric.[25]

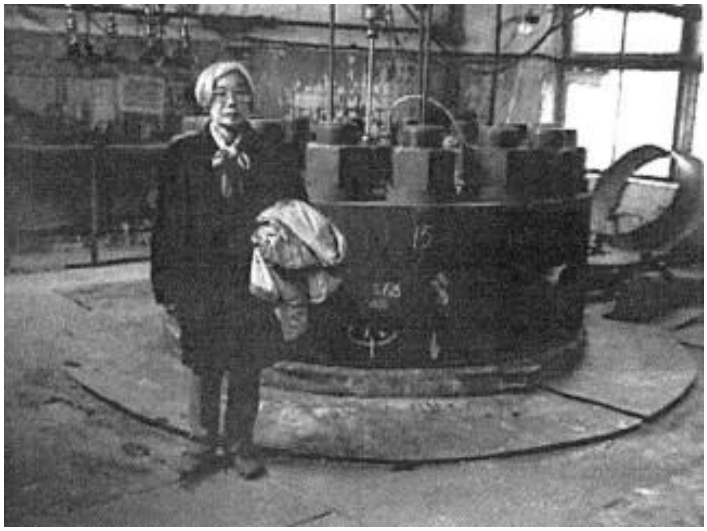

Figure 1.2. German autoclave transported to Russia after the World War II. Photo taken in 1999 by F. Iwasaki and H. Iwasaki.[26]

Another common example is the synthesis of lithium iron phosphate, $LiFePO_4$, which was reported by Goodenough, *et al.* to be used as a component in batteries.[27] The previous way to industrially obtain this material was by a solid state reaction. This reaction consisted of the reaction of two solid precursors at high temperature (400-800 °C). The reaction tends to be slow, as it is diffusion driven; and carbonates, sulfates, phosphates, or oxalates are used as precursors. Hydrothermal synthesis, on the other hand, is more viable for industrial scale. It is capable of generating pure samples and achieving a great phase and size control compared to the classic solid state route while spending less energy.[28] It has been pointed out as a green synthetic technique. Green chemistry is defined as the design of chemical reactions in the way that the least amount of hazardous waste and reagents are used without compromising the reaction outcome.[74,75] The foundations of this concept date from the early 1990s.[76] To help assess the design of Green Chemistry routes the Twelve Principles of Green Chemistry were codified to guide chemists to fulfil their intentional degree of sustainability. The twelve principles were reviewed extensively by P. Anastas and N. Eghbali.[77] Hydrothermal chemistry is well known to generate very low waste as well as allowing the design of reactions in the most efficient way by using most of the precursors for the products (atom economy). Additionally, it uses water over the boiling point as a solvent, avoiding

hazardous petrochemical alternatives. If all these factors are accompanied with a good experimental design, hydrothermal synthesis is a great candidate to unveil "greener" ways to synthetise materials.[78–81]

Hydrothermal synthesis has evolved to more complicated synthetic systems, where not only two precursors are introduced in a closed autoclave reacting to yield the target material. One of the most innovative hydrothermal processes, that is yet to be understood and fully exploited, is continuous flow hydrothermal systems.[29] It takes advantage of the superheated properties of water to yield materials in a continuous way, being easily transferrable to industrially required materials, where large demand of supplies are required

1.1.1 Superheated Water in Hydrothermal Synthesis

As mentioned, one of the main phenomena which hydrothermal synthesis exploits is the superheated nature of water. Aqueous reactions are commonly limited by the relatively low boiling point of water. In addition, the polarity of water hinders the use of many non-polar organic solvents. These limitations apply to the use of water in standard conditions, but they can be overcome by employing pressurised systems. That pressure can be applied, or the system can create it itself. In the case of a closed heated system like autoclaves, autogenous pressure is produced. The properties of water are then changed, particularly when getting close to the critical point of water (374 °C and 22.4 MPa). At that point water is reported to show a lower density and polarity.[30,31] The pK_w of water varies at those conditions too, as seen in Figure 1.3.

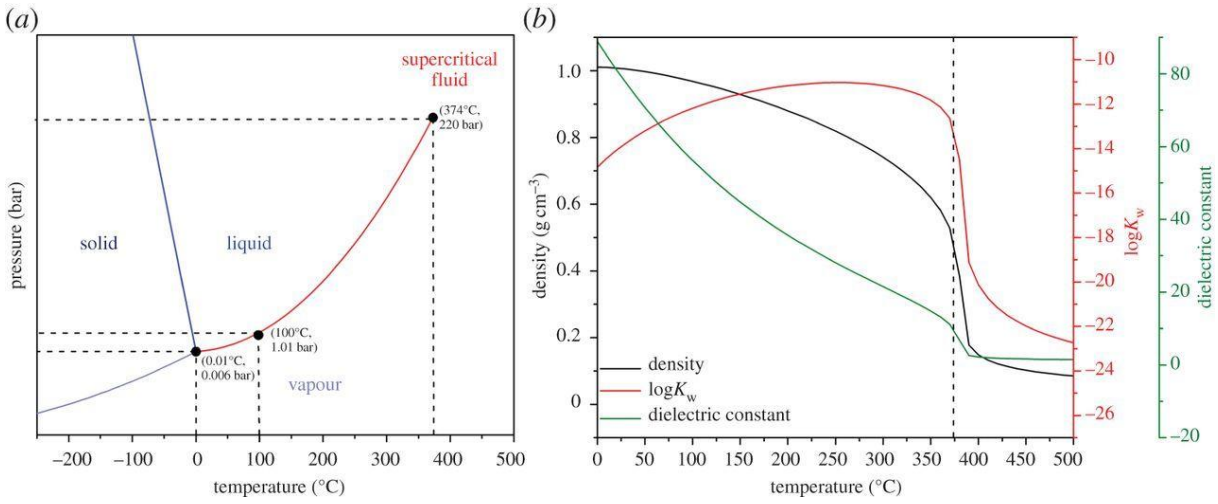

Figure 1.3. Simplistic diagrams of water phases (solid, liquid and vapour) as well as the supercritical point of water at 374 °C and 220 bar (22.4 MPa) (a), and the change of properties of water such as density, dissociation constant K_w and dielectric constant as it is heated in isochoric conditions (b). [29]

The hydrothermal method takes advantage of those features. Water is conceived as a good solvent for hydrophilic substances, but the properties and, by extension, the solubility during the reaction can be tuned in aqueous solvents just by changing the temperature and pressure. Therefore, solvents that were beforehand completely immiscible turn out to show a miscibility gap where both liquids can coexist in solution. These thermodynamic equilibria have been extensively studied.[32–34] Although hydrothermal syntheses don't explore strictly the critical point of water as it is above the conditions that classically hydrothermal encompass, there's still a certain change in the properties of water at "subcritical" conditions. It is usually defined as water used as the reacting medium, at temperatures ranging from 100 to 300°C. There are still some discrepancies on the definition of subcritical water (SBCW), whereby a number of definitions can be encountered. These are not related to a drastic change of properties like for supercritical water. Nonetheless when using this terminology, it is unambiguously referring to the gradual change of properties encountered at water over the boiling point. With increasing the temperature, the ion product increases from the standard value of $K_w = 10^{-14}$ mol^2 L^{-1} at room temperature, to around 10^{-11} mol^2 L^{-1} at 300°C. This value decreases from this point on, as shown in Figure 1.3. The enhanced ionic strength of superheated water promotes the presence of ions in solution and an elevated amount of H^+ and hydroxyl ions in solution. There is an additional change in the dielectric constant of water. The lowered number of hydrogen bonds due to the dissociation of water decreases the relative dielectric constant of water, D_{H_2O}. Therefore, the solubility of hydrophobic compounds is increased. There is an additional decrease of the viscosity of the solution and linked to it, a sharp drop of the density of water. Thus, SBCW allows the partial solubilisation of compounds never soluble at room temperature. It avoids the use of organic solvents for numerous reactions as water properties are effectively "tuneable" at this point. It also promotes the use of hydrothermal synthesis as a leading synthesis for material processing as it requires from less energy consumption that other analogous that require to create melt, vapour, gas or plasma.[6]

1.2 Nucleation and Growth

One of the main goals of materials science is to achieve control over the properties of synthetic products in order to make them suitable for use in some targeted application. That control of the features is essential for the later applicability in industry, medicine, *etc*.[35] To tackle this matter, the control of the nucleation and growth of the particles during the course of the reaction is essential. To fully understand it, several theories have been postulated along the decades to describe the intricacies of the nucleation and growth of materials.

1.2.1 Classic Nucleation Theory (CNT)

The way that materials are formed from solution was first explained by the Classic Nucleation Theory (CNT) formulated more than 70 years ago by Volmer[36], Becker and Döring.[37] It was first used to explain how a system lowers the free energy by, for example, increasing the entropy of itself in the condensation of a gas to liquid. This explanation relies on the Gibbs capillary effect; thus, the surface energy will be essential in this description. It was later extrapolated to the condensation of a liquid matrix into the solid state, which is more appropriate for the nucleation of crystal. In CNT, nucleation can be understood as the combination of two thermodynamic variables that, at a certain condition, will yield the driving force to form crystals by lowering the free energy of the system.

$$\Delta G = \Delta G_S + \Delta G_V \tag{1.1}$$

Where ΔG_S is the *interfacial free energy* of the interface that generates the boundary between the solid product and the media. It is a positive energy which needs to be overcome for nucleation to occur. On the other hand, ΔG_V, is the *volume excess free energy* per unit of volume, that will stabilise the nuclei. It has a negative value.

Simplifying this expression to a spherical nucleus, the following equation is derived:

$$\Delta G = 4\pi r^2\sigma - \frac{4\pi r^3}{3}\,\Delta G_V \tag{1.2}$$

It can be also written as,

$$\Delta G = 4\pi r^2\sigma - \frac{4\pi r^3}{3V}\cdot KT\,lnS \tag{1.3}$$

Where the interfacial energy, σ, will increase the value of the free energy by each new unit area created at the interface, but the excess volume will decrease this value consequently. $\frac{4\pi r^3}{3V}$ can be translated as the number of molecules that forms a cluster of radius *r* when the molecule has a volume of *V*. lnS represents the vapour supersaturation ratio. It is calculated by P/P^*, where P is the vapour pressure at the experimental temperature and P* is the saturation vapour pressure at the desired temperature. By using the Gibbs-Thomson equation it can be directly related to the concentrations, so that the theory is extended from gas to liquid systems, to liquid to solid which is directly related to the nucleation of materials.

$$ln\left(\frac{C}{C_0}\right) = lnS = \frac{2\sigma\Omega}{kTr} \tag{1.4}$$

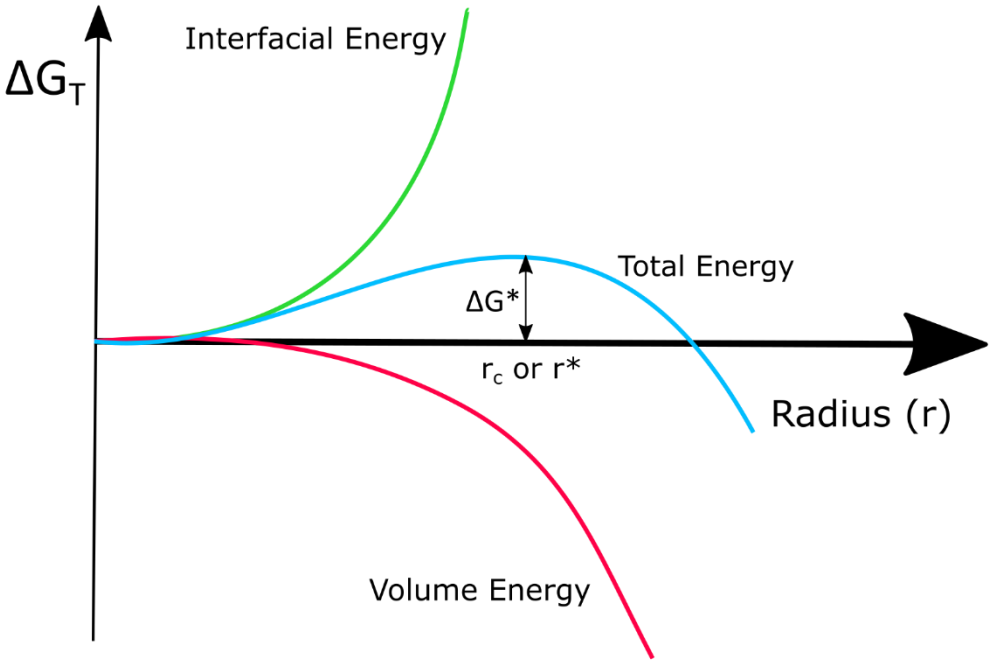

Figure 1.4. Graphic representation of eq. 1.2 comparing the free energy of the system (vertical axis) versus the radius of the nucleus (horizontal axis). The positive interfacial energy (green) and the volume energy (red) are combined in the total energy (blue).

In Equation 1.4, Ω, corresponds to the molecular volume in the condense phase. It can be seen that the interfacial energy increases by a quadratic relation to the radius, r^2, while the volume energy, also known as the bulk free energy, increases by a factor of r^3. For small nucleus radius the interfacial energy is predominant, so the formation of that

primal cluster will not be stable, and it will re-dissolve in the matrix. At a certain value the volume energy will overcome the interfacial energy, stabilizing the formation of the nucleus. That value of r is the critical radius (r_c or r^*). It is obtained when the variation of the free energy is equal to zero with respect to the radius.

$$\frac{dG}{dr} = 0 \rightarrow r^* = \frac{2\sigma}{\Delta G_V} = \frac{2\sigma}{KTlnS} \tag{1.5}$$

Classic nucleation theory carries a number of significant limitations and assumptions:

- The nucleus has the same properties as the stable phase, no change in shape is considered. It does not explain formation of metastable clusters prior to the crystal formation.
- The nucleus is approximated to be spherical, and the interface doesn't interact with the nuclei – it is considered a sharp boundary.
- The vapour-liquid interface is approximated to be planar. That same limitation is extended to liquid to solid nucleation.

As a result of these constrains, CNT has been subjected to numerous revisions and additions, and increasingly, non-classical nucleation pathways are being recognised.

1.2.2 Non-Classic Nucleation Theories - Step Processes

Different experiments have shown that the nucleation processes for various materials can't be fully described by the simplistic CNT. More complex approaches are required to precisely describe them. Examples of proteins, polymeric materials and various minerals have been shown, which follow the **rule of stages**.

This theory was firstly proposed by Ostwald in 1897.[38] He observed that the formation of certain materials is not as easily described as just going from solution to the final equilibrium stage. He observed that when nucleating certain materials, some transitional stages are achieved. Those intermediate species can be visualised as a different thermodynamically stable form of the target material down to molecule to molecule short range interactions creating clusters. In a more general manner he postulated that: "when leaving a given state and in transforming to another state, the state that is sought out is not the thermodynamically stable one, but the state nearest in stability

to the original state".[39,40] Looking at the process on a more structural basis, when looking at a polymorphic species the first one that will be formed is the easiest to be made, such as, the one with the lowest energy barrier.[41] Although there are few examples of systems that follow this pathway, it is logical to suggest that the transition of two structurally similar species will be preferred over two completely unrelated. The rearrangement of the atoms to form the final material is not as promoted as a formation of a structurally similar precursor metastable compound. Some structures will be first obtained being metastable in respect to the final equilibrium transitioning from that energetic position to the last one in timeframes from seconds to any longer time.

Following the step-mechanism proposed there are certain evidences of related mechanisms such as the two-step mechanism.[42] It establishes that prior to the crystallisation of the material a dense ordered liquid cluster is formed, called a pre-nucleation cluster (PNC). This cluster is more stable than the solution but energetically less favoured than the target material. The nucleation of the crystal is thereafter promoted due to the higher density of the metastable precursor, accelerating the rate of the growth. The nucleation of the material will be therefore influenced by the nature of the cluster. The characteristics of the target material can be tuned by the characteristics of the previous step, yielding, for example, pre-nucleation clusters that promote the formation of one polymorph or another, just by changing the conditions of the reaction.[43] The classic nucleation activation energy will be overcome by yielding metastable precursors, for which the total energy of formation is lower than the simplistic way as suggested in Figure 1.5.[44]

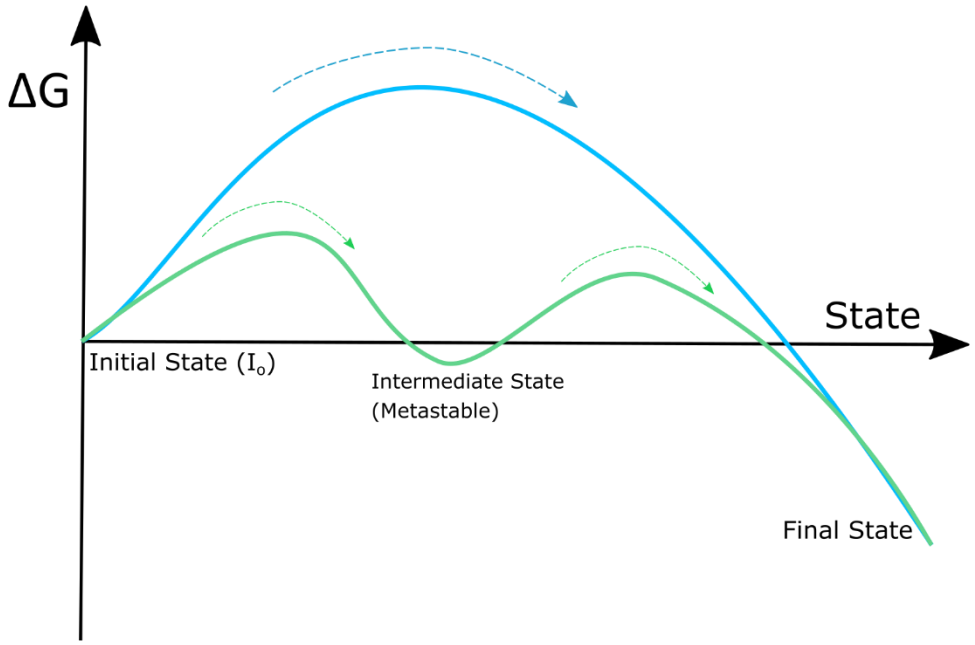

Figure 1.5. Energetic diagram where classic nucleation theory (CNT) in blue is compared with the two step mechanism in green.

A classic example of the two-step nucleation processes are materials that play an important role in living organisms. These materials are hugely influenced by the formation of prenucleation clusters prior to the formation of the crystal. These metastable polymeric materials are ordered, and the structure of these precursors will decide the final structure of the product. One of the most extensively studied biomaterials for this topic is calcium carbonate ($CaCO_3$). At the very first stages of formation, short-ranged ordered clusters are formed. They are, effectively, a higher-density fraction of the solution with short-range ordered ions that will evolve depending on pH and saturation conditions.[45,46] They then condense into an amorphous precursor, amorphous calcium carbonate (ACC). ACC is effectively energetically less stable than the crystalline calcium carbonate, so it will thereafter evolve to the most stable conformation. The amorphous prenucleation cluster process has also been proven for HAP crystallization in the study of collagen interactions with hydroxyapatite fibres during the growth of the bones.[47]

1.2.3 LaMer Model and Growth

The process doesn't end right after the formation of the nuclei as they will evolve to form the final crystals that precipitate from solution. One of the first interpretations of

the combination of the nucleation and growth processes was given by LaMer in the 1950s.[48]

This approach has been essentially one of the most acknowledged approximations receiving more than 1953 citation (Web of Science, March 2019) for his 1950s publication. The constant regard given to this theory along the years lies on the incapability of creating a better model capable of describing the formation of dispersed particles and their latter growth. It was first postulated to explain the nucleation and growth of monodisperse colloids in the growth of sulfur hydrosols from sodium thiosulfate. It was later extended to the synthesis of micro- and nanomaterials.

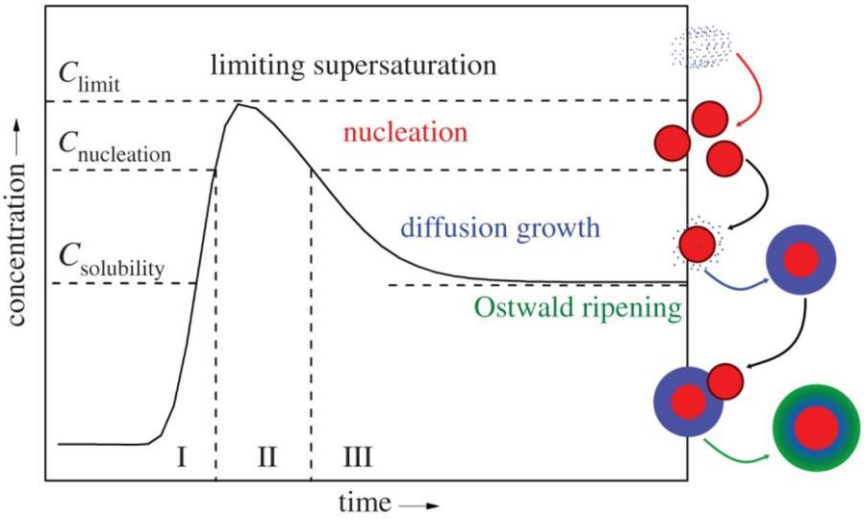

Figure 1.6 Schematic picture of La Mer model of nucleation and growth of monodisperse hydrosols.[49]

Regarding Figure 1.6, the process starts (I) with the increasing of the monomer concentration due to the introduction or formation of precursor. The increasing concentration of this building block is usually triggered by a change in the synthetic conditions such a variation in the pH, temperature or some other pertinent factor in such a way that the system reaches a certain concentration above the equilibrium concentration, $C_{solubility}$, and the system reaches a state of supersaturation (II). At some limiting supersaturation point, homogeneous nucleation takes place at an "effectively infinite" rate[48] — nucleation is reported by LaMer to be essentially instantaneous, described as a "burst of nucleation". It doesn't account for any kinetic model to justify the formation of the nuclei. The main reasoning for this assumption is that the step to be targeted as the limiting one is not the formation of the nuclei but the last stage related to

the growth of particles. The system will relieve the saturation by stabilizing small clusters, so that the concentration will decrease from that supersaturation level to the level of nucleation where step (III) will be forced into action. The created nuclei will grow by different processes to generate the final particles. The process is believed to be irreversible so that the growth of the particles is preferred versus the dissolution to form monomers back into solution. The monomers that didn't participate in the formation of the stable nuclei can become part of the bigger, stable precipitates by different processes – growth by diffusion or subsequent Ostwald ripening. Smaller nuclei will have a higher surface energy, so that the system will tend to redissolve these unstable precursors to yield the surface of the particle. This effect will essentially reduce the size disparity of the particles, an effect referred to as "focusing". It will only receed when the energies for dissolution of the particles are equalised, so that the size of them is comparable. The redissolution and deposition process is recognised as Ostwald ripening.[50] Other processes may occur, although they were never taken into account by LaMer. Agglomeration of the different particles, for example, is known to be a fairly common process in the synthesis of nanoparticles.[51–57]

It is required to clarify the simplicity of LaMer model. Although it is still used to exemplify many nucleation and growth processes in current times, it is still a simple model which is being more and more discarded in favour of new ways to understand the formation of particles. LaMer is a CNT based theory in which the formation of nuclei from solution is a single step processes and in which there is no structural disparity in the products formed, although the conditions of the reaction may change over time, such as the saturation of the precursors in solution that might drive to the formation of different polymorphs or even compounds. Secondly, as shown in Figure 1.6 the time frame is never discussed as the *x*-axis is usually described with no time magnitude, therefore there is no kinetic description available for the process as well as the growth of the particles can be extended from seconds to days and months. Thirdly, the growth process in this theory is only justified to be diffusion driven, neglecting on the description of different processes that they might suffer. Sticking to this last factor, the growing of the particles might be described as it is essential to understand the properties and the shape described by the particles obtained after reaction.

Hydrothermal synthesis has been shown to be able to generate complex structures after synthesis. This range of intricate shapes occur during the growth of the particles after nucleation, so it is critical to understand these processes in order to be able to control the morphology of the synthetic material and, by extension, their applicability. Crystals are known to grow by two different ways: crystal growth and agglomeration. To describe crystal growth it is necessary to set the starting point from the most simplistic point of view that is **classical growth theory**.

1.2.4 Classical Crystal Growth

This approach describes the development of the crystal by the addition of monomers, understood as any building block that after being clustered is capable of generate the particle. It can be either atoms, molecules or clusters.[58] Nonetheless, the driving force of this event is the activity difference of solution species, a, and when it is part of the precipitate described by the activity of the equilibrium solution-solid, a_{eq}.

$$\frac{\Delta\mu}{RT} = \ln\left(\frac{a}{a_{eq}}\right) \tag{1.6}$$

Equation 1.6 expresses the chemical potential difference ($\Delta\mu$) in terms of activity. In this first approach agglometarion is very unlikely to happen and only when the events that are directing the crystal to grow force them to attach. More recent studies on the kinetics of agglomeration defined the event by the numbers of collisions and the efficiency of them, which will depend on the geometry of the particles, the point of contact and the hydrodynamic forces that hinder their coalescence. Nonetheless, these theories were developed when the knowledge of the events at scales lower than the micrometer were completely unknown. More recent theories target understanding crystal growth as an assembly of nanosized particle (monomers) in a pattern or completely randomly oriented.

The process described is based on dissolution and reprecipitation of the monomers into energetically more favoured sites of the crystal. The energy for those events to happen can be driven by the solution or defects in the crystal: stacking faults and dislocations. As an example, screw stacking faults will promote spiral growth creating hillocks that will evolve by forcing the crystal to grow outwards.[59] This process was firstly explained by Burton, Cabrera and Frank in 1951.[60]

At higher supersaturation ratios the process will change from being driven by ordered diffusion onto the surface to generate the spiral patterns, to have an unstable interface at higher ratios in which the growth rate will be dependent on mass-transfer-controlled growth. At this level of supersaturation, the surfaces will be more chaotic due to the large number of nucleation events occurring at the surface. Where the events will happen in this case will be dependent on the shape of the particles where corners and edges will be in contact with areas of high concentration of the precursor. This will cause the growth of the particles in this direction preferentially over the central parts, causing the "hopper crystal" to be formed. This effect usually generates monocrystals with complicated shapes, but highly geometrical as shown in Figure 1.7.

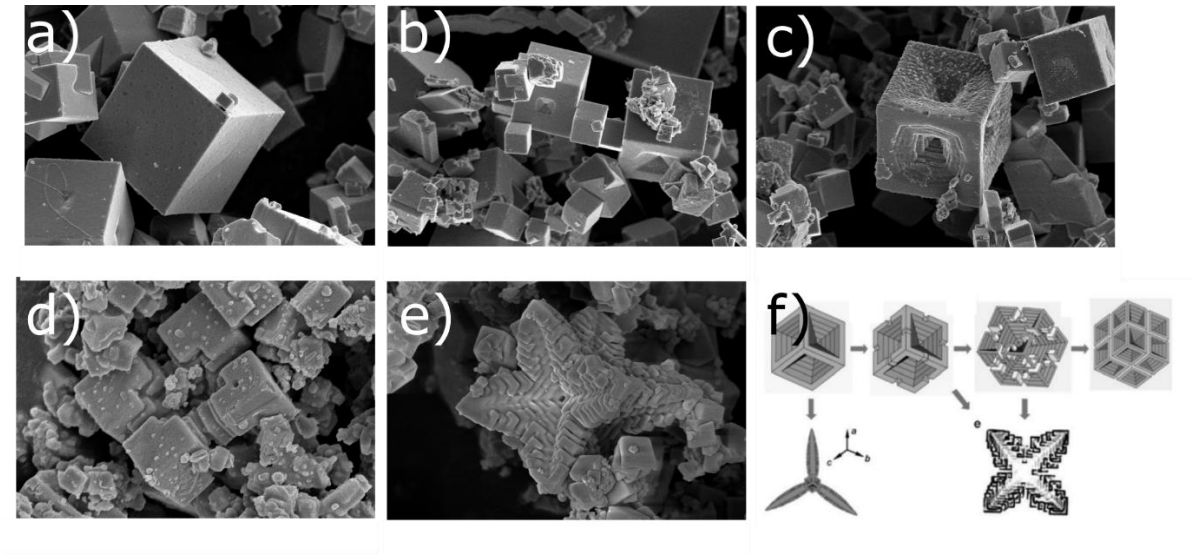

Figure 1.7. PbS growth as "Hopper crystals" a) – e) as the formation occur in different saturation conditions.[61] Picture f): Mechanism of growth of this kind of morphology.[62]

Nonetheless, when the driving force is even higher the growth is more chaotic and not as dependent on crystallographic direction, changing from the dendritic shapes into sphere-like shapes. This non-oriented polycrystalline growth is often called spherulitic growth. The shape of these spheres will depend on the factors that involve growth like, firstly, the concentration of precursors defined by the saturation and, secondly the type of spherules that are formed. When the formation of the spheres is driven from the core of the particles, isotropic growth – spherules type 1 are yielded. If, on the other hand, it is formed from the preferential growth of the two or more favoured

places on the surface generating a final sphere – spherules type 2. Both types of growth have been reported from the same material, for example $CaCO_3$. So that the compound nucleating won't be as critical as the external conditions of formation. Type 2 spherulitic growth has been used to explain other morphologies like dumbbells or sheaf-like particles.

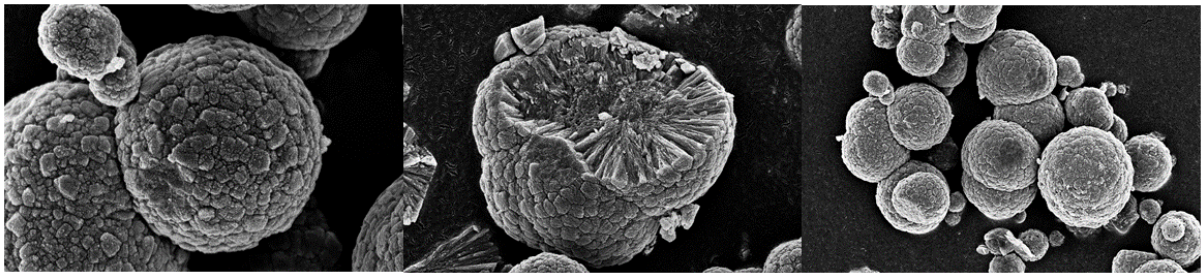

Figure 1.8. SEM images exemplifying the spherulitic ZnS particles.[61]

1.2.5 Non-Classical Growth

Non-classical growth derives from the idea that the growth of polycrystalline materials may proceed by the attachment of nanosized crystals. These aggregations have been summed to be rather non-directional (spheres) or directional (platelets, rods, prisms, *etc*.).[63] Later, oriented attachment (OA) was discovered from the hydrothermal treatment of TiO_2.[64] When the growth of the crystals is not perfectly driven, dislocations may appear. These processes have been extensively studied for a broad number of materials. For example, in calcium carbonate, the formation pathway will highly depend on the resulting polymorph present in the sample. While the formation of vaterite will drive to unoriented polycrystalline spheres, higher saturations of aragonite will promote oriented attachment to form rod-like shapes. Nonetheless spherulitic aragonite[65] and mesocrystal hexagonal plates of vaterite[66,67] have also been reported. It needs to be highlighted, that the separating line between the different processes is really thin making it sometimes impossible to discern when a particle is formed from one or another growth process. It is usually dependent on the growth related driving forces, such as the saturation or the use of additives.[68]

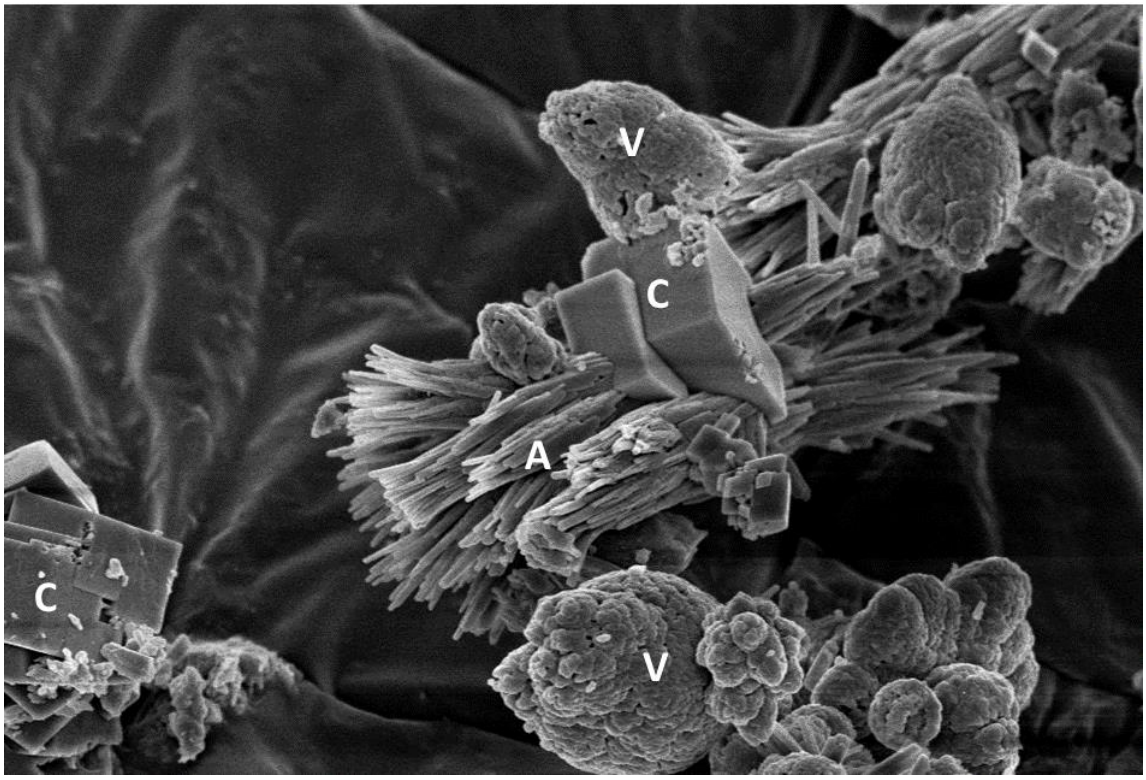

Figure 1.9. Typical morphologies for the different polymorphs of calcium carbonate: "spherulitic" vaterite (V), calcite (C) and "directional rod-like" aragonite (A).

The concept of oriented attachment has been developed over the last 10 years to the point where superparticles can be formed by clustering together previously made nanoparticles in solution. It is a multistep process where the building nanoparticles will be formed first to later form the final well-defined particle to be formed.[69,70]

The growth of crystals will be highly dependent on the conditions of synthesis. The selectivity addition of the precursor or additives in the synthesis will be critical for the morphology that the synthetised particles will adopt. Additionally, the synthetic technique in which these particles are formed will be reflected in various parameters like the saturation in solution, the temperature of formation, among others. To obtain a certain morphology for the particles yielded will extensively lie on the method chosen for that synthesis.

1.3 Synthetic Methods

In order to control the nucleation and growth of tailored materials, many different techniques have been developed over the years in order to obtain an optimum method capable of directing the characteristics of the materials for a specific application. These techniques range from more simplistic approaches such as batch methods (*e.g.,* hydrothermal) to more complicated approaches that require a great understanding of other fields beyond chemistry such as engineering (*e.g.,* continuous-flow synthesis). Here are detailed the characteristics of several relevant approaches and useful examples of reported experiments to highlight the positive and negative features of each in the context of the research reported in this thesis.

1.3.1 Hydrothermal synthesis

Although from the very classic point of view, hydrothermal synthesis is strictly a reaction carried out in a sealed autoclave, it should be designed to operate at the desired conditions in a safe and reliable way. There's not only one design of hydrothermal "autoclave" as it will depend on the reaction. Nonetheless, the reactor must exhibit some common characteristics.

- It should be inert to acids, bases and oxidizing agents used in the reaction.
- It requires a pressure relief system that allows the safe release of overpressure that could be generated inside the autoclave.
- Needs to be easy to assemble and disassemble.
- It requires a certain volume, sufficient enough to gather the solution and avoid high pressures. Usually, the reactions are designed in a way that the total internal volume of the reactor in never reached. The pressures generated at the interior of the reactor can be calculated and the outcome of the reaction relies on a good pre-experimental design.
- It should not change its features, like the internal volume, after extended time reactions.

Due to the high versatility of this method many different reactor set-ups are available, each with their own advantages and disadvantages.

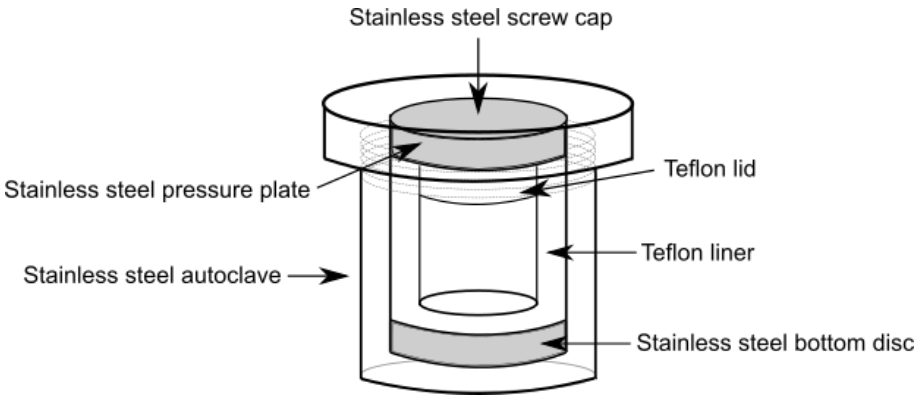

Figure 1.10. Schematic of a standard "batch" hydrothermal autoclave.

The most standardised reactor are the batch hydrothermal autoclaves or general purpose autoclaves, as shown in Figure 1.10. These typically consist of an inert Teflon® (polytetrafluoroethylene) container that is sealed into a stainless-steel system which provides the mechanical strength to allow for high pressures to be achieved, while a variety of safety features may also be incorporated. Most commonly in these general purpose autoclaves the upper assembly consists of a corrosion disk and a bursting disk that sit on top of the lid of the reactor cup. The corrosion disk serves as a sacrificial component, to minimise any corrosion of the structural steel body which may be caused by leakage of reactant mixtures. The bursting disk is designed with a weak point such that, should an overpressurisation occur, the reactor will fail in a predictable way – bursting upwards, rather than exploding outwards. On assembly the Teflon® cup, lid, and disk components are sealed by a spring system within the stainless-steel body and cap assembly.

There are modifications of this common sealed reactor design in which the temperature and pressure can be monitored and/or controlled *in situ* by a thermocouple and Bourdon gauge fixed at the reactor. Notably these designs cannot incorporate the Teflon cup, as the monitoring apparatus must be open to the reagent mixture. As such, these reactors are generally constructed of stainless-steel or specific alloys, to match or withstand the chemical conditions of the reactions being performed. In rare instances these reactors may consist of the primary stainless-steel body with an internal coating of an inert metal such as gold. In a standard hydrothermal reaction, the autoclaves are placed in a preheated oven, or heat is supplied through the use of hot-plates and/or heating jackets. Regardless of the specific design, it is of course necessary to ensure that the

pressure of the system will not exceed the safety rating of the reactor while under reactive conditions. This is achieved before ever starting a reaction by calculating the expected pressures under isochoric conditions based on the fill fraction (ff) of the reactor. These pressures may be estimated from pressure-volume-temperature plots by different binoidal solutions as reported by Kennedy.[71]

These conventional reactors, whereby all reagents are loaded into the system prior to sealing and heating, will suffer a ramp of temperature from the ambient loading conditions to the target temperature. This directly affects the nucleation and growth of the particles as they will experience a continuous gradient of conditions when nucleating and growing. Referring back to the 1950s LaMer approach, this translates to a broad size (and shape) distribution, which is generally undesirable. The simplest method to avoid this polydispersity in these systems is to employ long reaction times, allowing for Ostwald ripening and size focussing to occur. In itself this will have the effect of leading to larger particle sizes being favoured, as well as increasing time and energy costs associated with hydrothermal syntheses.

Although the technological advances around this system have allowed researchers to gain a better control at the synthetic conditions, the standard hydrothermal synthesis still carries several limitations. The main one is the lack of understanding of internal conditions during the reaction, like pressure and temperature. Those features hinder in a great way the understanding of the exact conditions during the nucleation and growth. It also plays a huge role on the reproducibility of the processes when being reported and replicated. Paraphrasing Afanasiev "The hydrothermal brines are used somewhat as a kind of magic hat from which this or that animal suddenly goes out".[72]

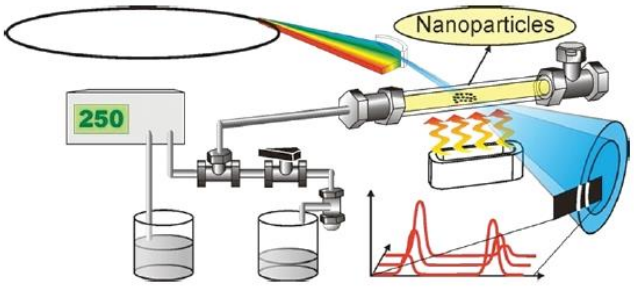

Figure 1.11. Setup used by B. Brummerstedt Iversen *et al*. to analyse the synthesis of tin oxide under hydrothermal conditions by using synchrotron X-ray In-Situ Scattering.[73]

Nonetheless, some new approaches have been targeted recently to unveil the process happening inside the reacting chamber. *In situ* direct probing of the reaction by the use of X-Ray diffraction have been reported. As an illustrative example of a set-up for tracking the reaction, in 2012 Iversen *et al*.[73] reported the synthesis of tin oxide (SnO_2) hydrothermally which was tracked in real time by means of total scattering measurements. The use of total scattering combined with the advantages of pair distribution function analysis (PDF) are capable of giving insightful information of the processes occurring during the reaction.

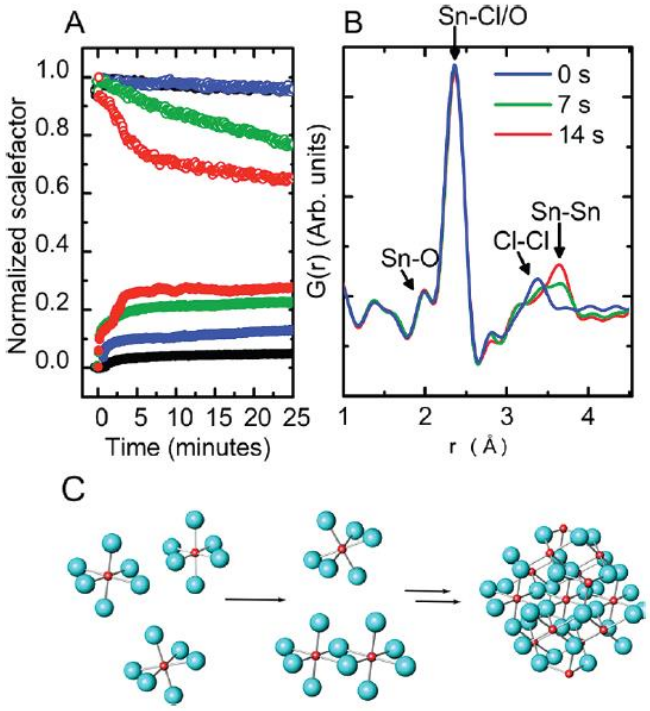

Figure 1.12. A) Normalised scale factor for the precursor complexes of the oxides (circumference symbols) and for the SnO_2 nanoparticles (circles symbols). B) Reduced pair distribution function (PDF) for the first three frames of an experiment. C) Mechanism of formation of the tin oxide nanoparticles from the complexes $[Sn(H_2O)_{6-y}(OH)_y]^{(4-y)+}$. Sn^{4+} is represented in red and O^{2-} in blue. The precursors cluster to form the final rutile structure particle of tin oxide.[73]

From the data collected it was possible to reveal the complexes formed in solution that will be the precursors of the final nanoparticles. The process followed to tailor them from the random disposition of the tin hexaaquatin(IV) complexes in solution to the arrangement in a specific pattern (rutile tin oxide) following the Equation 1.7 and shown in Figure 1.12 C).

$$\left[Sn(H_2O)_{6-y}(OH)_y\right]^{(4-y)+}(aq) \rightarrow SnO_2(s)_{rutile} + yH_2O(l) + (4-y)H_3O^+(aq) \quad (1.7)$$

Additionally, they discussed the growth of the particles after nucleation at different conditions showing that there is an initial growth promoted by ion-attachment of the mentioned precursors until Ostwald ripening takes place to further promote the growing of the particle. Finally, structural modifications of the particles are highlighted by the possible coexistence of two different polymorphs of the oxide. It shows the potential of this technique that is capable of giving information at every step of the particle's formation. This technique follows the process at different temperatures and concentration of precursors in an easy manner by using water as the solvent by hydrothermal synthesis. It also describes the formation of the solid at every step of its formation from the solution to the really low distance interactions between the species in solution giving the final solid structure at the end of the crystallisation. Nonetheless the main limitation of this technique resides in the complexity of the setup. For these measurements a high energy source of X-rays is needed as a synchrotron and the corresponding apparatus shown in Figure 1.11. It requires at the same time of the use of a large amount of energy, resources, and time. As well, for the analysis it is demanded to gather a high expertise in the topic. For the case of tin oxide, the formation process has been reported along the years and the mechanism of formation is known to be simple. This approach is therefore inefficient for multistep mechanism with a great complexity as it would require of many conditions and analysis to reveal every single precursor in the reaction. Therefore, although the limitations highlighted for hydrothermal synthesis are overcome this way, the conditioning of using high-end setups for the measurement limits the applicability to a small number of researchers and experiments.

1.3.2 Continuous Flow Synthesis

One step, scalable, processes have been targeted, like the already mentioned **continuous flow hydrothermal synthesis**. This technique pioneered by Adschiri *et. al*,[82,83] relies on the properties of superheated water to effectively tune the characteristics of metal oxides. By using flow systems a fast mixing of near-to-critical aqueous solutions generates a burst of nucleation that reduces the size disparity. The short reaction times, on the order of seconds, further limit growth leading to smaller particles driven by the nucleation dominated mechanism in play. While initially developed for the production of

metal oxides, continuous flow hydrothermal techniques are not limited to metal oxides, as they have been tested for the synthesis of metal sulfides,[84] metal organic frameworks (MOFs),[85] and hydroxyapatite (HAP) in various shapes,[86,87] among other classes of material.

To give an example of the employment of continuous flow the synthesis of metal sulfides has been extensively explored by this technique. For the formation of these compounds a source of sulfur needs to be introduced in the reaction. A common precursor for this end is thiourea. It is non-toxic, and non-volatile keeping the concentration always constant, it can be dissolve in water, and it can generate hydrogen sulfide in solution by a low-energy isomerisation process.[88]

$$NH_2CSNH_2 \leftrightarrow NH_4SCN \quad (1.8)$$

$$NH_4SCN + 4H_2O \rightarrow HS^- + (NH_4)_2CO_3{}^- + H_2O \quad (1.9)$$

$$M^{X+} + xHS^- \rightarrow MS_{X/2} + (x/2)\, H_2S \quad (1.10)$$

The use of thiourea requires its decomposition in order to have the sulfur precursor ready to react in solution. There are two ways of approaching this matter. Firstly, by separately decomposing the thiourea and later mixing with the metal precursor. Secondly, the cold mixing of the metal and sulfur precursor as a cold stream to finally being heated together. The decomposition of thiourea pre-mixing will allow the reaction to start as soon as the two streams encounter each other promoting a "burst of nucleation" similarly to the one described by the LaMer model. If, on the other hand both streams are mixed together before the thermal decomposition of thiourea, the reaction will depend on the kinetics of formation of hydrogen sulfide so that the growth of the particles will be promoted instead.[29]

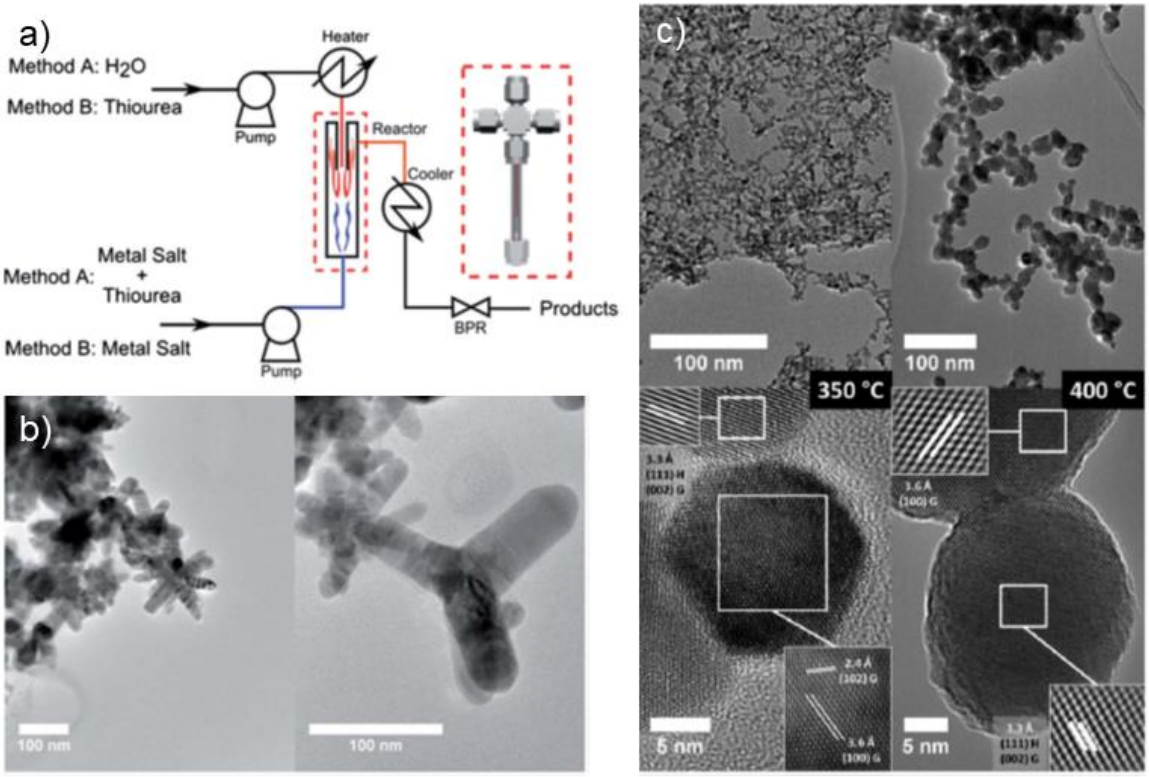

Figure 1.13. Synthesis of CdS by continuous-flow method. a) Setup used for the reactions using a pipe-in-pipe mixing point and two methodologies. b) TEM images of CdS synthetised by Method A at contact temperature ~400°C and short contact times. c) TEM images of the CdS particles prepared by Method B at 350 and 400°C. Squared insets show the crystal planes of the two polymorphs obtained: cubic hawleyite (H) and hexagonal greenockite (G).[84]

From Figure 1.13. the two different proposed methods were employed to synthesise nanoparticles of CdS as reported by Lester *et al.*[89]. When the cold metal salt and thiourea solutions were mixed with a heated stream inducing thiourea decomposition concurrently with metal sulfide formation, bigger particles were encountered as proposed. Alternatively, when two streams composed of a preheated thiourea solution and a cool solution containing the metal salt were mixed in flow, the immediate availability of hydrosulfide from the decomposition of thiourea in the pre-heated stream led to nanometric particles being obtained thanks to the burst nucleation driven mechanism. The main drawback of this technique is the poor control of homogeneity of the samples due to the complexity of thermal gradients in large volume of solution. Although it is capable of controlling the size and morphology of the samples to a greater extent than conventional hydrothermal synthesis, as it is suitable for obtaining nanoparticles by only using water as the solvent by mixing two streams of precursors, there is still a lack of knowledge of the intrinsic processes followed by the materials

obtained and *in situ* measurements are required (similar to hydrothermal synthesis). Additionally, every reaction may require modifications in the setup to control the flow and the temperature that are potentially costly, given the complexity of the reactors. In spite of the drawbacks mentioned above, it is a growing field with a large applicability in industry capable of generating large quantities of the target material in an efficient and controlled manner.

1.3.3 Hot-Injection Synthesis

The mixing reaction of a stream of one precursor with another preheated one used in continuous flow hydrothermal synthesis is in essence a replica of the hot-injection synthesis in which a room temperature precursor is injected into a pre-heated solution of a second reagent to induce a rapid reaction. This synthetic technique has been extensively used for the synthesis of quantum dots (QDs) where the tuning of the size and shape is essential to control its features.[90] By the sudden mixing of the precursors the reaction experiences a temporal separation of the nucleation and growth steps. When both precursors are mixed a "burst" of nucleation takes part in the reaction. It is achieved by the quick formation of one of the precursors, exceeding the critical nucleation threshold. Fast nucleation will then ease the supersaturation in the system. The residual concentration of the monomers will be lower than the critical nucleation concentration again, so no further nucleation is expected. The size discrepancies of the nuclei formed will be minimum avoiding any other growth process. Therefore, the size control will be only dependant on the reaction time and further addition of the precursor.

Although this approach has shown a great reproducibility and control of the particle properties it has a main drawback: the solvent required for the reactions. For pre-heating the solution and driving the nucleation of the precursors to a critical point, high-boiling point solvents are required. As an example, a commonly used solvent-capping agent is tri-n-octylphosphine oxide (TOPO).[91–93] The temperature at which the injection occurs is up to 300 °C. The kinds of solvents capable of reaching these temperatures are usually long-chained petrochemical organic solvents, which are costly and environmental hazardous.

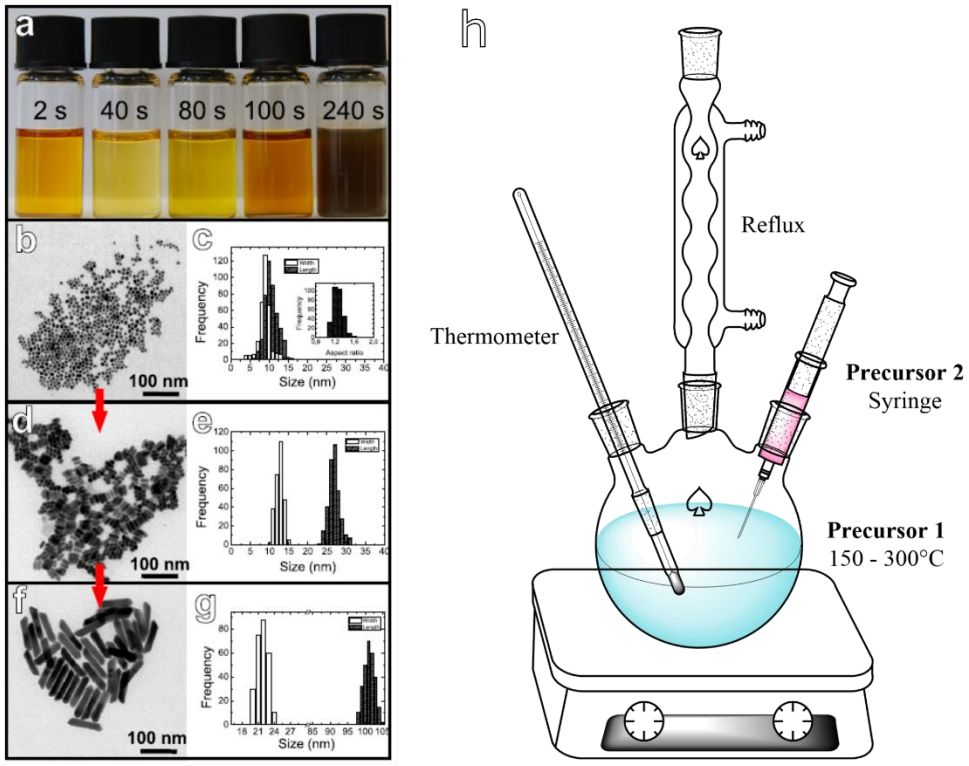

Figure 1.14. a)-g) are adapted from "Shape and Size Control of Colloidal Copper (I) sulfide nanorods".[35] a) photograph of the nanorods synthesised at different times after the injection of the sulfur precursor. b), d) and f) are TEM images from the nanorods obtained accompanied with c), e) and g) which are histograms of the width and length of the nanorods obtained. The times for b)-c) is 2:10 min., d)- e) 2:30 min and f)-g) 5 min. h) Standard setup for a hot injection reaction.

1.3.4 Hydrothermal Injection Synthesis

To overcome all the previously mentioned drawbacks it was decided to design a new type of reactor capable of gathering most of the best characteristics of the already mentioned techniques. A similar approach to the continuous-flow system was taken to design the hydrothermal injection reactor. It uses superheated water to carry out the reaction, where the aqueous solvents are confined in a stainless-steel reactor chamber. The precursor will be then heated over the boiling point under autogenous pressure, similar to hydrothermal processes. When the target temperature is reached, the other precursor is injected to the reaction point, undergoing a similar fast "burst" of nucleation as for hot-injection processes. Therefore, a temporal separation of nucleation and growth is achieved in water, with a complete track of the synthetic conditions. Its characteristics and commissioning will be extensively described in Chapter 2. Experimental.

Table 1.2. Comparison of the different synthetic techniques. In green are the positive features and in red the negative ones.

Hydrothermal Synthesis	Hot – Injection Synthesis	Hydrothermal Injection Reactor
Water as a solvent	Separation of nucleation and growth	Water used as a solvent
Poor tracking of temperature and pressure conditions	Good size and polymorph control	Great polymorph control
Thermal ramp to desired temperature. Not great polymorph control	Use of expensive and hazardous solvents	Real – time tracking of the internal temperature and pressure

The new reactor must be able to carry out the aqueous reactions at autogenous pressure without any leaks to contain the autogenous pressure effectively. At the same time, it must be capable of injecting the second precursor into the preheated solution safely. The design must comprise the ability of generating a closed system that avoid losses of pressure with the ability to pump the reactants at the injection point. The reaction conditions are monitored at all stages of the reaction for the sake of controlling the reaction conditions as well as avoiding any overpressure or leak. Therefore, the design must include a tracking system capable of precisely describe the internal conditions of the reaction. Finally, as this technique is expected to be extended to as many materials as possible, its constituents must be chemically inert to as many compounds as possible.

To achieve all these requirements the reactor was constructed with stainless-steel 316 Swagelok® components. These components are airtight, corrosion resistant stainless-steel, widely used for flow reaction setups, with tubing and joints ready for high temperature and pressure operation. The reactor is manufactured following Swagelok® standards. Below in Figure 1.15 the design of the hydrothermal injection reactor is given.

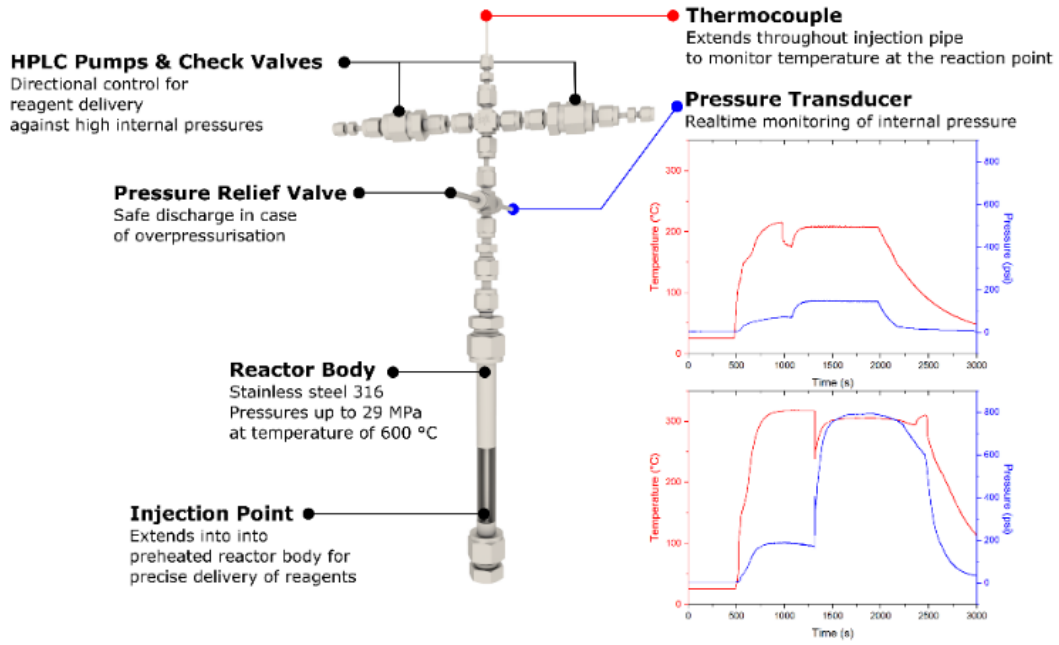

Figure 1.15. Schematic of the hydrothermal injection reactor, with insets showing typical temperature and pressure profiles of injection reactions at 200 °C (top) and 300 °C (bottom).

This technique has already been tested for a variety of compounds in particular CdS.[94] The effect of the use of different sulfur and cadmium sources as well as the employment of several variations of the technique, helped to provide a general idea of the mechanisms related to the formation of the different morphologies of the CdS synthesised. As the given example in Figure 1.16 the injection method was followed. It consisted of the injection of $Cd(NO_3)_2$ to a preheated solution of thiourea. The injection of the cadmium source occurred 5 minutes after the target temperature was reached in order to let the heating system stabilise and to ensure the maximum concentration of the active sulfur source in solution from the decomposition of thiourea, prior to injection of the cadmium source to induce reaction. At 200°C tetrahedra-like particles were observed while when increasing the temperature to 250 and 300°C hexagonal rods became the main feature. This may be explained by the influence of the cubic phase of CdS during the nucleation and growth of the particles at lower temperatures, while when the reaction temperature is increased the thermodynamically more favourable hexagonal phase is nucleated and drives subsequent growth. The intermediate feature of branched rods is expected to be the result of an interplay of the cubic and the hexagonal phases. The ability to test different conditions and methodologies helped to general a general idea of the

processes followed at the formation of the CdS materials. As well the tracking of the internal temperature and pressure before, during and after reaction is not only used as a safety feature avoiding over-pressurisation of the system, but it gives a full idea of the synthetic conditions.

By the use of this synthetic technique a great polymorph control was shown by XRD analysis and further morphological information could be extracted by SEM images. Therefore, the presence of the different structures and the subsequent shapes and growth processes could be related. It shows the great control of morphology and crystal structures by this technique by using water as the solvent and keeping the experimental conditions as simple as possible.

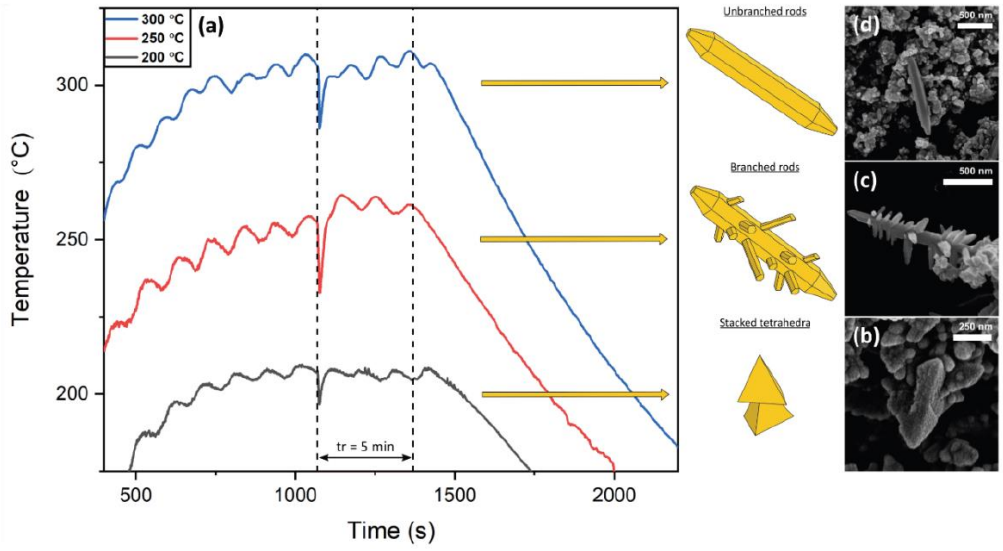

Figure 1.16. a) Temperature against time profile of the injection reactions at 200, 250 and 300°C. Each profile goes along with the schematic illustrations of the morphologies obtained and the SEM images for each temperature d), c) and b).[94]

1.3.5 Mapping of Synthetic Conditions

Regardless of the synthetic method chosen, the number of factors that affect the development of the reactions create an intricate set of data which are complicated to correlate to the resulting products. The large number of samples directly correlated to the synthetic variables (synthetic method, precursor choice, temperature, concentration of precursor, ratio, ….) can be presented in a large dataset. Obtaining trends from the correspondence of the factors playing a role in the reaction is not less than a herculean task. Therefore, statistical analysis can be applied to simplify the data and graphically

relate the different factors showing the correlations between the sample points. Principal Component Analysis (PCA) is a powerful statistical analysis capable of reducing the dimensionality without losing information of the variability of the data and graphically represent the correlation of the samples depending on the variables that affect the most the data, whatever it is. Although it is a mathematical approximation which accounts for no physical meaning it can be easily justified and explained. That way a simple correspondence of the conditions attempted *vs.* the characteristics of the samples can be generated with little extra effort. A more detailed explanation of this statistical approach is given in Chapter 2. Experimental, but here is highlighted its application to a range of cadmium sulfide samples prepared by conventional batch hydrothermal synthesis, and hydrothermal injection, as discussed above as shown in Figure 1.17.

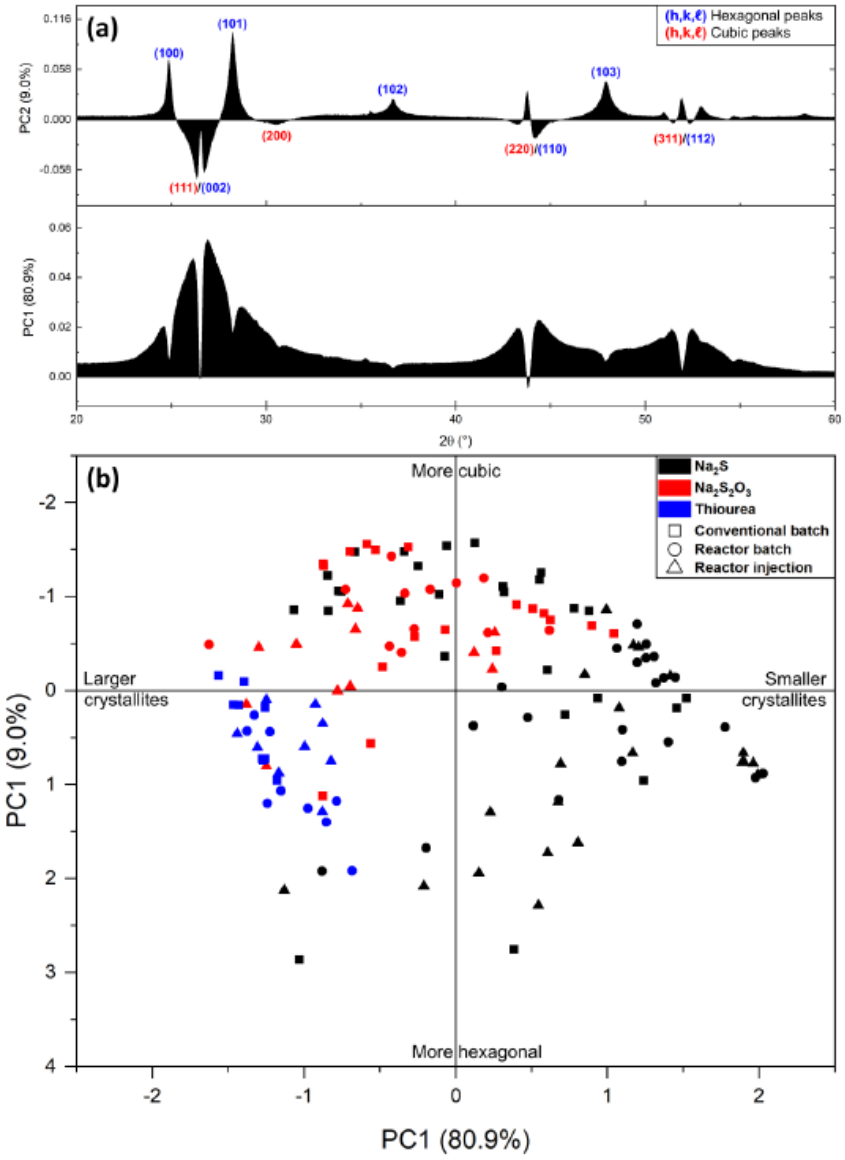

Figure 1.17. a) Loading plots of the Principal Component Analysis of 138 cadmium sulfide samples prepared in the lab. The first Principal Component (PC1) is plotted above and the second Principal Component below (PC2). b) Scoring plot of each sample defined by its colour (sulfur precursor) and shape (method). [94]

Figure 1.17 (a) shows that the component or direction that gives the largest variability to the patterns is the peak shape, closely related to the crystallite size, defined as PC1. Therefore, if that a sample is positioned in the more positive *x*-axis, the broader is the peak, so that the smaller will be the crystallite size for that condition. The opposite effect is expected when a sample is positioned at negative values of the PC1, showing bigger crystals. Additionally, when observing the loadings in Figure 1.17 a) for PC2 can be concluded that the second component is closely related to the peak positioning. That

peak position defines the polymorph present in the sample by the XRD pattern. The positive values will be more correlated to the cubic phase, at the positive values of the PC2 loadings, while negative ones to the hexagonal component of the chalcogenide.

Thus, after defining the meaning of the components, the different variables can be correlated and observe how the precursor affect at the polymorph selection and the crystal growth. Thiourea needs to decompose to yield the solution with reactive sulfur. It promotes a slower reaction kinetics, so that the concentration of sulfur in solution will be constant aiding larger particle size and the thermodynamically preferred hexagonal polymorph rather than the kinetic cubic one. On the other hand, Na_2S is readily decomposed in solution. The instant saturation of sulfur will be larger than for thiourea. As the cadmium is injected it will cause a burst of nucleation, with minimal size disparity. It is observed as the samples for sodium sulfide are preferentially clustered at positive values in the *x*-axis. This will hinder any additional grow. Therefore, the reaction conditions and the particle properties are easily correlated by PCA showing a polymorph-size selectivity depending on the precursor selection.

1.4 Aims and Objectives

The use of hydrothermal synthesis has led to the control of the size and shape of various materials of inorganic nature. It has also been highlighted as a green, cheap, and reliable synthetic method, by using water in superheated conditions as the solvent. Mineralisation processes in nature can be easily replicated *via* hydrothermal synthesis. Such natural hydrothermal mineralisation processes often involve the reaction of metals dissolved or partially dissolved in running water with the components of the ground (silicates, carbonates, phosphates, ...) to form minerals. These processes frequently occur in hydrothermal vents, but are also associated with biological processes (carbonate and phosphates) or might occur in natural repositories of Spent Nuclear Fuel (SNF), as for the silicates.

The primary aim of this thesis is to examine the scope of hydrothermal methods for the controlled synthesis of important mineral species. To this end, three mineral classes have been targeted: silicates, phosphates, and carbonates. In particular the potential of the newly developed hydrothermal injection reactor will be assessed in detail. A secondary aim of this work is to establish the possibilities offered by the statistical method of Principal Component Analysis in facilitating the mapping of synthetic landscapes which is a necessary facet of both process optimisation and materials discovery.

With regards to the silicates, the natural existence and formation of coffinite (uranium silicate, $USiO_4$), reported for decades as occurring in geological environments has, to the best of our knowledge, never been synthesised pure *in situ* in the lab. Given its relevance in natural systems, and importantly, its potential implications for the storage of spent nuclear fuels, the synthesis of pure coffinite is enormously important in order to understand its role in these systems. The overarching aim of this part of the project is thus to simulate how nature yields this material by an easy mild-hydrothermal process. Different conditions must be tested as the synthetic stability of this material is fairly narrow. Due to the low availability of uranium to perform these reactions, various silicates will be attempted firstly, as non-radioactive analogues. Zircon ($ZrSiO_4$) and stetindite ($CeSiO_4$) have been reported to have a zircon-type structure, as coffinite. This means that the atoms arrange periodically to form a lattice in a similar way. Additionally,

cerium has been proposed to have chemical similarities to Pu making it a great candidate to test the optimum conditions for the synthesis of other metal silicates. Zirconium, on the other hand, has been reported to yield mixed uranium silicates known as Chernobylite due to its appearance at chernobyl's nuclear plant residual "lava". The presence of uranium in this structure supports zircon to be a promising silicate to store uranium waste in long-term repositories as a vitrification material. Therefore, once the optimum synthetic conditions are known for these materials, they may prove to be transferrable for coffinite synthesis. Thirdly, thorite ($ThSiO_4$) is known to be the chemically closest silicate to coffinite. The optimum conditions obtained from the previous surrogates will be tested and optimised by the formation of this mineral. Once the conditions required for the synthesis of the pure form of three different structurally similar silicates and by reducing the synthetic parameters required for the stability of these materials the synthesis of coffinite is suggested to be achievable.

The optimisation of the parameters required to obtain a certain material, as for the coffinite synthesis, is time consuming and large numbers of samples are usually required prior to grasping the most effective synthetic protocol. Nonetheless, the improvement of the mineralisation techniques accompanied by the use of statistical approaches to reduce the complexity of the data has led to an easy and fast mapping of the relationship between synthetic condition parameters and compound selectivity. For that reason, Principal Component Analysis (PCA) is proposed as a great candidate for the identification of the main variables that play a role in the mineralisation, reducing the dimensionality of the data to the simplest possible and only expressing the main ones when being correlated. To test the applicability of the PCA approach, two minerals have been aimed to be subjected to this analysis: calcium orthophosphates and calcium carbonate. They are an example of non-classic nucleation materials and show a great complexity of composition and polymorph selectivity closely related to the synthetic conditions (temperature, pH, pressure, *etc*.).

Firstly, calcium orthophosphates are known to be a family of materials in which the crystallisation of one phosphate or another will be related to the conditions of synthesis. In particular, three calcium phosphates will be studied: brushite, monetite and hydroxyapatite. Monetite is known to be the dehydrated version of brushite. On the other hand, hydroxyapatite is reported to have a high biological significance. The selective

formation of the three compounds will be tested at different temperatures, phosphate precursor, Ca/P precursor ratio and pH. The presence of the different phosphate phases will be estimated by XRD and FTIR. Thereafter, in order to plot the relationship of conditions and compound formed, the XRD patterns will be subjected to Principal Component Analysis. The most optimised parameters for the selective synthesis of each phosphate will be represented by this analysis. For the sake of controlling the different synthetic conditions effectively and processing a high number of samples in the most efficient way, the injection hydrothermal reactor will be employed. By the *in situ* tracking of the temperature of mineralisation, the specific parameters at which each compound is formed will be known.

On the other hand, **calcium carbonate**, is known to be essential for different processes for life. The main difference with the phosphates is that although only calcium carbonate is yielded at different synthetic conditions, it exhibits different atomic arrangement in the structure when changing the external conditions. These differentiator atomic dispositions are known as polymorphs of a compound. Calcium carbonate is known to have three anhydrous polymorphs (calcite, aragonite and vaterite) with a different stability energy and properties. Calcium carbonate has been reported to follow a non-classical pathway, in which prenucleation clusters will lead to an amorphous phase that will influence the polymorphic selection. The conditions of mineralisation will drastically determine the polymorphic content in the samples. The way to recognise the presence of the different polymorphs is by Rietveld refinement of the structure against the XRD patterns. The presence of the different polymorphs will be corroborated by FTIR and Raman spectroscopy. The mapping of the conditions for the synthesis of each polymorph is aimed to be performed in a simple way by tuning the synthesis conditions in the hydrothermal injection reactor. A full tracking of the different precursors employed, their concentration and temperature of synthesis, among others, will be explored in this project. Nonetheless, due to the number of variables considered, the FTIR, Raman and XRD patterns will be subjected to PCA. It will correlate the polymorph present in the sample and the conditions of formation. As well, the effectiveness of this statistical analysis for the different analysis techniques will be tested aiming to point out which one is more effective to show the correlation of the polymorphs.

A full mapping of the optimal conditions for the phosphates and the polymorphs of calcium carbonate is targeted. As well, it is expected to show the capability of the reactor to control the properties of the material by an easy and fast synthesis of the compounds at different conditions. Finally, we aim to show how PCA is capable of showing the optimal synthetic conditions to obtain from different compounds, to more essential, such as the atomic arrangement expressed as polymorphs.

1.5 References

1 M. Yabushita, M. Yoshida, F. Muto, M. Horie, Y. Kunitake, T. Nishitoba, S. Maki, K. Kanie, T. Yokoi and A. Muramatsu, *Mol. Catal.*, 2019, **478**, 110579.
2 H.-Y. He, *Colloids Surfaces A Physicochem. Eng. Asp.*, 2020, **589**, 124149.
3 T. AlZoubi, H. Qutaish, E. Al-Shawwa and S. Hamzawy, *Opt. Mater. (Amst).*, 2018, **77**, 226–232.
4 B. Wang, J. Yu, L. Sui, S. Zhu, Z. Tang, B. Yang and S. Lu, *Adv. Sci.*, 2021, **8**, 1–8.
5 W. Jeong, G. Gwon, J. H. Ha, D. Kim, K. J. Eom, J. H. Park, S. J. Kang, B. Kwak, J. Il Hong, S. Lee, D. C. Hyun and S. Lee, *Biosens. Bioelectron.*, 2021, **171**, 112717.
6 K. Byrappa and M. Yoshimura, *Handbook of Hydrothermal Technology*, Noyes Publications, New Jersey, 2001.
7 A. Rabenau, *Angew. Chemie Int. Ed. English*, 1985, **24**, 1026–1040.
8 R. A. Laudise, 2007, vol. XXVIII, pp. 1–47.
9 R. A. Laudise and A. A. Ballman, *J. Am. Chem. Soc.*, 1958, **80**, 2655–2657.
10 C. Li, 1989, **82**, 1479–1482.
11 S. Wei Lu, B. I. Lee, Z. Lin Wang and W. D. Samuels, *J. Cryst. Growth*, 2000, **219**, 269–276.
12 W. J. Li, E. W. Shi, J. M. Ko, Z. Z. Chen, H. Ogino and T. Fukuda, *J. Cryst. Growth*, 2003, **250**, 418–422.
13 M. Manikandan, K. Subramani, M. Sathish and S. Dhanuskodi, *RSC Adv.*, 2020, **10**, 13632–13641.
14 P. Kumar, P. Kumar, H. Khanduri, S. Pathak, S. Pathak, A. Singh, A. Singh, A. Singh, G. A. Basheed, G. A. Basheed, R. P. Pant and R. P. Pant, *Dalt. Trans.*, 2020, **49**, 8672–8683.
15 J. L. Mi, K. M. Ø. Jensen, C. Tyrsted, M. Bremholm and B. B. Iversen, *CrystEngComm*, 2015, **17**, 6868–6877.
16 M. Panahi-Kalamuei, O. Amiri and M. Salavati-Niasari, *J. Mater. Res. Technol.*, 2020, **9**, 2679–2690.
17 D. Hariharan, P. Thangamuniyandi, A. Jegatha Christy, R. Vasantharaja, P. Selvakumar, S. Sagadevan, A. Pugazhendhi and L. C. Nehru, *J. Photochem. Photobiol. B Biol.*, 2020, **202**, 111636.
18 W. Martin, J. Baross, D. Kelley and M. J. Russell, *Nat. Rev. Microbiol.*, 2008, **6**, 805–814.
19 J. W. Deming and J. A. Baross, *Geochim. Cosmochim. Acta*, 1993, **57**, 3219–3230.
20 H. W. Jannasch and M. J. Mottl, *Science*, 1985, **229**, 717–725.
21 B. Sun and H. Sirringhaus, *Nano Lett.*, 2005, **5**, 2408–2413.
22 B. Sun and H. Sirringhaus, *J. Am. Chem. Soc.*, 2006, **128**, 16231–16237.
23 N. Mertzsch, *ChemTexts*, 2020, **6**, 1–12.
24 A. C. Walker, *J. Am. Ceram. Soc.*, 1953, **36**, 250–256.
25 A. Arnau Vives, *Piezoelectric Transducers and Applications*, Springer, Berlin, Heidelberg, 1st edn., 2004.
26 F. Iwasaki and H. Iwasaki, *J. Cryst. Growth*, 2002, **237**–**239**, 820–827.
27 A. K. Padhi, K. S. Nanjundaswamy and J. B. Goodenough, *J. Electrochem. Soc.*, 1997, **144**, 1188–1194.
28 P. Benedek, N. Wenzler, M. Yarema and V. C. Wood, *RSC Adv.*, 2017, **7**, 17763–17767.
29 P. W. Dunne, A. S. Munn, C. L. Starkey, T. A. Huddle and E. H. Lester, *Philos. Trans. R. Soc. A Math. Phys. Eng. Sci.*, 2015, **373**, 20150015.
30 H. Weingärtner and E. U. Franck, *Angew. Chemie - Int. Ed.*, 2005, **44**, 2672–2692.
31 N. Akiya and P. E. Savage, *Chem. Rev.*, 2002, **102**, 2725–2750.
32 G. M. Schneider, *Phys. Chem. Chem. Phys.*, 2002, **4**, 845–852.
33 R. Grzanna and G. M. Schneider, *Zeitschrift fur Phys. Chemie*, 1996, **193**, 41–47.
34 H. Weingärtner, D. Klante and G. M. Schneider, *J. Solution Chem.*, 1999, **28**, 435–446.
35 M. Kruszynska, H. Borchert, A. Bachmatiuk, M. H. Rümmeli, B. Büchner, J. Parisi and J. Kolny-Olesiak, *ACS Nano*, 2012, **6**, 5889–5896.
36 A. Z. Volmer, M. and Weber, *Zeitschrift für Phys. Chemie*, 1926, **119**, 277–301.
37 R. Becker and W. Döring, *Ann. Phys.*, 1935, **416**, 719–752.
38 W. Z. Z. Ostwald, *Phys. Chem.*, 1897, **22**, 289−330.
39 P. R. Ten Wolde and D. Frenkel, *Science (80-.).*, 1997, **277**, 1975–1978.

40 O. Gliko, N. Neumaier, W. Pan, I. Haase, M. Fischer, A. Bacher, S. Weinkauf and P. G. Vekilov, *J. Am. Chem. Soc.*, 2005, **127**, 3433–3438.
41 W. Ostwald, *Zeitschrift für Phys. Chemie*, 1900, **34U**, 495–503.
42 D. L. Kinser and L. L. Hench, *J. Am. Ceram. Soc.*, 1968, **51**, 445–449.
43 D. Gebauer and H. Cölfen, *Nano Today*, 2011, **6**, 564–584.
44 Y. Peng, F. Wang, Z. Wang, A. M. Alsayed, Z. Zhang, A. G. Yodh and Y. Han, *Nat. Mater.*, 2015, **14**, 101–108.
45 M. Farhadi-Khouzani, D. M. Chevrier, P. Zhang, N. Hedin and D. Gebauer, *Angew. Chemie - Int. Ed.*, 2016, **55**, 8117–8120.
46 D. Gebauer, *Science*, 2008, **120**, 1819–1823.
47 F. Nudelman, K. Pieterse, A. George, P. H. H. Bomans, H. Friedrich, L. J. Brylka, P. A. J. Hilbers, G. De With and N. A. J. M. Sommerdijk, *Nat. Mater.*, 2010, **9**, 1004–1009.
48 V. K. LaMer and R. H. Dinegar, *J. Am. Chem. Soc.*, 1950, **72**, 4847–4854.
49 P. W. Dunne, A. S. Munn, C. L. Starkey, T. A. Huddle and E. H. Lester, *Philos. Trans. R. Soc. A Math. Phys. Eng. Sci.*,
50 W. Ostwald, *Zeitschrift für Phys. Chemie*, 1900, **34U**, 495–503.
51 V. N. Richards, N. P. Rath and W. E. Buhro, *Chem. Mater.*, 2010, **22**, 3556–3567.
52 E. E. Finney, S. P. Shields, W. E. Buhro and R. G. Finke, *Chem. Mater.*, 2012, **24**, 1718–1725.
53 B. J. Hornstein and R. G. Finke, *Chem. Mater.*, 2004, **16**, 3972–3972.
54 C. Besson, E. E. Finney and R. G. Finke, *J. Am. Chem. Soc.*, 2005, **127**, 8179–8184.
55 C. Besson, E. E. Finney and R. G. Finke, *Chem. Mater.*, 2005, **17**, 4925–4938.
56 E. E. Finney and R. G. Finke, *Chem. Mater.*, 2008, **20**, 1956–1970.
57 P. D. Kent, J. E. Mondloch and R. G. Finke, *J. Am. Chem. Soc.*, 2014, **136**, 1930–1941.
58 S. E. Wolf and L. B. Gower, *New Perspectives on Mineral Nucleation and Growth*, Springer International Publishing, Cham, 2017.
59 M. Ocaña, R. Rodriguez-Clemente and C. J. Serna, *Adv. Mater.*, 1995, **7**, 212–216.
60 W. K. Burton, N. Cabrera and F. C. Frank, *Philos. Trans. R. Soc. London. Ser. A, Math. Phys. Sci.*, 1951, **243**, 299–358.
61 A. Sanz Arjona, "Hydrothermal Synthesis of ZnS and PbS . Phase and Shape Control", B.Sc. Thesis, Trinity College Dublin, 2018.
62 J.-P. Zhu, S.-H. Yu, Z.-B. He, J. Jiang, K. Chen and X.-Y. Zhou, *Chem. Commun.*, 2005, 5802.
63 M. Ocaña, R. Rodriguez-Clemente and C. J. Serna, *Adv. Mater.*, 1995, **7**, 212–216.
64 R. L. Penn and J. F. Banfield, *Geochim. Cosmochim. Acta*, 1999, **63**, 1549–1557.
65 C. Y. Sun, M. A. Marcus, M. J. Frazier, A. J. Giuffre, T. Mass and P. U. P. A. Gilbert, *ACS Nano*, 2017, **11**, 6612–6622.
66 J. Ahmed, Menaka and A. K. Ganguli, *CrystEngComm*, 2009, **11**, 927.
67 A. W. Xu, M. Antonietti, H. Cölfen and Y. P. Fang, *Adv. Funct. Mater.*, 2006, **16**, 903–908.
68 J.-P. Andreassen, R. Beck and M. Nergaard, *Faraday Discuss.*, 2012, **159**, 247.
69 F. Bai, D. Wang, Z. Huo, W. Chen, L. Liu, X. Liang, C. Chen, X. Wang, Q. Peng and Y. Li, *Angew. Chemie*, 2007, **119**, 6770–6773.
70 J. Zhuang, H. Wu, Y. Yang and Y. C. Cao, *Angew. Chemie - Int. Ed.*, 2008, **47**, 2208–2212.
71 G. C. Kennedy, *Am. J. Sci.*, 1950, **248**, 540–564.
72 P. Afanasiev, *Comptes Rendus Chim.*, 2008, **11**, 159–182.
73 K. M. Ø. Jensen, M. Christensen, P. Juhas, C. Tyrsted, E. D. Bøjesen, N. Lock, S. J. L. Billinge and B. B. Iversen, *J. Am. Chem. Soc.*, 2012, **134**, 6785–6792.
74 István T. Horváth and P. T. Anastas, *Chem. Rev.*, 2007, **107**, 2167–2168.
75 P. T. Anastas and I. T. Hovarth, *Green Chemistry: Theory and Practice*, Oxford University Press, New York, 1998.
76 T. J. Collins, *Green Chemistry, Macmillan Encyclopedia of Chemistry*, New York, 1997, vol. 2.
77 P. Anastas and N. Eghbali, *Chem. Soc. Rev.*, 2010, **39**, 301–312.
78 A. F. Ali, Z. A. Alrowaili, E. M. El-Giar, M. M. Ahmed and A. M. El-Kady, *Ceram. Int.*, 2021, **47**, 3928–3937.
79 S. Ahmadian-Fard-Fini, M. Salavati-Niasari and D. Ghanbari, *Spectrochim. Acta Part A Mol. Biomol. Spectrosc.*, 2018, **203**, 481–493.
80 F. Lorestani, Z. Shahnavaz, P. Mn, Y. Alias and N. S. A. Manan, *Sensors Actuators B Chem.*, 2015, **208**, 389–398.
81 M. Mulu, D. RamaDevi, N. Belachew and K. Basavaiah, *RSC Adv.*, 2021, **11**, 24536–24542.
82 T. Adschiri, K. Kanazawa and K. Arai, *J. Am. Ceram. Soc.*, 1992, **75**, 1019–1022.

83 T. Adschiri and K. Arai, *Supercrit. Fluid Technol. Mater. Sci. Eng.*, 2002, 227–235.
84 P. W. Dunne, C. L. Starkey, M. Gimeno-Fabra and E. H. Lester, *Nanoscale*, 2014, **6**, 2406–2418.
85 M. Gimeno-Fabra, A. S. Munn, L. A. Stevens, T. C. Drage, D. M. Grant, R. J. Kashtiban, J. Sloan, E. Lester and R. I. Walton, *Chem. Commun.*, 2012, **48**, 10642–10644.
86 A. A. Chaudhry, S. Haque, S. Kellici, P. Boldrin, I. Rehman, F. A. Khalid and J. A. Darr, *Chem. Commun.*, 2006, 2286–2288.
87 E. Lester, S. V. Y. Tang, A. Khlobystov, V. L. Rose, L. Buttery and C. J. Roberts, *CrystEngComm*, 2013, **15**, 3256–3260.
88 W. H. R. Shaw and D. G. Walker, *J. Am. Chem. Soc.*, 1956, **78**, 5769–5772.
89 P. W. Dunne, C. L. Starkey, M. Gimeno-Fabra and E. H. Lester, *Nanoscale*, 2014, **6**, 2406–2418.
90 C. De Mello Donegá, P. Liljeroth and D. Vanmaekelbergh, *Small*, 2005, **1**, 1152–1162.
91 C. B. Murray, D. J. Norris and M. G. Bawendi, *J. Am. Chem. Soc.*, 1993, **115**, 8706–8715.
92 S. N. Sharma, H. Sharma, G. Singh and S. M. Shivaprasad, *Mater. Chem. Phys.*, 2008, **110**, 471–480.
93 A. J. Morris-Cohen, M. T. Frederick, G. D. Lilly, E. A. McArthur and E. A. Weiss, *J. Phys. Chem. Lett.*, 2010, **1**, 1078–1081.
94 Andrew S. Bathe, "The Phase- and Shape-Controlled Synthesis of Metal Sulfide Nano- and Micromaterials", Ph.D. Thesis, Trinity College Dublin, 2021.

Chapter 2. Experimental

2.1 Outline

In this chapter the experimental procedures for the synthesis techniques employed in this thesis are outlined. The testing and requirements for the experimental operations are considered prior the experiment design. The two main synthetic approaches are classic "batch" hydrothermal and the novel injection reactor synthesis, all of them gathered around the concept of hydrothermal synthesis.

This chapter also includes a summary of the characterisation techniques employed to describe the synthesised materials. As well as the post-measurement analysis using the characterisation techniques such as Rietveld refinement and Pair Distribution Function analysis. Detailed experimental procedures for every material synthesis are given in each corresponding chapter.

2.2 Conventional Batch Hydrothermal Method

Conventional batch reactions are carried out by placing the reactants in a sealed autoclave. It consists of a PTFE (Teflon®) cup and cover, surrounded by a stainless-steel system as described in Chapter 1. Some of the reactions performed in this thesis were done by conventional hydrothermal batch reactions, so the standard operational procedure will be described, being similar for all of them.

The autoclaves were purchased from Parr instruments®. The 4749 model has an internal volume of 23 mL operating at a maximum temperature of 250 °C and 12.4 MPa. In a standard reaction the fill fraction, ff, should not exceed 0.52 (12 mL) of the total internal volume of the autoclave. The total ff given by the manufacturer that must never be exceeded for inorganic materials is two thirds of the volume (0.66). For dissolving materials strong mineral acids can be used including HF, HCl, H_2SO_4, HNO_3, *aqua regia*, *etc.* The fill volume which directly influences the internal pressure reached, and temperatures employed are given by the manufacturer as in Table 2.1 to ensure safe operation.

Table 2.1. Safety table given by manufactures manual.[1,2] Pressure developed at constant volume by 10 mL of 22.9% HCl in a 23 mL space.

Temperature (°C)	Pressure (psi)	Pressure (10^3bar)
132	70	1.0
159	125	1.81
191	265	3.84
220	510	7.40
250	920	13.3

The container for a standard hydrothermal synthesis is a dry and clean 23 mL Teflon® cup. Both inorganic precursors are prepared and pipetted in a pre-established order. A standard reaction in this thesis will use 10 mL of a solution conformed by 5 mL of each precursor, 0.43 of the fill fraction (ff). The container is placed in the stainless-steel case. Secondly, the bursting and corrosion discs are placed on the Teflon® lid. Finally, the coiled system is screwed tight by the means of a particular wrench and brace mounted to the lab bench. Once the reactor (autoclave) is closed, it is introduced into a preheated oven to the desired temperature, never exceeding 250 °C. The internal temperature of the oven has been proven to be constant and reliable by a thermometer attached to the top of the cubicle. The autoclaves are placed in the pre-heated oven and maintained at temperature for the desired reaction time. When the reaction time is finished, the autoclave is removed from the oven and left to cool down to ambient conditions on the lab bench and never opened until room temperature is reached. This is to avoid overpressure in the system and loss of the sample. After opening the reactor, the contents are decanted into a centrifuge tube with the washings of the cup. After every reaction the cups are cleaned by filling with 10 mL of nitric acid and following the procedure outlined above, sealing and heating at 100 °C overnight, washed with distilled water and dried at 75 °C for the next reaction. The samples synthesised are centrifuged, separated from solution, washed, and dried overnight at 65 °C.

2.2.1 Standard Operating Procedure - Conventional Batch Hydrothermal

From the characteristics described above for the batch reaction autoclaves a general standard operating procedure can be outlined. It will be followed for the reactions carried by this methodology in this thesis.

- When designing the reactions, the total volume of the reaction needs to be known and the recommended parameters of the manufacturers must never be exceeded. In the case of inorganic materials synthesis using water as the solvent, 10 mL of the precursors will never be exceeded, which is a total fill fraction of 0.43, well below the limit.
- The two solutions are pipetted in an established order that should be consistent throughout the whole experimental.
- The autoclave must be closed attaching every single piece of the instrumentation once both solutions are mixed. The autoclave should be hand screwed first and then tightened using a specific spanner making it air-tight.
- The oven must be set to the target temperature and preheated before starting the reaction. The internal temperature can be monitored by using a thermometer at the top of the oven.
- When the temperature is reached then the autoclaves are placed in the oven and kept there until the end of the reaction time.
- Once the time is over, they are taken from the oven and left to cool down before opening them.
- All the Teflon® parts of the reactor are then washed. To ensure that they are perfectly clean after all the reactions 10 mL of 10% nitric acid are pipetted in the reactor and followed the same process as a normal reaction to avoid any contaminant interacting in the following reactions.

2.3 The Hydrothermal Injection Reactor

To begin with, a full description of the technical characteristics of the reactor is given to gather a general idea of the different components of the reactor setup. Secondly, the safety considerations and thirdly, the standard procedure to be used for any reaction considering the design and keeping the operator as safe as possible.

The reactor is comprised of a 10 cm tall, ½" diameter and 0.065" wall thickness chamber. Into the reactor chamber protrudes an inner tube of ¼" of diameter. This is connected though a reducer to the HPLC pump. Aliquots are delivered by a Gilson 302 HPLC pump that injects the liquid against pressures over 400 bars. The reactor is heated by a Watlow heating jacket combined with a Proportional-Integral-Derivate (PID) controller. The temperature in the reactor is monitored by a k-type thermocouple extended through the inner tube. The PID controller calculates the error between the expected value and the obtained average based on measurements from the thermocouple and adjust the power input accordingly. The pressure is monitored by an internal pressure transducer. Lastly, the reactor has a pressure relief valve to avoid over pressurisation of the system while running the reaction to protect the reactor from damage. The data obtained from the reactor are recorded using a Picotech TC-08 datalogger operating through PicoLog software. The pressure and the temperature are monitored providing real time data of the precise temperature and pressure of the reaction. The data are visualised by a temperature-time and pressure-time graphic, as shown in Figure 2.3**.** The total internal volume of the reactor is 10 mL.

2.3.1 Safety Considerations

Hydrothermal reaction conditions involve high temperatures under autogenous pressure. Water, the solvent, is carried to superheated conditions. Therefore, every possible source of error needs to be considered. The hazards which can occur in a standard reaction procedure range from degradation of the components of the reactor to explosions. Because of this, the possible risks need to be tiered in terms of possible danger to the operator as well as how to mitigate them. Below the safety protocol is described in different tiers; upon failure of the reactor, the steps to undertake and mitigate the risks are given.

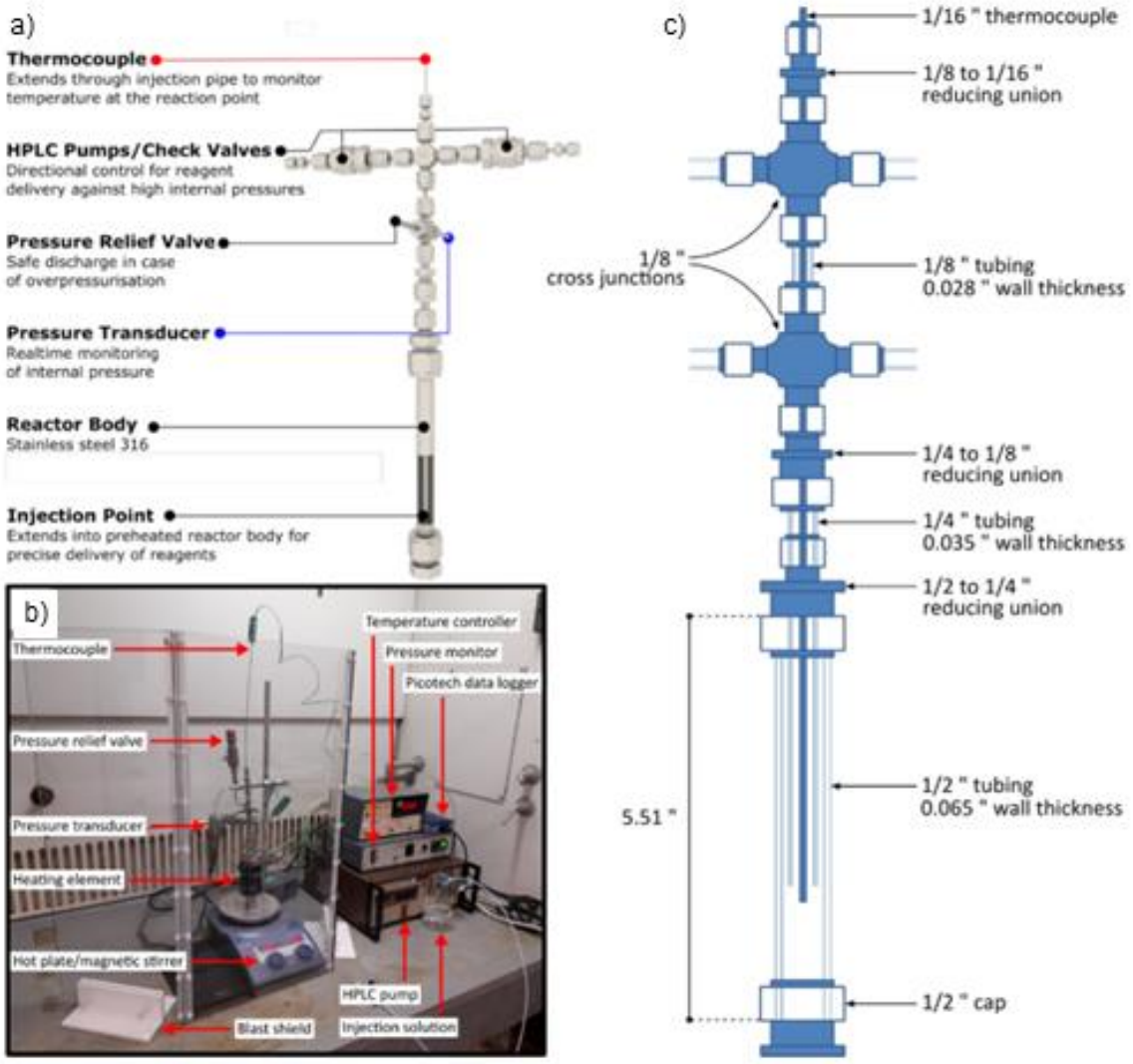

Figure 2.1. a) Schematic description of the parts composing the hydrothermal injection reactor. b) Picture of the reactor setup with the components labelled. c) Schematic of the fittings and components of the reactor.

- **Tier 1:** The main cause of explosion is the chamber being exposed to pressures exceeding the operational limits. To avoid over pressurisation due to experimental design the properties of water at those conditions need to be known. The pressure reached by water contained in a closed vessel has been measured through the years, giving a good picture of how water will behave at high pressure. The plot of those conditions can be obtained from the National Institute of Science and Technology (NIST).[3] It gathers the behaviour of water in a closed system with constant volume (isochoric)

where the content is heated into an inelastic container, comparable to the conditions found in our reactor set up.

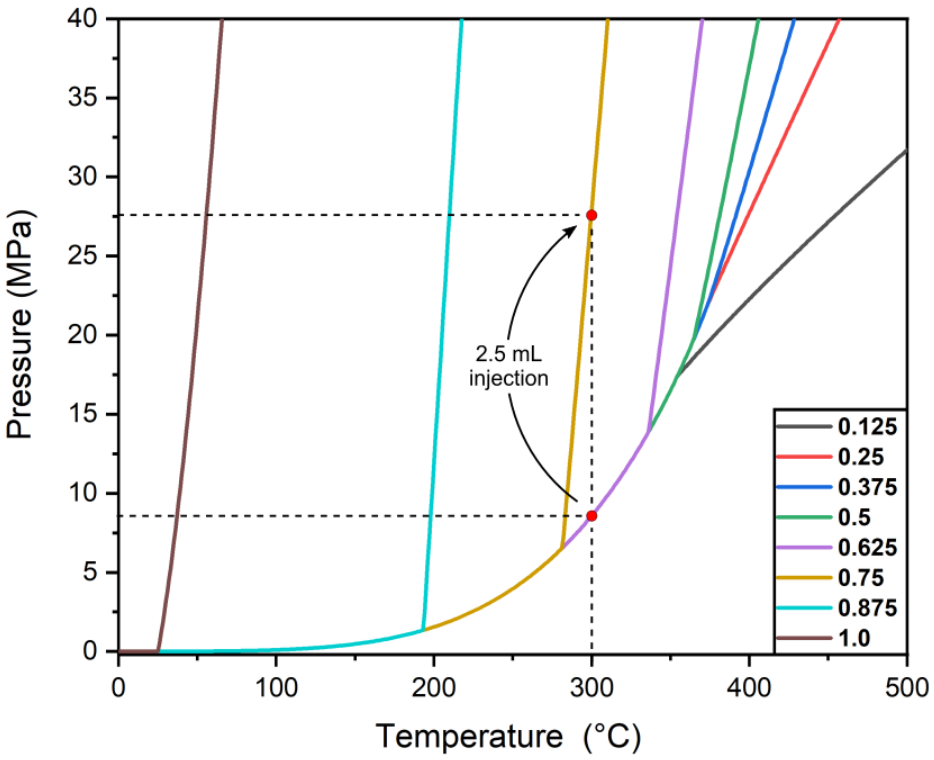

Figure 2.2. Graph of the relationship of autogenous pressure at different temperatures depending at the filling fraction shown by different colours. The dashed lines show the jump pressure when injection takes place. Data obtained for isochoric conditions.[3]

From Figure 2.2 the fill volume can be calculated for our setup. This ensures the reactor will stays in a safe operational region. For example, in a standard procedure 2.5 mL are injected on 5.0 mL (0.5 ff) making up a total of 7.5 mL (0.75 ff). Which will still be under the limits established for the reactor.

- **Tier number 2:** Involves the real time tracking of the internal temperature and pressure. The pressure transducer connected to the Picotech TC-08 data logger combined with the PicoLog software track the internal reactor conditions in real time. In case that the pressure of the reactor increases beyond the safe operation conditions this is always acknowledged by checking the tracking software. The user can see at all times a representation of the temperature *versus* time (s) as well as pressure in psi *versus* time (s). If experimental conditions get over the limit of action, the

heater must be turned off immediately and the operator steps away from the reactor.

- **Tier number 3:** It includes the pressure relief valve. Sudden pressure increases in the reactor, malfunctions of the tracking system or human errors are safeguarded. In case of overpressure, the pressure relief valve will safely release the pressure in the system. It is rated to trigger at 30 MPa. This is still below the pressure limit for the tubing and fittings given by the manufacturer for the design of this reactor (35.16 MPa). That way a passive safety measure that is not dependent on the user is established to release the unlikely sudden overpressure.
- **Tier number 4:** A polycarbonate blast shield is mounted always in front of the reactor in order to control the malfunction of the previous measurements. This shield in combination with the fumehood sash will prevent that the energy in case of an explosion gets away from the reaction area in case that the system gets over pressurised and the relieve valve is incapable of evacuating the built up pressure. The blast shield protects the operator of the reactor and other people present in the lab. By this means, there's a physical barrier between the high pressure system and the operator in case that the previous active and passive safety measures fail.
- **Tier number 5:** The fumehood is not only a physical barrier but also prevents that any fume is generated in the user's area. In case that any hazardous gas is generated by side-reactions when opening the chamber, the fumehood will be able to remove the gas from the area and avoid any intoxication in the lab.

With all these safety measures and by following the pre-established standard operating procedure described below, the safe handling of the reactor is ensured. The reactor safety features are designed to combine both active and passive measurements. It is not only based on the good read of the real-time data from the user, but as well some passive features like the pressure relief valve and the shield avoid any hazard derived from human error. The reactor has proven to be safe and reliable after proper

commissioning and being used over 6 years. Any change in the design will be done in conjunction with the previous statements and carefully tested before being employed.

2.3.2 Standard Operating Procedure - *Hydrothermal Injection Reactor*

From the commissioning and previous research work an optimal Standard Operating Procedure has been outlined for use of the hydrothermal injection reactor. Below the most important features and actions are described for the use of the reactor.

It is designed and tested to keep the user safe and also to keep the system as well functioning as possible for a long time. It requires some work and understanding of the limitations of the system before a reaction may even be attempted. Every time a part or the whole reactor is rebuilt it requires a minimum testing before it can be approved to start a new set of syntheses.

1. As described at the safety considerations, Section 2.3.1, the total volume introduced in the chamber needs to be considered. Every reaction performed in this thesis consisted of 5 mL of one precursor that is preheated to inject 2.5 mL of the second precursor to react. It makes in total 7.5 mL (0.75 ff). It is designed to avoid reaching the pressure (30 MPa) at which the pressure relief valve triggers at a maximum reaction temperature of 300 °C.
2. 5 mL of the known concentration of one of the precursors is pipetted into the dry and clean reactor chamber. The solution is introduced along with a stirring bar.
3. The reactor chamber is then attached to the system, first tightened by hand and then using two spanners of the right size to securely attach it to the reactor body. It is essential to ensure the two sections are tight enough to avoid pressure leakage.
4. Then the heating jacket is fixed to the reactor along with the two K-type thermocouples. One serves as a control temperature to the heating controller and the second one is connected to the data logger to monitor the temperature profile of the heating jacket on the computer. The heating jacket is securely fixed by the two nub screws.
5. The whole reactor is then placed on a stirring plate to maintain constant stirring during the reaction to ensure a homogeneous reaction mixture.

6. Then the connection that goes from the body to the HPLC is disassembled. The tubing end is placed in a conical flask with the stock solution of the second precursor. It is required to pump the solution three times to purge the tubing with the new solution. All the solution that is discarded is placed at a beaker labelled as “waste” to be properly disposed of. Then it is reassembled to the main body.

7. The internal thermocouple that measures the temperature of the reactor should not be removed and kept constantly in the same position at the top of the reactor.

8. After checking that every single part of the reactor is in the right position, a file is created with the name of the reaction, keeping the number of attempts of the reaction and the date of the reaction. Giving an example dd/mm/yyyy_AS000_00 (date_sample name_attempt).

9. The blast shield is then situated in front of the reactor and the target temperature is set at the temperature controller. The protective screen should not be removed from position unless the temperature controller is turned off and the reactor is cooled down.

10. The sash from the fumehood is closed. From this point on, the user must only control the data obtained from the internal conditions in the reactor. The rise in temperatures must be constant and in consonance the internal temperature with the heating jacket one. The pressure trend must be correlated to temperature reading at every time if the tracking system is properly working.

11. Once the temperature reaches the desired temperature, it is held for five minutes to check that there are not large variations of temperature with time.

12. As the set conditions for the reaction are reached, the user must inject the remaining precursor through the HPLC.

13. After injection there is usually a fast decrease and then rise in temperature, followed by an increment of the pressure due to the larger volume of solution in the reactor.

14. The reaction is kept for around ten minutes (600 s) before the temperature controller is turned off and the chamber is left to cool down.

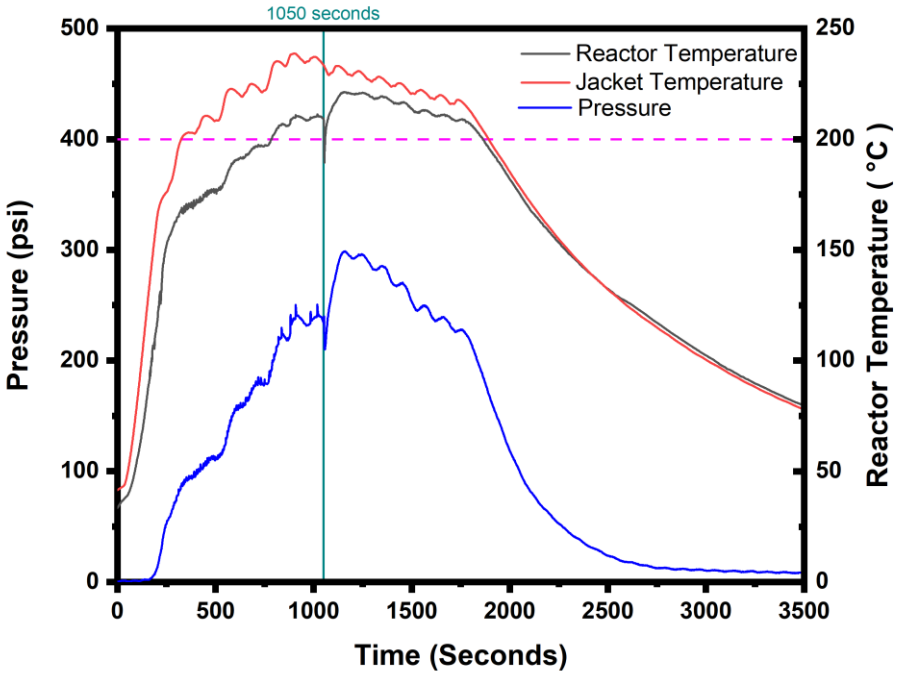

Figure 2.3. Reactor profile for a 200 °C reaction. It shows the pressure profile (blue line), the temperature profile followed by the heating jacket (red line) and the inside of the reactor measured by the K-type thermocouple (black line). Green vertical line shows the injection time and the dashed pink horizontal line the conditions when the second precursor is injected.

15. Once the reactor reaches room temperature the stirring is turned off and the main body of the reactor disassembled from the heating jacket. The reactor cell is detached while being careful not to lose any product along the process.

16. All the content is poured in a beaker and the chamber is cleaned with distilled water to collect any product left behind.

17. Then the end that connects the HPLC pump with the reactor is removed to be purged with water three times and reconnected to the reactor body. The whole reactor is cleaned with water by pumping it through and recovered at the product beaker.

An overall schematic figure of the reactor described is given in Figure 2.4.

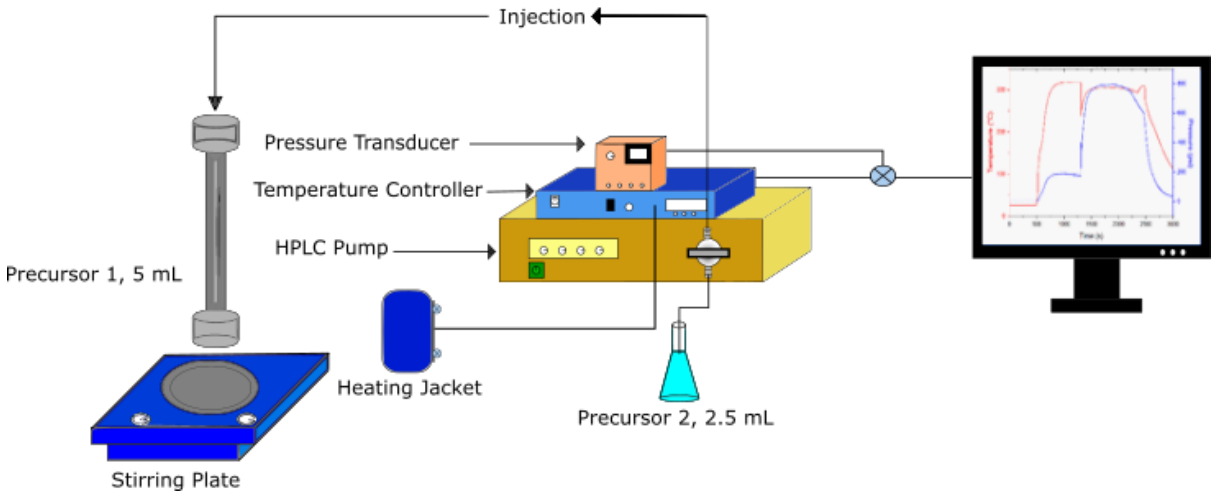

Figure 2.4. Schematic of the reactor setup.

2.4 Characterisation Methods

To describe the materials obtained synthetically by the methods described above, several characterisation methods are required to assess the composition and structural characteristics of the samples. The common characteristic of the samples is that they are solid material so that powder analysis are the ones required. For that reason, the characterisation techniques chosen will be X-ray Diffraction (XRD) to determine the crystal structure of the different compounds or polymorphs as well as corroborating the composition of the material by comparison to the materials' characteristic patterns. Fourier Transform infrared spectroscopy (FTIR) and Raman spectroscopy will be employed to gather information on the type of bonds present in the structure.

2.4.1 X-Ray Diffraction (XRD)

X-rays are a fraction of the electromagnetic spectrum in the range of 100 eV to 1 MeV. In terms of energy this is situated between ultraviolet and γ-rays. The wave nature of X-rays gives a wavelength ranging from 10 to 10^{-3} nm, at the same order as interatomic distances. In this case the physical phenomenon known as diffraction is employed to understand the atomic arrangement of the atoms in the sample.

When X-ray radiation interacts with a material several physical phenomena occur. The interaction can be divided in processes that cause energy loss of the leaving X-ray (inelastic) or the energy is conserved (elastic). X-ray diffraction is part of the elastic scattering subgroup. The wave generated in a crystal (leaving wave), which is characterised by an ordered array of atoms, when X-ray radiation source is scattered elastically will have a certain angular relation to the normal incident plane. The different scattered waves by the array of atoms will recombine to form a new wave. That combination or interference can be constructive or destructive. The wave combination will be constructive when the path difference between the incident and scattered X-rays is an integer of the wavelength value, λ, while the recombination value will be zero when the path difference is equal to $\lambda/2$. In a crystal structure with interplanar spacing equal to d, the angle that satisfies the condition for constructive interference is Bragg's angle, θ_B. This angle is equivalent to the angle between the incident beam to the normal and the diffracted beam to the normal. Therefore, the angular relationship between the incident and the refracted will be equal to $2\theta_B$. The relationship between the interplanar distance

and the diffracted angle is defined by the Bragg's Law (Equation 2.1) applied for the first time in 1913 by W. H. Bragg and W. L. Bragg:

$$n\lambda = 2dsin\theta_B \quad (2.1)$$

Where *n* is the order of reflection and corresponds to the number of wavelengths in the difference path between two adjacent planes. This geometrical relationships are described in Figure 2.5.

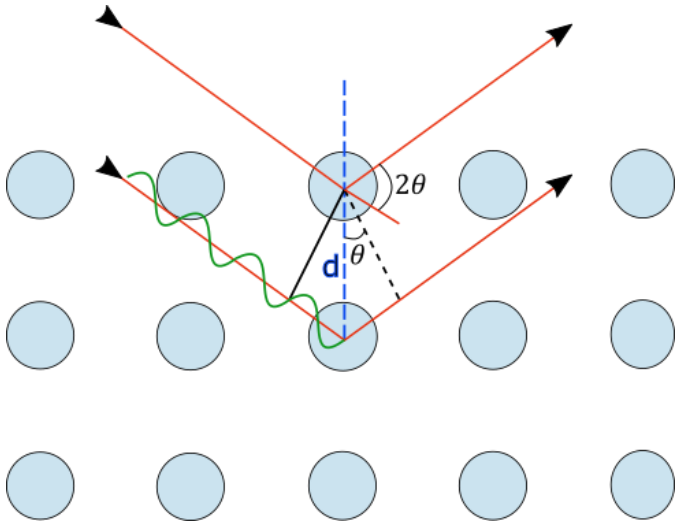

Figure 2.5. X-ray Diffraction in an array of atoms. The atoms are shown as circles that interact with the X-ray wave (red line). The angle with the normal is described as θ and with the leaving wave as 2 θ. The interplanar distance is defined as d.

X-ray diffraction patterns were obtained using a Bruker D2 Phaser. The X-ray source employed was Cu K_α = 1.5418 Å. A zero-background holder was used for the measurements to minimise the background observed.

2.4.2 Fourier-Transform Infrared Spectroscopy (FTIR)

IR radiation is situated in the electromagnetic spectrum at lower frequencies than the visible region, and higher than microwave radiation. It is frequently set in the 4000 to 400 cm^{-1} regions, corresponding to mid-IR region. IR spectroscopy measures covalent bond vibrations. Covalent bonds are approximated to be harmonic oscillators, as shown in Figure 2.6.

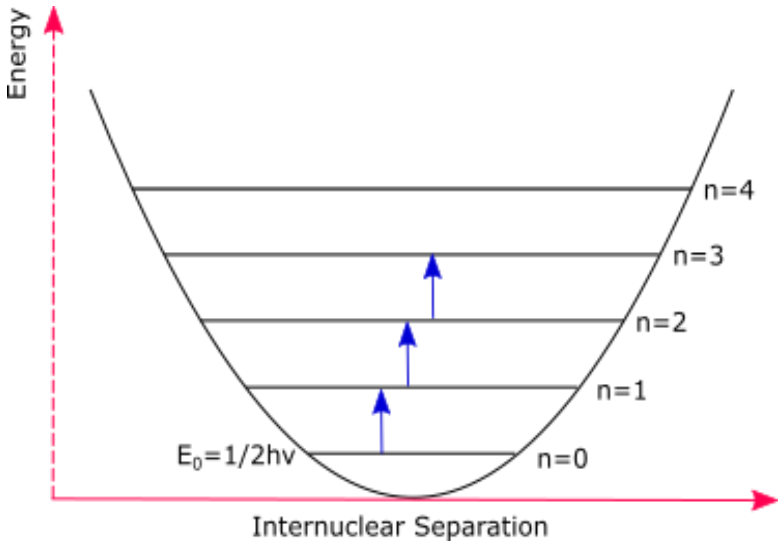

Figure 2.6. Quantum harmonic oscillator representation. The blue arrows show the transitions between vibrational states form the ground state (n = 0) to higher excited ones (n = 1, 2, 3 …)

The energy necessary to make a bond vibrate is calculated by Hooke's Law:

$$\nu = \frac{1}{2\pi}\sqrt{\frac{k}{\mu}} \tag{2.2}$$

Where k is a force constant and μ represents the reduced mass. For a more realistic approximation molecular bonds are non-harmonic systems where a dissociation energy takes place, and the energy levels are not equally levelled. Therefore, the frequency at which a bond vibrates will increase when the bond energy is increased, and the atomic weight decreased. Absorption peaks can be assigned to every bond in the molecule and changes in bonding energy and mass can be tracked. In order for a vibration to appear in IR spectroscopy it is required to generate a change in the dipole moment. Therefore, the *rule of mutual exclusion* needs to be considered. In centrosymmetric molecules every vibration that keeps the dipole moment constant will be IR inactive, but Raman active. An example of this phenomenon is highlighted in Figure 2.7 in relation to the CO_2 vibrational modes.

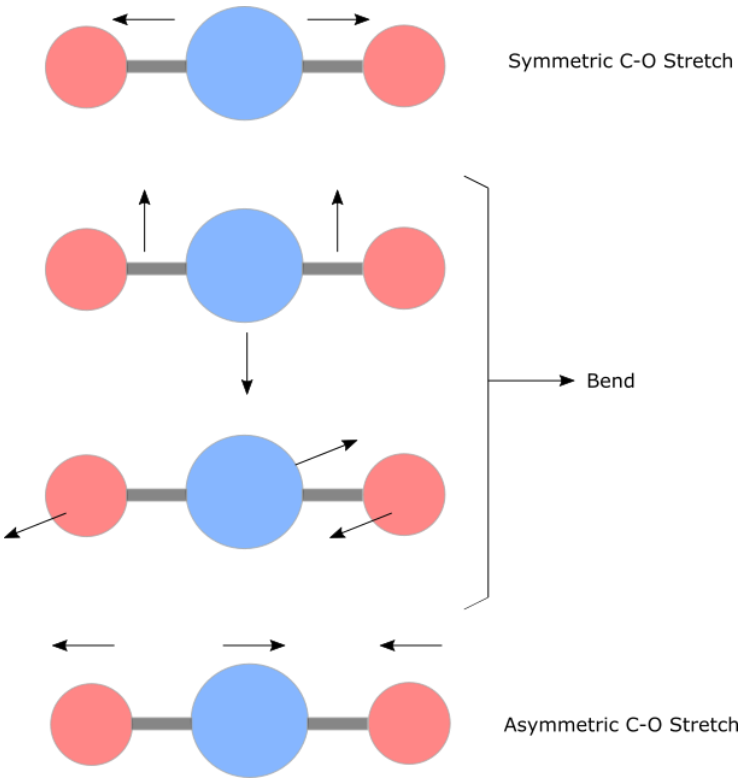

Figure 2.7. CO_2 vibrational modes. The carbon atoms are referred as blue circles while the oxygen atoms are shown as red circles. The symmetric stretch will not be IR active but Raman active. The atomic vibration is described by the arrows above the atoms.

FT-IR/ATR spectroscopy is a particularly useful tool in the analysis of solid samples. ATR stands for Attenuated Total Reflection. In this technique the sample is placed in contact with a special crystal with a high refractive index (*e.g.*, germanium, KRS-5 or ZnSe). In ATR spectroscopy the radiation will penetrate through the ATR crystal generating an evanescent wave, in which the sample will absorb radiation closely related to the transmission spectrum of the same kind. When the laser is situated on the interface with a less absorbent medium at an angle larger than the angle for total internal reflection the beam is totally reflectance. Although there is no wave going through the less dense medium, the evanescent wave (electrical field) exists, being reduced away from the surface. Every successive interaction with the sample will be part of the signal, increasing the sensitivity and the intensity of the IR technique. This reduces the quantity of sample required for obtaining the IR spectrum. It is non-destructive and the sample is directly measured by the contact of the sample with the refractive crystal. The process described above is schematically shown by Figure 2.8.

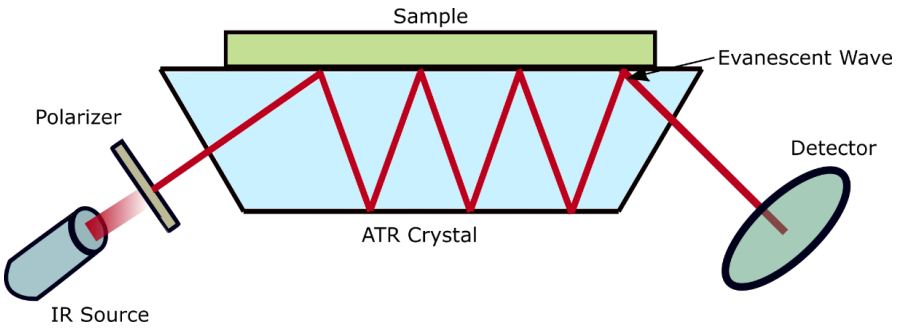

Figure 2.8. Schematic FTIR/ATR sample holder.

Infrared spectra were recorded using a Perkin Elmer ATR-FTIR spectrometer with ATR single reflection diamond accessory from Specac.

2.4.3 Raman Spectroscopy

Raman spectroscopy studies the dispersion of radiation when it encounters the sample. Radiation gets absorbed and the molecule is excited to a virtual state. The incident photon can be absorbed if its energy is equal to the difference between quantised levels. Nonetheless, that photon can collide with an atom and get dispersed. Most of the radiation doesn't suffer an alteration in the energy when they get dispersed (Rayleigh Scattering), while around 0.001% of the radiation gets dispersed, where from that percentage 1% is Raman scattering. Depending on the two energy levels involved in Raman scattering it can be described as Stokes or anti-Stokes Raman interaction as described in Figure 2.9.

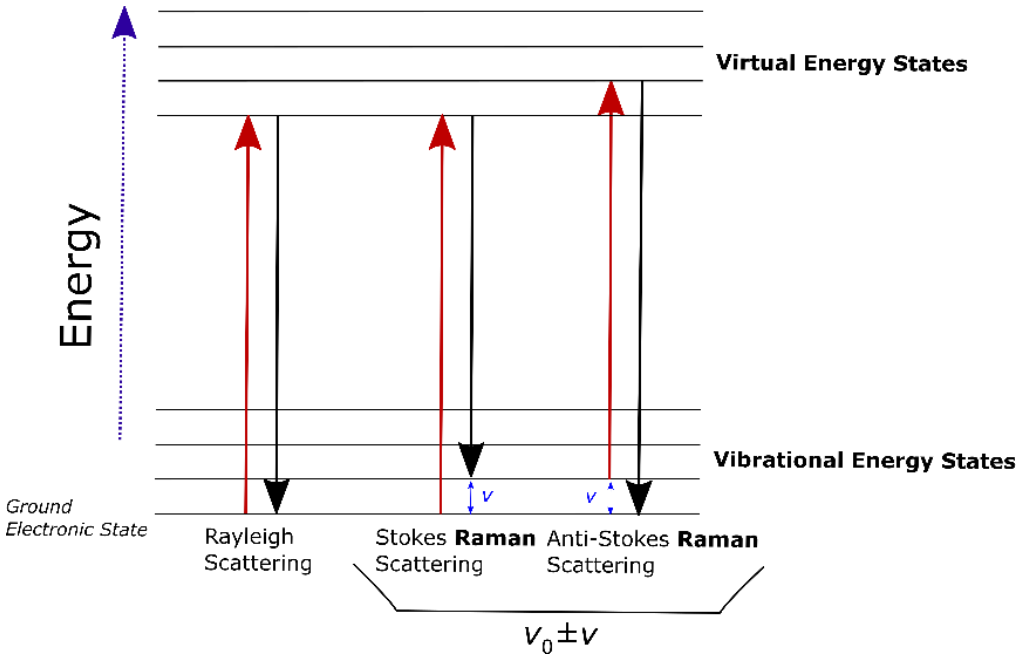

Figure 2.9. Raman scattering energetic transitions.

Raman scattering is not a resonant interaction. It is described as the polarisation of the electron cloud and the oscillating vector of the radiation. Therefore, for a vibration to be Raman active it is required that the radiation changes the polarisability of the molecule:

$$P = \alpha \cdot E \tag{2.3}$$

Where P is the dipole moment, E represents the external electric field and α is the polarisability of the molecule. In the case of solids there's an extra limitation that needs to be discussed. The vibration of the molecules, due to the nature of the solids, won't be as free as for the liquid and gas molecules, due to the bonding to other molecules in the lattice. Extra resonant vibrations will appear as lattice modes where the molecules will vibrate as an entity generating peaks of lower energy.

A standard Raman spectrometer consists of a light source and a laser that irradiates the sample. That radiation gets treated by several optic features before it reaches the detector, a CCD (charge-coupled device) detector.

Raman spectra were recorded using a Renishaw Raman Microscope with 785 nm laser.

2.4.4 Scanning Electron Microscopy (SEM)

Scanning Electron Microscopy (SEM) is one of the most widely used techniques to analyse surfaces of nano- andmicroparticles. The first scanning electron microscopes were constructed in the 1930s and 1940s. In the SEM a beam of electrons is ejected from a filament to the target material through vacuum conditions (10^{-4} to 10^{-10} Torr). The electrons previously generated are redirected by a series of electromagnetic lenses. The electrons interact with the sample and are emitted as backscattered electrons or secondary electrons. As the electrons are ejected from the sample, they are detected, often by an Everhart-Thornley scintillator-photomultiplier detector.

Secondary electrons are caused by inelastic scattering, resulting from the interaction of the beam with weakly bound electrons in the conduction band of the sample. These electrons are low energy (<50 eV), resulting in a low transmissibility through the samples. As a result, secondary electrons are more useful in the analysis of sample's surface morphology or topology.

High energy electrons from the beam are also scattered elastically forming backscattered electrons. As these electrons are higher energy they may travel farther than the direct low energy secondary electrons formed, they can travel away from the electron beam impact zone making the spatial distribution larger. As the scattering strength of an atom is highly dependent on atomic number, back scattered electrons can provide some information on composition or elemental distribution, though the larger mean free path leads to lower spatial resolution than that obtained with secondary electrons. Finally, the SEM image is formed by the intensity of the secondary electrons emitted from the sample at each x,y data point. [4]

SEM images were obtained by using a Zeiss Ultra SEM microscope running at 5.00 kV with in lens detection. All samples were prepared and deposited onto a carbon tab over an aluminium stub. A schematic figure of a standard scanning electron microscope is included in Figure 2.10.

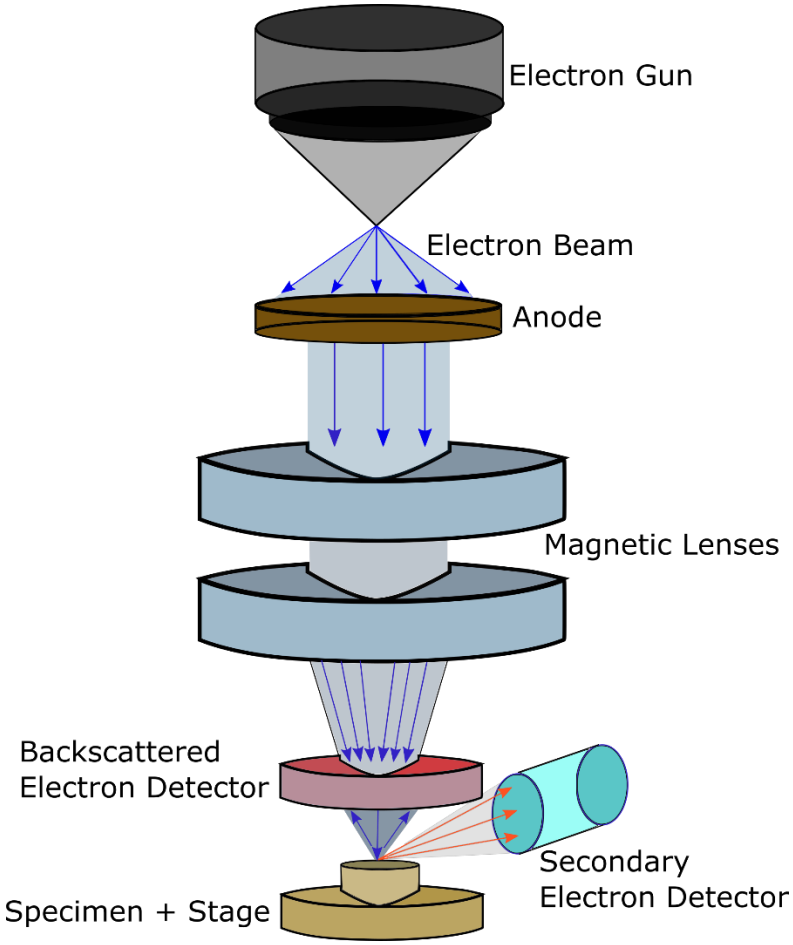

Figure 2.10. Schematic of a scanning electron microscope (SEM).

2.5 Analysis Methods

Although X-Ray diffraction is useful for the assignment of diffraction patterns to sort the chemical composition of a sample, it can give more complex information if required. Due to the nature of diffraction the peak position, intensity and shape depend on many factors that require specific mathematical analysis of the pattern obtained. For that reason, in this section of the chapter two different XRD pattern analysis techniques will be described. These techniques require a deep understanding of the mathematics and physics involved, beyond what will be discussed here, although the references mentioned will guide the reader to more in depth knowledge of the numerical factors involved.

2.5.1 Rietveld Refinement

Rietveld refinement consists of the calculation of a model pattern that "fits" the experimental one as much as possible given by a statistical error that can be calculated. Rietveld refinement was firstly used for clear patterns (high peak intensity and low background) obtained by neutron diffraction, and it required a tedious point by point calculation. It later got extended to data from high energy X-ray sourced diffractometers and finally to powder X-Ray samples (PXRD)

Nowadays although the mathematical approach is similar it requires the use of computer software like EXPGUI/GSAS[5,6] which is used in this thesis to perform Rietveld refinement of the PXRD patterns obtained. An example of the interface of this software for the Rietveld refinement of a XRD pattern is given in Figure 2.11. Firstly, a mathematical structure-free approach like the Le Bail method (1998) is used to begin the refinement. It consists of an approach in which the peak intensities are adjusted to the observed ones. The background needs to be well refined to make a good approximation for the peaks. As a rule, a semi-empirical and a polynomial approach can be used. Both are employed to subtract the background and only estimate the refinement of the data. Several cycles of calculations are required at this step. Once the background is ruled out, the peak-shape of the pattern can be approximated. The most common way to do it in X-Ray measurements is to use the pseudo-Voigt function. It consists of a linear combination of a Gaussian and a Lorentzian component with the ratio of each described as:

$$\frac{\eta}{1-\eta} \tag{2.4}$$

Where η is known as the mixing parameter. In a standard profile the components usually vary in a linear weight where the Gaussian shape is predominant at low angles and Lorentzian at higher ones. A peak can be dismissed as background when the intensity is less than 0.1 – 1.0% of the peak maximum. For the peak shape at low angles and the relation with the background a "peak cut-off" option is displayed to refine it. Once the peak shape is corrected, the fitting parameters can be adjusted to the empirical ones by the Rietveld refinement. This pattern refinement method was first reported by Rietveld at the I.U.Cr. congress in Moscow (1966) and published in 1969[7] but it wasn't until 1977 that Malmros and Thomas[8] extended this technique from neutron diffraction to X-Ray diffraction techniques.[9] In this first analysis the peak shape was assumed to be a convolution of different factors that affect the peak shape like the nuclear and magnetic contribution and the Lorentz factor. At lower angles the Gaussian peak starts showing some asymmetry which are corrected by a semi-empirical correction factor. For the peak width the formula given by Caglioti, Paoletti and Ricci (1958) is used to compare the full width at half maximum (FWHM) with the scattering angle of the Gaussian component of the peak shape by:

$$FWHM^2 = U \tan^2\theta + V \tan\theta + W \tag{2.5}$$

And the Lorentzian,

$$FWHM = X \tan\theta + \frac{Y}{\cos\theta} \tag{2.6}$$

Although they are good approximations for most of the patterns obtained, anisotropic behaviours in the peak shape cannot be described by this approximation.

The preferred orientation effect on the peak width needs to be corrected as well, due to the non-random orientation of the crystallites in the cylindrical sample holder. For plate like materials, the angle of the normal of the crystals and the scattering (α) is considered and corrected by,

$$I_{corr} = I_{obs}\, e^{-G\alpha^2} \tag{2.7}$$

Where G is the preferred orientation parameter.

By this refinement several data like the precise cell parameters of a pattern of mixed components or the percentage of each polymorph present in a sample can be calculated.

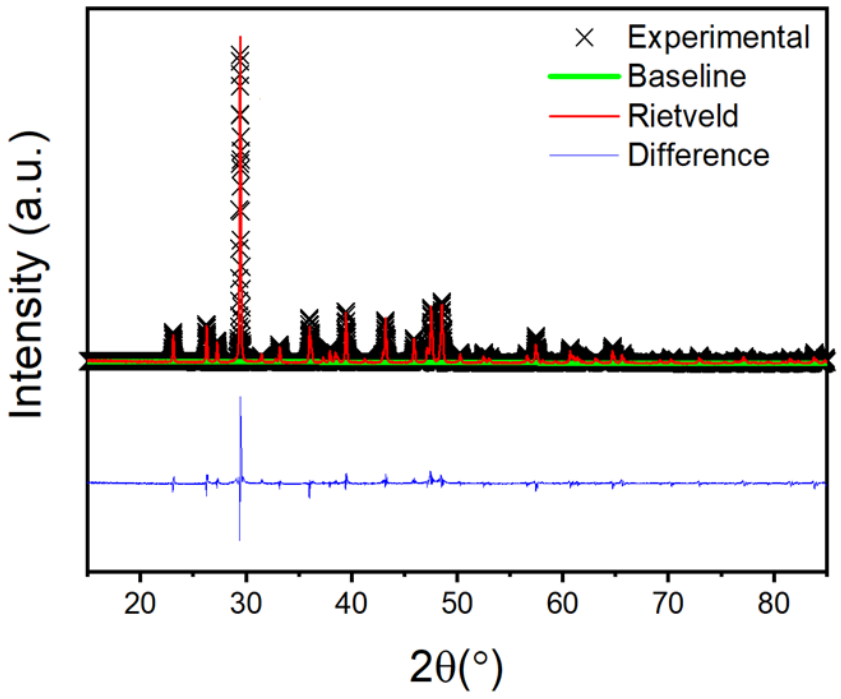

Figure 2.11. Example of the graphical interface of EXPGUI/GSAS. [5,6] The experimental data points are compared to the calculated one (red line). The base line corresponds to the green line underneath. The difference of intensity between the experimental and the calculated is plotted with a blue line.

When performing Rietveld refinement it is necessary to establish when is the refined structural model is good enough to be considered finalised. Several parameters may be used to indicate the goodness of fitting of the calculated pattern against the experimental one. The first approach and fastest way to assess it is to observe the difference both patterns, shown as a blue line in Figure 2.11. Secondly it can be established by the use of agreement indices or R values. The first one to be defined is the weighted-profile R value or R_{wp}.

$$R_{wp} = \left\{ \frac{\sum_i w_i [y_i(obs) - y_i(calc)]^2}{\sum_i w_i [y_i(obs)]^2} \right\}^{1/2} \quad (2.8)$$

Where $y_i(obs)$ are the intensity that can be observed at every step i. $y_i(cal)$ is the intensity directly obtained from the refinement. When a refinement approaches well the observed pattern the difference between the experimental intensities and the calculated ones are minimised. Nonetheless the main limitation resides in the background

contribution to the data. If the background is intense and not subtracted the R_{wp} will account the background intensity. The final R_{wp} obtained from the structure-less fitting is a good indication of what Rietveld refinement R must be approached.

In order to estimate how well the peaks are expressed by the fitting R_{wp} should approach the statistically expected R value, R_{exp}.

$$R_{exp} = \left\{\frac{(N-P)}{\sum_i w_i[y_i(obs)]^2}\right\}^{1/2} \quad (2.9)$$

Where N is related to the number of points obtained and P is the number of parameters. The numerator is usually defined as the degree of freedom. The relationship between this two factors will be expressed by the "goodness of fitting" or the ratio between both parameters, χ^2.

$$\chi^2 = \frac{R_{wp}}{R_{exp}} \quad (2.10)$$

This number must approach 1 as the weighted profile R and the statistically expected are targeted to be similar. Although, this numbers are helpful to gather an idea of the degree of fitting, it should always be accompanied by a good match between the calculated pattern and the experimental one. A refinement is usually stablished to be finished when good fitting parameters are obtained and the visualisation of the calculated and the experimental patterns show a good correlation.

2.5.1.1 Preferred Orientation Determination by the March-Dollase Approach

Although XRD patterns are usually represented as symmetric peaks showing different intensities and centred at a specific angle for each plane of the material, these features can suffer certain modifications. The most common factors are peak asymmetry and peak shift. Among others, the limited performance of X-ray analysis is subjected to the small active volume that diffracts due to absorption of the sample. It is dependent on the size of the grain and how well packed the holder is, causing variances in the pattern measured. The roughness of the material can cause additional absorption or a change in

the intensity due to preferred orientation. Here the latter will be described in order to establish how it can be corrected to obtain a precise refinement of the materials.

Preferred orientation is a feature that almost all polycrystalline materials show to a certain extent. It is intrinsically related to the nucleation and especially the growth of the materials. Due to the different energy barriers that a material needs to overcome to grow and the large number of interactions that take place along this process the growth of certain planes will be promoted. This effect can be thermodynamically driven where some faces, or planes of the unit cell will show a lower energy to grow or kinetically due, among others, to the interaction of the solvent with the material hindering or promoting the attachment of the atoms in a certain direction. A change in different factors such as the reaction media, addition of solvation agents or even any change in the speed of the growth given by temperature fluctuations or precursor availability will be critical to the degree of preferential orientation exhibited by the materials. This effect, also called texture, can be reduced in various ways when the sample is prepared for the measurement. For example, it can be minimized by a softer packing of the sample however it maximises the complexity to obtain a homogeneous sample to characterise. Sufficient compression maximises the homogeneity of the sample and although it doesn't avoid texture effects promotes them to be regular. Some measures can be taken at the procedure of the measurement. If the sample is spun around a certain axis, the preferred orientation parameters are simplified and reduced. It will simplify the description of the pattern and therefore the degree of preferred orientation can be described and corrected. Another improvement in the technique was the implementation of 2-D detectors instead of the 1-D classically used for these measurements. It allows the collection of information from a larger area of the diffraction cone and reduces the measurement time. The number of improvements developed to reduce the effect caused by texture all fail to give a number to the degree of effect that it has on the measurement.

The March-Dollase approach can be used to parameterise and correct preferential-orientation effects in the patterns measured.[10]. It reduces the complexity of the effect to a simple parameter (*r*, March parameter) that describes the amount of preferential orientation in the sample measured ($0 < r \leq 1$). This avenue can be introduced in Rietveld refinement as a way of further refining the pattern and gaining a better fitting.[6] Although it helps in the quantification of the texture of materials, it will be used in this

thesis as a simple way to better resolve the fitting of the materials refined. No direct physical explanation can be directly extracted from this parameter.

The degree of preferred orientation is defined as:

$$\eta = 100\% \, (1 - r) \tag{2.11}$$

When r = 1 then η = 0% so the sample is said to be randomly oriented, but, when r = 0 then η = 100% then there is what is called a perfect uniaxial orientation. Once the parameters are defined, the maths involved in the justification of this approach can be described. It is worth to note that all the parameters were not calculated but obtained from the fitting software (EXPGUI/GSAS) as well as not physical meaning is sought when calculating these parameters.

The description can be started by defining the weight function, $W(\alpha)$, to state the portion of crystallites for which the reciprocal lattice vector h is parallel to the normal of the surface measured. It is by extension the direction of the texture H.

$$W(\alpha) = \left(r^2 cos^2 \alpha + \frac{1}{r} \sin^2 \alpha \right)^{-\frac{3}{2}} \tag{2.12}$$

The angle α in Equation 2.9. is the one that relates both vectors h and H in a crystal. The degree of preferred orientation r will determine the shape of the function. If r = 1 the weighted function is equal to unity, therefore the orientation does not depend on the angle α, so that it is randomly disposed. At intermediate values of r the function has a maximum when α = 0. For the perfect uniaxial value r = 0 it is converted into a delta function $\delta(0)$. As this is a fraction of the total number of crystallites this function must be normalised.

$$\int_0^{\pi/2} M(\alpha) \sin(\alpha) \; d\alpha = 1 \tag{2.13}$$

The right way to state the amount of preferred orientation is to relate it to the fraction of crystals with an angle α within (0, α_0).

$$P(\alpha_0) = \int_0^{\alpha_0} M(\alpha) \sin(\alpha) \; d\alpha \tag{2.14}$$

The equation that is used in the refinements is then reduced and simplified as

$$\cos\alpha_0 = \left(\frac{1-r}{1-r^3}\right)^{1/2} \rightarrow \eta = 100\% \left[\frac{(1-r)^3}{1-r^3}\right]^{1/2} \quad (2.15)$$

At the refinement the March parameter r will be deduced to obtain a degree of preferred orientation, η. It gives different values as the linear one stated in Equation 2.8. The final equation is nonetheless valid for all the cases where$r \neq 1$. The difference between both equations is highlighted in Figure 2.12.

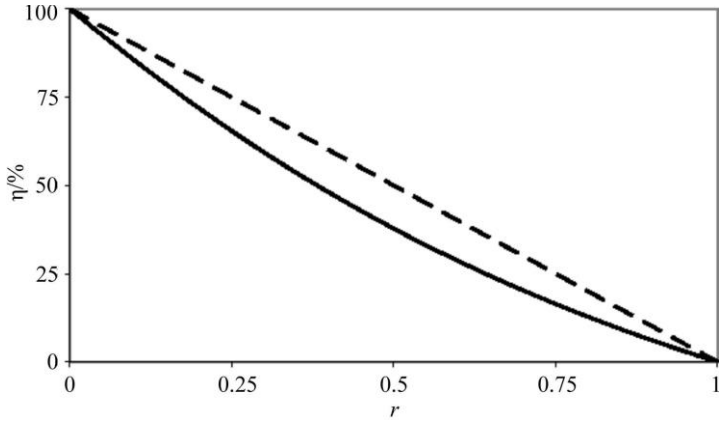

Figure 2.12. Relationship of r with the degree of preferential orientation from Equation 2.12. (solid line) and the linear relationship in Equation 2.8 (dashed line).[11]

In specific to the samples measured the degree of preferred orientation will be calculated for the Rietveld refinement. Due to intense anisotropies caused by this effect it will improve drastically the fitting of the calculated parameters with the experimental pattern.

2.5.2 Pair Distribution Function (PDF) Analysis

Although useful information can be extracted from the Rietveld refinement, the appearance of materials where the size-dependent properties are critical, like nanomaterials has led to the development of new analytical approaches. The atomic disposition in these nanomaterials will be critical for their properties. Small anisotropic disarrangement of the atoms is completely legible in classic XRD analysis as the effect in the pattern of this disparagements will be minimal and not revolved. However, for small particles it is essential as their domain size is rather small so any distortion will be critical for the structure exhibited. For example, any diffuse scattering from partially amorphous to small crystals is discarded as background in Rietveld refinement. These poorly crystalline materials can be visualised by microscopic techniques such as TEM,

as only punctual information can be derived from the images. To tackle these limitations Pair Distribution Function Analysis (PDF) evolved from being a niche technique for high-end solid-state physics to be key in the study of material formation and structure determination in present times.

PDF is defined as the Fourier transform of the scattering data. It essentially gives information on the interrelationship of the distances between the atoms in a crystal in real space. Gathering data in real space is complicated as high quality data is required. The feature that will define the appropriateness of the data collected to be converted into real space is the magnitude *Q*, or *momentum transfer*. It is defined by the wavelength of the incident radiation.

$$Q = \frac{4\pi \sin\theta}{\lambda} \tag{2.16}$$

In order to define how a PDF is obtained, a good starting point is to define the *structure function, S(Q)*. It is a normalisation of the coherent scattered intensity of a certain material.

$$S(Q) = \frac{[I_c(Q) - \langle f(Q)^2\rangle + \langle f(Q)\rangle^2]}{\langle f(Q)\rangle^2} \tag{2.17}$$

I_c is defined as the *coherent scattering intensity* diffracted by a sample. *f(Q)* is the *atomic form factor*, which describes the efficiency or ability of coherent scattering per atom. It is the ratio between the amplitude of the wave scattered by the atom compared to that of an electron in the same conditions. A PDF plot represents the arrangement of the interatomic distances in a structure, by defining the atoms in pairs, in real space and taking an atom in the cell as the origin described in Figure 2.13.

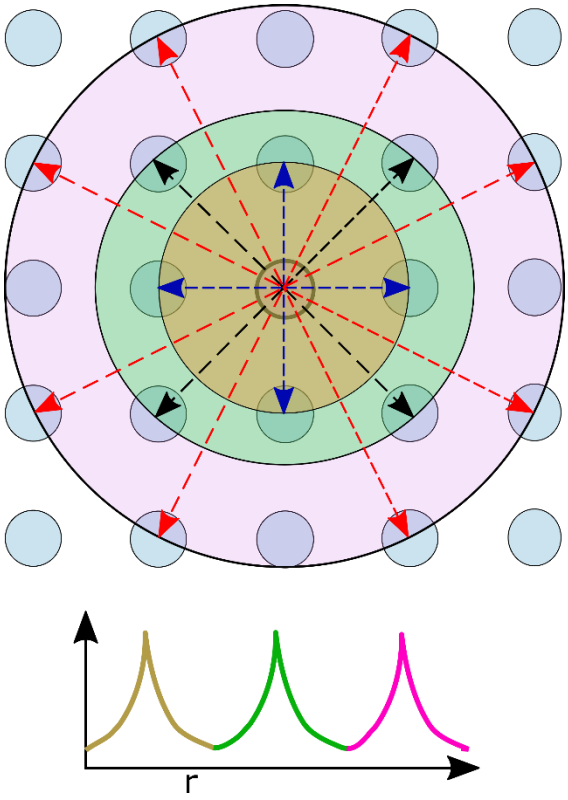

Figure 2.13. Description of how a pair distribution function is obtained. A random atom in the lattice is taken as the origin and the vectors are described from this origin to the 2D situated atoms. The resultant graph is shown underneath with symmetric sharp peak for same type of surrounding atoms. Vibrational and thermal effects are not considered in this figure.

The equations above can be obtained from a structural description. The Radial Distribution Function (RDF) is obtained from the sum of the delta functions with all the interatomic distances in the sample as described in Figure 2.13.

$$R(r) = \sum_i \sum_j \frac{f_j^* f_i}{\langle f^2 \rangle} \delta(r - r_{i,j}) \tag{2.18}$$

The RDF is one of many equations that describes the same information in a different way. The reduced distribution function can be obtained:

$$G(r) = \frac{R(r)}{r} - 4\pi r \rho_0 \tag{2.19}$$

ρ_0 is the average atomic number density. Equation 2.16. is often used.

The PDF were calculated from the powder XRD patterns obtained from the samples by using PDFgetX2.

2.5.3 Principal Component Analysis (PCA)

Materials science has as one of the main topics: the nucleation and growth of crystals. The variability of formation of the aforementioned will depend on what structure they adopt generating different polymorphs to what mineral will precipitate at the end of the reaction. All these processes and the final material selection will depend on energetically closely related pathways. Therefore, the formation of one or another polymorph will be correlated to the synthetic conditions. Nonetheless, due to the experimental limitations in the lab the different parameters may not always be isolated in such a way that the end result is a huge range of different factors like temperature, concentration, precursor selection or time. This means that experimentally a matrix of different samples produced at different conditions is needed to examine how those external conditions affect the resultant sample. This matrix of samples increases in size as more variables are added to the experimental conditions. In order to even acknowledge how that factor has affected the final result a large quantity of techniques are required to characterise the materials formed. Those techniques are usually, at the same time, not as simple to analyse and will depend in many factors to even obtain a conclusion or a trend. Thus, when performing a set of reactions to map their behaviour at different variables large, complicated datasets are the final outcome after their analysis. Mapping these conditions to the obtained materials and the intricacies of their crystallisation it is often found to be time-consuming and hard to correlate all the factors among different techniques to generate a broader view of what is happening at different conditions. This bottleneck is classically tackled by designing the experiments in a way that each variable can be isolated and analysed on its own. Nonetheless, many times those factors don't directly depend on the synthetic technique or are not even acknowledged prior to the experimental procedure. When this preventive measure cannot be implemented and to promote the automatisation of the processes in where the data is analysed post-synthesis not estimating what are going to be the main factors that influence the results, statistical approaches are usually employed. Although this statistical modelling doesn't usually give a chemically meaningful result as it requires to be corroborated by the data introduced, it helps to correlate large dataset between each other and acknowledge trends not that easy to be observed at first-sight.

PCA statistical analysis is capable of discerning the mentioned factors that affect the samples obtained and reduce the dimensionality of the results to a meaningful easier to handle sets of directions or components. Those factors that gives variability to each set of data and characterise them versus the others are called Principal Components (PC). These new variables are linear combinations of the old ones that accounts for the greatest possible variance, with each subsequent PC being calculated in the same way on the conditions that it is uncorrelated (orthogonal) to the previous calculated ones, so that they are independent variables to each other. The number of components will be equal to the number of samples or variables present, and it will depend on which is the smaller. Usually when calculating the variables that affect a dataset there are a few ones that will carry most of the variability of the samples, with the other factors being effectively meaningless to discern between one pattern or another. If only the factors that give the largest variability are accounted to define our dataset, there will be an effective reduction of dimensionality in the data keeping most of the meaningful variation between them. So that, the data will undergo a reduction of dimensions from thousands that can affect it to a few that are the main ones. All the components are affecting all the samples in the dataset, although it will not interact the same way with all of them. If the strength of this interaction can be calculated numerically and plotted, common and differentiator features can be extracted to observe trends. The samples that are correlated or affected by a PC in a similar way will cluster, in contrast if they are not correlated, they will be plotted in a completely different place in the graph.

Once the concepts behind PCA are understood, it is necessary to explain the mathematical concepts that this analysis involve. It was first formulated by Pearson who described the analysis as "lines and planes of closest fit to systems of points in the space".[12] In chemistry PCA was first used in around 1960 by Malinowski, although it was named as principal factor analysis.[13] The starting point for every multivariable data analysis is to organise the data in a matrix (table of data) which will be named **X**. The number of samples that will correspond to the number of rows in the table will be ***I***. For every sample the number of columns or variables will be defined as ***J***. The corresponding matrix will have a size of $I \times J$. In a chemical test it is usual to face very large number of observations corresponding to a big matrix of data. It is very complicated for the user

to discern trends in that situation, therefore PCA will allow the creation of models and correlation in the matrix. PCA target can be defined as:

$$\mathrm{X}(data\ matrix) = \mathrm{M}\ (\mathrm{PC}\ model) + \mathrm{E}\ (Noise) \tag{2.20}$$

The corresponding variables that will be presented in the columns are denoted as x_j (where $j = 1, \dots, J$). They are all vectors in the *I*-Dimensional space. It can be expressed as a linear combination $\mathrm{t} = w_1 \times x_1 + \cdots + w_J \times x_J$. t is defined as a new vector which belongs to the same space as the variables *x*. The matrix can be denotated as $\mathrm{t} = \mathrm{X}w$. The data that are contained in X express all the variability so it is reasonable to think that t will keep most of the variability as well. This process has downgraded the J number of variables to a variable named t keeping the information relevant. The variability of t can be calculated by its variance, var(t) — a common calculation in statistics. The number of the weights (w_j) needs to be chosen wisely to maximise the variance. If that number is decided to be a very large random number, then the variance of t will depend in the same way of an arbitrary large number. Therefore, to anchor this value it needs to be normalised. Then a norm needs to be introduced, such as, the sum-of-squared values is equal to unity. This norm is denominated as the Frobenius norm ($\|.\|^2$).

$$\underset{\|w\|^2=1}{\operatorname{argmax}} \operatorname{var}(t) \tag{2.21}$$

Where $\| w \|^2 = 1$ can be also read as $\| w \| = 1$. The operator argmax gives the value for *w* that maximises the function. If the dependence of t with X and *w* is expressed in the equation:

$$\underset{\|w\|=1}{\operatorname{argmax}} \operatorname{var}(t^{\mathrm{T}}t) = \underset{\|w\|=1}{\operatorname{argmax}} \operatorname{var}(w^{\mathrm{T}}\mathrm{X}^{\mathrm{T}}\mathrm{X}w) \tag{2.22}$$

This is a classic problem in linear algebra. The optimal *w* is the eigenvector with the largest value of the covariance matrix $\mathrm{X}^{\mathrm{T}}\mathrm{X}/(\mathrm{n}-1)$ or the cross-product value $\mathrm{X}^{\mathrm{T}}\mathrm{X}$.

It can be valued how well t represents the variation of X. This is achieved by the projection of the matrix X in the t dimensions. How well they correlate will be established by the residuals that are the discrepancies from the original data, previously assessed as noise.

$$\mathrm{X} = \mathrm{t}\mathrm{p}^{\mathrm{T}} + \mathrm{E} \tag{2.23}$$

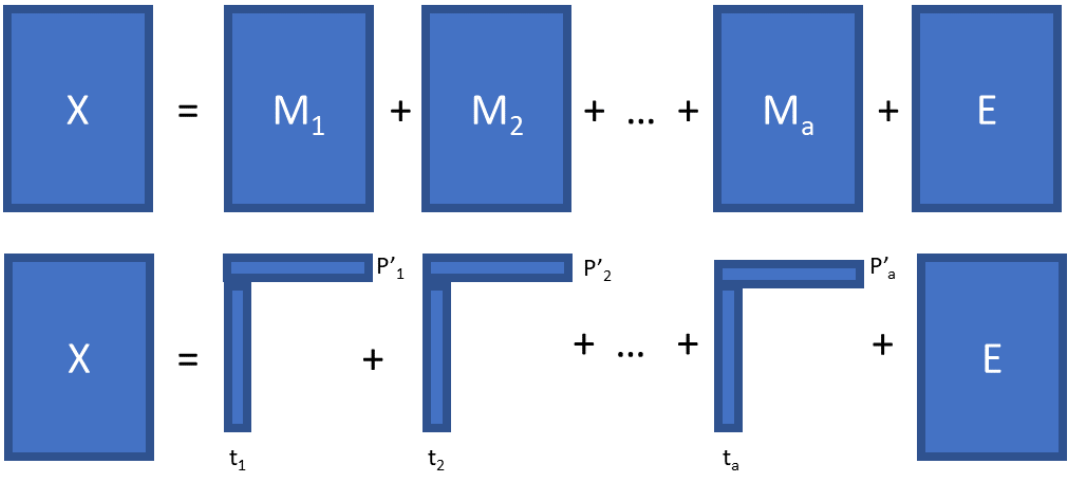

Figure 2.14. Matrix X as a function of the loading and scores vectors defined by the matrix M and the residuals as expressed by the matrix E.

p is the coefficient that is obtained after the regression and corresponds to the weighted numbers. How well the resultant values expressed the data is usually calculated by the percentage variation:

$$\frac{\|X\|^2 - \|E\|^2}{\|X\|^2} 100\% \tag{2.24}$$

It is called variation and not variance, usually referred in statistics, as for it to be a variance would need to be referred to the degrees of freedom from the model which is not simple to discern. t is usually named as the score vector and p is denominated as loading vector. In chemistry p is usually normalised to length 1. The vectors need to be not dependent, so by definition they are orthogonal to each other. The term of principal component is not really established as it can either refer to the loadings, the scores, or a combination of them.

The best way to show the many advantages of using PCA for the analysis of large datasets is to give a reported example. The use of PCA is restricted to large datasets and spectra with a reasonable number of characteristic features capable of giving variability to the sample. FTIR and Raman are usually employed techniques to be subjected to chemometric analysis like PCA. The fast measurement of the samples and the presence of characteristic features for a mix of components enhance the applicability of this analysis techniques for a huge range of fields. The use of PCA for simplifying large dataset of these techniques has been applied for numerous fields: recognition of explosive

compounds by Raman,[14] quality control in food science by FTIR[15] and forensic recognition of red lipstick or cocaine by FTIR;[16,17] among many others. To describe the process and highlight the applicability of this analysis technique the "Identification of Newly Emerging Influenza Viruses by Detecting the Virally Infected Cells Based on Surface Enhanced Raman Spectroscopy and Principal Component Analysis" was carried out by Choi *et al.*.[18] New influenza viruses are described every year, emerging worldwide. This huge variability of virus genome is produced by mutations of the virus. Thus, the rapid diagnosis of these new variants to isolate the infected individual in an effective way is required. Avoiding the fast spreading of new variants is essential to avoid any disturbance for humanity as shown for recent pandemics like H1N1 pandemic[19,20] or even best exemplified by the current Covid-19 pandemic with the numerous variants reviewed.[21,22] Nonetheless, there is still a lack of rapid detection methodologies, most of them requiring of specific molecules for the virus studied. These techniques required long, multi-step processes that last several days to achieve any result. Therefore, the finding of a rapid method capable to discriminate different variants is critical to beat any pandemic spread. Since PCA is capable of simplifying multivariable datasets showing the variability on the specific variables required, it can highlight the difference between past infections and potential new variants in within minutes by following the protocol described in Figure 2.15.

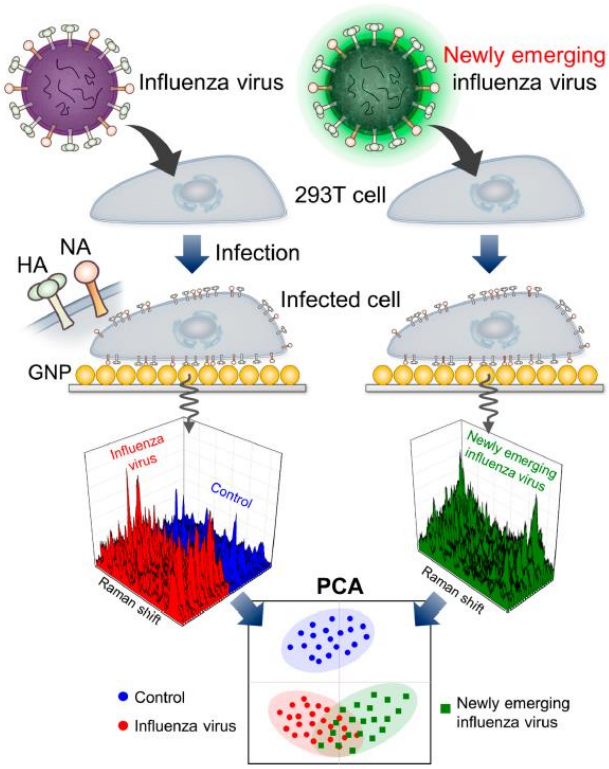

Figure 2.15. Analysis protocol followed to analysed new influenza variants from infected cells.[18]

Influenza viruses carry hemagglutinin (HA) and neuraminidase (NA) as protein envelopes. These proteins are shown on the surface of the infected cells. They serve as a target for the immune system to discriminate virus-containing cells and attack them. So, it is expected that HA and NA can be used as analytes for the infected cells by spectroscopic techniques. Due to the low intensity and complexity of the system gold nanoparticles-enhanced Raman spectroscopy is required. The data obtained for two different SARS infected cells are expected to be extremely similar, so to discern differences between them PCA analysis of the spectra is required. The cells were manipulated to show only NA, HA or both at the same time for two different SARS strains: the WSN strain (A/WSN/33 H1N1) and the CAL strain (A/California/04/2009 H1N1).

The variation of the Raman shift dependent on the present of one strain or another is completely minimal, so that, PCA is required to acknowledge those differences. The signals were required to be normalised as the intensity in Raman spectroscopy is randomly distributed. When analysed by PCA they were plotted in 2-D comparing two different PCs. The main Principal Component (PC1) are the features or magnitudes that

gives the most variability to the spectra and will be potted at the *x*-axis. The second Principal component analysis (PC2) is usually plotted in the *y*-axis. Nonetheless, the selection of the Principal Component to be plotted depends hugely on what is required to analyse. For that reason, it is convenient to determine what the main different PCs are referring to. The most common way to diagnose the meaning of the components is by the selected loading plots of the components as shown in Figure 2.16.

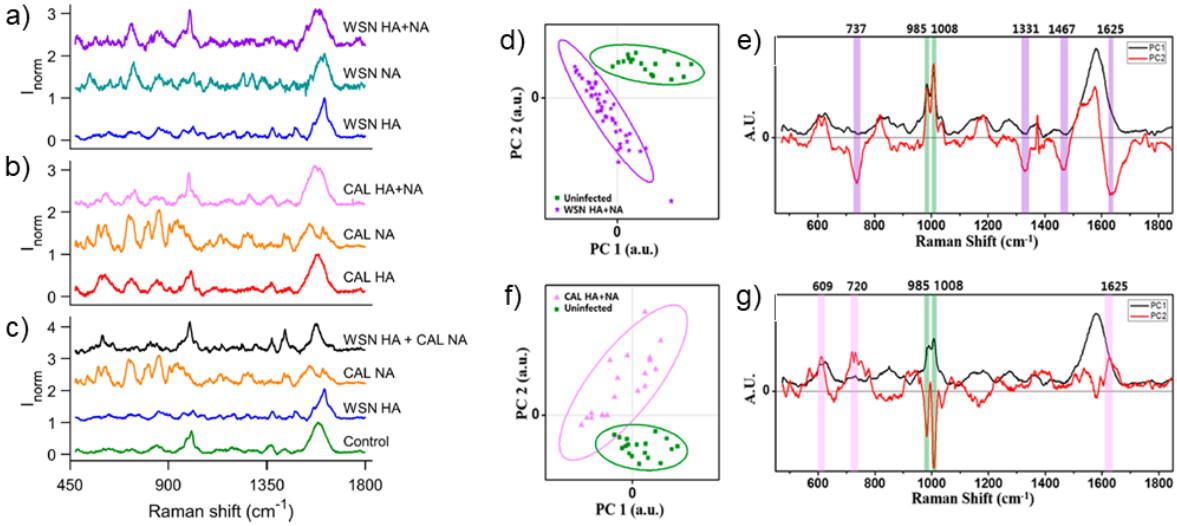

Figure 2.16. Averaged Raman spectra from the cells infected with a) WSN strain, b) CAL strain and c) cells with the WSN HA or CAL NA or both. Control shows the cells with no viral proteins. PCA plots of the Raman spectra from the prepared cells. d) 2D score plots of the PC1 and PC2 for the unaffected cells and the WSN strain with the HA + NA proteins on the surface. Purple stars and the green squares are related to the type of sample to be analysed as shown in the legend. The enclosing shapes represent the area were with a 95% of probability a similar sample would be encountered. e) Loading plot of the PC1 and PC2. The purple and green vertical lines are related to the main Raman shifts of each the affected and the uninfected cells, respectively. f) 2D score plots of the PC1 and PC2 of the cells presenting the CAL strain with HA+NA proteins and the control samples. The pink triangles represent the projection of the CAL_{NA+HA} Raman spectra and the green squares the projection of the Raman spectra for the uninfected cells. The enclosing shapes represent the area were with a 95% of probability a similar sample would be encountered. g) Loading plots for PC1 and. The pink and green vertical lines are related to the main Raman shifts of each the affected and the uninfected cells, respectively.[18]

The number of measurements were: 9 (WSN_{HA}), 9 (WSN_{NA}), 12 (WSN_{HA+NA}), 11 (CAL_{HA}), 10 (CAL_{NA}), 18 (CAL_{HA+NA}), 20 ($WSN_{HA} + CAL_{NA}$) and 18 (control). This shows significant differences from the control samples and the infected ones. At the same time, the main Raman features are defined from the loading plots. This way is easier to determine what the Raman peaks that correspond to one or the other strain analysed. Without PCA it would have been almost impossible to discern which characteristics are

representative of the proteins shown at the surface of the infected cells. After comparing how every Raman shift interact with each type of cells, they can be compared to each other in order to discover if PCA is a suitable analysis method to distinguish new variants from old ones.

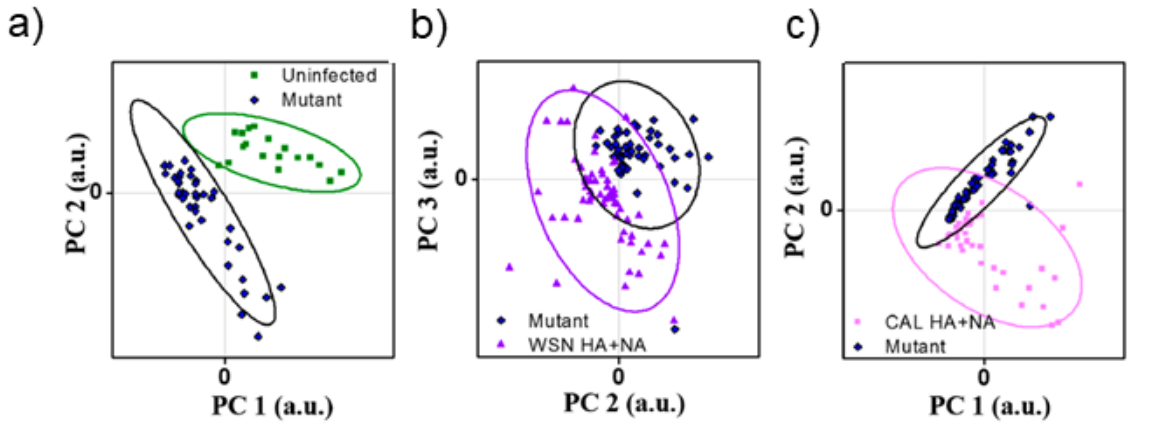

d)

Infection type	Raman shift(cm^{-1})												
WSN HA+NA				737						1331	1467		1625
CAL HA+NA	609		720										1625
WSN HA+CAL NA		696		737									
Uninfected						985	1008					1578	

Figure 2.17. a) PCA obtained from the mutant variant corresponding to $C_{WSN\ HA+CAL\ NA}$ (blue squares) with the uninfected ones (green squares). b) PCA comparison of the cells infected with the SARS defined as mutant (blue squares) with the parental $C_{WSN\ HA+NA}$ (purple triangles). c) PCA of the cells infected with the mutant virus (blue squares) and the parental $C_{CAL\ HA+NA}$ (pink squares). d) Main Raman shifts for the analysed variant of the virus. They were obtained in a similar way as Figure 2.16. [18]

From Figure 2.17 significant differences in the PCA disposition can be acknowledged between the mutant variant and the uninfected a) and the parental SARS infected cells b) and c). Not only is PCA is capable of discerning what samples correspond to a variant virus but can also help to distinguish the main Raman shift for each one of the variables measured. It helped to reduce the information from a large number of samples measured in Raman with almost no obvious difference from the spectra, to differentiate the content of each sample and giving information on the behaviour of the surface proteins when they are measured by Raman scattering. This reduction of information is merely a mathematical process with no physical meaning *per*

se, but when it is accompanied with knowledge about the topic it can differentiate between variants of a virus within minutes. This reduction in time is critical compared to the standard procedure currently followed, and very advantageous in order to control possible pandemics.

2.6 References

1 C. L. Gordon, W. G. Schlecht and E. Wichers, *J. Res. Natl. Bur. Stand. (1934).*, 1944, **33**, 457.
2 Parr Instrument Company, *Acid Digestion Vessels: Operating Instruction Manual*, 2020.
3 National Institute of Science and Technology, https://www.nist.gov/.
4 P. Russell, D. Batchelor, A. I. Facility and P. E. Russell, *Microsc. Anal.*, 2001, 9–12.
5 B. H. Toby, *J. Appl. Crystallogr.*, 2001, **34**, 210–213.
6 A. C. Larson and R. B. Von Dreele, "General structure Analysis System (GSAS)", *Los Alamos National Laboratory Report*, LAUR, 86-748 (2000).
7 H. M. Rietveld, *J. Appl. Crystallogr.*, 1969, **2**, 65–71.
8 G. Malmros and J. O. Thomas, *J. Appl. Crystallogr.*, 1977, **10**, 7–11.
9 H. M. Rietveld, *Aust. J. Phys.*, 1988, **41**, 113–116.
10 W. A. Dollase, *J. Appl. Crystallogr.*, 1986, **19**, 267–272.
11 E. Zolotoyabko, *J. Appl. Crystallogr.*, 2009, **42**, 513–518.
12 K. Pearson, *London, Edinburgh, Dublin Philos. Mag. J. Sci.*, 1901, **2**, 559–572.
13 R. Vidal, Y. Ma and S. S. Sastry, in *Interdisciplinary Applied Mathematics*, 2016, vol. 40, pp. 25–62.
14 J. Hwang, N. Choi, A. Park, J.-Q. Park, J. H. Chung, S. Baek, S. G. Cho, S.-J. Baek and J. Choo, *J. Mol. Struct.*, 2013, **1039**, 130–136.
15 R. Ríos-Reina, R. M. Callejón, C. Oliver-Pozo, J. M. Amigo and D. L. García-González, *Food Control*, 2017, **78**, 230–237.
16 R. Chophi, S. Sharma and R. Singh, *Forensic Chem.*, 2020, **17**, 100209.
17 M. C. A. Marcelo, K. C. Mariotti, M. F. Ferrão and R. S. Ortiz, *Forensic Sci. Int.*, 2015, **246**, 65–71.
18 J. Lim, J. Nam, H. Shin, J. Park, H. Song, M. Kang, K. Lim and Y. Choi, *Anal. Chem.*, 2019, **91**, 5677–5684.
19 G. Neumann, T. Noda and Y. Kawaoka, *Nature*, 2009, **459**, 931–939.
20 J. Cohen, *Science*, 2009, **324**, 997.
21 J. S. Tregoning, K. E. Flight, S. L. Higham, Z. Wang and B. F. Pierce, *Nat. Rev. Immunol.*, 2021, **21**, 626–636.
22 M. Cevik, N. D. Grubaugh, A. Iwasaki and P. Openshaw, *Cell*, 2021, **184**, 5077–5081.

Chapter 3. Mild Hydrothermal Synthesis of Zircon-Type Silicates $MSiO_4$

3.1 Introduction

Silicates are known to be very abundant in nature, comprising more than 95% by volume of the earth crustal rock.[1] These minerals are not just confined to Earth, however, as amorphous silicate particles are believed to be one of the main components of oxygen-rich evolved stars and might originate the crystals of forsterite and enstatite detected by the Infrared Space Observatory (ISO).[2,3] The study of these silicates is critical to understand the evolution of the earth and can be transferred to more complex systems like the Solar System. Silica can be found in different forms than solid state, as it is present in the hydrosphere as dissolved silica, from erosion and dissolution of silicate minerals. It affects the biosphere as it is present in the soil and plays a huge role in the growth of plants by the ability of clay to absorb and release water, as well as different cations that are essential for the quality of the soil. It is present in living organisms with a structural function. As an example, the presence of very pure silica in the structure of diatoms,[4] sponges[5] and grasses.[6]. These organisms take the silica dissolved in water, where it is kept as silicic acid and then deposit it as silica with a high control over the process.[7] That degree of control has led to the research of bioinspired materials for a range of applications, as evidenced in the exploration of the interaction of silica and collagen for biomedical devices with a promising future in medicine. In addition, it is one of the main components in the building industry being a component of granite and limestone. It works as well as a refractory material in paints or being doped for the design of LEDs .[8] The ubiquity of silica in different environments shows the flexibility and importance of silica and silicates for various applications.

This extended presence of silicon and more specifically of silicates results from the vast number of different types of them that can be formed and their large number of structural variations. Through the second half of the twentieth century crystal diffraction studies unveiled several hundreds of silicate minerals.[9] Silicon is the element involved in the second highest number of combinations with other elements behind carbon.[1] The main difference between the core formation of carbon chains, and partly why living organisms are carbon-based, rather than silicon-based, is the difference between the bonding energy of X-O, X-H and X-X, where X= C/Si. For carbon all the three possibilities have almost the same energy, generating many different iterative compounds with the almost same energy cost. In the case of silicon, the Si-O bonding energy is larger

than the Si-H and almost double that of Si-Si, hindering the possibility of formation of -Si-Si- silicon chains.

Table 3.1. Selected mean bond energies for carbon and silicon.

Bond	X=C (kJ/mol)	X=Si (kJ/mol)
X-X	346	222
X-O	358	452
X-H	413	318

This factor evidently limits the chemistry of silicon as the formation of Si-O bonds will be promoted in most cases. The fundamental structural building block of silicate minerals is thus the tetraoxosilicate anion, which is shown in Figure 3.1.

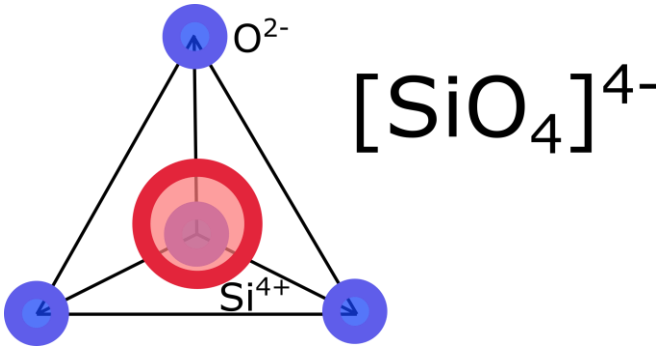

Figure 3.1. Tetraoxosilicate building block: Silicon atom (red) bound to oxygens atoms (blue) at the vertices of a tetrahedron.

Despite their apparent simplicity, these tetrahedral units may link together through bridging oxygens in a variety of ways generating the vast array of structures encountered in the silicate mineral family. Defining the silicates on the basis of their structures or topology leads to classifications such as nesosilicates (containing isolated $[SiO_4]^{4-}$ units), sorosilicates (containing "double-island" $[Si_2O_7]^{6-}$ units), through to cyclosilicates, inosilicate (corner sharing chains) and tectosilicates (extended framework silicates). With the exception of the framework silicates, all other conformations require the incorporation of other cationic species, to provide charge balancing. This all naturally leads to the huge structural and compositional variety which makes the silicates so important. A broad and generalised formulation for the silicates can be taken as $X_mY_n(Z_pO_q)W_r$, where O is oxygen, Z is Si^{4+} (or Al^{3+}), W is OH^-, F^-, *etc.* and X and Y represent large 8-12 coordinate cations and medium sized octahedrally coordinated cations, respectively. Within this formulation the values *p* and *q* will depend on the

connectivity of the silicate tetrahedra, and from this all other coefficients must lead to charge balance.

Among the nesosilicates, $MSiO_4$ (M = Th, Pa, U, Np, Pu, Am, Hf, Ce and Zr) are known to be isostructural.[10–12] They all adopt the zircon, $ZrSiO_4$, structure (tetragonal, $I4_1/amd$). It is defined as silicate tetrahedra (SiO_4) which share corners and edges with ZrO_8 dodecahedra. The ZrO_8 are connected by sharing edges to four ZrO_8 polyhedra. Two in the [100] direction and two in [010] direction. These <100> chains are related to the silicates by sharing corners. The silicon and the zirconium polyhedra are connected by edges as well by alternating with each other in the [001] direction. This arrangement leaves empty channels parallel to [001]. The different connections of the structure (corner *vs*. edge sharing) plays an important role in the behaviour of the materials, like anisotropic mechanical behaviour[13] and He-gas diffusion.[14,15] A graphical description of this structure is given in Figure 3.2.

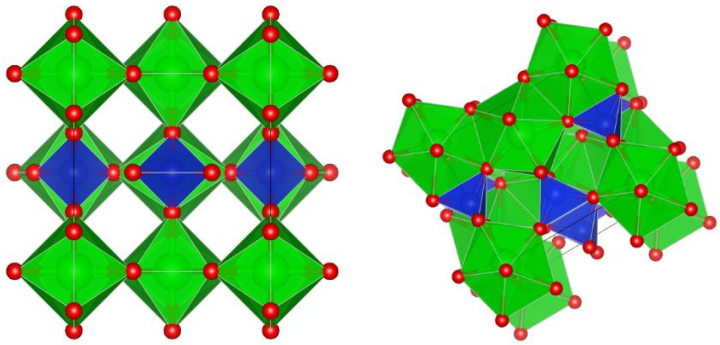

Figure 3.2. Zircon polyhedral structures. Blue tetrahedral represents [SiO_4] connected to green dodecahedra [ZrO_8].

3.1.1 Zircon, $ZrSiO_4$

Zirconium silicate, $ZrSiO_4$, gives the name to this silicate series. This mineral is known to be crucial in understanding Earth´s crustal evolution, as it is widely used in geology to date mineral environment, as a geochronological study, by U-Pb isotopic analysis of zircon.[16,17] The main reason for this applicability may be understood by considering the great stability of zircon in nature and the long lasting release of the trapped metal in the silicate structure. It has been reported to have a low expansion coefficient and it only decomposes at high temperatures.[18,19] Regarding this, zircon type materials have been suggested to be great candidate minerals for geological

immobilisation of rare earth metals.[20–22] The use of zircon sand is not limited to Spent Nuclear Fuel (SNF) disposal as it plays an important role in the fabrication of ceramics, refractories, fibre optics and fuel cells, among others.[23] Zircon synthesis has been attempted by solid state method under 1400 °C as a starting point, nonetheless for the complete reaction high temperatures and reaction time are required (>15h, ~1500°C).[24–29] This method is time and energy consuming, hindering its applicability for industry. As zircon is a natural occurring material[30–35] hydrothermal synthesis might be a good attempt to replicate those conditions under which it is naturally formed.[36–38] An example of hydrothermal zircon in nature is the low temperature and high pressure metamorphic minerals in Syros (Greece).[39]Although it seems quite simple to solve this synthesis process, very little research has been devoted to this topic. The applications are not only limited to geology, zircon application is in broader fields such as photonics.[40,41]

3.1.2 Coffinite, $USiO_4$

Underground repositories have been proposed as the best alternative to store spent nuclear fuel (SNF) in Europe, and a number of sites have been identified as possible storage locations.[42] Linked to this idea, there is an obvious concern about the environmental evolution around these storage facilities. Around the world there are approximately 10,000 metric tonnes of heavy metal (MTHM) generated by nuclear energy processes per year. From this production around 300,000 MTHM are already stored in pools or dry casks.[43] The majority of this SNF is destined to be stored for long-term. The real composition of this waste is dependent of the process followed in the reactor where two main reactions may occur. Firstly, the fission of nuclides such as enriched ^{235}U and ^{239}Pu. Secondly, the capture of neutrons with the beta decay of the transuranic isotopes. Nonetheless, by the end of the process the main component of the SNF is about a 96% UO_2.[44] Along with it fission gasses (Xe, I and Kr) and fission products (such as Zr, Nb, Mo, Tc,… and the corresponding oxides precipitated) can be acknowledged in the final waste. Directly after the SNF is generated, it is highly radioactive, so it needs to be heavily contained in pools. After five to ten years, the radiation is smaller and safe to handle so it can be stored in metal containers surrounded by thick walls of concrete (called dry cask) where it can be stored for hundreds of years. An example of a water containing pool and a dry-cask is given in Figure 3.3. There exists a risk of leaking after the steel containers are corroded and further reaction of the

radioactive material with the surroundings. Many side-products are possible as there is a possibility of reaction of UO_2 with the environment, particularly the sand and groundwater from the surroundings. The first reported observation on the corrosion of uranium oxide (UO_2) was performed by a 10 year drip test by simulating the aqueous conditions from the Nevada region, showing the retarded release of uranium by the formation of secondary phases with formation of long term very stable alkali and alkaline uranyl silicates.[45] In addition, there are studies on unirradiated UO_2, which show the presence of silicates. When the UO_2 solid phase is exposed to similar conditions to ground waters (Ca^{2+}, CO_3^{2-} and various silicates) anoxic conditions at room temperature and hydrothermal temperatures (180°C), minerals with similar composition to coffinite ($USiO_4$) and U-bearing ekanite ($UCa_2Si_8O_{20}$) are observed.[46] Although anticipating the evolution of the materials which may potentially be released under storage conditions is rather complicated,[47] due to the unstable nature of uranium chemistry and the amount of different conditions that it can face along the process, phosphates and silicates are good possible ending recipients to the released uranyl species due to their low solubility in water. Among many other transformations some will react with silicate ions ($[SiO_4]^{2-}$) to yield a whole range of silicates.[48] One of those potential transformations is coffinite, $USiO_4$.

Figure 3.3. Spent nuclear repositories. a) Sellafield (UK) and b) Centre de l'Aube and Morvilliers, Cires (France)

Coffinite, $USiO_4$, is a natural occurring mineral first described by Stieff *et al.*[49] from several sediment deposits along America, although it was first suggested by Goldschmidt[50] to appear in small quantities in thorite minerals, $ThSiO_4$. Classically, it has been defined as a very rare uranium containing compound. This conception was changed as deep studies on uranium ores were carried out, where coffinite was previously

assumed to be impure uraninite, UO_2. From then on it has been reported to be the second most prominent U(IV) bearing phase. It was observed from micro- to nanoscale in different geomaterials from organic surroundings to apatites,[51–53] and geochemical environments such as the natural nuclear reactor of Oklo (Gabon) and hydrothermal deposits in Canada.[54–56] Resembling these natural conditions seems to be key in order to obtain this pure silicate. Although it is abundant in natural repositories coffinite is so fine-grained that any attempt to obtain information about its chemical and physical properties seems to be very challenging.[51] The properties need to be fully understood in order to fully comprehend the chemical release the presence and degradation of uranium in nature. This necessity to obtain thermodynamic data has driven researches to attempt to obtain pure coffinite and extrapolated information from the urano-thorite solid solution.[57–60]

Although coffinite is reported to be stable in nature (as shown in Figure 3.4), its synthesis in a pure form, to the best of our knowledge is yet to be unveiled. Fuchs *et al*.[61] were the first to report the formation of coffinite by precipitation under hydrothermal conditions (T = 250°C, 1 day) using UCl_4 and Na_2SiO_3. In this synthesis, the initial pH conditions were found to be critical to obtain coffinite, with a significant number of pH controlling steps prior to heating. A number of subsequent studies have modified this protocol in order to ensure the tetrapositive oxidation number of uranium while avoiding UO_2 formation. Pointeau *et al*.[62] reported the formation of coffinite, but with an extremely low yield and nano-sized crystals. Labs *et al*. have reported the synthesis with silica excess.[63] Despite these numerous attempts, any synthesis protocol reported seems to be hardly reproducible, with very narrow temperature and pH ratios of stability. The difficulties surrounding the synthesis of phase pure coffinite have even been investigated themselves, with a number of published papers highlighting the difficulty in finding a systematic synthesis of coffinite.[57,64]

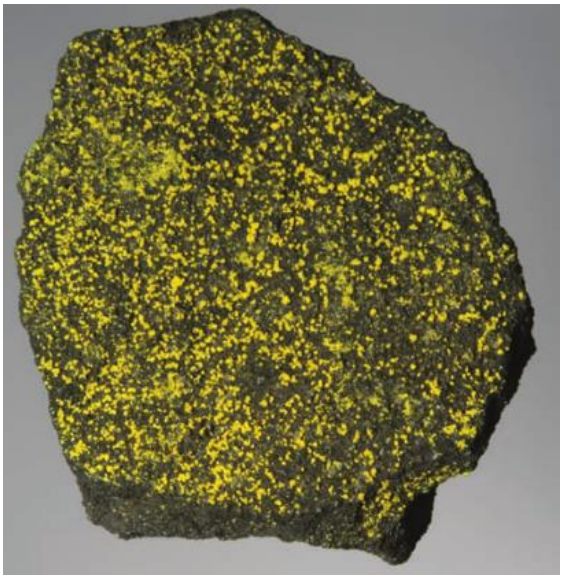

Figure 3.4. Black coffinite rock with a ~1 mm uranyl sulfate yellow coating.[65]

3.1.3 Thorite, $ThSiO_4$

Coffinite has been extremely challenging to synthesise, but the formation of structurally similar compounds has been previously reported. The most closely related silicate compound is thorite. Thorium silicate, $ThSiO_4$, can be found in two different crystal structures, thorite with the zircon-type structure and huttonite which has a monazite type structure (monoclinic, $P2_1/n$). Thorite was first observed in 1828,[66] and huttonite which is metastable to thorite appearing at high temperatures and pressure,[67] but defined as an individual crystal structure by Hutton.[68]

The synthesis of thorite has been approached by hydrothermal synthesis, obtaining the pure silicate by sol-gel hydrothermal assisted synthesis (240 and 800°C).[69] Nonetheless, high temperatures may not be necessary to obtain thorite.[70] Multiparametric studies on the hydrothermal formation of thorite have been reported more recently, showing the synthesis of thorium silicate is favoured in acidic to intermediate conditions. The hydrothermal synthesis of thorite was tested from predominantly acidic conditions in the presence of a strong acid such as nitric acid (C_{nitric}= 0.3 mol/L) to more basic such as for pH = 9.1, mild temperatures (120-250 °C) and higher concentrations than C_{Th} = $2.1 \cdot \times 10^{-3}$ M.[71] Similar research using carbonate as a reaction buffer, showed the impact of carbonate in the shape of the particles obtained from square based pyramids, to lens-

type. As well carbonate has a complexation effect on the metal, stabilizing it in solution and avoiding the hydrolysis into the stable oxide.[72]

Beyond a fundamental interest in thorite itself, a major motivation underpinning many of these investigations is that thorium can be used as an analogue or surrogate for uranium in exploring silicate synthesis, with the added advantage that Th(IV) is stable under a wider array of synthesis conditions than U(IV), thus narrowing the search parameters for viable synthetic routes to coffinite. The structural description of thorite and huttonite is included in Figure 3.5.

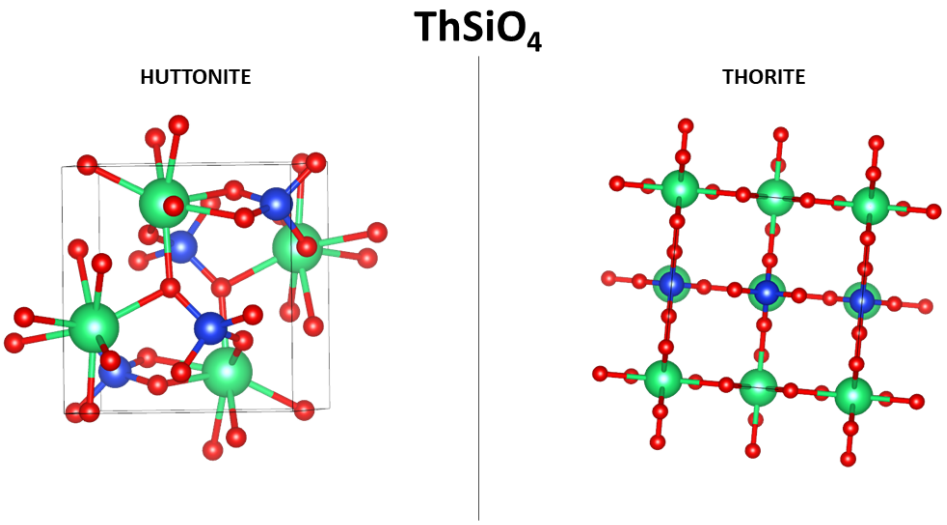

Figure 3.5. $ThSiO_4$ structures: huttonite and thorite. Figure seen along the (001) direction. Thorium atoms are shown in green, silicon in blue and oxygen in red.

3.1.4 Stetindite, $CeSiO_4$

Cerium is also known to yield a zircon structured silicate known as stetindite. This mineral was first reported in nature in 2009 as shown in Figure 3.6.[73] It was named after the the Stetind pegmatite locality, where it was first found. The first synthetic evidence is dated to the 2000s on a study of cement alteration.[74,75] It has been suggested to have a huge applicability as a promising luminescent material and catalyst.[76] Cerium is also commonly used to understand plutonium chemistry due to its similarities. The first reported procedure to synthesise this compound was by Dickson and Glasser.[74,76] The reactions reported involved hydrothermal reactions of $Ce(NO_3)_2$, SiO_2 and CaO (from the thermal decomposition of calcium carbonate) at mild temperatures ranging from 55 to

180 °C for a prolonged time (14 - 700 days). Stetindite only crystallised at lower temperatures than 85 °C yielding the oxide at higher than 130 °C. The presence of amorphous CeO_2 was never fully avoided. More recently, cerium silicates have been effectively synthesised under soft hydrothermal conditions[79] in much milder conditions and with high reproducibility. Coffinite formation showed a strong dependence on the pH, due to the formation of several complexes that would determine the final product. The formation of those varied species limits the availability of cerium in solution hindering its precipitation as a hydroxide promoting the transformation to ceria (CeO_2). The temperatures where the silicates were obtained ranged from 40 to 150°C. It was suggested that the use of Ce(III) precursors was preferred rather than Ce(IV) ones in order to avoid the formation and precipitation of the oxide. Stetindite is promoted by the formation of Ce(III) silicate complexes that evolve into the target orthosilicate. The synthesis was performed under hydrothermal conditions ($T \leq 150$°C, 7 days, nitric acid media) choosing A-$Ce_2Si_2O_7$ and $Ce_{4.67}(SiO_4)_3O$ as the precursors.[80] Mimicking these results, $PuSiO_4$ and $HfSiO_4$ has been successfully obtained in HCl media.[81,82] The main crystallographic data from the zircon-type silicates studied are included in Table 3.2.

Table 3.2. Selected crystallographic data of the zircon-type silicates.[78,83–85]

Compound	Zircon	Stetindite	Coffinite	Thorite
Formula	$ZrSiO_4$	$CeSiO_4$	$USiO_4$	$ThSiO_4$
Lattice Parameter a (Å)	6.5800	6.9564	6.9950	7.1328
Lattice Parameter b (Å)	6.5800	6.9564	6.9950	7.1328
Lattice Parameter c (Å)	5.9300	6.1953	6.2630	6.3188
Volume ($Å^3$)	256.75	299.80	306.45	321.481

Figure 3.6. Stetindite crystal in yttrian fluorite surroundings.[73]

3.2 Aims

Hydrothermal synthesis has been reported as an ideal candidate for the synthesis of natural occurring coffinite. Due to the low availability and the radioactive nature of uranium, however, the scope for extensive mapping of reaction conditions towards coffinite synthesis is limited. Therefore, to explore what are the optimal synthetic conditions for the synthesis of this uranium silicate, here we will primarily target various analogues: zircon, stetindite and thorite. The main feature that characterises them is a common crystal structure – zircon. Due to this commonality with coffinite zircon has been shown to be able to accommodate uranium within its structure, as has been reported for chernobylite mineral ($Zr_{1-x}U_x)SiO_4$) encountered at Chernobyl lava analysis.[65] Similarly, cerium has been used as a surrogate for other radioactive materials that can be encountered in nuclear waste, such as plutonium due to its more complex chemical behaviour. Finally, thorite has been classically used to understand the physicochemical characteristics of coffinite by extrapolation from its uranothorite solid solution compound.[63,86–88]

The development of reliable synthetic routes to these zircon-type silicates is thus expected to present a platform from which a great deal of information may be extracted around these environmentally important minerals, and crucially the ultimate determination of optimal synthetic conditions for the preparation of phase pure coffinite.

Here, we will explore the mild hydrothermal synthesis of the non-radioactive coffinite analogues zircon and stetindite, and their mixed solid solutions. Synthetic conditions identified in these studies will also be applied to the production of thorite, and finally the common optimal synthetic characteristics will be applied to the synthesis of coffinite. All products will be analysed by powder X-ray diffraction in order to corroborate the formation of the target material and FTIR to gain a further insight on how the synthetic conditions affect the synthesis of the different minerals.

3.3 Experimental

3.3.1 Synthesis

All the syntheses were performed using the "standard batch hydrothermal synthesis" as described in Chapter 2.

The silicate precursor solution consisted of sodium metasilicate, Na_2SiO_3, dissolved in distilled water to the desired concentration, specified in each section. In cases that basic pH adjustment was required the sodium metasilicate was dissolved in an aqueous sodium hydroxide solution of desired NaOH concentration.

The acidic metal solution consisted of the corresponding metal salt $ZrOSO_4$ or MCl_x (where x is the oxidation state of the metal source, $M^{x+} = ZrO^{2+}$, Ce^{3+}, Th^{4+}, U^{4+}) dissolved in water and pH adjusted by use of either HNO_3 or HCl solutions as solvents. The selection of the acid will be discussed in each section.

The order of addition was kept constant through all the reactions. The volume of the silicate precursor for all the set of reactions was 5 mL and was the first solution to be pipetted in the reaction container. The second solution to be poured was the acidic metal solution with a total volume of 2.5 or 5 mL, depending on the reaction. The total volume of the reacting solution will be 10 or 7.5 mL (0.43 and 0.33 ff, respectively).

Upon addition of every solution in the autoclave and proper closing of the system, it is introduced into the preheated oven at the desired temperature. Once the reaction time is finished, the autoclave is removed from the oven and cooled down to room temperature. The products were decanted to a centrifuge tube with all the washing waters and centrifuged at 6000 rpm, until all the solid products had pelletised at the bottom of the tube. The clear supernatant is discarded and the solid is washed three times with distilled water by repeated centrifugation and decantation. The remaining clean solid is dried in air overnight at 75 °C.

Specific synthetic conditions such as the metal precursors chosen, the temperature of synthesis or the concentration of the acid or the base will be shown in the discussion section as it is key to understand the role that those parameters play at the optimisation of the reaction procedure. The general reaction is given below in equation 3.1:

$$M^{4+} + SiO_3^{2-} \xrightarrow{H_2O} MSiO_4 \qquad (3.1)$$

3.3.2 Characterisation

3.3.2.1 Powder X-Ray Analysis (PXRD)

The X-ray diffraction patterns for zircon and stetindite were recorded on a Bruker D2 powder diffractometer using Cu Kα = 1.5418 Å. The patterns were recorded from 5 to 80° 2θ at 1.5 s per step. The samples were deposited on a zero background holder made of 9N semiconductor grade silicon.

For the radioactive samples containing thorium and uranium the measurements were carried in a silica capillary in a Bruker X–ray Duo machine with Cu Kα = 1.5418 Å. The patterns were recorded from 20 to 60° 2θ.

For the quantification of diffraction data, Rietveld refinement will be employed. The software required for these calculations was GSAS/EXPGUI.[89,90] Example of the models patterns used for zircon and stetindite are given in Figure 3.7.

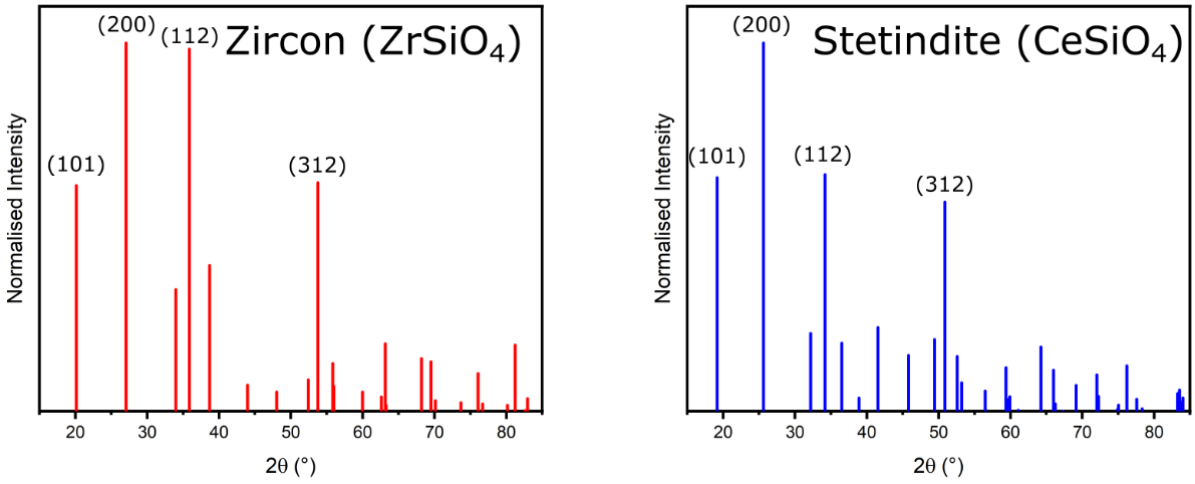

Figure 3.7. XRD simulated models of zircon and stetindite. 4 most intense peaks are labelled. [78,91]

3.3.2.2 Fourier Transform Infrared Spectroscopy

FTIR spectra were recorded using a Perkin Elmer Spectrum 100 instrument with Perkin Elmer Universal ATR Sampling Accessory from 4000 cm^{-1} to 500 cm^{-1} in steps of 2 cm^{-1}.

3.4 Results and Discussion

In order to explore the optimum conditions for the synthesis of coffinite, it was decided to start testing the synthesis of zircon. Due to the complicated nature of the procedure with radioactive materials and in particular with uranium, procedures need to be optimised beforehand with different surrogates. Those aforementioned compounds will be zircon ($ZrSiO_4$) and stetindite ($CeSiO_4$). The variables identified to be tuned during the reactions were: temperature, concentration, precursor, pH, and time. All of those are feasible to be changed and seem to play a huge role in the outcome of the synthesis.

3.4.1 Synthesis of Zircon, $ZrSiO_4$

The initial attempts to produce zircon used zirconyl sulfate, $ZrOSO_4$, as the zirconium source and sodium metasilicate as the silicate source. 0.12 M solutions of $ZrOSO_4$ were prepared by dissolution of appropriate amounts of the zirconyl sulfate in 5 M and 1.25 M nitric acid solutions. 0.06 M solutions of Na_2SiO_3 were prepared in 0.6 M and 2.5 M NaOH solutions. 5.0 mL of the appropriate basic silicate solution was first added to the dry Teflon® cup, followed by 2.5 mL of the appropriate acidic zirconium solution, to give a reaction mixture of a total 7.5 mL volume with a 1:1 Zr:Si molar ratio. Solutions were chosen to yield molar ratios of the acid to the base from 2:1, 1:1 to 1:4. Reactions were performed at temperatures of 200°C for times of 2, 3 and 4 days as summarised in Table 3.3.

Table 3.3. Summary of reactions for the first attempts of zircon synthesis. $ZrOSO_4$ 0.125 M was dissolved in HNO_3 and Na_2SiO_3 0.0625 M was dissolved in NaOH. The reactions were performed at 200°C.

C HNO_3 (M) - 2.5 mL	C NaOH (M) - 5 mL	Ratio (HCl : NaOH)	Days
5	0.625	2:1	2
5	2.5	1:1	2
1.25	2.5	1:4	2
5	0.625	2:1	3
5	2.5	1:1	3
1.25	2.5	1:4	3
5	0.625	2:1	4
5	2.5	1:1	4
1.25	2.5	1:4	4

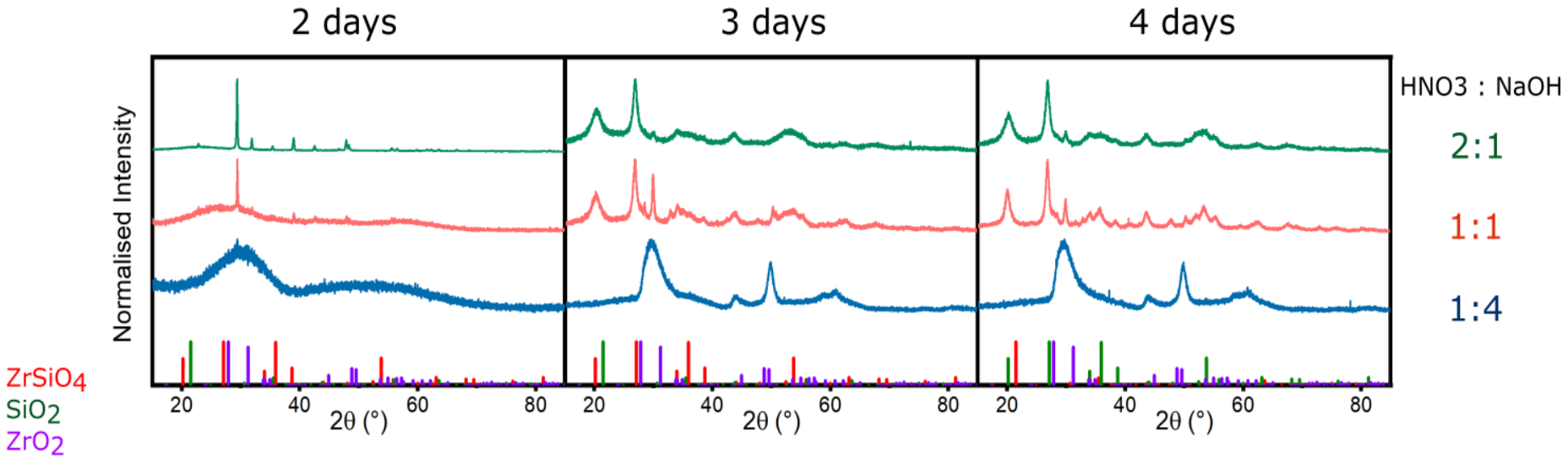

Figure 3.8. XRD patterns of the first reaction attempts for zircon synthesis. $ZrOSO_4$ is used as the zirconium source in all of the reactions. The model PXRD patterns for zircon ($ZrSiO_4$), silica (SiO_2) and zirconia (ZrO_2) are shown as vertical lines in red, green and purple, respectively, at the bottom of each graph.

For reaction time of 2 days only zirconia (ZrO_2) is formed at more basic conditions, while a mix of the oxide and sodium nitrate is formed at the more acidic conditions. After 3 and 4 days similar behaviour can be seen for the basic conditions where only the oxides are made, while more acidic conditions promote the formation of zircon. The main peaks of this silicate are present at around 20 and 27° 2θ corresponding to the (011) and (020) planes. Although zircon was obtained, it is formed with impurities of oxides. From these results in can be concluded that reaction times longer than 2 days are required and higher presence of the acidic solution than the basic is required for the formation of zircon.

There are two possible pathways for the formation of these silicates. It can be either formed directly form the interaction of the metal with a solution saturated in silicate, precipitating as the target silicate or as a surface effect of the dissolution of the oxides previously formed reprecipitating as silicates. Following the first justification the oxide formation must be avoided as the reactants need to be in solution to react, while for the second point the oxides need to suffer a fast precipitation to be as small and reactive as possible serving as the precursors of the silicates. Long term reactions for UO_2 with silicate solution suggest the formation of this silicate from the oxides.[92] Although this coffinite was obtained at pH = 9 and a solution undersaturated in respect to silica there is not consensus for the hydrothermal synthesis of zircon as it has been reported for both acidic and basic conditions.[36,93–95] Therefore, a more precise optimisation of the pH is required for the next steps.

It should be noted that, while these initial syntheses showed some promise, the choice of $ZrOSO_4$ as a precursor proved problematic. This was initially chosen as it was envisaged that these reactions would be adapted to use on the injection reactor, and thus any precursors or reagents chosen needed to be compatible with stainless-steel. It was found however that although zirconyl sulfate is meant to be soluble in these conditions it was rather complicated to solubilise it in acidic conditions (sulfuric acid for example did not yield solutions of appropriate concentration). Therefore, $ZrOCl_2$ was used for later test reactions using HCl as the acid. While this limits the investigations to conventional Teflon-lined autoclaves it has the advantage of avoiding the formation of $NaNO_3$ and simplifying the anionic presence in solution as only Cl^- will be the common counterion.

Additionally future work on coffinite stemming from these zircon studies becomes more comparable, as uranium chlorides are much more readily available.

Due to the contradictory information encountered between this first series of reactions and those previously reported ones, the pH needs to be optimised for the reactions. To optimise the process the zirconium source zirconyl chloride, $ZrOCl_2$, dissolved in 1.0 M HCl solution to give a 0.25 M zirconium solution, used for every reaction, while the equimolar (0.25 M) sodium metasilicate basic solution was prepared in 0.25, 0.50, 0.75 and 0.90 M NaOH to modify pH. The reactions were carried at 150 °C for 3 days. A summary of the reaction conditions is given in Table 3.4. Additionally, to promote the pressure in the reaction bombs, the total volume was 10 mL, formed by the mix of 5 mL of the metal solution and 5 mL of the silicate solution (Figure 3.9). This is expected to destabilise the oxides which are needed to redissolve and form the corresponding silicate.

Table 3.4. Zircon reactions at 150°C changing base concentration.

C $ZrOCl_2$ (M) $HCl_{(aq)}$ 1.0 M	C NaOH (M) Na_2SiO_3 R (Si/Zr) = 1:1.03	Temperature (°C)	Time (Days)	pH measured
0.25	0.25	150	3	0.50
0.25	0.5	150	3	0.94
0.25	0.75	150	3	1.90
0.25	0.9	150	3	4.40

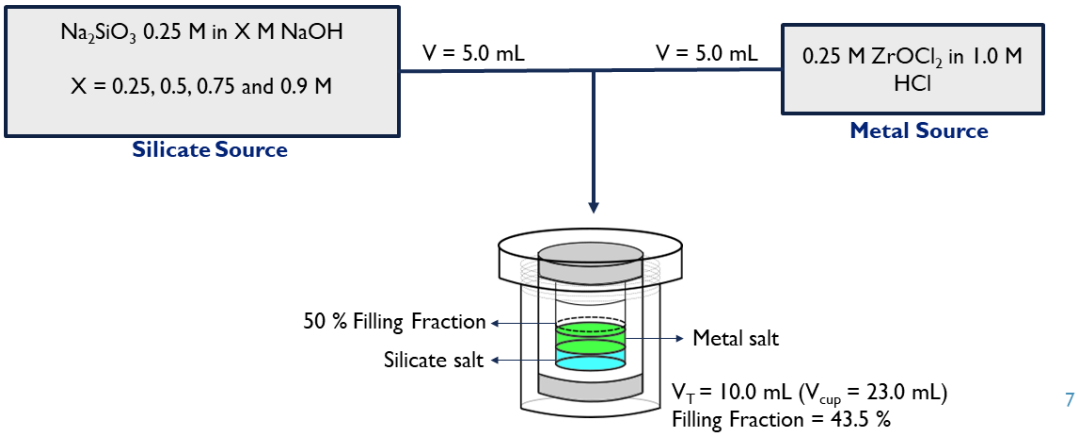

Figure 3.9. Experimental set up for the zircon optimum pH test reactions.

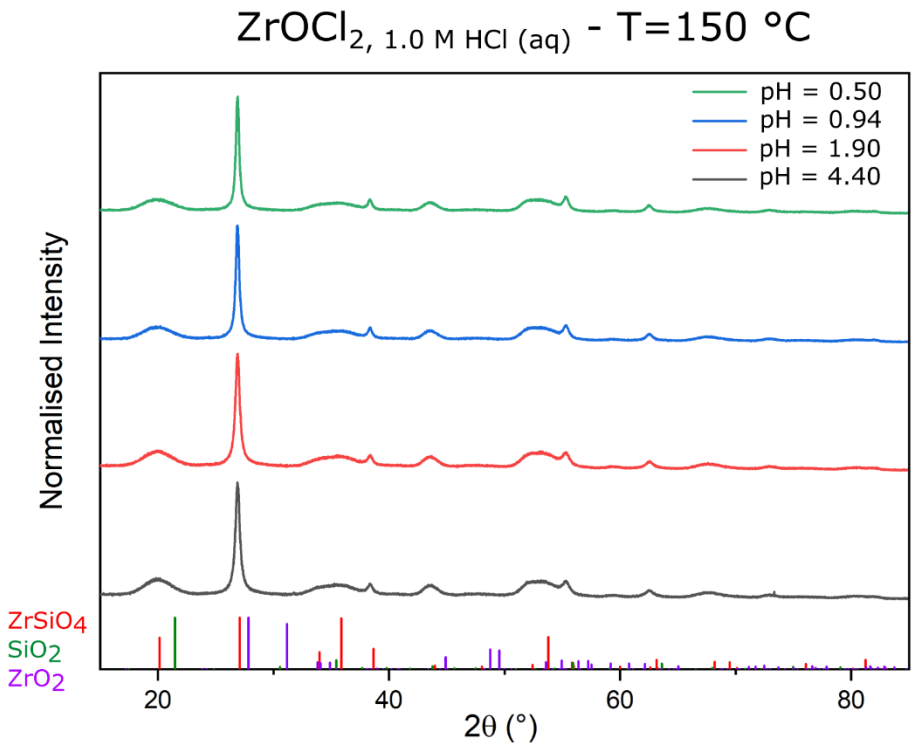

Figure 3.10. XRD patterns of products obtained from the reaction of 5 mL of 0.25 M zirconyl chloride in 1.0 M HCl with 5 mL of 0.25 M sodium metasilicate in the variable concentration of sodium hydroxide for 3 days at 150 °C.

From Figure 3.10 pure zircon is obtained under all acidic conditions. This shows an improvement from previous attempts and a wider optimum condition range than suspected. Additionally, it suggests that lower temperatures (150 °C) are needed to yield the silicate. The XRD patterns show anisotropic behaviour at the peaks shape, with many very broad peaks, and several sharp peaks, most evident when looking at the (200) peak at around 27° 2θ. The higher intensity and sharper peak shape of that peak implies a higher crystallinity in that direction than in the other crystallographic planes. The broad peaks correspond to (hkl) planes in which $l \neq 0$, while the sharp peak at ~ 27°, 38°, 56° and 63° 2θ all have Miller indices (hk0). This is indicative of a plate-like crystal habit, *i.e.*, the zircon is well-crystallised in the *ab* plane, but poorly crystalline in the *c*-direction. Similar behaviour has been reported for mild synthesis of zircon in acidic conditions.[94] It has been suggested that the acidic conditions promote the radial growth in the a and b directions, by yielding edge-sharing dodecahedra of ZrO_8.[96]

As zircon synthesis was optimised, the next step is to explore how robust these synthetic conditions are when they are applied to the formation of a similarly structured mineral like stetindite, $CeSiO_4$.

3.4.2 Synthesis of Stetindite, $CeSiO_4$

Similar conditions to the last attempts of zircon synthesis were performed for $CeSiO_4$ synthesis. Ammonium cerium nitrate, $(NH_4)_6Ce(NO_3)_2$, 0.25 M was dissolved in an aqueous solution of HNO_3 1.0 M. For the equimolar (0.25 M) sodium metasilicate basic solution prepared, 0.25, 0.50, 0.75 and 0.90 M NaOH were dissolved in water to modify the pH of the solution. A summary of the synthesis conditions is given in Table 3.5. For the reaction 5 mL of the basic silicate solution were pipetted into the reacting cup along with 5 mL of the acidic metal solution. The total volume of the reaction was 10 mL.

Table 3.5. Stetindite reactions at 150°C changing base concentration.

C $(NH_4)_6Ce(NO_3)_2$ (M) $HNO_{3(aq)}$ 1.0 M	C NaOH (M) Na_2SiO_3 R (Si/Zr) = 1:1.03	Temperature (°C)	Time (Days)	pH measured
0.25	0.25	150	3	0.50
0.25	0.5	150	3	0.94
0.25	0.75	150	3	1.90
0.25	0.9	150	3	4.40

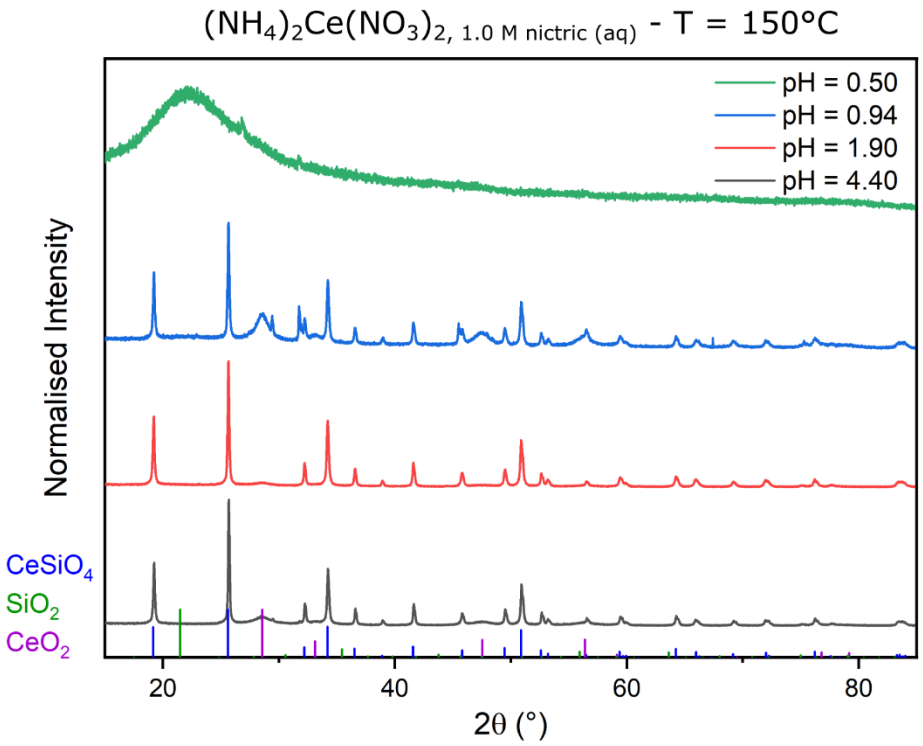

Figure 3.11. XRD patterns of products obtained from the reaction of 5 mL of 0.25 M ammonium cerium(IV) nitrate in 1.0 M HNO_3 with 5 mL of 0.25 M sodium metasilicate in variable concentration of sodium hydroxide for 3 days at 150 °C.

The results were plotted from more acidic conditions to more basic in Figure 3.11. Stetindite was present in 3 out of 4 reacting conditions attempted. Cerium oxide is formed for pH = 4.40 and 0.94. The version with the purest version of cerium orthosilicate is seen for pH = 1.90, which corresponds to NaOH = 0.75 M. More acidic conditions promote the formation of amorphous silica, as seen for pH = 0.50.

Therefore, the optimum conditions for the formation of this silicate goes in consonance with zircon synthesis. 0.75 M NaOH is required to be dissolved in the basic silicate solution for obtaining the most optimised reaction.

As both silicates were formed at similar synthetic conditions, the mixed version of the silicates can be attempted to observe the range of stability of these silicates.

3.4.3 Synthesis of Mixed Silicates, $Ce_xZr_{1-x}SiO_4$

The robustness of this synthetic protocol was assessed by examining synthesis of the mixed cerium-zirconium silicate $Ce_xZr_{1-x}SiO_4$ was tested using $ZrOCl_2$ and $CeCl_3$ as the metal precursors. The Ce(III) is readily oxidised under reaction conditions by

dissolved oxygen. The metal precursor is dissolved, as in previous reactions described, in 1.0 M aqueous HCl and the silica precursor concentration is Na_2SiO_3 = 0.25 M in 0.75 M aqueous NaOH. 0.75 M NaOH was chosen here as these conditions were found to produce both extremes of x = 0 and x = 1 in the previous sections. The concentration of zirconium and cerium will be varied in order to obtain different ratios in the resultant silicate. The resultant silicate can be described by the formula $Ce_xZr_{1-x}SiO_4$ (where x = 0, 0.2, 0.4, 0.6, 0.8 and 1.0), so that the substitution will be in steps of x = 0.2. The volume of the metal and the silicate solutions pipetted will be the same, 5 mL each. It makes up a total of 10 mL in the autoclave. The complete scheme of reactions with a description of the minerals observed in the XRD patterns is shown at Table 3.6 and the XRD patterns of the resulting products in Figure 3.12.

Table 3.6. Summary of reactions for the mixed-silicates ($Ce_xZr_{1-x}SiO_4$) at 150 and 200°C. (A) amorphous, *only traces are visible.

x	Temperature (°C)	Time (days)	Product
0	150	1	Zircon
		2	Zircon
		3	Zircon
	200	1	Zircon, Zirconia
		2	Zircon, Zirconia*
		3	Zircon, Zirconia*
0.2	150	1	$Ce_{0.2}Zr_{0.8}SiO_4$
		2	$Ce_{0.2}Zr_{0.8}SiO_4$
		3	$Ce_{0.2}Zr_{0.8}SiO_4$
	200	1	Zircon, Zirconia and/or Ceria*
		2	$Ce_{0.2}Zr_{0.8}SiO_4$
		3	Zircon, Zirconia and/or Ceria*
0.4	150	1	(A) Zirconia and (A)Ceria
		2	(A) Zirconia and (A) Ceria
		3	(A) Zirconia, Ceria and Stetindite*
	200	1	Zircon and Ceria*
		2	Zircon and Ceria*
		3	Zircon and Ceria*
0.6	150	1	(A) Zirconia and (A) Ceria
		2	Zirconia and Stetindite
		3	Ceria or zirconia and Stetindite
	200	1	Zirconia and Stetindite*
		2	Zircon and Stetindite
		3	Zircon and Ceria*
0.8	150	1	Zirconia and Stetindite
		2	Zirconia and Stetindite
		3	Ceria, Zirconia and Stetindite
	200	1	Ceria and/or Zirconia
		2	Stetindite and (A) Zircon*
		3	Stetindite, Ceria and Zirconia*
1.0	150	1	Stetindite and Ceria *
		2	Stetindite
		3	Stetindite
	200	1	Stetindite and (A) Ceria
		2	Stetindite
		3	Stetindite and Ceria

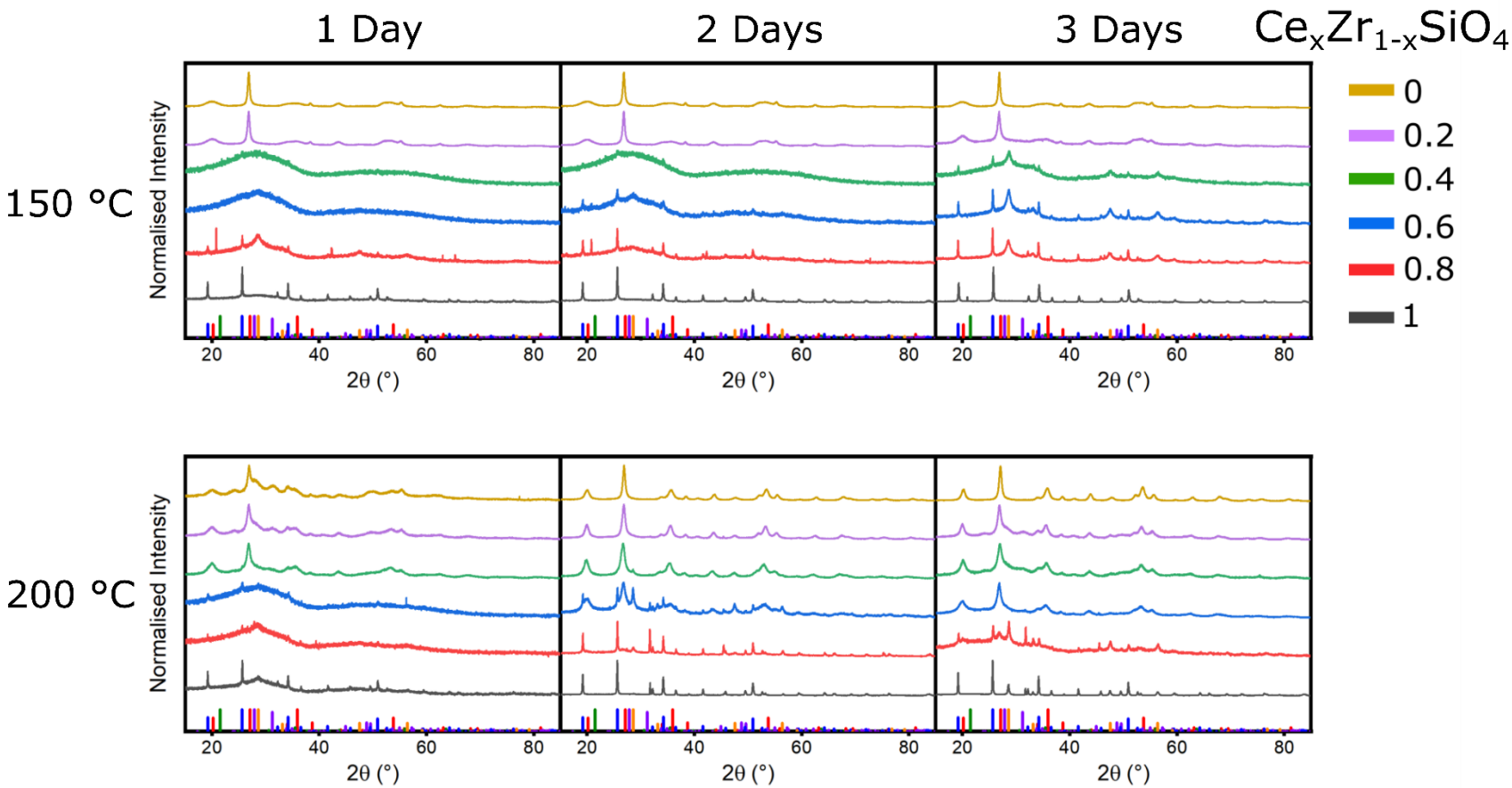

Figure 3.12. XRD patterns of mixed silicates $Ce_xZr_{1-x}SiO_4$ in steps of substitution of x = 0.2. Vertical lines from the model patterns are included under the plot, where red is zircon, blue stetindite, green silica, purple zirconia, and orange ceria.

The XRD patterns in Figure 3.12 are organised from top to bottom in increasing cerium concentration in the mixed silicates. The results will be discussed systematically by increasing the metal substitution defined as *x* for the different reaction times and temperature. A full description of the compounds obtained is shown in Table 3.6. Starting with the silicates obtained for x = 0 at lower temperature, 150 °C, only zircon as a silicate can be obtained. This silicate is observed pure, showing crystalline peaks at every reaction time attempted, from 1 to 3 days. Nonetheless when observing the results for higher temperatures, 200 °C at shorter reaction times zircon and zirconia (ZrO_2) peaks are visible in the pattern. Longer reaction times promote the formation of single zircon in the sample. There is a noticeable anisotropic behaviour for the peak shape for lower temperatures. The effect is not as evident for 200 °C. The possible reasoning for the appearance of this irregularity of the crystallisation of the silicate will be discussed further in the thesis along with the results obtained from FTIR and TEM in Figure **3.13**.

When observing x = 0.2 the mixed version of the silicate can be acknowledged, $Ce_{0.2}Zr_{0.8}SiO_4$, for lower temperatures (150 °C) at every timeframe. When assessing the higher temperature, it is observed that a component with zircon structure obtained along with the presence of a metal oxide for 1 and 3 days. It can be either zirconia or ceria (CeO_2). The intermediate silicate is obtained for 2 days of reaction.

When increasing the cerium presence to x = 0.4 the results are drastically different to the previous ones. The XRD patterns show a major presence of an amorphous oxide formed that can be either ceria or zirconia for 1 and 2 days at 150 °C. For 3 days that amorphous oxide is formed along with peaks of a crystalline material that can be assigned to stetindite. At x = 0.4 at 200 °C, zircon can be observed for every reaction time. Although the silicate is formed, it shows a shoulder broad peak next to the most intense feature for zircon at 27° 2θ related to the (020) direction. That broad feature can be assigned to ceria showing a peak at around 28° 2θ related to the (111) orientation.

At cerium presence in the reaction of x = 0.6 at 150 °C an amorphous material is obtained for 1 day of reaction that transforms into stetindite and either ceria or zirconia at longer reaction times, with increasing crystallinity from 2 to 3 days of reaction. At 200°C reactions a similar effect is shown as for lower temperatures where there is a progressive crystallisation from lower reaction times to crystalline silicate corresponding

to zircon and a small shoulder corresponding to the oxide as the reaction time is prolonged.

For x = 0.8 at lower reaction temperatures, 150 °C, a lower crystalline material is obtained, potentially zircon, along with stetindite are observed at every reaction time. For 200 °C an amorphous feature is seen for lower reaction times that correspond with the metal oxides, crystallising into stetindite, zirconia and ceria at longer reaction times.

x = 1 corresponds to the synthesis of pure stetindite so only cerium precursor is chosen as metal reacting precursor. For lower temperatures stetindite and a small presence of ceria is seen for lower reaction times. Pure stetindite is observed at 2 and 3 days of reaction times. When looking at 200 °C reactions a similar behaviour is observed with the formation of ceria and the silicate at 1 day of reaction and pure stetindite for 2 and 3 days of reaction.

Thermodynamic studies of the formation of each silicate have been reported.[97] The doping of zirconium into the stetindite framework hasn't been previously reported but cerium is often used as a Pu surrogate due to various chemical similarities.[98,99] When analysing the coordination environment of Ce^{4+}, in the case of silicate structures is similar to Pu^{4+} in which they are both eight-coordinated with ionic radius of 0.97 and 0.96 Å, respectively.[100] Therefore, any silicate study that involves Pu will be transferable to Ce. It has been found that for the system $(Zr,Pu)SiO_4$ it is extremely rare for the mixed silicate to occur when the presence of Pu is higher than 10 wt %.[101] The obstacle to the inclusion of Pu as a silicate in the zircon structure is attributed to the metastable behaviour of $PuSiO_4$ in relation to the oxides, PuO_2 and SiO_2. Stetindite is also metastable with respect to its oxides ($\Delta H_{f,ox,25°C}$ of $CeSiO_4$ = 27.5 ± 3.1 kJ/mol).[97] The formation of $PuSiO_4$ is reduced to a very narrow range of conditions, closely related to the ones for stetindite as shown by Estevenon *et al.*.[79,81] This results of the formation of intermediate phases are supported by similar cases illustrated in the literature. Zircon on the other hand is thermodynamically more stable than the oxides giving it the ability to adopt other metals in the structure, such as cerium, by a negative calculated enthalpy of formation ($\Delta H_{f,ox,25°C}$ of $ZrSiO_4$ = -24.2 ± 2.8 kJ/mol).[102] It is seen that if the substitution is targeted around a synthetically more favourable silicate, like zircon, there is a higher possibility of presence of the additional metal in the lattice. The more optimal use of zircon (than stetindite for example) as a storing mineral is potentially related to the distortion of the polyhedra in

the structure or additional ordering of the metal in the lattice that lowers the energy required for introducing that additional atom.

This inability of zircon to accommodate a larger amount of certain metals in the structure such as Pu, is one of the main concerns for applying this material as a repository for metals obtained from SNF. Therefore, a synthetic strategy is needed to optimise this orthosilicate for its use as a storage ceramic for actinides (An^{4+}).

To yield the extreme versions of x = 0 and x = 1, common synthetic conditions are seen from Figure 3.12, where 150°C and 3 days seems to yield the most pure and crystalline products possible. Furthermore, clear differences in the nucleation and growth behaviour of the pure zircon and stetindite can be inferred from their XRD patterns. Firstly, $CeSiO_4$ is expected to have a narrower range of formation conditions as seen for shorter reaction times. Secondly, the shape of the XRD patterns might suggest an anisotropic behaviour in the growth of zircon, not seen in stetindite. This effect is evidenced by TEM images of the end-samples as seen in figure 3.13.

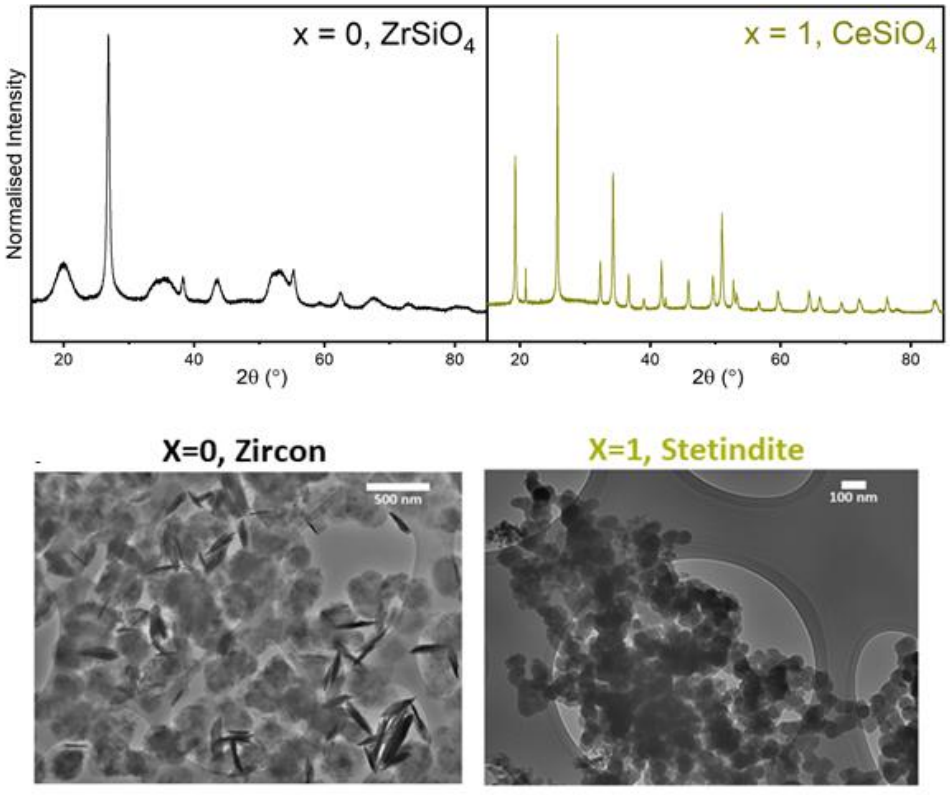

Figure 3.13**. TEM images with their corresponding XRD patterns from the end-products at 3 days and 150°C. It shows a different crystallisation behaviour between zircon and stetindite.**

From Figure **3.13** obvious differences between the particle shapes of both materials can be acknowledged. Zircon is observed to have an anisotropic behaviour, where there are platelets with different stacking and a second shape of apparent rods. The rod-like morphologies may simply be the result of viewing the stacked plates in an edge-on orientation, or the particles rolled over itself creating these sharp-looking rods. Stetindite shows a more uniform behaviour. They are spherical looking and highly isotropic particles. That growth behaviour is correlated to the results shown in the XRD patterns. For further explanation spectroscopy studies are required.

The FTIR spectra of the mixed silicate reactions at 150°C are shown below in Figure 3.14.

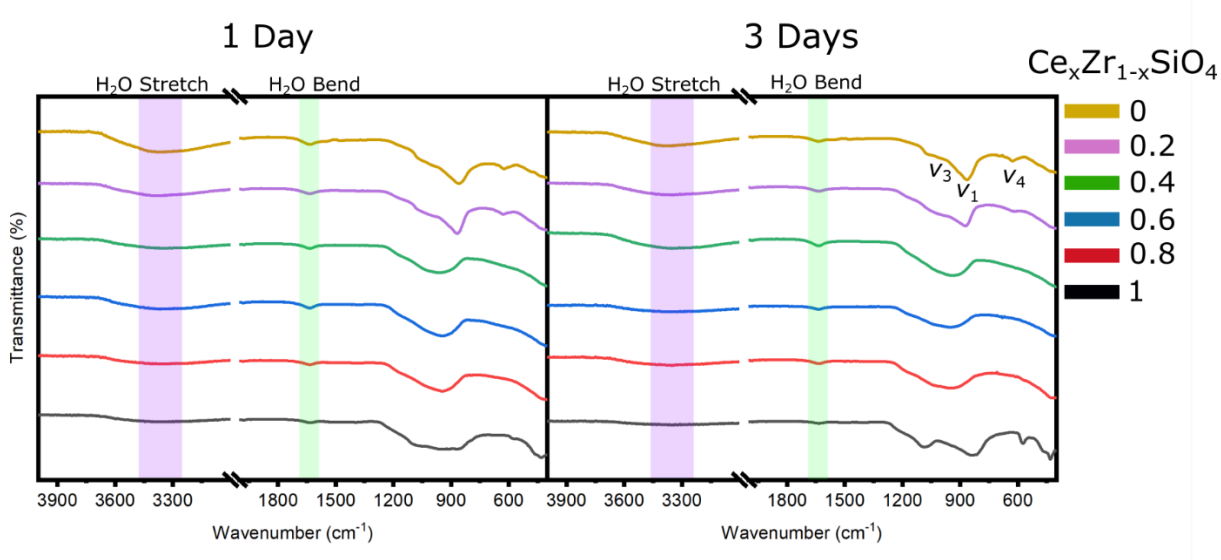

Figure 3.14. FTIR spectra of the mixed silicate samples obtained at 150°C with a metal substitution in steps of x = 0.2 for 1 and 3 days.

Seven FTIR vibrational modes have been calculated for a $I4_1/amd$ space group cell.[103,104] Four are internal modes ($\Gamma_{int} = 2A_{2u} + 2_{Eu}$) and three external ($\Gamma_{ext} = A_{2u} + 2_{Eu}$). In Figure 3.15 three internal modes can be assigned near 1000, 800 and 600 cm^{-1}. Similar spectra have been already reported for equivalent materials.[105]

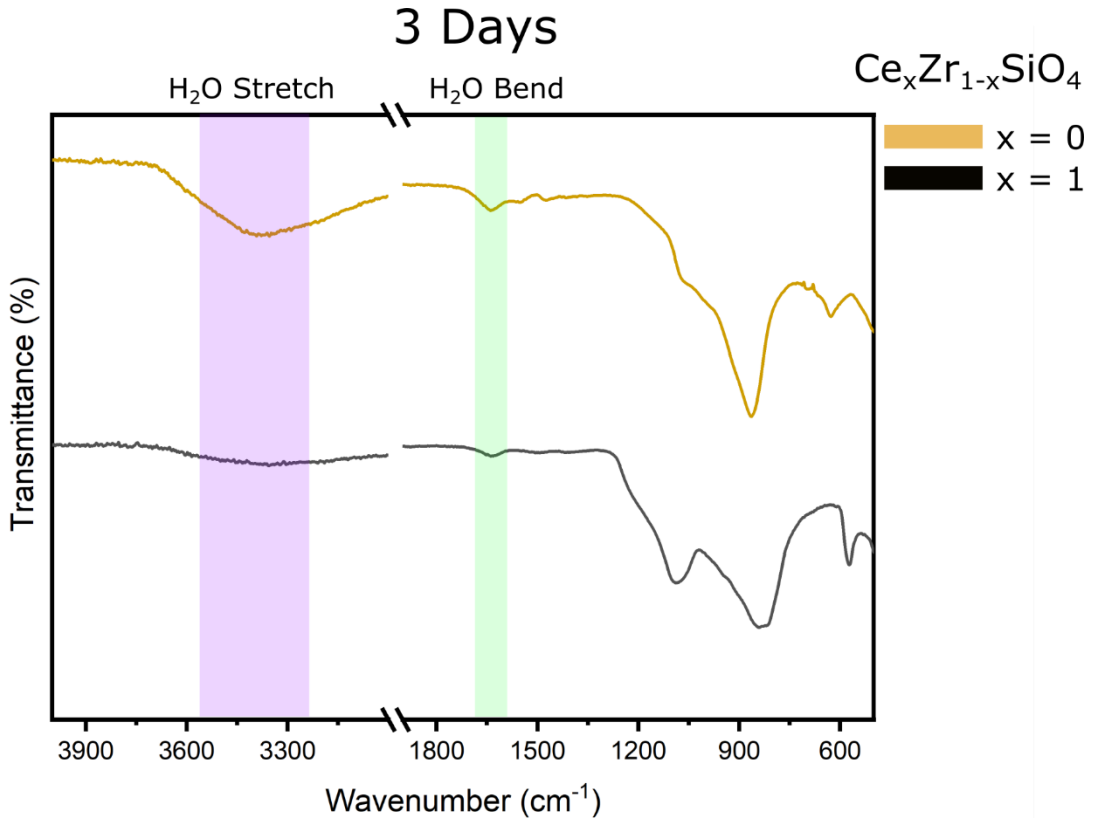

Figure 3.15. FTIR spectra for the extreme mixed silicate samples obtained for x = 0 and x = 1 obtained at 150°C for 3 days. The main water bands are shown by the purple and blue translucid bands.

In addition to the internal modes expected, water stretching and bending modes are also observed in Figure 3.14 and Figure 3.15. The stretching vibration for water appears in the range of 3500-3200 cm^{-1}. The bending mode on the other hand is expected to appear around 1600 cm^{-1}. The appearance of water seems to be more pronounced for zircon (x = 0) than for stetindite (x = 1) samples. There are three types of water linked to the zircon type structure. (1) weakly bonded molecular water adsorbed at the surface of the material,[58] (2) internally embedded at the structural channels in the [001] direction,[105] and (3) H_2O or OH^- substituting the oxygen atom at the $[SiO_4]^{4-}$ tetrahedra.[106] Water has been shown to play an important role for the growth of zircon-type silicates.[105] TGA with FTIR analysis after calcination shows that the removal of the water in the structure and disappearance of H_2O stretching and bending modes affects the lattice at the c-axis related peaks at the XRD where the water is confined in the channels by a non-linear variation in the unit cell of the a and b – axis *vs.* the c – axis due to the directional removal of the confined water. The disappearance of water causes a contraction in the lattice competing with thermal expansion. At the same time ν_1 and ν_3 are shifted to higher frequencies due

to the decrease in Si-O bond length after water removal,[105] similar to the behaviour of those silicates at high pressures.[107–109] These reported results corroborate the trend seen when comparing the zircon and stetindite samples obtained here. The disappearance of the water band from zircon to stetindite is closely related to the change in XRD and morphology shown for in Figure **3.13**. Water enclosed in the [001] channel causes disruption to the growth along the c-axis. While b-axis related peaks are enhanced such as seen for the most intense peak at 27° 2θ corresponding to the (020) orientation. That crystallographic effect influences the promoted growth in TEM and the preferential growth effect.

Although they are both structurally similar materials, they follow different nucleation and growth processes where the presence of water plays an important role on the shape of the particles and in the way that the metal is accommodated in the lattice.

3.4.4 Synthesis of Thorite, $ThSiO_4$

The different optimal conditions obtained for zircon and stetindite were reproduced to obtain thorium silicate, $ThSiO_4$. Thorite is reported to have a wider range of synthetic conditions than coffinite.[110] Uranium and thorium silicate species are one of the biggest deposits of both elements and the formation through colloids[111] has been proven. Nonetheless, the later crystallisation of the orthosilicates has never been fully expressed. Solid solutions of $Th_{1-x}U_xSiO_4$ have been successfully prepared by soft hydrothermal reaction at 250°C of the corresponding chlorides in bicarbonate buffer.[112] The uranium end-member, coffinite, to the best of our knowledge has never been yielded pure under those conditions.[64,87,112] Nonetheless, although thorite is more stable than the corresponding oxides while coffinite is metastable, the appearance of both minerals in similar environments leads to the conclusion that there must be a common ground of synthetic conditions between both minerals.

The synthesis of thorite was attempted starting from the simplest way possible with a high reproducibility, thus the variables considered are increased after every reaction attempt. Every diffraction pattern reported here will show amorphous silica background due to the capillary employed for the measurements.

A similar experimental procedure for the previous samples was followed in targeting thorite production. $Th(NO_3)_4{\cdot}5H_2O$ was used as the thorium precursor. Due to

the radioactive and toxic nature of this element the concentrations in solution for the reaction were kept lower than for zircon and stetindite test reactions. Sodium metasilicate, Na_2SiO_3, was maintained as the silicate precursor. 20.7 mg of Na_2SiO_3 were dissolved in 5 mL of distilled water, and separately 91 mg of $Th(NO_3)_4 \cdot 5H_2O$ were dissolved in 5 mL of distilled water. 5 mL of each solution were poured in the autoclave, making up a total of 10 mL with a Si/Th ratio of 1.06. The reactor was placed in the electric oven, pre-heated to 200 °C for 24 hours. The product was isolated and washed by repeated centrifugation and dried overnight at 75 °C. Despite that the formation of zircon and stetindite required lower temperatures than 200°C, these samples were proposed to be synchrotron measured, therefore the presence of water need to be avoided for them to be subjected to the measurement. As suggested by Dacheux *et al.*[71] the hydrothermal synthesis of thorite at high hydrothermal temperatures promoted the disappearance of water and hydroxyl groups bonded in the silicate, thus, temperatures over 200 °C were targeted in this case.

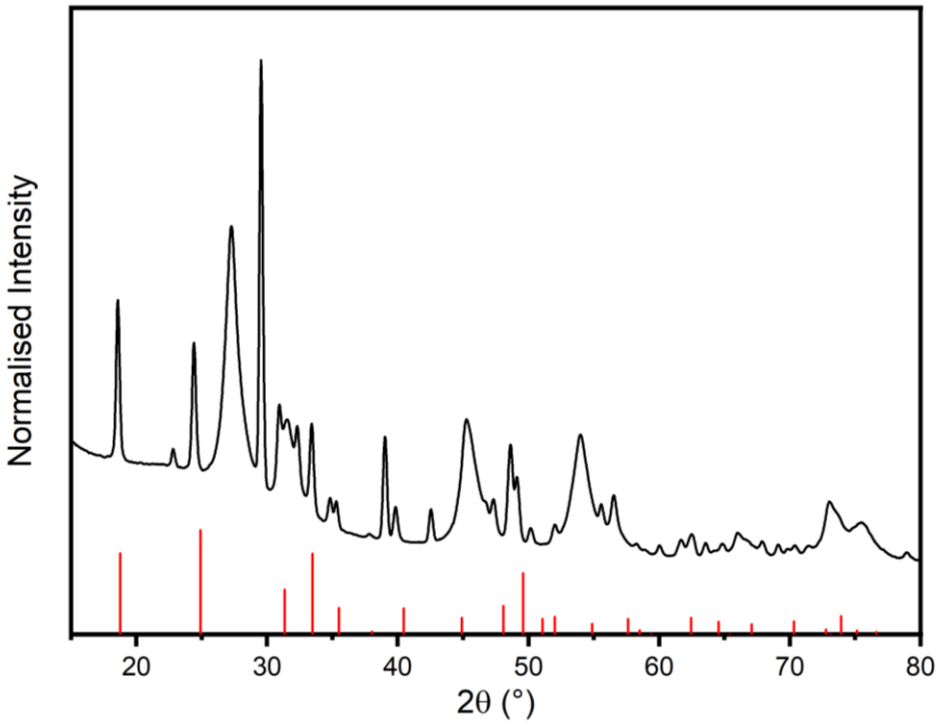

Figure 3.16. XRD pattern for the first attempt at synthesising thorite from thorium nitrate and sodium metasilicate with no control of the pH. The reaction was carried for 24h and 200°C. Red vertical lines correspond to the peak positioning of thorite model pattern.

The XRD pattern for the first samples prepared for thorite shows a mixture of products. Although there are certain peaks that could belong to the desired silicate such as the reflections at around 18° and 24° 2θ corresponding to the (011) and (020) planes respectively of $ThSiO_4$. ThO_2 is also present in the sample at seen at 27°, 45° and 54° 2θ which are related to the (111), (022) and (113) reflections for the oxide. For this reaction no control of the pH was carried out. Nonetheless, it was estimated by litmus paper giving a pH in the range of 5-6. Therefore, the optimum pH range for this reaction seems to be narrower than for the test silicates.

From previous reactions pH seems to be most important variable in this kind of reactions. It will dictate the species we will have in solution and whether secondary products will be yielded after the reaction. For the pH control two solutions of 5 mL were prepared from the same quantity of $Th(NO_3)_4{\cdot}5H_2O$ precursor and adjusted to the corresponding pH by dissolving it in an aqueous solution of nitric acid. For pH 5 and 10 the solutions were buffered with NaOH dissolved in the silicate solution. A slightly higher amount of silicate is targeted, to avoid the formation of the oxide by ensuring complete availability of silicate precursor at every moment. The volume introduced from each solution was 5 mL, having a total volume of 10 mL in the autoclave. The reactions were carried for 24 h at 215°C in a preheated oven. A summary of the reaction conditions is given in Table 3.7.

Table 3.7. Table of condition tested for the pH test reactions for thorite synthesis.

$[Th(NO_3)_4{\cdot}5H_2O]$ (M)	**V (mL)**	**$[Na_2SiO_3]$ (M)**	**V (mL)**	**Si/Th**	**Temperature (°C)**	**Time (h)**	**$pH_{measured}$**
$1.96{\cdot}\times 10^{-2}$	5	$2.10\times{\cdot}10^{-2}$	5	1.07	215	24	1
$1.96{\cdot}\times 10^{-2}$	5	$2.09\times{\cdot}10^{-2}$	5	1.07	215	24	2
$2.44{\cdot}\times 10^{-2}$	5	$2.50\times{\cdot}10^{-2}$	5	1.04	215	24	5
$1.85{\cdot}\times 10^{-2}$	5	$1.97\times{\cdot}10^{-2}$	5	1.06	215	24	10

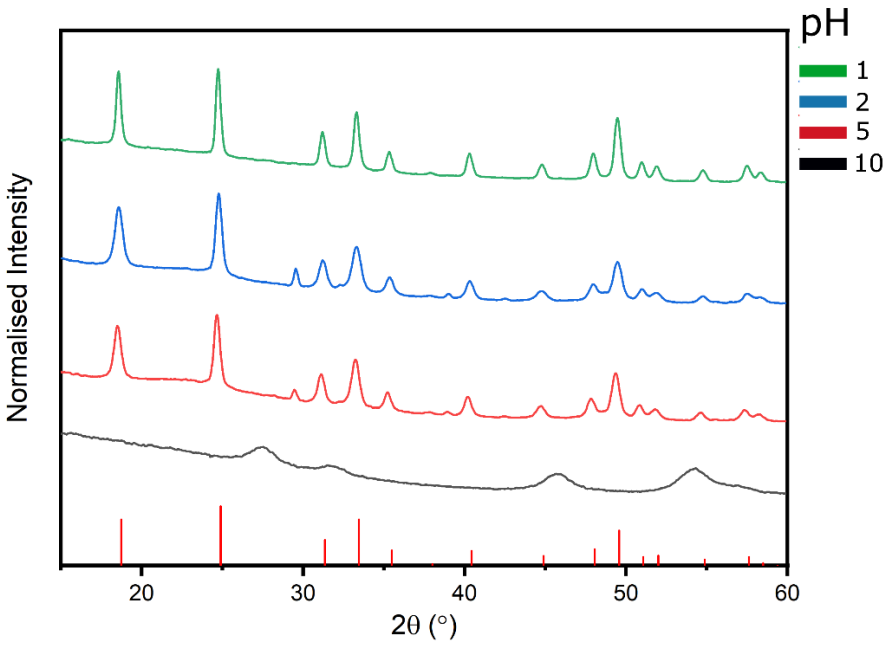

Figure 3.17. XRD patterns of the second attempted reactions. The reactions were carried out for 24h and 215°C changing the pH as shown. Conditions for the reactions are summarised in Table 3.7. Red vertical lines show the peak positioning for thorite model pattern.

From Figure 3.17 it can be seen that thorite is made at acidic conditions (pH 1-5) preferentially over the basic conditions (pH 10), under which ThO_2 is obtained as seen by that low intensity peak at around 27° 2θ, corresponding to the (111) orientation of the oxide. Reactions performed at the two intermediate pHs of 2 and 5 yield products which also exhibit two extra peaks not belonging to the silicate. They are centred at around 29° and 39° 2θ. Both additional features are accompanied by the peaks at 31 and 40° 2θ, corresponding to the (121) and (031) peaks for thorite. These additional peaks with similar shape as the closer ones in position may be the result of a transformation in the unit cell, changing its symmetry. It is often referred as phase transition. Nonetheless, those peaks have not been yet confirmed to be related to a change in the structure or the formation of a secondary phase, further study needs to be carried to justify this effect.

The reaction at pH 1 yielded pure, relatively crystalline thorite. Due to the clarity of the pattern the main characteristics can be calculated and compared to the literature. Le Bail refinement against the diffraction pattern, despite being a structure-less refinement, can be used to efficiently calculate parameters such as the lattice constants. The refinement was performed as shown in Figure 3.18 by using GSAS/EXPGUI software. The calculated results obtained are tabulated in Table 3.8.

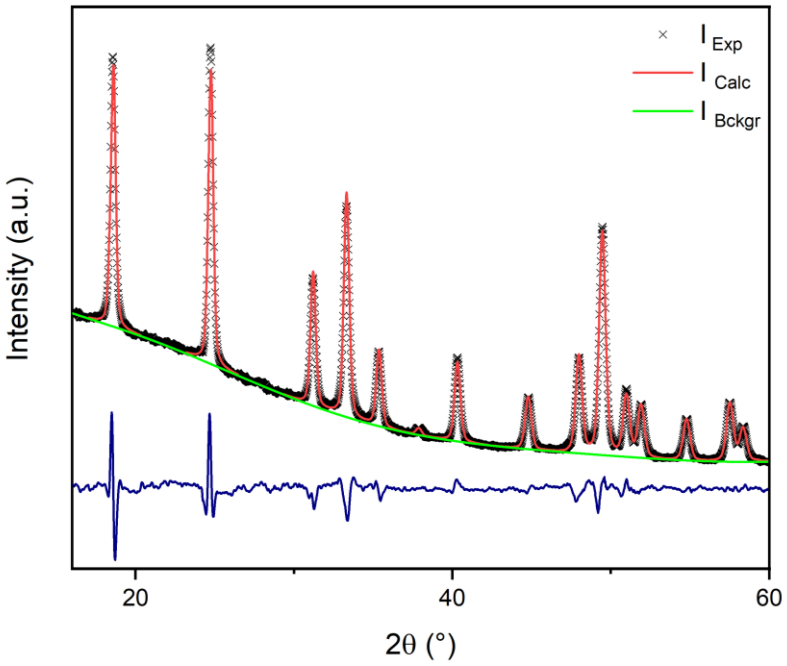

Figure 3.18. LeBail refinement for obtaining thorite cell parameters. The blue line below the graph represents the difference between the data observed and the calculated. wR_p = 0.0355 and R_P = 0.0220.

Table 3.8. Table of cell parameters calculated and reported.[113]

Cell Parameters	**Calculated**	**Reported**
a = b (Å)	7.15	7.1568
c (Å)	6.31	6.3152
Volume ($Å^3$)	323.0	323.46

As shown in Figure 3.18 the calculated pattern matches well the experimental one. As well from Table 3.8 the cell parameters match with the reported ones evidencing the presence of thorite.

3.4.5 Synthesis of Coffinite, $USiO_4$

Finally, the different attempts for the synthesis of coffinite ($USiO_4$) are described in this section. The synthesis of coffinite was performed as the results for the rest of the experiments were obtained.

For the first attempt the simplest reaction possible was carried just by mixing the different precursors at a mild temperature, for 3 days. The process that needs to be followed in order to pursue the most efficient synthesis possible is by going from really simple reactions to more complicated ones as different conditions are required in the

reaction. Therefore, for the first attempts there's not control of the pH or additives, but the temperature as a defining factor is tested as 150 and 200°C. The experimental conditions for the synthesis are given in Table 3.9.

Table 3.9. Table of conditions tested for the synthesis of coffinite at 150 and 200°C with no control of the pH.

[UCl_4] (M)	V (mL)	[Na_2SiO_3] (M)	V (mL)	Si/U	Temperature (°C)	Time (h)
$3.95 \cdot \times 10^{-2}$	5	$4.07 \cdot 10^{-2}$	5	1.03	150	72
$3.95 \cdot \times 10^{-2}$	5	$4.07 \cdot 10^{-2}$	5	1.03	200	72

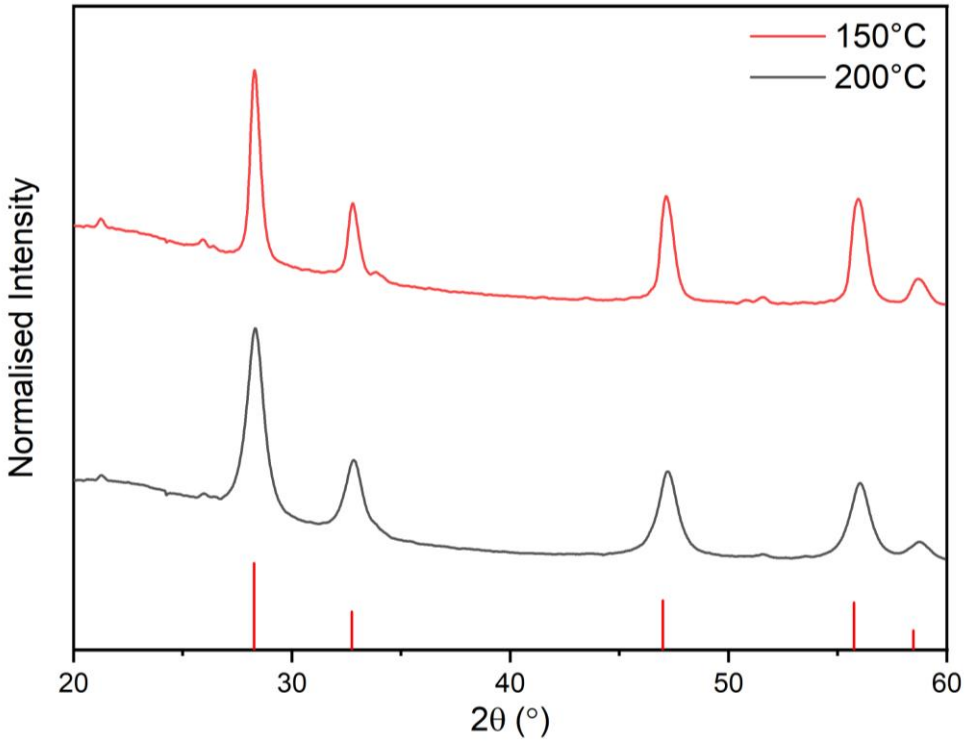

Figure 3.19. XRD patterns for the first attempts of synthesising coffinite. The pattern in red corresponds to the 150°C reaction, while the pattern in black to the higher temperature 200°C. The red vertical lines correspond to the peak positions for UO_2.[114]

In Figure 3.19 the two different patterns for the conditions attempted are shown. The main difference synthetically is that the top pattern (red) corresponds to the reaction performed at milder conditions, 150°C. On the other hand, the pattern in black refers to the reaction at higher temperatures, 200°C. For both samples the peak positions can be assigned to uranium (IV) oxide, UO_2. There are very small differences between both patterns. The main contrast between both patterns is that at lower temperatures uranium oxide shows sharper peaks highlighting a higher crystallinity for the particles obtained.

Nonetheless, no evidence of any other uranium containing species can be acknowledged. This results from the lower thermodynamic stability of coffinite *vs.* the oxides.[87] Therefore, if the reaction is simple enough to yield the thermodynamically preferred compound the oxides will be the predominant component in the sample.

In order to change the stability of the oxides in the reaction, the pH can be varied. It will vary the solubility of the oxides when they are precipitating from solution.

Table 3.10. Reaction conditions for the second attempts of synthetising coffinite. The main factor is the variation of pH.

[UCl_4] (M)	V (mL)	[Na_2SiO_3] (M)	V (mL)	U/Si	Temperature (°C)	Time (h)	pH_{mix}
$3.95 \cdot \times 10^{-2}$	5	$4.07 \cdot \times 10^{-2}$	5	1.03	150	72	9 (NaOH)
$7.90 \cdot \times 10^{-2}$	5	$8.13 \times \cdot 10^{-2}$	5	1.03	150	72	1 (HCl)

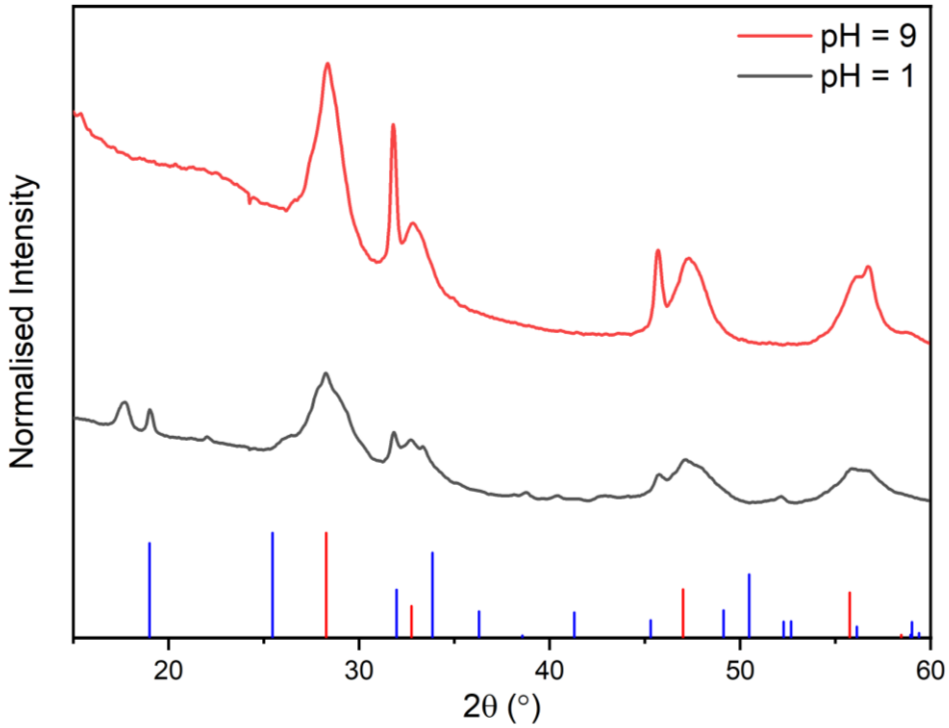

Figure 3.20. Second attempt of coffinite synthesis. The vertical lines at the bottom of the figure corresponds to the peak positions for UO_2[114] (red) and $USiO_4$[84] (blue).

In Figure 3.20 the reactions carried out at different conditions are plotted, showing the reaction at higher pH at the top (pH = 9) and the lower pH reaction at the bottom of the graph (pH = 1). There are some new features compared to the reaction where the pH wasn't controlled. Nonetheless, UO_2 is still the main component for both of the samples

obtained. At higher pH additional crystalline peaks can be seen next to every peak or overlapping with the oxide peak forming a broader feature. These features may be related to the formation of structurally equivalent non-stoichiometric uranium oxide, but to the best of our knowledge these additional peaks do not match to any of the uranium oxide patterns reported, and no other structural matches could be identified. It needs to be reiterated that these diffraction patterns were recorded in a capillary, causing a high intensity background that might overlap silica peaks present in the sample further hindering the analysis of the purity of the material.

When the reaction is carried out at lower pH the intensity of the oxide peaks seems to be lower, probably due to a smaller crystallite size. Additional peaks are observed at the same time, somewhat matching with the positions reported for coffinite. As previously reported the shoulder peak present at around 28° 2θ can be related to the (200) intense peak for coffinite, from reactions of UO_2 and SiO_2.[92] Due to the low crystallinity and the high background it can't be completely concluded that small amounts of coffinite were obtained, although the preferred use of lower pH for obtaining any silicate is a common trend shown for the previous synthesis of silicates surrogates. The smaller crystallinity of the oxides and the potential presence of the silicate can be caused by a higher solubility of these oxides in acidic conditions. It might cause the precipitation and redissolution of UO_2 to yield coffinite. This dependence on the solubility of UO_2 with pH has been extensively studied and reported as shown in Figure 3.22.[115]

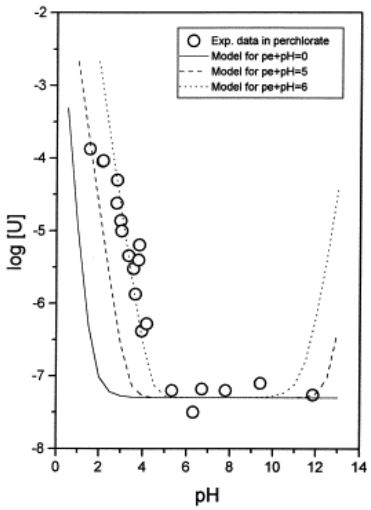

Figure 3.21. Solubility expressed as concentration of uranium present in solution for the dissolution of uranium dioxide in 8 mmol dm^{-3} sodium perchlorate.[115]

Uranium dioxide is a common end-form for uranium as it is very stable, so that the formation of the oxide in large quantities for yielding coffinite must be avoided. Nonetheless, the formation process of coffinite has been periodically discussed in the literature. The argument lies on the small range of optimal conditions for the formation of coffinite *versus* the oxides, although these oxides are the precursors to the formation of the silicates. Therefore, these oxides need to be yielded and destabilised in solution to yield the silicate, being a complicated process. The transition from uranite (UO_2) to the silicate have been suggested to be caused by self-irradiation of the oxide and radiolysis which carries oxidation of the surface at moderate oxygen fugacity. The alteration of uranium dioxide and reaction to the silicate is commonly named as coffinisation, as it is expected to be one of the main processes occurring at the SNF repositories.[116]

Although similar conditions to thorite have been attempted to synthetise coffinite, the reactions carried out didn't succeed to yield this silicate. When looking at the reported synthesis of the ($Th_{1-x}U_xSiO_4$) system, thorite formation energy as the end-member is calculated to be slightly negative ($\Delta H_{f,ox,25°C}$ of $ThSiO_4$ = -6.4 ± 5.7 kJ/mol).[12] Coffinite enthalpy of formation obtained, extrapolating from the previous one, is positive ($\Delta H_{f,ox,25°C}$ of $USiO_4$ = 25.6 ±3.9 kJ/mol).[12] Therefore coffinite is metastable in respect to the oxides and the conditions of synthesis will be narrower than for thorite, which is energetically promoted to crystallise.

3.5 Conclusions and Future Work

Firstly, the optimal synthesis conditions for zircon and stetindite have been shown by mild-hydrothermal conditions. The synthesis of zircon was achieved by the use of 0.25 M zirconyl chloride in 1.0M of HCl at 150°C for 3 days with an equimolar concentration of sodium silicate. It has been shown that there's a broad range of stability of zircon when tuning the pH of the reaction by use of sodium hydroxide solutions for the dissolution of sodium silicate. Pure zircon is evidenced by powder XRD when these reactions are performed at 150 °C at pHs between 0.5 and 4.4.

Secondly, those optimal conditions have been translated to the synthesis of a structurally similar silicate, stetindite, and the intermediate silicates described by the formula $Ce_xZr_{1-x}SiO_4$. The best version of $CeSiO_4$ was encountered when the synthesis was carried at longer times than 1 day and at 150 °C and a pH of 1.9. When looking at zircon and stetindite obtained by XRD, TEM and FTIR there is observed an anisotropic growth in the case of zircon. $ZrSiO_4$ shows preferential growth from both XRD patterns and TEM images. It is justified by the presence of water in the structure disrupting the lattice, promoting a higher crystallinity in the b-axis. The water molecules are shown by a broad water band in FTIR. Although the formation of zircon and stetindite is achieved in similar conditions, the growth process is proved to be different, as the stetindite obtained does not show the same anisotropic behaviour. On the other hand, when looking at the intermediate silicates, the zircon structure is capable to accommodate cerium in the structure up to x = 0.2, while when starting from higher proportions of cerium only pure stetindite is possible to be obtained. It is justified by the thermodynamic difference between zircon and the cerium containing equivalent. While zircon is reported to be more stable than the corresponding oxides, $CeSiO_4$ is metastable to them. Similar behaviour has been shown for $(Zr,Pu)SiO_4$ series. It establishes the preferred use of zircon as a metal containing mineral for SNF repositories, although the process needs to be optimised in order to achieve the higher loading of external metals in the silicate structure.

Thirdly, once the best conditions for the synthesis of both surrogates was achieved a more chemically similar compound to coffinite was targeted. $ThSiO_4$ was synthesised in mild-hydrothermal conditions. The purest version was obtained when pH = 1 for 1 day and 215°C. It shows a high crystallinity and purity. The synthesis is shown to be effective

for acidic pH rather than basic one, as corroborated by the previous surrogate attempts. The synthesis of thorite has been carried again several times to prove the reproducibility and samples have been submitted to the High-Resolution Powder Diffraction Beamline (HRPD) and high-pressure diffractometer (PEARL) in the ISIS Neutron and Muon Source in the UK. High-resolution diffraction data is expected to be obtained. In addition, the measurement in the high-pressure facilities might show the structural transition of thorite to huttonite when high pressure is applied.

Lastly, the synthesis of coffinite was attempted by following similar synthesis conditions, however the respective UO_2 and SiO_2 were obtained. Nonetheless, the synthesis carried out at the most acidic conditions (pH = 1) shows a low intensity feature that may be attributed to the formation of the silicate. Higher-resolution patterns and extra experiments are required. Due to the multiple oxidation states of uranium, the optimum oxidation state needs to be stabilised, so a potential reducing agent such as hydrazine might be attempted in the future. As well, it is suggested in the literature that the formation of this silicate is driven by the dissolution of the oxides, so the optimal conditions that enhance the solubility of these oxides will be required.

The optimum synthesis and intake of cerium in the zircon structure might suggest its use as a possible container of rare earth-metals and SNF derivates in its structure. So that, the doping of zircon with elements like Eu, Tb or Yb can be attempted for this mineral, reproducing the already known optimal conditions and modifying the synthesis in order to explore the conditions for zircon to host those metals in the greatest way possible. Cerium has been proven to be a great candidate for optoelectronic applications, so that the doping of the structure with rare earth metal would enhance its applicability and allow these minerals to be applied in new fields barely previously explored.

Due to the reproducibility of the synthetic conditions obtained they could be translated other similar silicates such as cuprosklodowskite, $Cu[(UO_2)_2(SiO_3OH)_2]\cdot 6H_2O$. This silicate named after Marie Sklodowska-Curie, have been never synthetically obtained pure although it has been observed in uranium ores around the world.[117,118] In addition, the formation of lead orthosilicate, $PbSiO_4$, has been suggested to be possible although it has never been observed or synthesised.[119] Therefore, if the optimum conditions are applied to the formation of this silicate it could lead to the formation of a new mineral never acknowledged.

In addition, if coffinite is successfully synthesised pure, precise thermodynamic data can be measured in order to generate a broader idea of the properties of this material. It is critical for the understanding of the evolution of uranium in the storing conditions in case of accidental release. For example, testing the range of stability at different pH and redox environments. Or exposing the silicate at high temperatures and pressure to unveil a possible degradation into the oxides. That will support the idea of the silicate being an end mineral for uranium.

Finally, finding the optimal conditions for the synthesis of the silicates required many reactions in different conditions. Despite the positive results acquired from the experiments carried out, coffinite synthesis was not achieved absent of secondary phases. The continuous mapping of different parameters and the subsequent analysis to grasp the effect of those in the mineralisation of the materials, is time consuming and requires a great deal effort from the researcher. A systematisation of the mapping of variables and the gaining of knowledge about the trends observed when they are changed will be discussed further in the thesis, showing that an statistical analysis of the empirical data (such as Principal Component Analysis) is a great candidate to lower the time of analysis and makes easier to gain an idea of the optimum conditions for the synthesis of several materials (calcium orthophosphates and calcium carbonate) and potentially for narrowing the synthetic conditions to obtain coffinite.

3.6 References

1 F. Liebau, Structural Chemistry of Silicates, 1985.
2 F. Kemper, W. J. Vriend and A. G. G. M. Tielens, *Astrophys. J.*, 2004, **609**, 826–837.
3 C. Jäger, J. Dorschner, H. Mutschke, T. Posch and T. Henning, *Astron. Astrophys.*, 2003, **408**, 193–204.
4 M. Sumper and E. Brunner, *Adv. Funct. Mater.*, 2006, **16**, 17–26.
5 H. Ehrlich, E. Brunner, P. Simon, V. V. Bazhenov, J. P. Botting, K. R. Tabachnick, A. Springer, K. Kummer, D. V. Vyalikh, S. L. Molodtsov, D. Kurek, M. Kammer, R. Born, A. Kovalev, S. N. Gorb, P. G. Koutsoukos and A. Summers, *Adv. Funct. Mater.*, 2011, **21**, 3473–3481.
6 J. W. Hunt, A. P. Dean, R. E. Webster, G. N. Johnson and A. R. Ennos, *Ann. Bot.*, 2008, **102**, 653–656.
7 S. V. Patwardhan, N. Mukherjee, M. Steinitz-Kannan and S. J. Clarson, *Chem. Commun.*, 2003, **3**, 1122–1123.
8 M. Zhao, Q. Zhang and Z. Xia, *Accounts Mater. Res.*, 2020, **1**, 137–145.
9 D. Y. Pushcharovsky, N. V. Zubkova and I. V. Pekov, *Struct. Chem.*, 2016, **27**, 1593–1603.
10 R. J. Finch and J. M. Hanchar, Zircon, 2018, 1–26.
11 J. A. Speer, in Orthosilicates, ed. R. G. Burns, De Gruyter, Berlin, Boston, 2018, pp. 113–136.
12 X. Guo, S. Szenknect, A. Mesbah, N. Clavier, C. Poinssot, D. Wu, H. Xu, N. Dacheux, R. C. Ewing and A. Navrotsky, Chem. Mater., 2016, **28**, 7117–7124.
13 T. Beirau, W. D. Nix, U. Bismayer, L. A. Boatner, S. G. Isaacson and R. C. Ewing, *Phys. Chem. Miner.*, 2016, **43**, 627–638.
14 A. J. Anderson, M. C. van Soest, K. V. Hodges and J. M. Hanchar, *Geochim. Cosmochim. Acta*, 2020, **274**, 45–62.
15 M. Reich, R. C. Ewing, T. A. Ehlers and U. Becker, *Geochim. Cosmochim. Acta*, 2007, **71**, 3119–3130.
16 S. Bowring and T. Housh, *Science.*, 1995, **269**, 1535–1540.
17 R. Buick, J. R. Thornett, N. J. McNaughton, J. B. Smith, M. E. Barley and M. Savage, *Nature*, 1995, **375**, 574–577.
18 N. M. Rendtorff, S. Grasso, C. Hu, G. Suarez, E. F. Aglietti and Y. Sakka, *J. Eur. Ceram. Soc.*, 2012, **32**, 787–793.
19 T. Mori, H. Yamamura, H. Kobayashi and T. Mitamura, *J. Am. Ceram. Soc.*, 1992, **75**, 2420–2426.
20 R. C. Ewing, W. Lutze and W. J. Weber, *J. Mater. Res.*, 1995, **10**, 243–246.
21 Y. Ding, X. Lu, H. Dan, X. Shu, S. Zhang and T. Duan, *Ceram. Int.*, 2015, **41**, 10044–10050.
22 Y. Ding, X. Lu, H. Tu, X. Shu, H. Dan, S. Zhang and T. Duan, *J. Eur. Ceram. Soc.*, 2015, **35**, 2153–2161.
23 J. Gediga, A. Morfino, M. Finkbeiner, M. Schulz and K. Harlow, *Int. J. Life Cycle Assess.*, 2019, **24**, 1976–1984.
24 R. Udaykiran, S. Vasanthavel and S. Kannan, *Cryst. Growth Des.*, 2015, **15**, 4075–4086.
25 C. E. Curtis and H. G. Sowman, *J. Am. Ceram. Soc.*, 1953, **36**, 190–198.
26 S. V. Ramani, E. C. Subbarao and K. V. G. M. Gowhale, *J. Am. Ceram. Soc.*, 1969, **52**, 619–623.
27 T. Itoh, *J. Cryst. Growth*, 1992, **125**, 223–228.
28 N. Guo, P. Huang, N. Yan, P. L. Wang and W. F. Li, G.H. Jish, *Journal Solid Rocket Technol.*, 2010, **33**, 519–523.
29 D. R. Spearing and J. Y. Huang, *J. Am. Ceram. Soc.*, 2005, **81**, 1964–1966.
30 X. Wang, J. Chen and M. Ren, *Ore Geol. Rev.*, 2016, **74**, 63–75.
31 J. C. Claoué-Long, R. W. King and R. Kerrich, Earth Planet. *Sci. Lett.*, 1990, **98**, 109–128.
32 E. Dubińska, P. Bylina, A. Kozłowski, W. Dörr, K. Nejbert, J. Schastok and C. Kulicki, *Chem. Geol.*, 2004, **203**, 183–203.
33 P. W. O. Hoskin, G*eochim. Cosmochim. Acta*, 2005, **69**, 637–648.
34 J. K. W. Lee, I. S. Williams and D. J. Ellis, *Nature*, 1997, **390**, 159–162.
35 P. W. O. Hoskin and L. P. Black, J. Metamorph. *Geol.*, 2002, **18**, 423–439.
36 R. Valéro, B. Durand, J. L. Guth and T. Chopin, *Microporous Mesoporous Mater.*, 1999, **29**, 311–318.
37 Y. Ding, Z. Jiang, Y. Li, Y. Tang, J. Li and X. Dong, *J. Alloys Compd.*, 2018, **735**, 2190–2196.

38 R. Uhrin, R. F. Belt and R. C. Puttbach, *J. Cryst. Growth*, 1974, **21**, 65–68.
39 F. Tomaschek, J. Petrol., 2003, **44**, 1977–2002.

40 V. K. Kim, V. A. Rassulov, N. A. Popova, A. I. Zakharov and V. A. Chashchin, *Glas. Ceram. (English Transl. Steklo i Keramika)*, 2016, **73**, 128–131.
41 M. Wu, S. Liu, Y. Sun, W. Chen, L. Huang, G. Chen and Z. Zheng, *Mater. Chem. Phys.*, 2020, **251**, 123086.
42 W. E. Falck and K. Nilsson, Geological Disposal of Radioactive Waste : Moving Towards Implementation, 2009.
43 H. Feiveson, Z. Mian, M. Ramana and F. Von Hippel, Managing spent fuel from nuclear power reactors: Experience and lessons from around the world, 2011.
44 R. C. Ewing, *Nat. Mater.*, 2015, **14**, 252–257.
45 D. J. Wronkiewicz, J. K. Bates, S. F. Wolf and E. C. Buck, *J. Nucl. Mater.*, 1996, **238**, 78–95.
46 M. Amme, T. Wiss, H. Thiele, P. Boulet and H. Lang, *J. Nucl. Mater.*, 2005, **341**, 209–223.
47 C. Walther and M. A. Denecke, *Chem. Rev.*, 2013, 113, 995–1015.
48 B. Ritherdon, C. Phelps, H. Neff, A. G. Sowder and S. B. Clark, *Radiochim. Acta*, 2003, **91**, 93–96.
49 L. R. STieff, T. W. Stern and A. M. Sherwood, *Science*, 1955, **121**, 608–609.
50 V. M. Goldschmidt and A. I. Muir, Geochemistry, Gloucestershire (U.K.), 1954.
51 A. P. Deditius, S. Utsunomiya and R. C. Ewing, *Chem. Geol.*, 2008, **251**, 33–49.
52 A. P. Deditius, S. Utsunomiya, V. Pointeau and R. C. Ewing, *Eur. J. Mineral.*, 2010, **22**, 75–88.
53 A. P. Deditius, V. Pointeau, J. M. Zhang and R. C. Ewing, *Am. Mineral.*, 2012, **97**, 681–693.
54 M. Fayek, J. Janeczek and R. C. Ewing, *Appl. Geochemistry*, 1997, **12**, 549–565.
55 R. Finch and T. Murakami, *Uranium Mineral. Geochemistry, Environ.*, 2019, 91–179.
56 J. Janeczek and R. C. Ewing, *J. Nucl. Mater.*, 1992, **190**, 157–173.
57 D. T. Costin, A. Mesbah, N. Clavier, N. Dacheux, C. Poinssot, S. Szenknect and J. Ravaux, *Inorg. Chem.*, 2011, **50**, 11117–11126.
58 X. Guo, S. Szenknect, A. Mesbah, S. Labs, N. Clavier, C. Poinssot, S. V. Ushakov, H. Curtius, D. Bosbach, R. C. Ewing, P. C. Burns, N. Dacheux and A. Navrotsky, *Proc. Natl. Acad. Sci.*, 2015, **112**, 6551–6555.
59 S. Szenknect, D. T. Costin, N. Clavier, A. Mesbah, C. Poinssot, P. Vitorge and N. Dacheux, *Inorg. Chem.*, 2013, **52**, 6957–6968.
60 J. Mulak, *J. Solid State Chem.*, 1977, **21**, 117–126.
61 L. H. Fuchs and H. R. Hoekstra, *Am. Mineral.*, 1959, **44**, 1057–1063.
62 V. Pointeau, A. P. Deditius, F. Miserque, D. Renock, U. Becker, J. Zhang, N. Clavier, N. Dacheux, C. Poinssot and R. C. Ewing, *J. Nucl. Mater.*, 2009, **393**, 449–458.
63 S. Labs, C. Hennig, S. Weiss, H. Curtius, H. Zänker and D. Bosbach, *Environ. Sci. Technol.*, 2014, **48**, 854–860.
64 A. Mesbah, S. Szenknect, N. Clavier, J. Lozano-Rodriguez, C. Poinssot, C. Den Auwer, R. C. Ewing and N. Dacheux, *Inorg. Chem.*, 2015, **54**, 6687–6696.
65 R. M. Hazen, R. C. Ewing and D. A. Sverjensky, *Am. Mineral.*, 2009, **94**, 1293–1311.
66 J. J. Berzelius, Ann. der Phys. und Chemie, 1829, **92**, 385–415.
67 D. E. Harlov, R. Wirth and C. J. Hetherington, *Am. Mineral.*, 2007, **92**, 1652–1664.
68 A. Pabst, *Nature*, 1950, **166**, 157–157.
69 F. A. Mumpton and R. Roy, *Geochim. Cosmochim. Acta*, 1961, **21**, 217–238.
70 D. Prasad Sinha and R. Prasad, *J. Inorg. Nucl. Chem.*, 1973, **35**, 2612–2614.
71 P. Estevenon, E. Welcomme, S. Szenknect, A. Mesbah, P. Moisy, C. Poinssot and N. Dacheux, *Inorg. Chem.*, 2018, **57**, 9393–9402.
72 P. Estevenon, E. Welcomme, S. Szenknect, A. Mesbah, P. Moisy, C. Poinssot and N. Dacheux, *Inorg. Chem.*, 2018, **57**, 12398–12408.
73 J. Schlüter, T. Malcherek and T. A. Husdal, *Neues Jahrb. für Mineral. - Abhandlungen*, 2009, **186**, 195–200.
74 J. M. S. Skakle, C. L. Dickson and F. P. Glasser, *Powder Diffr.*, 2000, **15**, 234–238.
75 C. L. Dickson and F. P. Glasser, *Cem. Concr. Res.*, 2000, **30**, 1619–1623.
76 X. Zhang, S. Liu, H. Tong and G. Yong, *Appl. Catal. B Environ.*, 2012, **127**, 105–111.
77 C. . Dickson and F. . Glasser, *Cem. Concr. Res.*, 2000, **30**, 1619–1623.

78 J. M. S. Skakle, C. L. Dickson and F. P. Glasser, *Powder Diffr.*, 2000, **15**, 234–238.
79 P. Estevenon, E. Welcomme, S. Szenknect, A. Mesbah, P. Moisy, C. Poinssot and N. Dacheux, *Dalt. Trans.*, 2019, **48**, 7551–7559.
80 P. Estevenon, T. Kaczmarek, F. Vadot, T. Dumas, P. L. Solari, E. Welcomme, S. Szenknect, A. Mesbah, P. Moisy, C. Poinssot and N. Dacheux, *Dalt. Trans.*, 2019, **48**, 10455–10463.
81 P. Estevenon, E. Welcomme, C. Tamain, G. Jouan, S. Szenknect, A. Mesbah, C. Poinssot, P. Moisy and N. Dacheux, *Dalt. Trans.*, 2020, **49**, 6434–6445.
82 P. Estevenon, T. Kaczmarek, M. R. Rafiuddin, E. Welcomme, S. Szenknect, A. Mesbah, P. Moisy, C. Poinssot and N. Dacheux, *Cryst. Growth Des.*, 2020, **20**, 1820–1828.
83 O. Hassel, *Zeitschrift fur Krist.*, 1926, **63**, 247–254.
84 L. H. Fuchs and G. Elizabeth, *Am. Mineral.*, 1958, **43**, 243–248.
85 G. Ma and X. Y. Liu, *Cryst. Growth Des.*, 2009, **9**, 2991–2994.
86 R. J. M. Konings and A. Plyasunov, *Geochim. Cosmochim. Acta*, 2017, **212**, 372–373.
87 X. Guo, S. Szenknect, A. Mesbah, N. Clavier, C. Poinssot, D. Wu, H. Xu, N. Dacheux, R. C. Ewing and A. Navrotsky, *Chem. Mater.*, 2016, **28**, 7117–7124.
88 D. T. Costin, A. Mesbah, N. Clavier, N. Dacheux, C. Poinssot, S. Szenknect and J. Ravaux, *Inorg. Chem.*, 2011, **50**, 11117–11126.
89 A. C. Larson and R. B. Von Dreele, Los Alamos Natl. Lab. Report, 2000.
90 B. H. Toby, *J. Appl. Crystallogr.*, 2001, **34**, 210–213.
91 O. Hassel, *Zeitschrift für Krist. - Cryst. Mater.*, 1926, **63**, 247–254.
92 S. Szenknect, D. Alby, M. López García, C. Wang, R. Podor, F. Miserque, A. Mesbah, L. Duro, L. Zetterström Evins, N. Dacheux, J. Bruno and R. C. Ewing, *Sci. Rep.*, 2020, **10**, 1–10.
93 R. Caruba, A. Baumer, M. Ganteaume and P. Iacconi, Am. Mineral., 1985, **70**, 1224–1231.
94 B. Lei, C. Peng and J. Wu, J. Am. Ceram. Soc., 2012, **95**, 2791–2794.
95 H. Kido and S. Komarneni, in Transactions of the Materials Research Society of Japan, eds. S. Sōmiya, M. Doyama, M. Hasegawa and Y. Agata, Springer Netherlands, Dordrecht, 1990, pp. 358–369.
96 G. Calas, L. Galoisy, N. Menguy, P. Jollivet and S. Gin, *J. Am. Ceram. Soc.*, 2019, **102**, 3123–3128.
97 A. C. Strzelecki, C. Bourgeois, K. W. Kriegsman, P. Estevenon, N. Wei, S. Szenknect, A. Mesbah, D. Wu, R. C. Ewing, N. Dacheux and X. Guo, *Inorg. Chem.*, 2020, **59**, 13174–13183.
98 M. V. Zamoryanskaya and B. E. Burakov, *Mater. Res. Soc. Symp. - Proc.*, 2001, **663**, 301–306.
99 R. L. Putnam, A. Navrotsky, E. H. P. Cordfunke and M. E. Huntelaar, *J. Chem. Thermodyn.*, 2000, **32**, 911–921.
100 R. D. Shannon, *Acta Crystallogr. Sect. A*, 1976, **32**, 751–767.
101 E. D. A. Ferriss, R. C. Ewing and U. Becker, *Am. Mineral.*, 2010, **95**, 229–241.
102 A. Navrotsky and S. V. Ushakov, in Materials Fundamentals of Gate Dielectrics, Springer-Verlag, Berlin/Heidelberg, 1989, vol. 53, pp. 57–108.
103 N. Clavier, S. Szenknect, D. T. Costin, A. Mesbah, C. Poinssot and N. Dacheux, *Spectrochim. Acta - Part A Mol. Biomol. Spectrosc.*, 2014, **118**, 302–307.
104 P. Dawson, M. M. Hargreave and G. R. Wilkinson, J. Phys. C Solid State Phys., 1971, **4**, 240–256.
105 A. C. Strzelecki, T. Barral, P. Estevenon, A. Mesbah, V. Goncharov, J. Baker, J. Bai, N. Clavier, S. Szenknect, A. Migdisov, H. Xu, R. C. Ewing, N. Dacheux and X. Guo, Inorg. Chem., 2021, **60**, 718–735.
106 X. Guo, S. Szenknect, A. Mesbah, S. Labs, N. Clavier, C. Poinssot, S. V. Ushakov, H. Curtius, D. Bosbach, R. C. Ewing, P. C. Burns, N. Dacheux and A. Navrotsky, Proc. Natl. Acad. Sci. U. S. A., 2015, **112**, 6551–6555.
107 F. X. Zhang, V. Pointeau, L. C. Shuller, D. M. Reaman, M. Lang, Z. Liu, J. Hu, W. R. Panero, U. Becker, C. Poinssot and R. C. Ewing, *Am. Mineral.*, 2009, **94**, 916–920.
108 J. D. Bauer, S. Labs, S. Weiss, L. Bayarjargal, W. Morgenroth, V. Milman, A. Perlov, H. Curtius, D. Bosbach, H. Zänker and B. Winkler, *J. Phys. Chem. C*, 2014, **118**, 25141–25149.
109 E. Knittle and Q. Williams, *Am. Mineral.*, 1993, **78**, 245–252.
110 J. J. Katz and G. T. Seaborg, The Chemistry of the Actinide and Transactinide Elements, Springer Netherlands, Dordrecht, 2006.
111 I. Dreissig, S. Weiss, C. Hennig, G. Bernhard and H. Zänker, *Geochim. Cosmochim. Acta*, 2011, **75**, 352–367.

112 S. Labs, C. Hennig, S. Weiss, H. Curtius, H. Zänker and D. Bosbach, *Environ. Sci. Technol.*, 2014, **48**, 854–860.
113 M. Taylor and R. C. Ewing, *Acta Crystallogr. Sect. B Struct. Crystallogr. Cryst. Chem.*, 1978, **34**, 1074–1079.
114 J. Thewlis, *Acta Crystallogr.*, 1952, **5**, 790–794.
115 I. Casas, J. de Pablo, J. Giménez, M. E. Torrero, J. Bruno, E. Cera, R. J. Finch and R. C. Ewing, *Geochim. Cosmochim. Acta*, 1998, **62**, 2223–2231.
116 J. Janeczek and R. C. Ewing, MRS Proc., 1991, **257**, 497.
117 H. Li, P. Kegler, D. Bosbach and E. V. Alekseev, *Inorg. Chem.*, 2018, **57**, 4745–4756.
118 A. Rosenzweig and R. R. Ryan, *Am. Mineral.*, 1975, **60**, 448–453.
119 R. A. Jackson and M. Montenari, in Case Studies in Isotope Stratigraphy, Elsevier Inc., 1st edn., 2019, vol. 4, pp. 217–227.

Chapter 4. Hydrothermal Injection Synthesis of Calcium Orthophosphates

4.1 Introduction

Calcium phosphates constitute a family of materials that take place in biological systems.[1–3] For example, hydroxyapatite (HAP, $Ca_{10}(PO_4)_6(OH)_2$) as a member of this group is remarkable for being the constituent of bone and teeth.[4] Nonetheless, the scope of these materials is broader than just medicine[5] or dental science.[6] Calcium phosphates are defined by the presence of its three major components: Ca^{2+}, P^{5+} and O^{2-}. Calcium orthophosphate (PO_4^{3-}) is structurally different to meta- (PO_3^-), pyro- ($P_2O_7^{4-}$) and poly- $(PO_3)_n^{n-}$ phosphate. Although, phosphoric acid has 3 acidic protons in its structure (H_3PO_4), orthophosphates may be encountered in the $H_2PO_4^-$ or HPO_4^{2-} form. Additionally, water molecules can be part of the structure as in the case of dicalcium phosphate dihydrate or brushite (DCPD, $CaHPO_4{\cdot}2H_2O$). One of the main factors to define the different orthophosphates is the Ca/P ratio as shown in Table 4.1**.** Three different crystal structures for three different calcium orthophosphates are shown in Figure 4.1.

Table 4.1. Selected crystallographic data for the three calcium orthophosphates.[7]

Name	Ca/P ratio	Formula	Space group	Unit cell parameters (Å)
Brushite (DCPD)	1.00	$CaHPO_4{\cdot}2H_2O$	Monoclinic, *Ia*	a = 5.812(2), b = 15.180 (3), c = 6.239(2)
Monetite (DCPA)	1.00	$CaHPO_4$	Triclinic, *P*-1	a = 6.910(1), b = 6.627(2), c = 6.998(2)
Hydroxyapatite (HAP)	1.67	$Ca_{10}(PO_4)_6(OH)_2$	Monoclinic, *P*21/*b* or Hexagonal *P*63/*m*	a = 9.84214(8), b = 2a, c = 6.8814(7) or a = b = 9.4302(5), c = 6.8911(2)

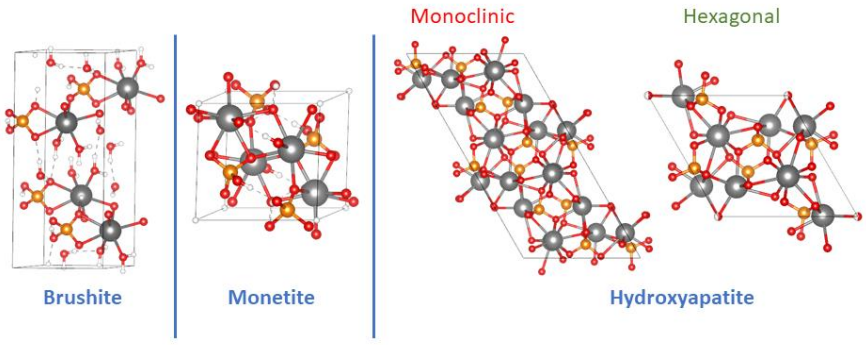

Figure 4.1. Crystallographic structures of three selected calcium orthophosphates. The different atoms that compose the structure are differentiated by their colour: grey (calcium), yellow (phosphorus) and red (oxygen). Water molecules are not shown for clarity.

The selective formation of this family of phosphates has been reported to be driven by intermediate phases that are metastable to hydroxyapatite and more crystalline phases, like octacalcium phosphate ($Ca_8H_2(PO_4)_6 \cdot 5H_2O$, OCP) .[8,9] A common feature in biomaterials is the appearance of amorphous precursors that lower the activation energy for the latter crystallisation. This process is commonly known as two-step process (reviewed in Chapter 1). Therefore, the conditions of formation of each phosphate will be highly dependent on the external parameters (T, P, calcium and phosphate saturation, …) that will stabilise one or another precursor *via* a multistep path.

4.1.1 Multistep Nucleation of Calcium Phosphates

The study of biomimetic nucleation serves to understand the formation of biologically important materials in relevant environments. Due to the variety of the different related compounds or the polymorphic nature of the components in biosystems, their nucleation and growth tend to not be trivial. CNT and heterogeneous nucleation have been used over the years to understand the crystallisation process of this family of materials.[10] Although it is an easier explanation, CNT has more recently failed to explain the overall process.[11,12]

There are several models that have replaced more simplistic ways to unveil of the transition from solution to crystal. Among others, there have been reported aggregation-based crystallisation processes,[13,14] the formation of structurally related prenucleation clusters (PNCs)[15–18] and the appearance of structurally related amorphous phases prior crystallisation (Amorphous Phase Mediated Crystallisation, APMC).[18–21] Calcium carbonate and calcium phosphates are the most studied examples of non-classic nucleation grown materials.

Calcium phosphates are known to yield prenucleation clusters that will determine the crystallisation of the material. The first observation of the formation of these clusters was by Posner and Betts, proposing the formation of the so-called “Posner’s clusters” with a chemical composition of $Ca_9(PO_4)_6$ with a size around 1 nm.[22,23] They are reported to be energetically preferred compared to possible alternatives like $Ca_3(PO_4)_2$ or $Ca_6(PO_4)_4$.[24] The relationship between the formation of this prime compound and the formation of the calcium phosphate crystal has been a topic of discussion recently. These

prenucleation clusters have been suggested to act as the building block of the amorphous intermediate phase (amorphous calcium phosphate, ACP) later in the reaction. [25]

Years later, Habraken *et al.*[9] combined microscopic evidences with *ab initio* calculations to report the transformation of the prenucleation clusters based on ion-association complexes $[Ca(HPO_4)_3]^{4-}$ to generate several 3D structures. When the solubility limit of the amorphous phase is surpassed, the complexes collect Ca^{2+} ions from solution to form an insoluble cluster with the form of $[Ca_2(HPO_4)_3]^{2-}$, that will later yield the insoluble ACP.

Amorphous defines a material with no long-range order, but that can present regular arrangements in the short-range surroundings of the atoms or molecules. The first observation of ACP dates from the 1950s (as mentioned by Eanes[23]) when Watson and Robinson found a "finely granular" solid precipitated from mixing Na_2HPO_4 and $CaCl_2$ in saturation conditions. This material was not crystalline as no regular pattern was obtained from diffraction.[26] In current times, it is known that this amorphous phase is formed from the mixing of two saturated solutions of phosphate and calcium giving a Ca/P ratio between 1.18 and 2.50. Its formation is defined as a kinetic phenomenon. When the saturation of calcium and phosphate in the media reaches a sufficiently high concentration, a sudden interaction between the calcium and the phosphates is generated. Therefore, there is a transitory separation of the bulk solution to a gel-like state.[27]

The crystallisation of this ACP involves various stages (Ostwald rule of stages, Chapter 1) prior to the formation of the crystal. It is not a classic single step transformation. There are two types of amorphous calcium phosphates, ACPs. They can only be differentiated by their morphology and solubility, also known as ACP1 and ACP2.[24] More recent studies have shown that although amorphous phases are usually taken as equal with no discrimination there is a variation in the bonding of the amorphous phases when synthesis conditions are changed.[28]

To investigate the characteristics of ACP and the transformation to more crystalline phases, the stabilisation of the transitory amorphous phase is required. Classically it can be accomplished by adding big ions to disrupt the lattice and avoid further growth, as well as proteins and organic ligands to stabilise ACP.[29–31] Additionally, The pH can be increased by strong bases like hydroxides or buffers.[31,32] Thirdly, the

incorporation of Mg^{2+} has also been attempted. This cation is found in hard tissues where it interacts with HAP.[33] It is also suggested that magnesium ions slow down the transition from ACP1 to ACP2, ACP1 being fast appearing and more soluble amorphous phase that changes in time to the second state.[30,34] It is also suggested that Mg^{2+} substitutes Ca^{2+} in Posner's clusters creating strains hindering the formation of HAP. This transitory state will evolve to hydroxyapatite at basic to neutral conditions and to brushite at acidic pH.[35] The whole transition from solution to crystalline phase is described in Figure **4.2**.

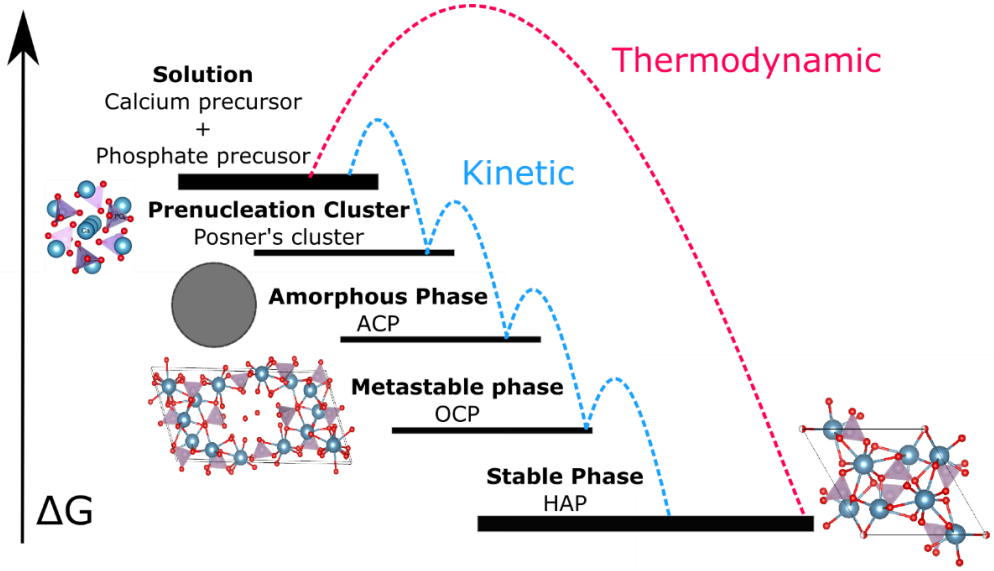

Figure 4.2. **Schematic of the proposed kinetic vs. thermodynamic pathway for hydroxyapatite formation.**

4.1.2 Crystalline Calcium Phosphates

4.1.2.1 Hydroxyapatite (HAP)

Hydroxyapatite belongs to the calcium orthophosphate family due to the nature of the phosphate molecules present in the structure. Its chemical formula is $Ca_{10}(PO_4)_6(OH)_2$ with a characteristic Ca/P ratio of 1.67. This compound can be found in two different crystal structures, monoclinic and hexagonal. The monoclinic structure is the most thermodynamically stable.[36] It is described as rows of phosphate ions placed along the *a* axis. The calcium and hydroxide ions are placed in between these anions. It can also be visualised as hexagons surrounding the calcium atoms. The hydroxides can be seen as above or below the calcium planes.

The hexagonal polymorph is structurally similar but with columns of parallel calcium and hydroxides. It is the most frequent in nature.[36] The steric interaction of the hydroxides implies an easy ionic substitution in the structure by other ions like F^-, Cl^-, *etc*.[37] Hydroxyapatite is well-known to be one of the main components in biological systems, especially being the main component of human bones.[16] An example of the process followed for bone mineralisation is given in Figure 4.3.

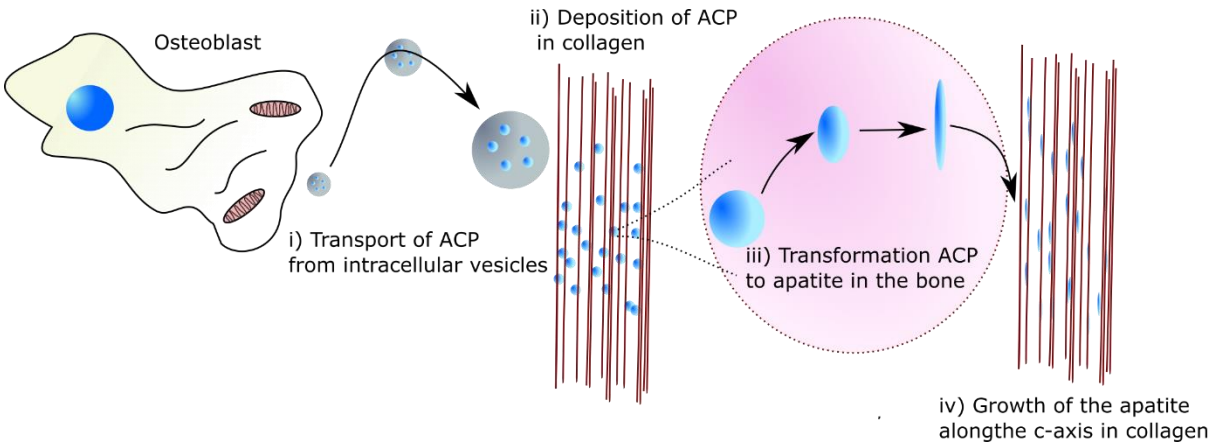

Figure 4.3. Proposed mechanism for bone mineralisation. i) Vesicles transport ACP precursors from the osteoblast to the empty zones of the collagen matrix. ii) Deposition of ACP on the collagen. iii) Crystallisation of ACP into bone apatite with a morphology influenced by the shape of the collagen along the vertical axis. iv) Fully developed collagen matrix.[15]

The synthesis techniques for hydroxyapatite can be divided into two main groups: solid-state and wet techniques.[38] In both cases the ratio of precursors, defined as Ca/P ratio, needs to be equal to 1.67. Nonetheless, the existence of non-stoichiometric HAP is reported to exist, *e.g.* calcium deficient apatites.[39]

Well-defined HAP has been obtained from aqueous solutions at pH 10 – 11 and relatively high temperatures, higher than 90°C.[40] Although there exist some common features between the particles yielded by each synthetic technique, they have been shown to have their own advantages and disadvantages.

By sol-gel pure HAP can be obtained with a high homogeneity at relatively low temperatures. The main inconveniences are the vigorous stirring, the extended time required for the gel formation and the mandatory control of the pH for the synthesis.[41] Co-precipitation is known to be another cheap technique suitable for morphological selective synthesis (needle-like or spherical HAP). That control relies on the addition of

surfactants to avoid the aggregation and imparts low crystallinity to the materials yielded.[42] Emulsion techniques yield a large variety of shapes for HAP (rods, spheres, plates, *etc*.) but it relies on a complex process and longer reaction times.[43] An additional technique for the synthesis of HAP is the mechanochemical technique. It yields fibrous aggregations and spherical particles. The main drawbacks are the use of specialised equipment and the spontaneous aggregation of the crystals formed.[44] Ultrasonic technique has been used for the synthesis of HAP promoting a fast crystallisation and the formation of needle and spherical apatites. Nonetheless, the reaction yields tend to be low and requires the use of specialised devices.[45]

Among these various techniques hydrothermal synthesis has been shown to be a highly advantageous technique for HAP fabrication. It is a cheap technique that uses water as the solvent avoiding surfactants to control the formation of the crystals. The materials obtained show a high crystallinity with little or no post-processing of the sample. These are some of the multiple advantages of this technique.[46] The simplicity of this approach doesn't affect the multitude of shapes that can be obtained. Spheres, needles and plate-like particles have been hydrothermally synthesised.[47–50] Hydrothermal synthesis is not fully exempt of limitations as, due to the nature of the heat-up step of this synthesis, it exhibits a poor control of the morphology and size of the particles.

The different external conditions for the synthesis affect the material yielded and the morphology adopted. The presence of other ions, for example, as part of the calcium salt might impact the lattice formation. It will also be influenced by the pH of the solution, or the pressure reached in the system. All those factors are critical for HAP formation. For calcium precursors calcium nitrate tetrahydrate is the most used.[51–55] The phosphates precursors are more varied including: diammonium hydrogen phosphate,[56] ammonium hydrogen phosphate,[51] phosphoric acid,[57] *etc*.

Temperature is a common way to control the nucleation and growth in hydrothermal synthesis. In a typical reaction, higher temperature will drive to bigger particles and crystallinity. HAP follows this trend. The increase of temperature starting from 120°C promotes the growth of directional nanorods. Lower temperatures generate less crystalline products with more poorly-defined morphologies.[58] Parallel to temperature, pH plays a huge role in the formation of hydroxyapatite and the morphology it shows. Unfortunately, the information regarding the formation of nanorods at different

pH is not yet clear. Rod-like HAP have been obtained in acidic,[59–61] neutral[62,63] and alkaline conditions.[64,65] pH conditions also influence the selection of the calcium phosphate compounds in the sample. pH lower than 4 will incentivise the formation of other calcium orthophosphates like monetite and brushite. The different synthetic conditions for the synthesis of calcium orthophosphates are highlighted in Figure 4.4.

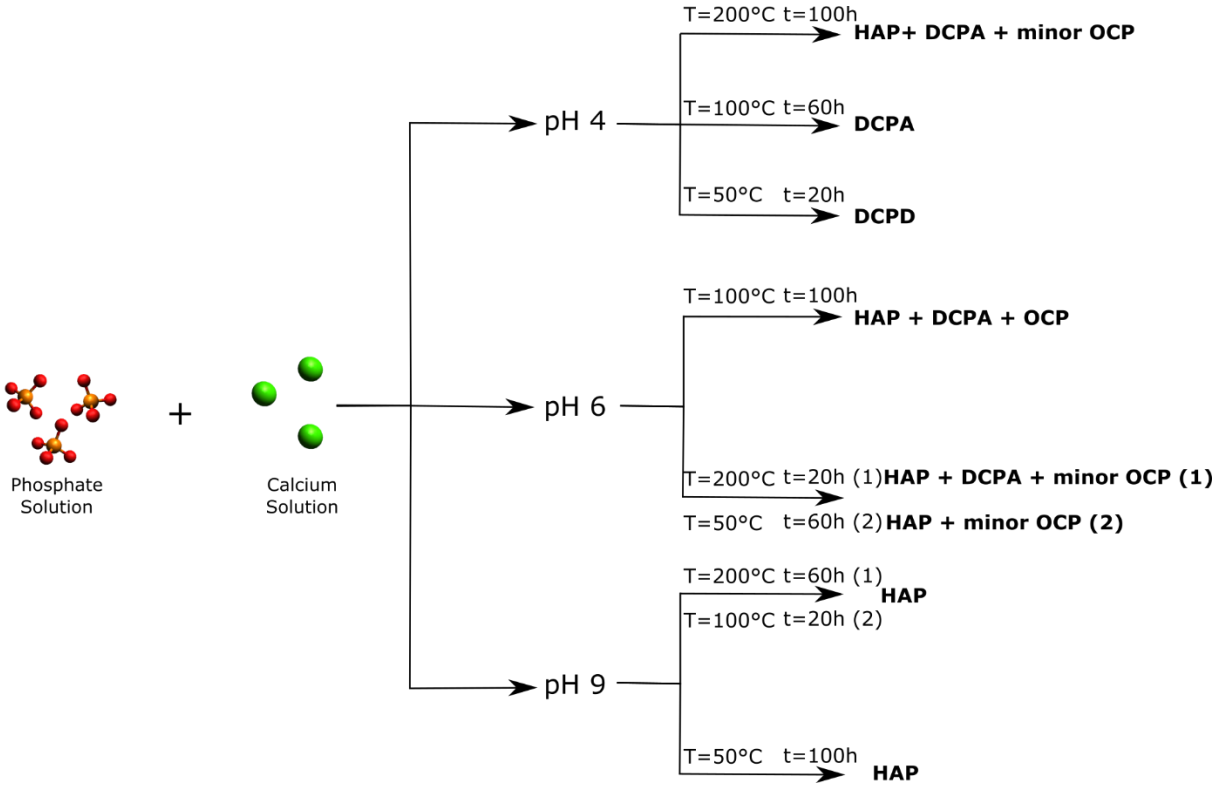

Figure 4.4. Diagram of the CaP compounds obtained at different experimental conditions (T, pH and time) by hydrothermal synthesis.[53]

4.1.2.2 Brushite and monetite

Brushite is also called dicalcium phosphate dihydrate (DCPD) as it contains two water molecules within the structure. The framework of this material consists of chains of $CaPO_4$ parallel to each other.[66] The water molecules will be positioned between the chains. The non-hydrated version of this material is commonly named monetite or anhydrous calcium phosphate (DCPA). Brushite is very unlikely to be seen *in vivo*, probably due to the weak diffraction of this material, being impossible to acknowledge it by X-ray techniques. It was firstly evidenced by Mirtchi and Lemaître from mixing a solution of monocalcium phosphate monohydrate with basic calcium phosphate. The resultant solid material solidifies exothermically, creating a solid cement-like substance

primarily composed of brushite.[67] Although the presence of these materials is very uncommonly observed in living organisms, it is known to be biocompatible. One of the main advantages to be used in biological environments is the ability to be reabsorbed in representative conditions, although its limited properties make it really difficult to be employed.[68,69] Nonetheless, over the years the research on this material has improved its characteristics for its future applicability.[70]

Monetite can be obtained by modifying the synthetic conditions of brushite.[71] As a dehydrated version of brushite low pH, absence of water and the intercalation of ions will promote the formation of monetite.[71–74] It can be obtained directly from brushite by thermal treatment at 900°C.[71]

To understand the relationship between the different calcium phosphates mentioned, the hydrothermal transition from brushite to HAP has been studied. It follows the equation:

$$\mathrm{CaHPO_4 \cdot 2H_2O}\ [DCPD] \rightarrow \mathrm{CaHPO_4[DCPA] + 2H_2O} \qquad (4.1)$$

$$\mathrm{6CaHPO_4 + 2H_2O + 4Ca(OH)_2 \rightarrow Ca_{10}(PO_4)_6(OH)_2\ [HAP] + 8H_2O} \qquad (4.2)$$

The main requirement for the formation of HAP to take place is that the stoichiometric ratio must correspond to Ca/P = 1.67. Therefore, it is mandatory to introduce a calcium source like $Ca(OH)_2$. Crystalline HAP is obtained at 200°C and 10 h. Therefore, the conditions desired for obtaining each phosphate will range from low pH with Ca/P = 1, where monetite and brushite can be obtained, to a Ca/P = 1.67 and neutral to basic conditions where HAP will be primarily formed (Figure 4.4). This experiment proposes a mechanism of selective formation of calcium phosphate by direct transformations between crystalline compounds. It makes the overall picture of nucleation and growth of these materials even more dynamic.

4.2 Experimental

As already highlighted, the selective formation of the different calcium phosphates will be dependent of the synthetic conditions chosen. The main parameters to be considered when planning a reaction will be Ca/P ratio, temperature, pH, and precursors used. In order to track and precisely control the internal conditions during the reaction the hydrothermal injection reactor designed will be used for this task. The results obtained after analysis will help to create a general picture of the optimum conditions for the formation of the different calcium orthophosphates.

4.2.1 Hydrothermal Injection Reactor.

The standard general procedure was followed as described in Chapter 2. In the case of precursor selection two phosphate sources will be chosen as precursors: $(NH_4)_2HPO_4$ and $Na_2HPO_4{\cdot}7H_2O$ in various concentrations (as seen in Table 4.2). The precursor buffered to pH = 10 was prepared by adjusting the pH by dissolving NaOH in the solution. The pH was measured under continuous stirring by a Mettler-Toledo SevenCompact™ Advanced pH-meter, previously calibrated by a three point linear calibration as assessed by the manufacturer.

In order to simplify the different variables, the Ca^{2+} precursor and concentration will be the same in all cases, $Ca(NO_3)_2$ 1.5 M. The concentration of the phosphates will vary to achieve different Ca/P ratios 0.5,1.5, 1.67 and 3. The phosphate concentrations will be 0.4, 0.45 0.5 and 1.5 M, respectively.

The proposed general equations for the reactions are:

$$Ca(NO_3)_2 + (NH_4)_2HPO_4 \xrightarrow{H_2O} CaHPO_4 + CaHPO_4 \cdot 2H_2O + Ca_{10}(PO_4)_6(OH)_2 \quad (4.3)$$

$$Ca(NO_3)_2 + Na_2HPO_4 \xrightarrow{H_2O} CaHPO_4 + CaHPO_4 \cdot 2H_2O + Ca_{10}(PO_4)_6(OH)_2 \quad (4.4)$$

For every reaction 5.00 mL of the selected phosphate precursor was pipetted into the chamber. The HPLC pump was then filled with the calcium precursor by repeating a pump-refill cycle three times with the solution. The magnetic stirrer was then placed in

the chamber and the reactor body assembled. The heating jacket was placed around the reactor and tightened. The stirring rate was constant for every reaction 600 rpm.

The reactions were carried out at 25 (room temperature), 50, 100 and 200°C. Once the target temperature was achieved, it was maintained for 5 minutes prior injection to ensure stable conditions after mixing. 2.5 mL of the calcium precursor solution were injected by the HPLC. It was left to react for 10 minutes before it was switched off and left to cool down to room temperature. Once it was safe to open the reactor the product was decanted into a beaker and filtered *via* vacuum filtration. The product was washed three times before placed in a preheated oven at 75°C overnight.

Table 4.2 Experimental precursors, concentration, and Ca/P ratio.

Precursor	Concentration (M)	Ca/P ratio
$(NH_4)_2HPO_4$	1.5	0.5
$(NH_4)_2HPO_4$	0.25	3
$(NH_4)_2HPO_4$	0.5	1.5
$Na_2HPO_4 \cdot 7H_2O$	0.25	3
$(NH_4)_2HPO_4$	0.45	1.67
$Na_2HPO_4 \cdot 7H_2O$	0.45	1.67
$Na_2HPO_4 \cdot 7H_2O$ (Buffered to pH 10.8)	0.45	1.67

4.2.2 Characterisation

Every sample produced was analysed by XRD and FTIR. Raman spectroscopy was carried out only on certain samples to corroborate the results given by the rest of techniques. In order to quantify the amount of each compound in the samples, Rietveld refinement was performed. For visualising the possible trends from the different materials obtained, Principal Component Analysis (PCA) of the diffraction patterns was attempted.

4.2.2.1 XRD

The XRD patterns will be compared with the model patterns obtained from the Crystallographic Open Database (COD).[75]

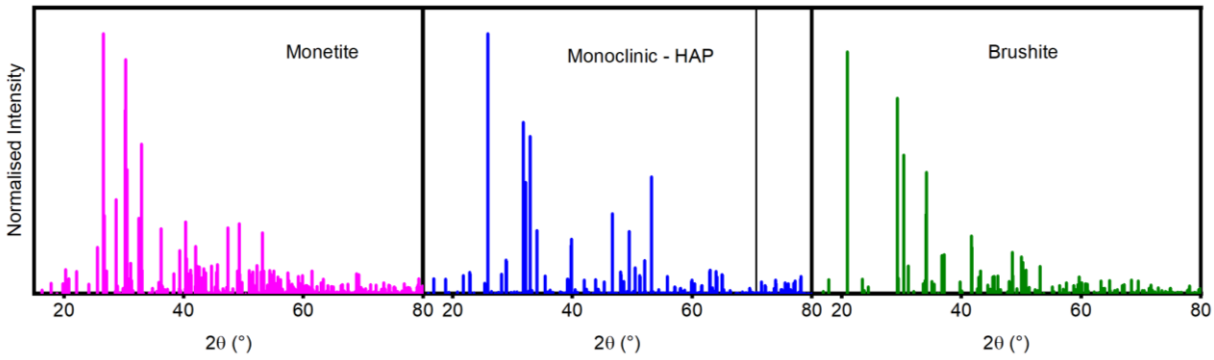

Figure 4.5. Reference patterns for monoclinic HAP, brushite and monetite.[76–79]

The XRD patterns were acquired by using a Bruker D2 Phaser with CuKα = 1.5418 Å as the source of radiation. The angles chosen for the measuring range from 15 to 85° 2θ with step-size of 0.01° at 1s per step, using a silicon zero background holder.

4.2.2.2 Rietveld Refinement

The XRD patterns were analysed to obtain the percentage of each mineral. Some anisotropic corrections were required for the refinement. Due to the high preferential orientation shown by these materials, March-Dollase (MD) corrections were considered as described extensively in Chapter 2. The software employed for the refinement was EXPGUI/GSAS[80,81] using the built-in MD correction for a selection of planes.

For simplicity only monoclinic HAP has been discussed as no features from hexagonal HAP have been observed during the analysis of the patterns. The lack of hexagonal HAP has been confirmed by the impossibility of Rietveld refinement to give any percentage result for this compound as no characteristic feature was found in the XRD patterns.

4.2.2.3 FTIR

To corroborate the formation of the different phosphates the FTIR spectra were obtained using a Perkin Elmer ATR-FTIR spectrometer with a Perkin Elmer Universal ATR Sampling Accessory. Spectra were measured from 4000 to 500 cm^{-1}. Four recording iterations were collected and averaged. The main vibration modes and the assignment for brushite, monetite and hydroxyapatite are collected in Table 4.3, Table 4.4 and Table 4.5, respectively.

Table 4.3. FTIR wavenumbers for the modes of brushite.[82]

Functional group	Wavenumber (cm^{-1})
O-H stretching of lattice water	3541, 3480, 3282, 3166
(P)O-H stretching	2930
Combination	2385
H-O-H bending and rotation of residual water	1600, 1720
H-O-H bending of lattice water molecules	1649
P-O-H in-plane bending	1208
P-O stretching	1135, 1065
P-O stretching	987
P-O(H) stretching	877
P-O-H out-of-plane bending	795
Water librations	661
O-P-O(H)	576, 528

Table 4.4. FTIR wavenumbers for the modes of monetite.[82]

Functional group	Wavenumber (cm^{-1})
O-H stretching of residual water	3447
(P)O-H stretching	3190, 2849, 2360
H O H bending and rotation of residual free water	1600-1700 (broad)
P-O-H in-plane bending	1450-1300 (broad)
P-O stretching	1170,1131,1081
P-O stretching	996
P-O(H) stretching	891
O-P-O(H)	578, 532

Table 4.5. FTIR wavenumbers for the modes of HAP.[83,84]

Functional group	Wavenumber (cm^{-1})
O-H stretch	3744
Structural O-H	3565
Water absorbed	3440
Water absorbed (v_2)	1645
PO_4 asymmetric stretching(v_3)	1096, 1031
PO_4 symmetric stretching (v_1)	961
Structural O-H	635
PO_4 bending (v_4)	604, 574, 565
PO_4 out-of-plane bending (v_2)	471

4.2.2.4 Scanning Electron Microscopy (SEM)

In order to corroborate the shape of the particles synthesised, SEM images were obtained by using a Zeiss Ultra TEM microscope running at 5.00 kV with *in Lens*

detection. All samples were prepared and deposited onto a carbon tab over an aluminium stub.

4.3 Results and Discussion

The data obtained from the samples will be shown and discussed in this section. XRD patterns and FTIR were obtained for all the samples, whereas only certain Raman spectra were recorded to corroborate the results and shown in Appendix A . The data will be presented following the order in Table 4.2. In order to quantify the amount of each compound in each XRD pattern presented, the results from Rietveld refinements are plotted side by side. In order to simplify the results obtained due to the large number of variables and the number of samples obtained, Principal Component Analysis was carried out. Some SEM images were taken to observe the change of shape of the particles when changing the synthetic conditions.

4.3.1 Structural Characterisation

4.3.1.1 Ca/P = 0.5 – $(NH_4)_2HPO_4$ phosphate precursor

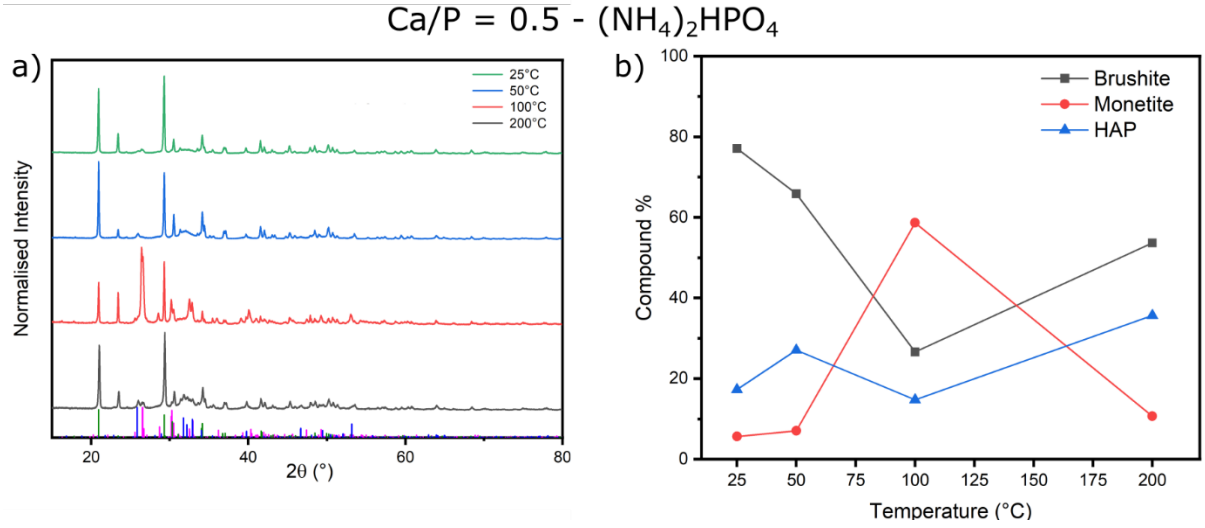

Figure 4.6. a) XRD patterns for Ca/P ratio 0.5 using $(NH_4)_2HPO_4$ as the phosphate precursor in the reaction. Vertical lines correspond to the position of the model patterns for HAP (blue), brushite (green) and monetite (pink). b) Sample composition as determined by Rietveld analysis of the XRD patterns.

Figure 4.6 shows the XRD patterns obtained for the calcium orthophosphate samples obtained using a Ca/P ratio of 0.5 with ammonium hydrogen phosphate,

$(NH_4)_2HPO_4$, as the phosphate precursor. The temperature of injection is increased from 25°C to 200°C from top to bottom in Figure 4.6 a).

Although XRD gives information relevant to the presence of the different minerals in the sample Rietveld refinement is required to obtain the real mathematical description of the sample composition, giving percentages of each of the phosphate phases present. In many of these cases the diffraction patterns also exhibited preferred orientation effects. As a general trend the planes that showed the larger preferred orientation will be mentioned in this section, nonetheless, all the refinements were treated the same way. Brushite shows preferred orientation evidenced by a change in the intensity for the (040) and (041) peaks. An example of the effect of that preferential orientation is seen in Figure 4.7. Monetite will be mainly corrected for the (002) and (201) peaks. Lastly, HAP shows weak texture at the (002) peak, which despite not being a strong effect must still be corrected. As already highlighted, these are the most common planes that needed to be addressed using the March-Dollase correction during the refinement. In case it was necessary, extra planes were adjusted when required to improve the fitting parameters.

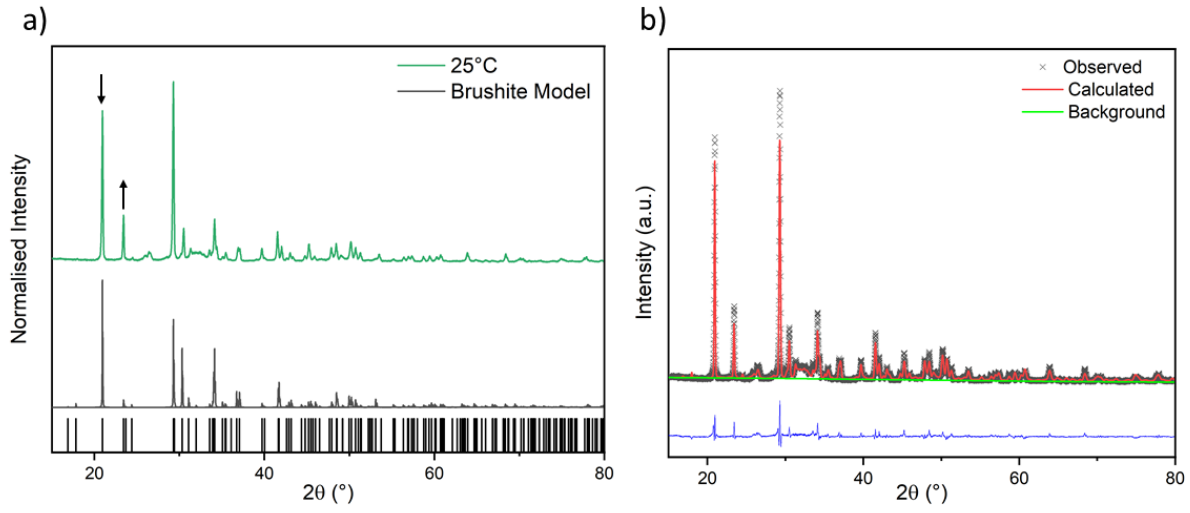

Figure 4.7. a) Comparison of the XRD pattern obtained for Ca/P = 0.5 using $(NH_4)_2HPO_4$ phosphate precursor at room temperature and the peak position for the brushite model. The arrows show the preferred orientation effect exhibited by the sample synthetised. b) Rietveld refinement with MD texture correction. Plotting of the graphical interface from EXPGUI/GSAS.[80,81]

From Figure 4.6. brushite is the main component for every synthesis temperature studied except 100°C. It is evidenced by the sharp peaks at 21° and 29° 2θ corresponding

to the (021) and (041) directions, respectively. On the other hand, monetite is the most prevalent phase in the sample prepared at 100°C. Monetite content is increased from less than 10% of the total, to almost 60% under those conditions. It can be also acknowledged by the peak at 26° 2θ, corresponding to the (002) plane. Finally, the third calcium phosphate phase in the samples is hydroxyapatite (HAP). Following Figure 4.6 b) its presence never surpasses 40%. Its contribution increases from 25 to 50°C, lowers at 100°C and reaches its highest percentage at 200°C – 35.65%. The Rietveld refinement of the sample obtained at 200 °C is plotted in Figure 4.8.

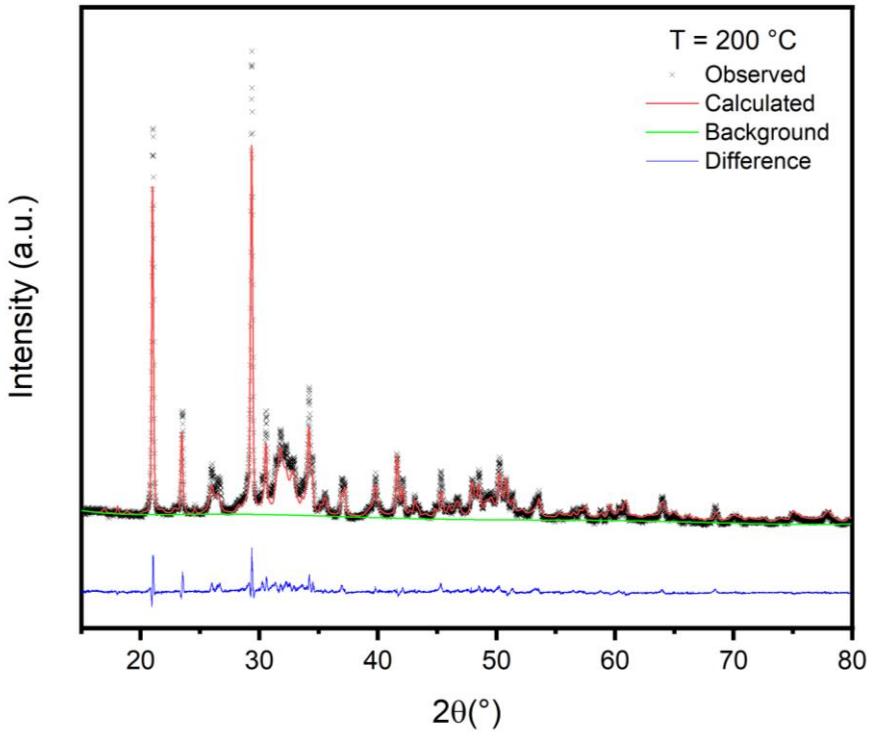

Figure 4.8. Rietveld refinement for the sample obtained at 200 °C. The compound percentages obtained by Rietveld refinement are: brushite 53.67%, monetite 10.68% and hydroxyapatite 35.65%. The pattern shows a good fitting for a mix of components in the sample.

It was highlighted in Figure 4.4 that the presence of monetite is mainly expected at mild to high temperatures and low pH conditions. Brushite, in contrast, is observed at lower temperatures (50°C). The selective formation of these two compounds at the conditions described, is therefore very linked to the temperature of formation. Monetite seems to have a narrower optimal conditions range, whereas brushite is formed from reactions at room temperature to 200 °C.

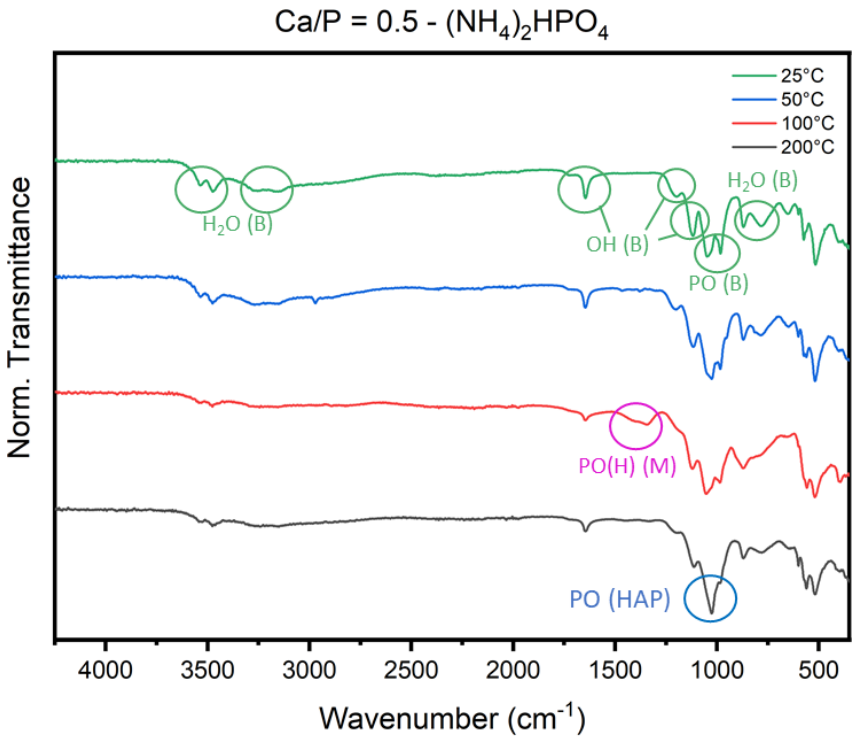

Figure 4.9. FTIR spectra for Ca/P ratio 0.5 using $(NH_4)_2HPO_4$ as the phosphate precursor in the reaction. The main features for the different calcium orthophosphate minerals are highlighted as (B) Brushite, (M) monetite and (HAP) hydroxyapatite.

The results from the Rietveld refinement and the XRD patterns are corroborated by FTIR. At room temperature, characteristic features of brushite are observed such as the two double peaks in the 3000 – 3500 cm^{-1} region, corresponding to the characteristic stretching of water. The sharp peak at 1661 cm^{-1}, the broader feature at around 1200 cm^{-1}, the peak at 1107 cm^{-1} and the lower in frequency observed at 875 cm^{-1} are characteristic of various vibrational modes of water and hydroxyl groups in brushite. This compound is known as dicalcium phosphate dihydrate (DCPD) which points out the presence of two characteristic waters in the structure. Those molecules are clearly seen at the FTIR, and they serve as a differentiator feature from the dehydrated compound. At 50°C, brushite is the main component of the sample. Although the main peaks at room temperature are kept the same, new features are observed. Due to the similarity of the structural bonds between brushite and monetite the phosphate region around 500 to 700 cm^{-1} will be similar to each other. Anyways there is a third lower-intensity shoulder next to the high intensity double peak in that region. It is reported as a peak around 630 cm^{-1} related to structural OH in HAP as enunciated in Table 4.5. Although in XRD peaks related with

HAP can be observed, the intensity of them is low compared to the ones for brushite, with calculated phase percentages of 27 and 66%, respectively. Therefore, no HAP features are expected to be clearly observed in the FTIR due to the low presence of this mineral from diffraction refinement. At 100°C monetite-related peaks are observed. A small but evident peak is seen at 1300 cm^{-1}, associated to P-O-H in-plane bending for this compound. Finally, at 200°C the peaks at highest frequencies related to water appear weaker and broader. The double peak at 1000 cm^{-1} disappears and a single, very defined peak is then seen at slightly higher frequency, 1090 cm^{-1}. It is related to the v_3 P-O bending mode of HAP. The presence of brushite is indicated by the characteristic water peaks. Nonetheless, the phosphate features for hydroxyapatite seem to overlap the brushite ones.

The rise in temperature promotes the formation of anhydrous versions of the calcium orthophosphates, such as monetite at 100°C, although at the highest temperature brushite is yielded back again. HAP follows a similar percentage trend as brushite, but always in a lower presence.

Selected calcium phosphate samples were chosen to be imaged to show the different shapes of the compounds present in the sample. Shape changes can be acknowledged along the different temperatures of formation with correlation to the XRD patterns

The first set of images in Figure 4.10 correspond to the Ca/P = 0.5 using ammonium hydrogen phosphate as the precursor. The samples were obtained at temperatures of synthesis: 25, 100 and 200°C.

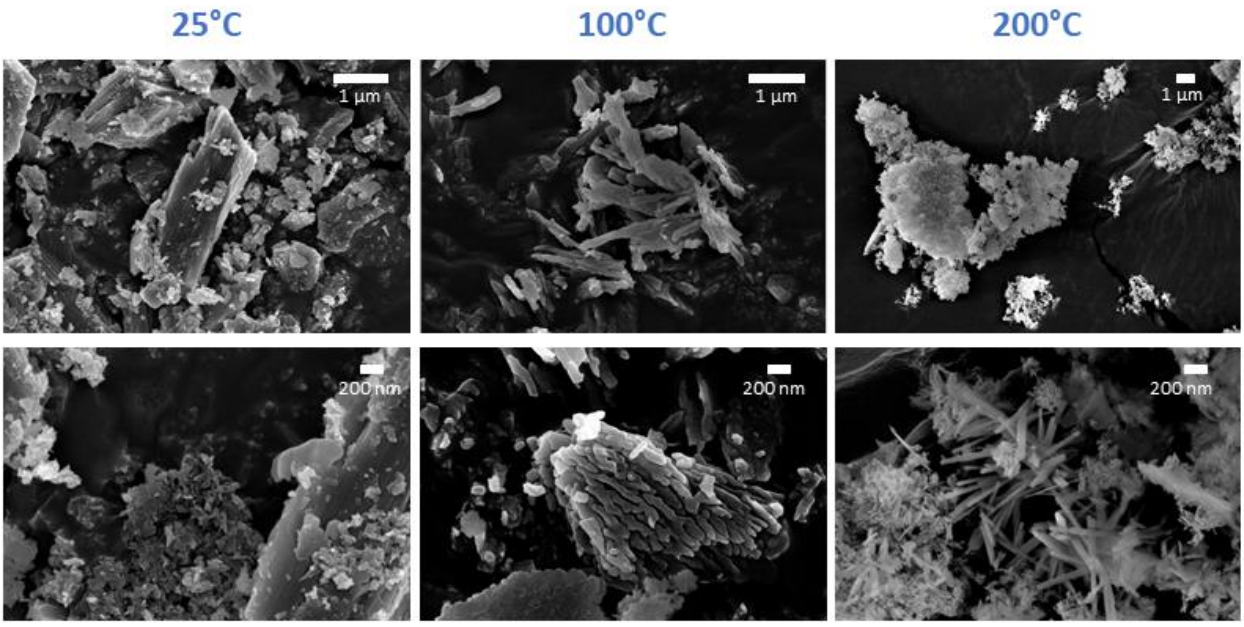

Figure 4.10. SEM images taken from Ca/P = 0.5 using ammonium hydrogen phosphate $(NH_4)_2HPO_4$ as the precursor.

From XRD analysis the main compound at room temperature is brushite. When observing the SEMs some loose particles with poorly defined features can be seen as the main shape obtained. It was observed that when looking closer at these futures, they are comprised of randomly oriented platelets creating a porous network as shown in Figure 4.11. Brushite has been reported to show similar features in previous syntheses under hydrothermal conditions.[85]

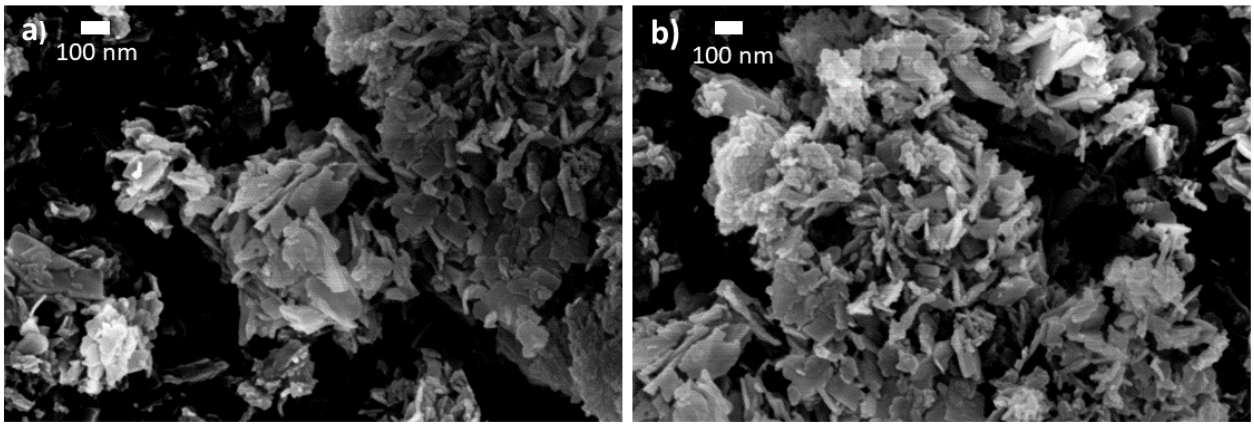

Figure 4.11. SEM images taken from Ca/P = 0.5 using ammonium hydrogen phosphate $(NH_4)_2HPO_4$ as the precursor at room temperature.

As the temperature is raised up to 100°C monetite is the main component of the sample. The main shape for this compound, as shown in Figure 4.10, is the formation of condensed pinacoidal shapes as well as not fully defined rod-like particles which justifies the texture shown by the XRD patterns in Figure 4.6.

For the highest temperature the percentage of monetite decreases, with brushite and HAP being the main components of the sample. It is observed as two types of particles can be distinguished in the sample as shown in Figure 4.12. SEM images taken from Ca/P = 0.5 using ammonium hydrogen phosphate $(NH_4)_2HPO_4$ as the precursor at 200°C. Main features for the particles are highlighted: a) brushite platelets and b) HAP rod-like particles.. Brushite exhibits less crystalline particles, shaped as platelets. HAP, on the other hand, shows very directional particles forming rods and whisker-like particles, justified by the corresponding XRD patterns' preferential orientation effects. Similar features are reported for hydroxyapatite under similar hydrothermal conditions.[86]

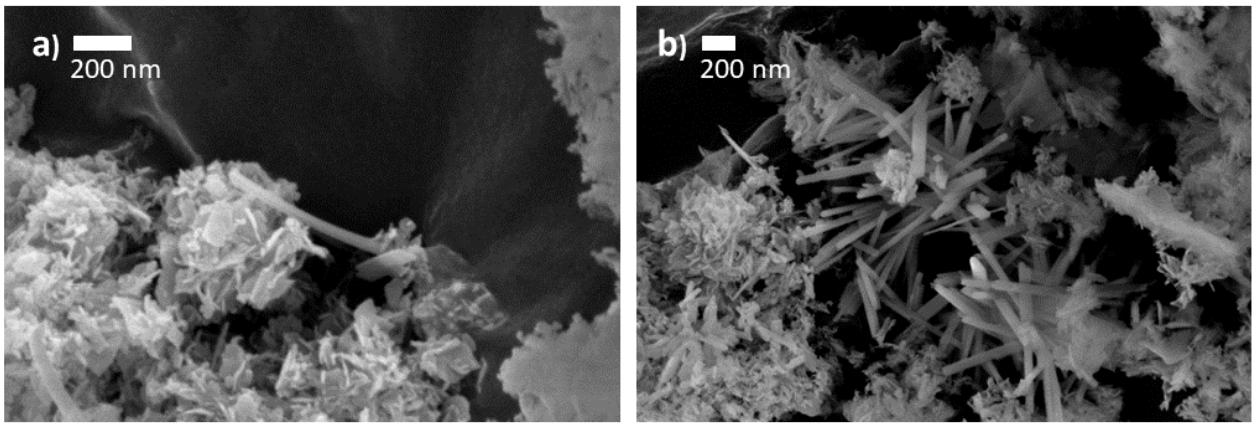

Figure 4.12. SEM images taken from Ca/P = 0.5 using ammonium hydrogen phosphate $(NH_4)_2HPO_4$ as the precursor at 200°C. Main features for the particles are highlighted: a) brushite platelets and b) HAP rod-like particles.

4.3.1.2 Ca/P = 3 – $(NH_4)_2HPO_4$ phosphate precursor

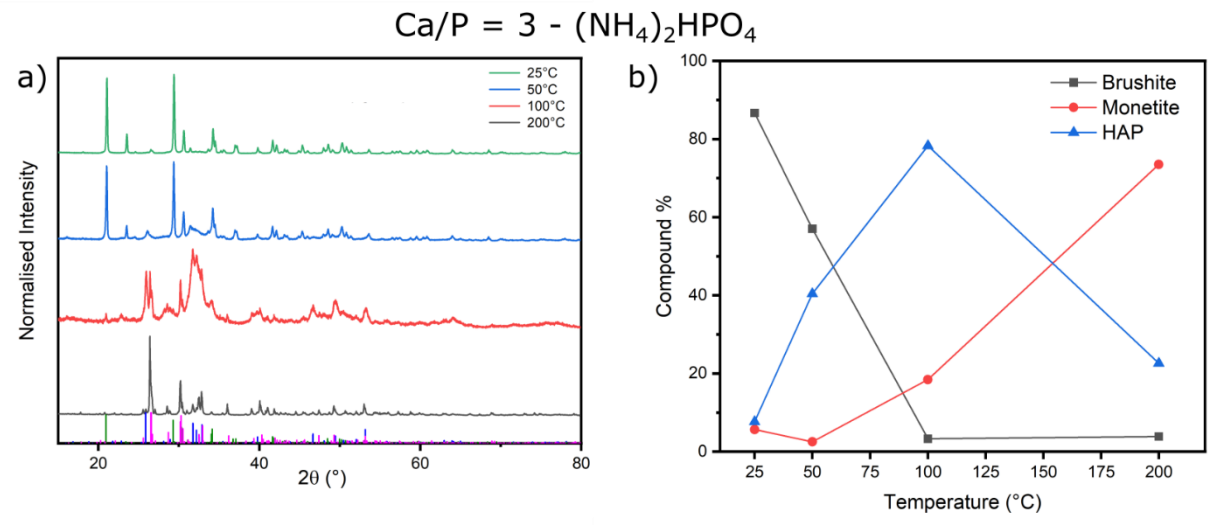

Figure 4.13. a) XRD patterns for Ca/P ratio 3 using $(NH_4)_2HPO_4$ as the phosphate precursor in the reaction. Vertical lines correspond to the position of the model patterns for HAP (blue), brushite (green) and monetite (pink). b) Sample composition as determined by Rietveld refinement of the XRD patterns.

The data obtained from Figure 4.13 correspond to samples obtained at a higher Ca/P ratio than the previous one (Ca/P = 3) and using ammonium hydrogen phosphate as the phosphate precursor. It shows that at lower temperatures brushite is still the main component of the samples (almost 87%). At 50°C, although brushite is still the main component in the sample, some new features may be seen. A broad asymmetric peak can be observed at around 31 - 32 ° 2θ, corresponding to a cluster of various HAP peaks. Hydroxyapatite is reported to show 10 peaks with similar intensity in the angle range of 31.26 to 32.64° 2θ. Due to the nature of the XRD measurement they can't be resolved, generating the broad feature described. At a synthesis temperature of 100°C those peaks are centred at 32° 2θ increasing in intensity. HAP features are not as defined as for the other calcium orthophosphates, brushite and monetite. Nonetheless from refinement hydroxyapatite is the main component at that condition (78.2%). Two peaks at 25.9° and 26.5° 2θ further evidence (002) HAP direction and the cluster of (002) and (200) monetite planes, respectively. At higher temperatures (200°C) monetite features are more clearly seen. It is calculated to be the main component in the sample (73.5%).

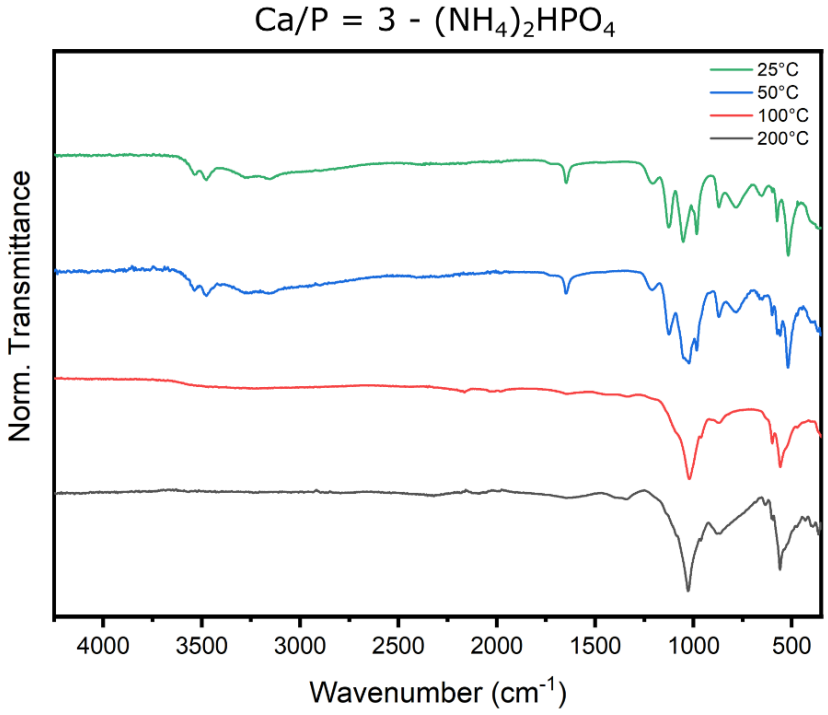

Figure 4.14. FTIR spectra for Ca/P ratio 3 using $(NH_4)_2HPO_4$ as the phosphate precursor in the reaction.

The infrared spectra of these samples are shown in Figure 4.14. The sample prepared at room temperature shows two sets of peaks at 3534 and 3474 cm^{-1} as well as 3273 and 3154 cm^{-1}. Those features correspond to lattice water stretching modes for brushite. It corroborates the presence of brushite at those synthesis conditions. Two extra features are seen in the spectrum at 1055 and 985 cm^{-1}. They are related to phosphate stretching modes for brushite. At 50°C the water stretching modes are kept similar, although the phosphate modes start to overlap forming a single peak, in the region ranging from 800 to 1200 cm^{-1}. It is due to the increase of HAP in the sample showing a phosphate stretching (ν_3) at 1030 cm^{-1}. In the case of samples prepared at 100 and 200°C the features of the spectra are similar. The main peaks observed correspond to the already mentioned phosphate related stretching (ν_3) at 1030 cm^{-1} and phosphate bending (ν_4) at 557 cm^{-1} for HAP. Due to the XRD analysis features from monetite would be expected to arise. Nonetheless, the FTIR spectra only show clear signs of the presence of HAP and almost no peaks from monetite can be clearly evidenced. A low intensity broad peak from 1300 to 1400 cm^{-1} might be related to the P-O-H in plane bending for monetite.

Overall, HAP is obtained at a high percentage at higher ratios than the exact Ca/P ratio for the mineral composition as shown in Table 4.2 (1.67). It further supports the idea that mild synthetic conditions, as 100°C, is the optimum temperature for the larger presence of HAP. Brushite is the preferred calcium orthophosphate at lower temperatures while monetite is formed at the higher temperatures. It additionally shows that FTIR seems to be more specific to show the presence of HAP than monetite. Although from XRD, at higher temperatures monetite seems to be the main component, in FTIR only HAP features can be clearly seen.

4.3.1.3 Ca/P = 1.5 – $(NH_4)_2HPO_4$ phosphate precursor

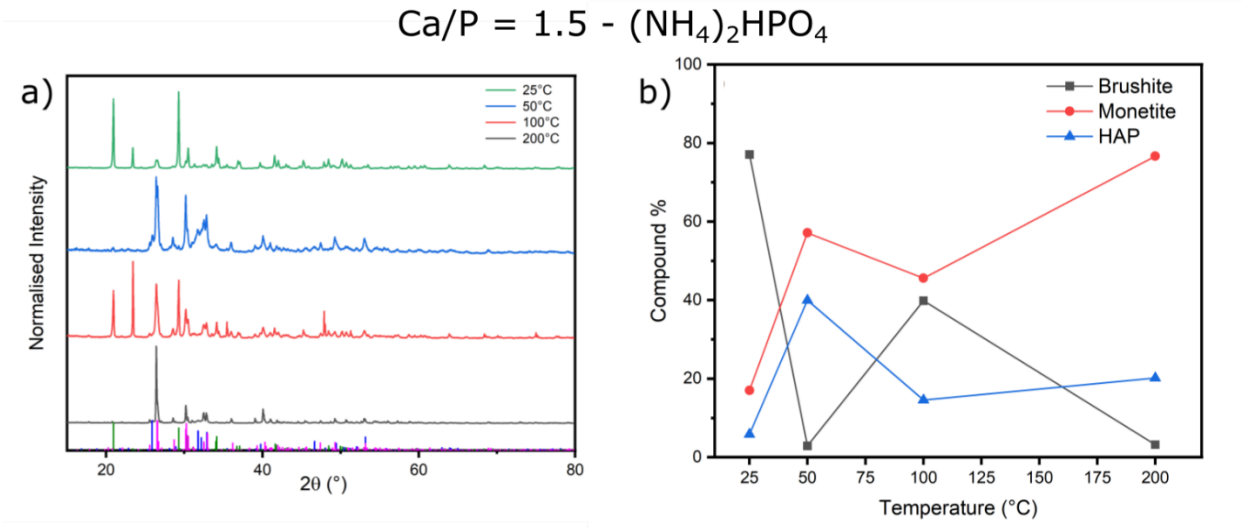

Figure 4.15. a) XRD patterns for Ca/P ratio 1.5 using $(NH_4)_2HPO_4$ as the phosphate precursor in the reaction. Vertical lines correspond to the position of the model patterns for HAP (blue), brushite (green) and monetite (pink). b) Sample composition as determined by Rietveld refinement of the XRD patterns.

The XRD patterns and the results of the corresponding Rietveld refinement are shown in Figure 4.15 for the samples obtained at a Ca/P ratio = 1.5 and using ammonium hydrogen phosphate as the phosphate precursor. It shows that at room temperature brushite is the main component of the sample. It is evidenced by the presence of the sharp peaks at 21° and 29° 2θ corresponding to the (021) and (041) planes, respectively. At 50°C monetite (57.1%) increases to be the main component in the sample along with HAP (40.0%) as the second most abundant one. Monetite is revealed in the XRD by two sharp peaks at 26.5° and 30.2° 2θ which are the addition of (200) and (002), and (-120) planes, respectively. On the other hand, HAP shows, a sharp peak at 26° 2θ which

overlaps with the main feature of monetite. It is related to the (002) plane for this compound. HAP presence is also shown by a broad characteristic set of peaks in the range of 31 – 32° 2θ. At 100°C brushite (39.8%) and monetite (45.6%) are present in the sample. Brushite's main peaks are seen at 21° and 29° 2θ. They show a similar intensity with the main monetite peak at 26.5° 2θ. A really intense peak at around 23.4° 2θ gains importance in the pattern. It corresponds to a low intensity brushite peak that, due to preferential orientation, increases in intensity. It is correlated to the (040) plane for brushite. This feature is seen at a lower degree at room temperature. Hydroxyapatite is also evidenced at a lower presence (14.6%) by the congregation of peaks in the 31° to 32° 2θ region. At 200°C, the highest temperature, monetite is the main component of the sample (76.7%). A clear sharp peak at 26.4° 2θ shows the presence of monetite. It corresponds to monetite's (200) and (002) orientations. Its intensity is unambiguously higher than the calculated for this compound showing a clear preferential orientation for that orientation.

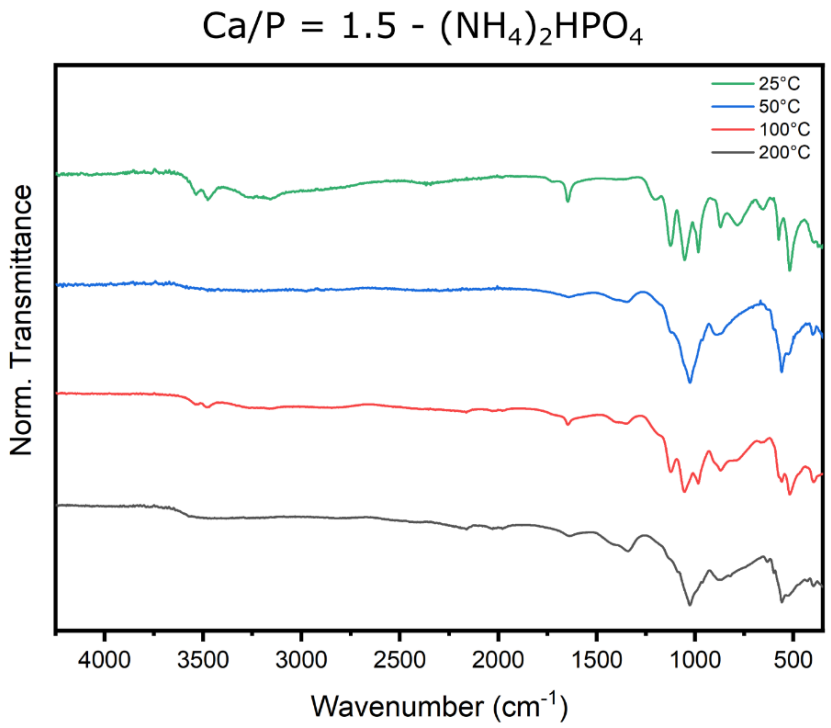

Figure 4.16. FTIR spectra for Ca/P ratio 1.5 using $(NH_4)_2HPO_4$ as the phosphate precursor in the reaction.

From FTIR spectra, at room temperature, brushite features can be seen by the water stretching modes in the 3000 – 3500 cm^{-1} region. Three phosphate stretching modes

are seen at 1126, 1052 and 984 cm^{-1} also related to brushite. Finally at 790 cm^{-1} there's a characteristic broad peak that corresponds to P-O-H out of plane bending for brushite. At 50°C water stretching modes fade away, evidencing the presence of anhydrous orthophosphates such as monetite and hydroxyapatite in the sample. There's also the formation of a larger peak at 1030 cm^{-1}, characteristic of the asymmetric phosphate stretching (v_3) for HAP. An additional characteristic feature is seen at 560 cm^{-1} where PO_4 bending (v_4) for HAP is usually seen. Regarding the 100°C FTIR spectrum, although the features are not as sharp as for room temperature, the three phosphate modes for brushite gain importance along with the water modes in the higher frequency region (3000 to 3500 cm^{-1}). At 200°C the water modes are absent and only one peak is seen in the phosphate characteristic region. In particular, at 1030 cm^{-1} the v_3 phosphate mode for HAP is clearly seen. It evidences the presence of anhydrous phases, in particular hydroxyapatite and monetite.

Monetite at these synthetic conditions is the most abundant component at intermediate to high temperatures. Brushite is obtained at lower temperatures, while HAP shows a preference to be formed at intermediate ones showing a higher presence at 50 °C.

4.3.1.4 Ca/P = 3 - $Na_2HPO_4 \cdot 7H_2O$ phosphate precursor

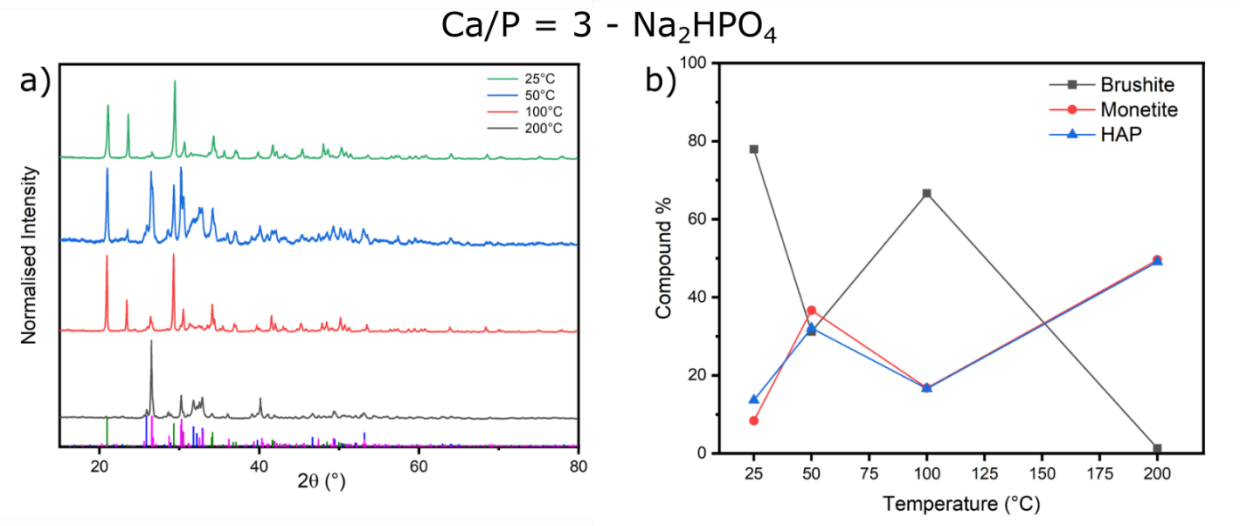

Figure 4.17. a) XRD patterns for Ca/P ratio 3 using Na_2HPO_4 as the phosphate precursor in the reaction. Vertical lines correspond to the position of the model patterns for HAP (blue), brushite (green) and monetite (pink). b) Sample composition as determined by Rietveld refinement of the XRD patterns.

From Figure 4.17 at lower temperatures brushite is the main component of the sample (78.0%). It is seen by the main brushite peaks at 21° and 29° 2θ corresponding to the (021) and (041) planes, respectively. There is an increase of the peak intensity for the (040) direction at 23.4° 2θ, relative to the predicted pattern, arising from preferential orientation effect for brushite. No extra peaks of any additional compound can be highlighted from the plot. As the synthesis temperature is increased to 50°C monetite (36.7%) starts competing in intensity with brushite (31.2%) as shown by the comparable intensity of the peaks around 26.5° 2θ corresponding to the overlapping (200) and (002) planes of monetite and the peak situated at 21° 2θ that is the (021) plane of brushite. Hydroxyapatite (32.1%) can be observed in this sample by the broad peak in the range of 31 – 32° 2θ. There is an additional HAP sharp peak at 26° 2θ linked to the (002) plane for this compound. At 100°C brushite (66.6%) is the main component of the sample showing analogous features to the room temperature pattern. Nonetheless the preferential orientation effect in the (040) is not as critical as for the lower temperature equivalent. Finally, at 200°C monetite (49.6%) is the main component along with HAP (49.1%). The presence of monetite is again shown by a sharp peak at 26.5° 2θ which is linked to the (200) and (002) planes. Hydroxyapatite can be observed by the broad peak in the range of 31 – 32° 2θ.

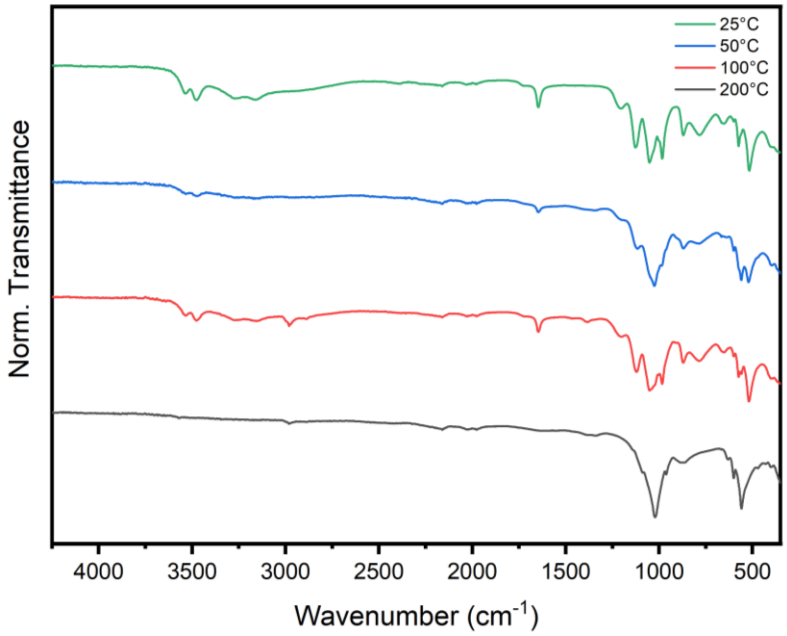

Figure 4.18. FTIR spectra for Ca/P ratio 3 using Na_2HPO_4 as the phosphate precursor in the reaction.

From Figure 4.18 at room temperature the two sets of two peaks for H_2O stretching peaks for brushite are evidenced in the 3000 to 3500 cm^{-1} area. The three additional modes for phosphate are seen at 1126, 1052 and 984 cm^{-1} related to brushite. There's an additional lower frequency peak at 790 cm^{-1} that corresponds to P-O-H out of plane bending for brushite. At 50°C a sharp peak appears in the phosphate region (800 – 1200 cm^{-1}) corresponding with the characteristic ν_3 phosphate mode for HAP. It broadens the brushite phosphate modes still present in the spectrum. The previously mentioned water modes seem to broaden and lower in intensity, although they are still present, showing that a certain percentage of brushite is still being formed. At 100°C the highly intense hydroxyapatite phosphate mode fades as the characteristic phosphate modes of brushite intensify. Two phosphate modes can be seen separately back again. The water modes for brushite at higher intensity (3000 – 3500 cm^{-1}) can be noticed. That corroborates the increasing presence of brushite at this temperature although HAP is still acknowledged. Finally, at 200°C all the mentioned brushite modes vanish showing a clear, single HAP phosphate related mode at 1030 cm^{-1}, corresponding to the ν_3 stretching mode. The water modes at higher frequency are not perceived. It shows the increase of anhydrous phases like monetite and hydroxyapatite at this synthetic conditions.

Overall brushite keeps appearing at lower temperatures as it is the dihydrate version of the calcium orthophosphates. As the temperatures increases the water molecules are lost to yield the monohydrate calcium phosphate equivalents, monetite and HAP, at the highest temperature attempted.

In the previous set of reactions SEM imaged (calcium orthophosphate samples obtained using a Ca/P ratio of 0.5 with ammonium hydrogen phosphate, $(NH_4)_2HPO_4$, as the phosphate precursor) the different shapes adopted for the three different calcium phosphate compounds were shown. The preferential orientation effect was also justified. Nonetheless, the three compounds can coexist in the same sample. The next conditions chosen to show the SEMs shows the most similar content of the three calcium orthophosphates from Rietveld analysis. The conditions to be analysed are Ca/P = 3 using Na_2HPO_4 as the phosphate precursor. The samples analysed were the synthesised at 50 and 200°C, Figure 4.19 and Figure **4.21**, respectively.

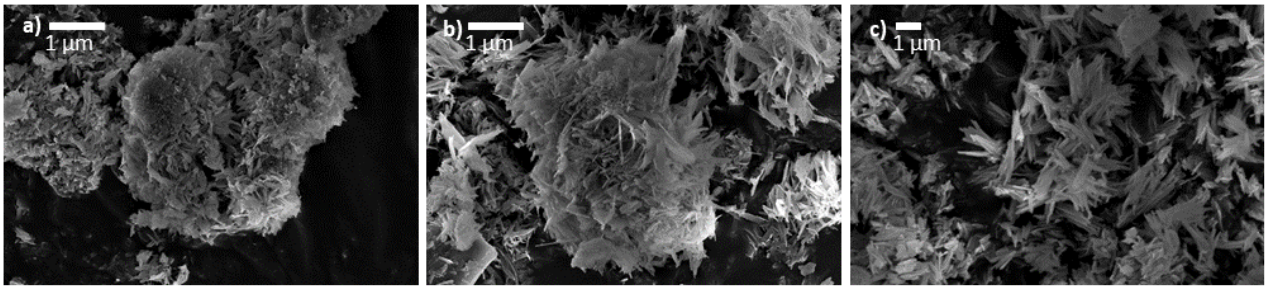

Figure 4.19. SEM images taken from the sample synthetised at Ca/P = 3 - Na_2HPO_4 at 50°C.

The SEM images shown in Figure 4.19 correspond to the sample synthesised at 50°C using Na_2HPO_4 as the phosphate precursor in a Ca/P = 3 ratio. Although from XRD the three compounds are expected to be in a similar concentration the sample at SEM looks homogeneous. It is comprised of rod-like particles randomly organised and stacked. There exists the possibility of the non-hydrated compounds monetite and hydroxyapatite to adopt the rod- and plate- like conformation.[86] The formation of these kind of particles have been extensively studied as they can be applied in the reinforcement of bone structures.[87] Brushite on the other hand is reported to have not as defined conformation, conventionally forming a flat-plate type of particles.[85]

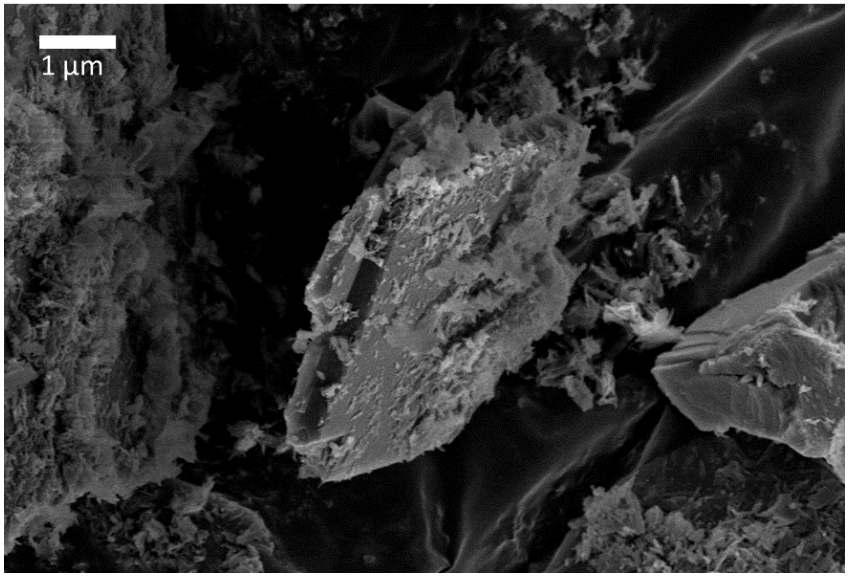

Figure 4.20. SEM image taken from the sample synthetised at Ca/P = 3 Na_2HPO_4 at 50°C. Brushite flat-plate like particle.

As the temperature is increased to 200 °C, monetite and hydroxyapatite content in the sample is increased to a similar percentage, as seen at the XRD analysis in Figure

4.17. From Figure 4.20, the sample at higher temperatures remains homogeneous but shows more defined shapes than at 50°C. Monetite and HAP adopt a more directional growth showing clear rods than can be agglomerated around the sample. No plate-like particles are clearly seen in the sample due to the low amount of brushite content. The higher intensity of the XRD pattern along the (002) plane is clearly evidenced for HAP. Very homogeneous rods are seen for that compound.

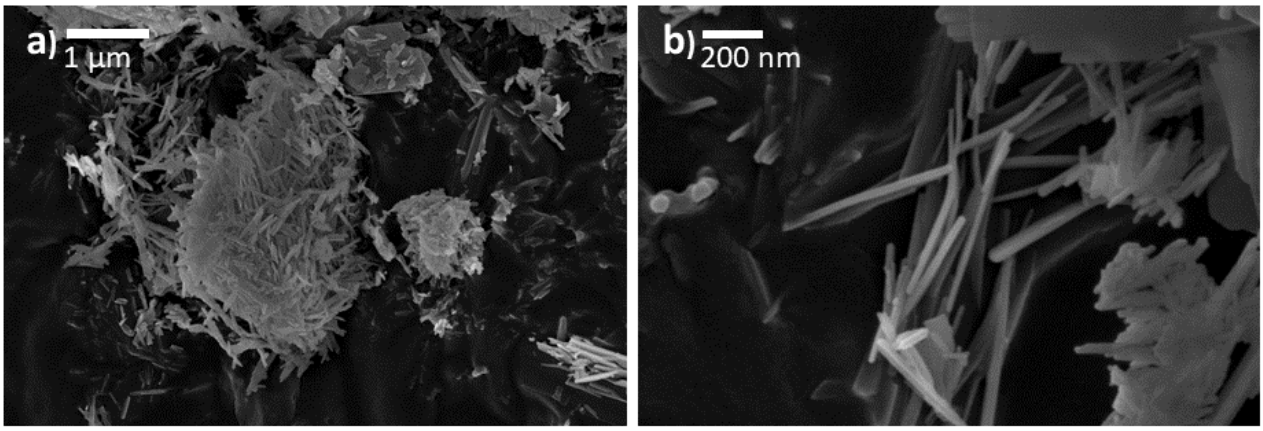

Figure 4.21**. SEM images taken from the sample synthetised at Ca/P = 3 Na_2HPO_4 at 200°C.**

4.3.1.5 Ca/P = 1.67 - $(NH_4)_2HPO_4$ phosphate precursor

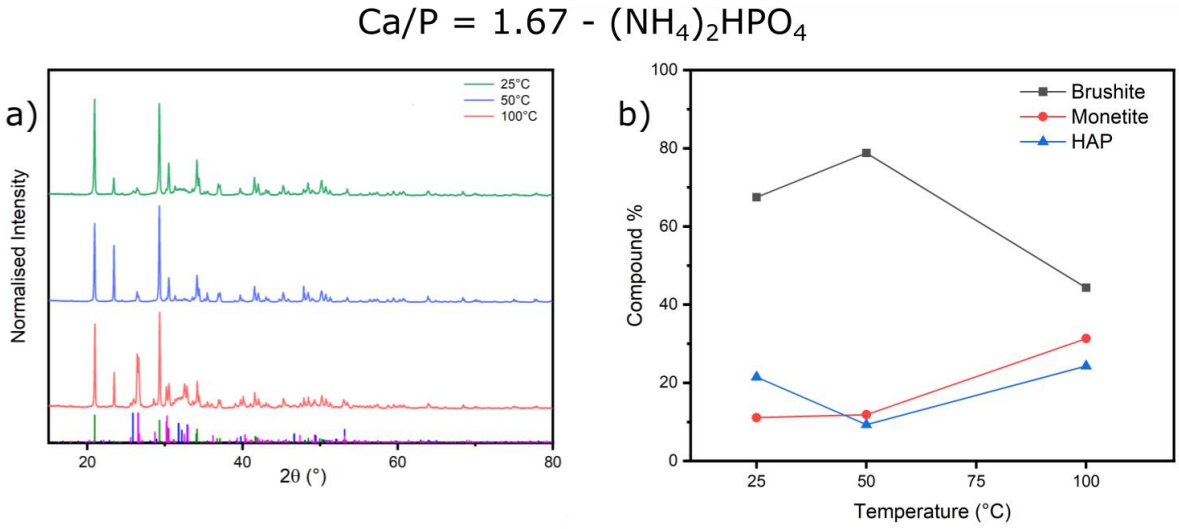

Figure 4.22. a) XRD patterns for Ca/P ratio 1.67 using $(NH_4)_2HPO_4$ as the phosphate precursor in the reaction. Vertical lines correspond to the position of the model patterns for HAP (blue), brushite (green) and monetite (pink). b) Sample composition as determined by Rietveld refinement of the XRD patterns.

After several attempts, very little sample was obtained at 200°C, therefore no XRD data was collected from that condition.

At every condition brushite is the main component in the sample. The percentages are 67.5, 78.8 and 44.4% at 25, 50 and 100 °C, respectively. It is manifested by two main peaks at 21° and 29° 2θ assigned to (021) and (041) planes, respectively. At 25°C a small amount of hydroxyapatite (21.4%) can be seen by the distinctive cluster of peaks from 31 – 32° 2θ. Nonetheless brushite is the main phosphate at that temperature showing clear crystalline features. At 50°C the peak for the (040) plane at 23° 2θ shows an increase of intensity arising from a preferred orientation effect, already mentioned in previous samples. Apart from that fact, the sample shows a high brushite content. At 100°C some new features can be perceived showing the increasing content of monetite (31.3%) in the sample from the peak around 26.5° 2θ corresponding to the (200) and (002) directions of monetite. There are also arising features of HAP (24.3%) by the broad peak situated at the region of 30 – 32° 2θ.

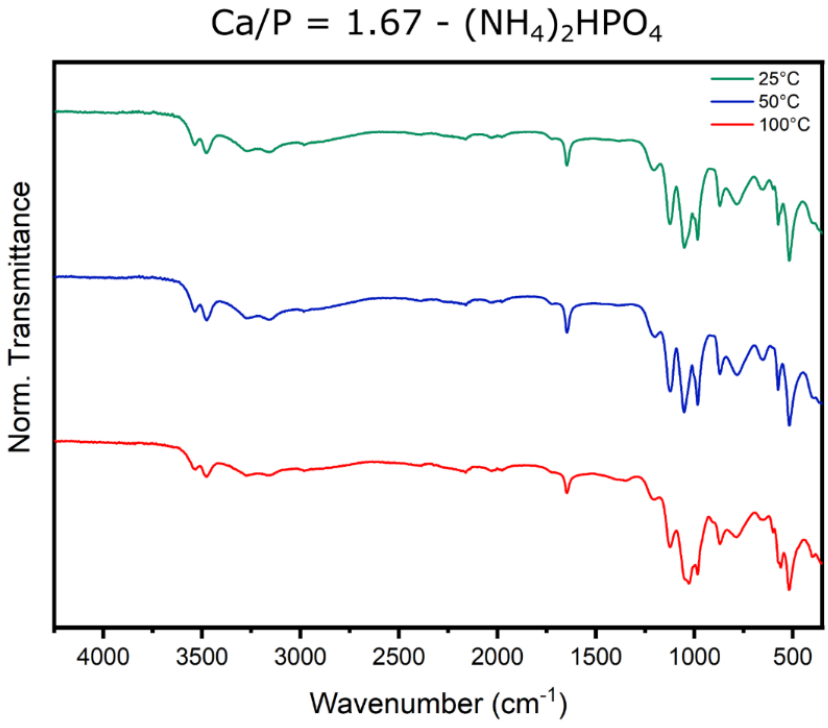

Figure 4.23. FTIR spectra for Ca/P ratio 1.67 using $(NH_4)_2HPO_4$ as the phosphate precursor in the reaction.

The IR spectra of these samples are shown in Figure 4.23. At 25°C brushite features are observed by the water modes at the higher frequency region 3000 to 3500 cm^{-1}. The phosphate peaks are also visible although they appear to be not as defined due to the presence of HAP v_3 phosphate mode in the same region (800 – 1200 cm^{-1}). At 50°C all the features clearly correspond to brushite as the main component of the sample by the two sets of two peaks for H_2O stretching modes shown from 3000 to 3500 cm^{-1}. As well as the three extra modes for phosphate observed at 1126, 1052 and 984 cm^{-1} related to brushite. Finally, at 100°C brushite features are visible but not as defined.

4.3.1.6 Ca/P = 1.67 - $Na_2HPO_4 \cdot 7H_2O$ phosphate precursor

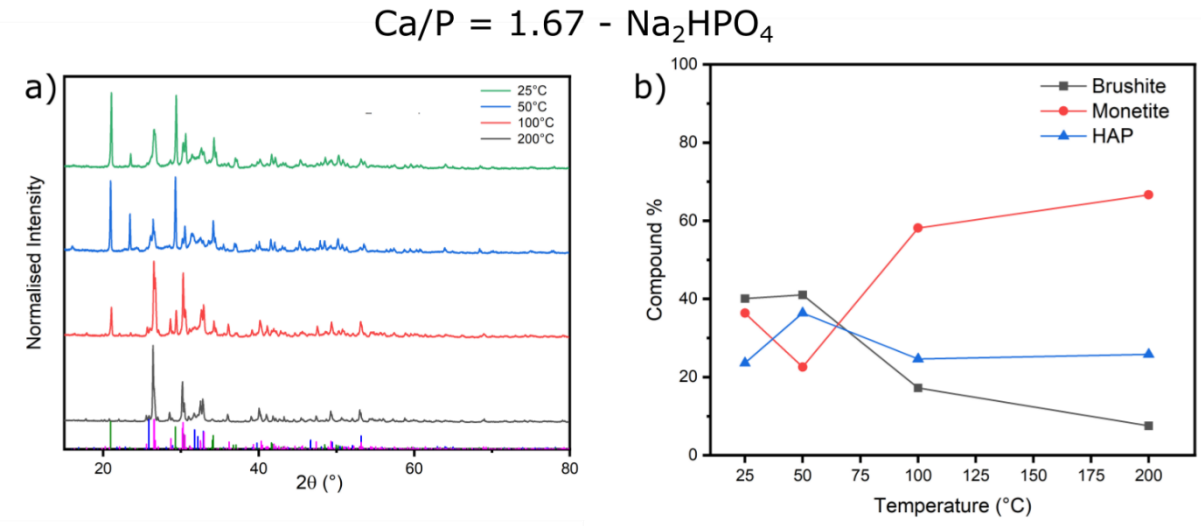

Figure 4.24. XRD patterns for Ca/P ratio 1.67 using Na_2HPO_4 as the phosphate precursor in the reaction. Vertical lines correspond to the position of the model patterns for HAP (blue), brushite (green) and monetite (pink). b) Sample composition as determined by Rietveld refinement of the samples.

The XRD patterns and the corresponding Rietveld refinement are shown in Figure 4.24 for the samples obtained at a Ca/P ratio = 1.67 and using monosodium hydrogen phosphate as the phosphate precursor. At 25°C features from brushite (40.1%), monetite (36.4%) and HAP (23.6%) are distinguished. Brushite is evidenced by the by two main peaks at 21° and 29° 2θ related to (021) and (041) orientations, respectively. Monetite main features are acknowledged from the peak around 26.5° 2θ corresponding to the mixing of (002) and (200) direction of monetite. And HAP is seen by the broad peak from 31 to 32° 2θ. So that all the three compounds show clear features at that temperature. At 50°C brushite (41.0%) characteristic peaks are kept constant although monetite (22.6%)

and hydroxyapatite (36.4%) presence in the sample is changed. At this condition, HAP related peaks grow in intensity while monetite feature at around 26.5° 2θ is lower when compared to room temperature. At 100°C monetite peaks are the most intense ones. The broad characteristic peak from HAP situated at the 31 – 32° region is still visible. Brushite (021) and (041) peaks, although with a lower intensity, are still defined. Finally at 200°C, monetite (66.6 %) peaks are more intense and crystalline, being the major component of the sample.

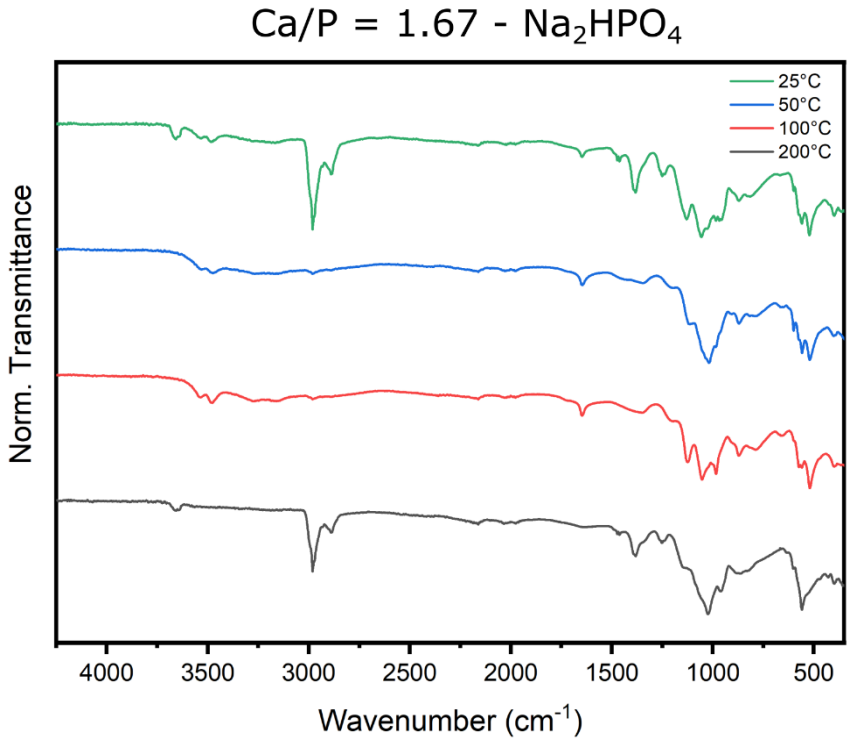

Figure 4.25. FTIR spectra for Ca/P ratio 1.67 using Na_2HPO_4 as the phosphate precursor in the reaction.

From Figure 4.25, room temperature, the peaks from FTIR are not very well defined but there is evidence of monetite presence. The main feature is situated at around 2850 cm^{-1} which corresponds to a hydroxyl stretching mode for monetite. Around 1400 cm^{-1} the monetite hydroxyl bending mode can be acknowledged. The phosphates modes are not clearly defined. It is explained by the presence of several different calcium orthophosphate minerals. There is expected to coexist several peaks situated in the same region and clustered. Brushite presence is justified by the water bands from 3000 to 3500 cm^{-1}. At 50°C the water features can be visualised showing that brushite is still part of the sample. Monetite hydroxyl main band at 2850 cm^{-1} fades away. On the other hand, at

the phosphate region (800 – 1200 cm^{-1}), although the features are not very detailed, a single growing peak can be acknowledged. It corresponds to the HAP v_3 phosphate mode. It justifies the trend shown on XRD where the presence of monetite is decreased as the HAP content increases with temperature. At 100°C the hydration water molecules for brushite are still present in the spectrum. The phosphates features are more defined although some presence of the single peak for HAP can be confirmed. From XRD data monetite characteristic peaks would be expected to be observed for this sample. But, as shown in previous spectra, FTIR is not as specific from monetite as for the rest of calcium orthophosphates. Finally, at 200°C the peak centred at 2850 cm^{-1} corresponds to a hydroxyl stretching mode for monetite. It shows the presence of monetite in the sample. The characteristics water bands for brushite are not clearly defined. In the phosphate region a single most intense peak at 1030 cm^{-1} is linked to the ν_3 phosphate mode for HAP.

4.3.1.7 Ca/P = 1.67 - $Na_2HPO_4 \cdot 7H_2O$ phosphate precursor buffered pH = 10

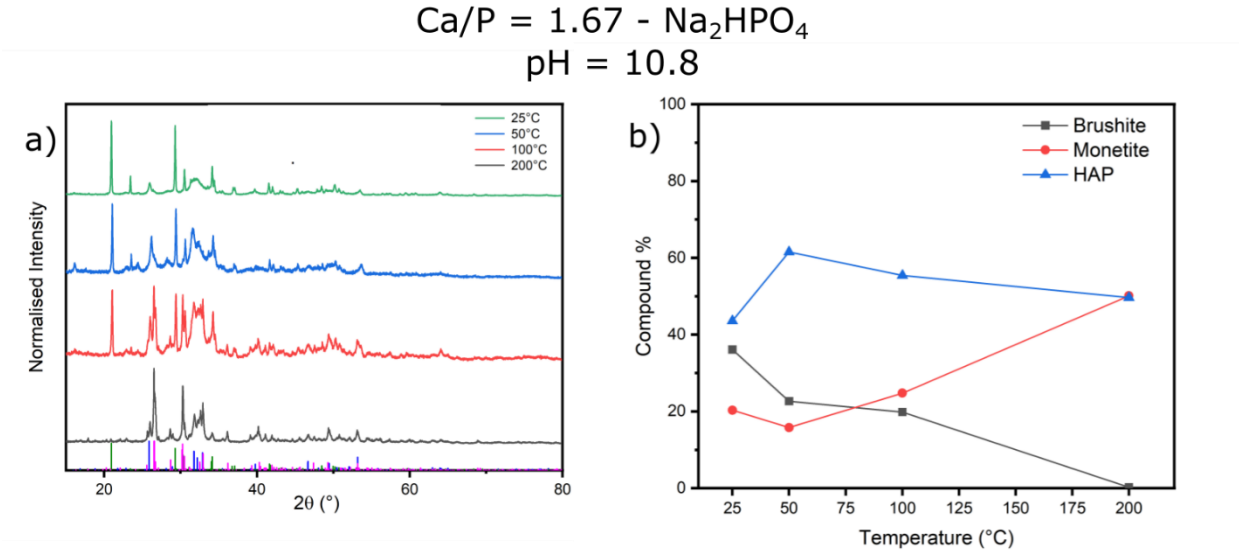

Figure 4.26. XRD patterns for Ca/P ratio 1.67 using Na_2HPO_4 as the phosphate precursor in the reaction, buffered to pH = 10.8. Vertical lines correspond to the position of the model patterns for HAP (blue), brushite (green) and monetite (pink). b) Sample composition as determined by Rietveld refinement of the samples.

From Figure 4.26, at room temperature, two different set of peaks can be observed. The most intense and crystalline ones correspond to brushite (36.1%), while

the broader ones are closely related with hydroxyapatite (43.6%). Brushite's characteristic features are two peaks at 21° and 29° 2θ related to (021) and (041) orientations. The characteristic broad HAP peak from 31 – 32° 2θ is observed as well. An additional feature for this calcium orthophosphate is a broad peak at around 25.7° 2θ which is related to the (002) plane. At 50°C the hydroxyapatite (61.5%) features a rise in intensity compared to the rest of the peaks corresponding to other calcium orthophosphates, brushite (22.7%) and monetite (15.8%). It shows an increase in presence of HAP at this temperature. At 100°C hydroxyapatite (55.4%) peaks are the most prominent maintaining that mentioned broader shape. Brushite (19.8%) peaks are still observed. Monetite (24.8%) start to gain importance evidenced by the peak around 26.5° 2θ related to the (200) and (002) planes of monetite. At 200°C monetite (50.1%) peaks increase, showing a sharper shape than HAP (49.7%) ones, although they have a similar presence in the sample.

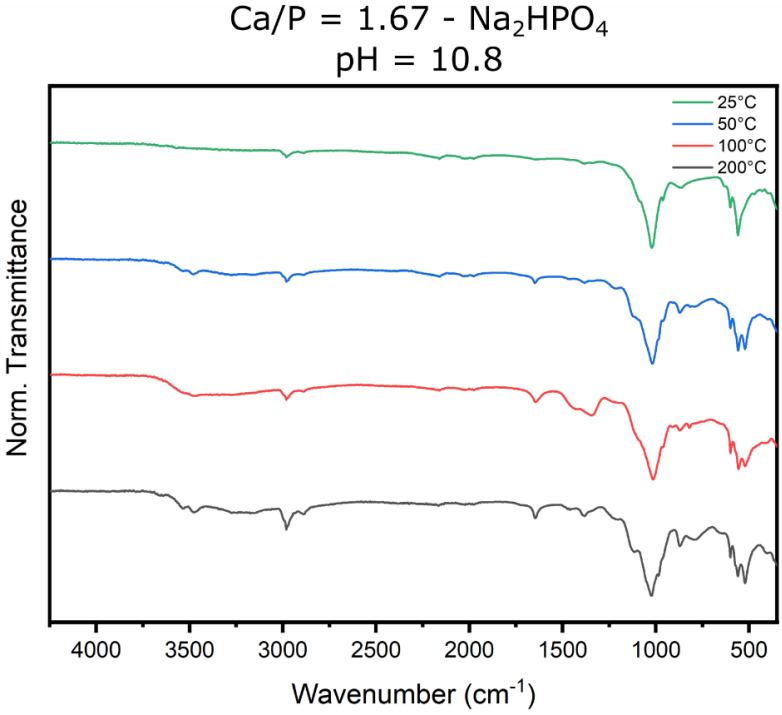

Figure 4.27. FTIR spectra for Ca/P ratio 1.67 using Na_2HPO_4 as the phosphate precursor in the reaction buffered to pH = 10.8 with NaOH.

From Figure 4.27. at room temperature the main feature is related to the presence of hydroxyapatite with a sharp peak around 1090 cm^{-1}. It corresponds to phosphate ν_3 mode for HAP. At 50°C the phosphate feature for HAP is maintained. Some broad peaks

are shown in the water-related region of the spectrum (3000 – 3500 cm^{-1}). It evidences the presence of water, closely related to brushite mineral. Although they can be discerned, the intensity is still low. The peak centred at 2850 cm^{-1} corresponds to a hydroxyl stretching mode for monetite. At 100°C the shapes described for the 50°C spectrum are kept constant, showing a similar composition for the sample. At 200°C HAP features are kept similar to the previous ones, though the monetite hydroxyl peak at 2850 cm^{-1} increases in intensity. Although from the XRD calculations there is a low presence of brushite in the sample, the broad water related peaks (3000 – 3500 cm^{-1}) are observed in the sample with low intensity.

4.3.2 PCA Analysis of the XRD patterns

So far, the samples have been analysed by XRD and FTIR. Additionally, the percentage of the compounds forming each one has been calculated by Rietveld refinement. Nonetheless, due to the large amount of data processed in which different synthetic parameters influence the outcome, such as temperature, ratio and precursor, the data needs to be simplified to show any kind of trend in a simple way.

Principal Component Analysis (PCA) is a powerful statistical transformation of the data, capable of distinguishing and reducing the variables or dimensions that comprises a measurement. Given the XRD patterns that we will subject to analysis, it can be understood as the mix of different variables or dimensions loaded in a different percentage to make the whole pattern observed. The difference between two patterns will rely on the variability that each single parameter gives to the final picture. For example, XRD will depend on the compounds present, showing characteristic peak positions which will give the variability to the final diffraction pattern. Nonetheless, there are some other factors such as peak shifting due to external effects (*e.g.* sample loading) or internal effects (strain). Broadening is an aspect that can change the overall shape of the patterns and it is mainly due to the size of the particles conforming the sample. All these factors are defined in this analysis as directions or components. PCA defines what components give a maximal variation of the data. By defining the most important directions the data can be expressed in a few variables instead of the initial thousands. It helps to generate a shorter, significant, dataset, that when it is plotted its conversion is clear and relevant enough to show differences and similitudes between samples.

From our samples, PCA which will estimate what set of parameters gives the most variability to the patterns and rate them in percentages. The first step will be getting rid of the redundant information of the patterns, as it gives zero variability, and then it establishes the different “Principal Components” (PCs) that shape the XRD. The most redundant information in the calcium orthophosphate patterns are brushite peaks. It is the compound that is present in a larger percentage in the most samples obtained.

Table 4.6. Three main Principal Components Analysed

Number of Principal Component (PC)	Percentage of Variance (%)	Cumulative (%)
1	55.12426	55.12426
2	21.10233	76.22658
3	9.25577	85.48235

From Table 4.6 the two main Principal Components percentages (PC) are PC1 (55.12%) and PC2 (21.10%). The combination of both components gives an overall of 76.22% of the total variability of the XRDs. Once the importance of them is rated, it is necessary to define what the real physical significance of the principal components is.

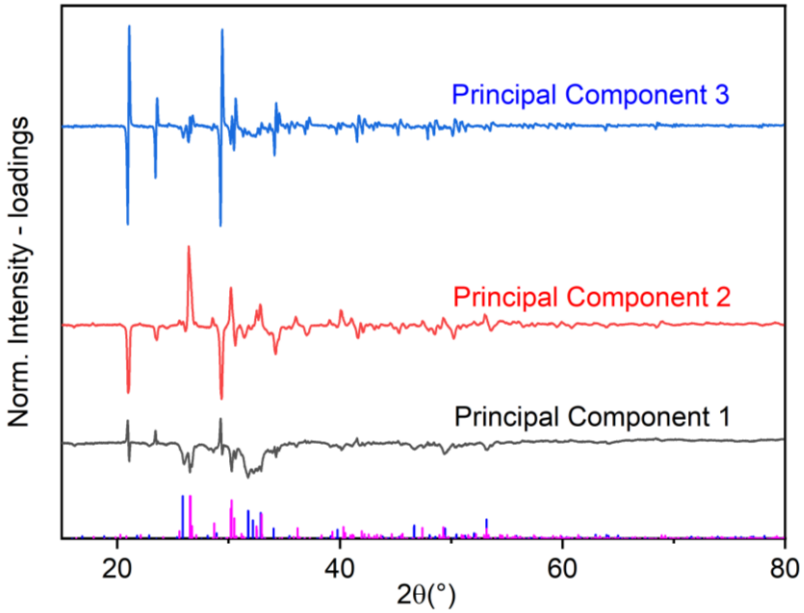

Figure 4.28. Principal components (PC) plot. The vertical lines below represent the XRD position of two calcium orthophosphates, HAP (blue) and monetite (pink).

In Figure 4.28 the three main PCs are plotted along with the peak position of the two more "unique" calcium orthophosphates present in the samples synthesised. By the shape and position of the features in the plots PC1 corresponds mainly to HAP. PC2 corresponds mainly to monetite peak positions in the XRD. This denotes that the variability expressed by those PCs are closely related to the presence of that compound in the XRD pattern. Therefore, the higher the variability expressed by that PC, at that sample the higher amount of that compound is present.

PC3 does not correspond to any XRD pattern for the calcium orthophosphates but to the position of the peaks. The plot consists of "derivate-like" peaks which are

symmetric at both sides of the axis. This shape classically corresponds to peak shifting. When some of the samples move towards right or left the difference pattern will show this kind of characteristic peaks, as shown in Figure 4.29.

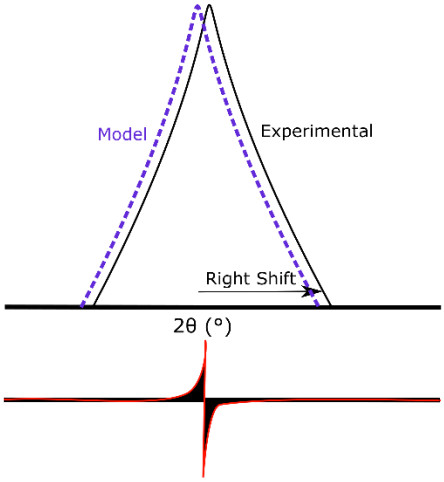

Figure 4.29. Representation of the difference between the experimental (black) and expected (purple) peak position.

Nonetheless, this asymmetry corresponding to the shifting of the peaks only comprises the 9% of the total variance of the sample. So, it can be concluded that there is no major loss of information when only PC1 and PC2 are considered.

When PCA is plotted, by convention, the *x*-axis corresponds to the magnitude that gives the largest variability of the sample, therefore PC1. Secondly, the *y*-axis is linked to the second largest, PC2. Therefore, along the *x*-axis HAP content will be represented and at the *y*-axis, monetite. Finally, the samples clustered around (0,0) will be related to the presence of brushite, giving the least amount of variability as shown in Figure 4.30.

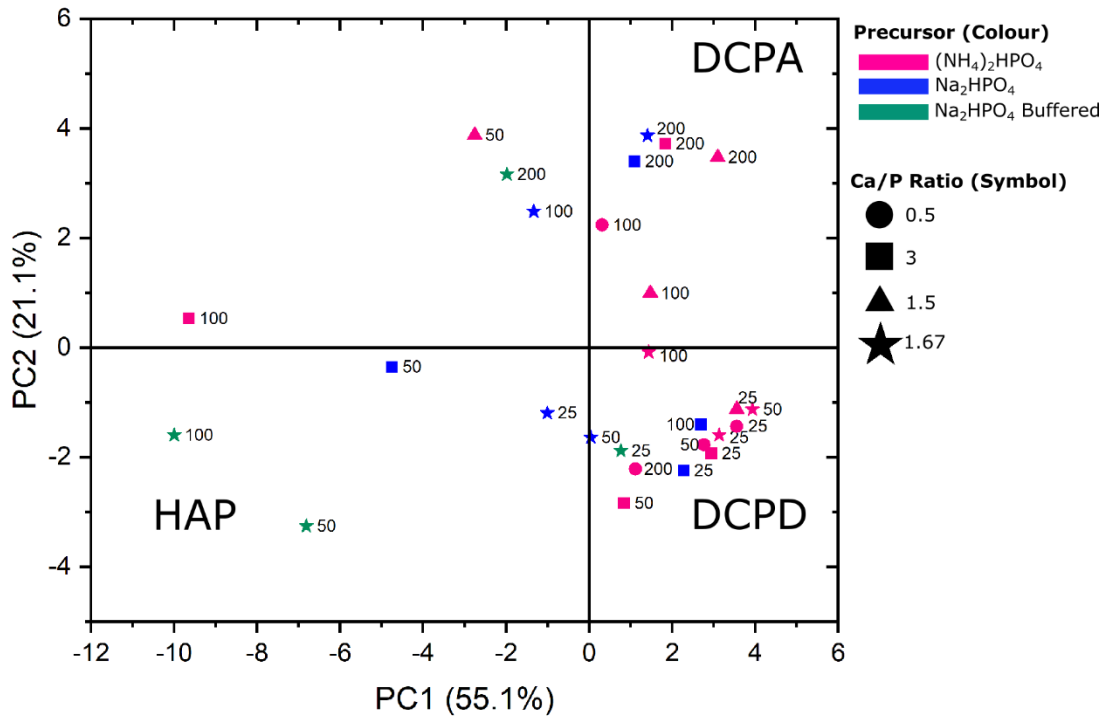

Figure 4.30.Principal Component Analysis of the normalised XRD patterns of the calcium orthophosphates. The numbers next to the data points represent the temperature of synthesis. The colour the precursor used for the synthesis and the symbols the Ca/P ratio, as shown in the legend. Brushite is referred as DCPD and monetite as DCPA.

It is worth mentioning that the relative position from an axis and the compound percentage calculated is not necessary linearly related. PCA is capable of giving trends and significant relationship between variables but not absolute numbers. Therefore, when doing a PCA of the XRD patterns a previous Rietveld refinement is required to corroborate the percentage of the compound or the polymorph present in the sample and obtaining the real percentages to justify the trends observed. Anyway, when looking at the dataset from Rietveld and the PCA graph it can be seen that the relative position to the axis is related to the percentage of the compound in the sample at those conditions, so it is a valid representation to obtain trends.

From Figure 4.30 it is evident that the vast majority of the samples are clustered around the centre of the axis, at the brushite corner. The second largest number of samples is situated along the *y*-axis and the rest along the *x*-axis. It means that although HAP is giving the most variability to the patterns, a lower number of those samples show HAP features, as previously suggested by XRD and Rietveld refinement.

Brushite is mainly seen at low temperature samples, 25°C. No room temperature samples are observed in the other corners. A similar trend is observed for 50°C where, although it shows a higher presence of the rest of calcium orthophosphates, 4 out of 6 of the samples at that temperature are closer to brushite corner.

For 100°C there is a change in behaviour. Only two samples are seen at brushite area for that temperature. They are plotted either at monetite or HAP zones. The highest presence of HAP is seen at that temperature, only showing milder conditions in that corner (50 and 100°C). It supports the idea that hydroxyapatite is preferably obtained at milder conditions, whereas DPCA is obtained at higher temperatures evidenced by its presence in a larger number of 200°C samples. The correlation of the temperature of synthesis and their relative position in the PCA plotting is highlighted in Figure 4.31. It serves to demonstrate the higher temperature expressed by the red colour to obtain monetite and the milder temperatures required to yield HAP.

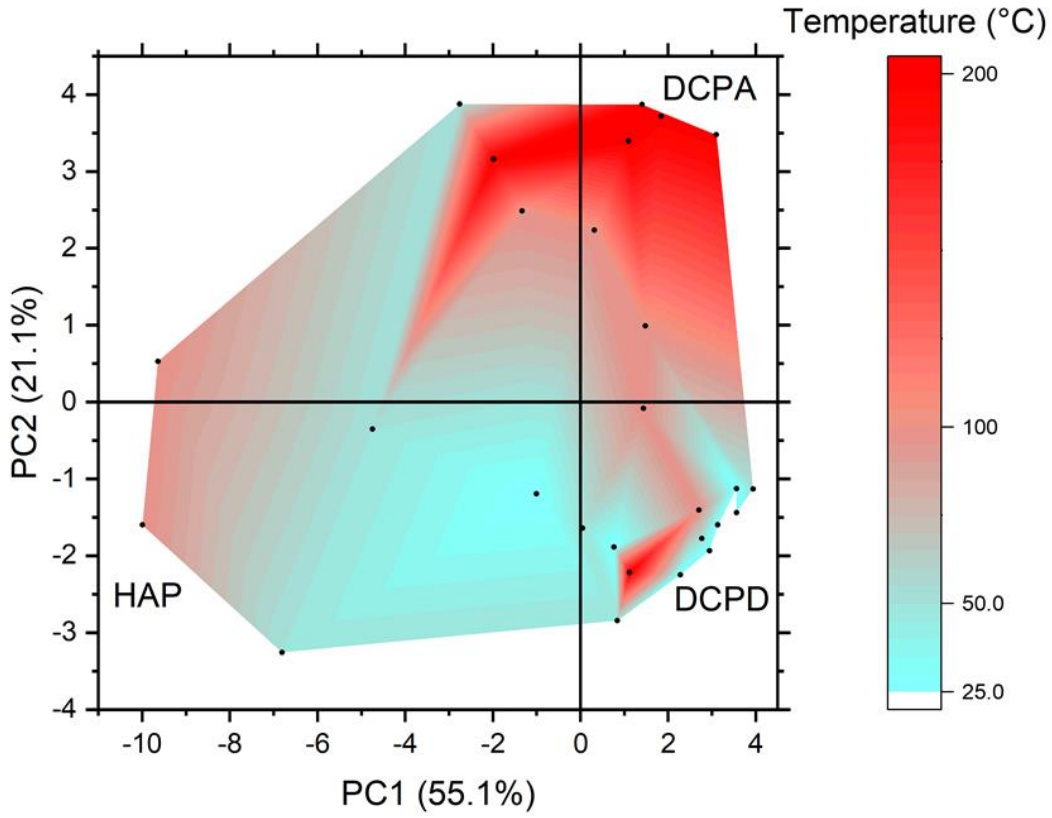

Figure 4.31. Heat-map of the linearly temperature distribution for PCA. This figure shows graphically the temperature distribution in PCA for different compounds. The black dots represent the sample positions where the data is extracted. Ca/P and precursor selection is excluded from this graph. Brushite is referred as DCPD and monetite as DCPA.

Once the effect of the temperature is described, the calcium orthophosphate selection related to the precursor used, must be described. For ammonium hydrogen phosphate, $(NH_4)_2HPO_4$, there is a trend to yield either brushite at lower temperatures or monetite at higher ones. Only one sample has a significant presence of HAP at intermediate temperatures, 100°C. The pH measured for this precursor at a concentration 0.45M is 8, having a typical buffer range at pH 7.5 – 8. Therefore, after the incorporation of a salt like $Ca(NO_3)_2$ the pH change must be minimal. HAP at the precise ratio (Ca/P = 1.67) or higher must be seen as it is suggested by Figure 4.4. Nonetheless, no HAP or very little is seen in these samples. A similar effect is seeing when incorporating Na_2HPO_4. On the other hand, when the pH of the phosphate solution is forced above the buffer limit of the solution by using a strong base like NaOH reaching pH = 10, HAP is the major component at intermediate temperatures.

Finally, the Ca/P ratio used for the synthesis will play an important role at the compound selection. To explore this factor the Ca/P ratios chosen were 0.5, 1.5, 1.67 and 3. Firstly it is worth mentioning that the formation of monetite and brushite does not seem to depend as much on the ratio employed, while it is critical for yielding HAP. The exact ratio at which hydroxyapatite is often reported to be formed is at the stoichiometric 1.67. The Ca/P ratio chosen is not relevant for the formation of brushite, as it was obtained at every calcium to phosphate ratio attempted. On the other hand, monetite and, specially, HAP show a more selective behaviour around the ratio of formation. Ca/P = 0.5 mainly forms brushite compounds. When it is increased to close-to-stoichiometric conditions for HAP at Ca/P = 1.5 there is a larger selection of monetite formation. Finally, hydroxyapatite is only formed at the stoichiometric or calcium-in-excess conditions for Ca/P ratio of 1.67 and 3.

To sum up, brushite is the major component in the largest number of samples, being the major component overall. Monetite is mainly obtained at high temperatures, such as 200°C and higher ratios are preferred for the formation of monetite, from Ca/P = 1.5 onwards. Finally, hydroxyapatite is the compound with the narrowest accessibility range from the three compounds encountered at temperatures of 50 and 100°C. The Ca/P required for the formation of this orthophosphate acts as the major selective factor only observed at stoichiometric or over-stoichiometric conditions, Ca/P = 1.67 and 3.

A summary of the results for the different compounds relating the ratio of synthesis, temperature, the compound formed and the morphology exhibited is given in Table 4.7.

Table 4.7. Phosphate reactions conditions with the corresponding mineral percentage calculated by Rietveld refinement. The morphology of the samples are described for the selected conditions that were SEM imaged.

PO_4^{3-} Source	Ca/P Ratio	T (ºC)	Brushite (%)	Monetite (%)	Hydroxyapatite (%)	Morphology from SEM
$(NH_4)_2HPO_4$	0.5	25	77.09	5.6308	17.279	Random oriented platelets
		50	65.885	7.0557	27.059	
		100	26.596	58.666	14.738	Pinacoidal and not-well defined rod-shaped particles
		200	53.674	10.678	35.648	Brushite platelets and directional rod- and whisker-like HAP
	1.5	25	77.089	17.047	5.8644	
		50	2.8983	57.13	39.972	
		100	39.847	45.58	14.573	
		200	3.1851	76.65	20.165	
	1.67	25	67.483	11.079	21.438	
		50	78.8	11.851	9.2774	
		100	44.351	31.333	24.316	
	3	25	86.684	5.6551	7.6605	
		50	57.058	2.5278	40.414	
		100	3.2922	18.439	78.269	
		200	3.8717	73.521	22.607	
Na_2HPO_4	1.67	25	40.11	36.37	23.618	
		50	41.032	22.575	36.393	
		100	17.222	58.151	24.627	
		200	7.5276	66.648	25.825	
	1.67 (pH 10.8)	25	36.102	20.324	43.574	
		50	22.666	15.79	61.543	
		100	19.832	24.753	55.415	
		200	0.23205	50.117	49.65	
	3	25	77.964	8.3793	13.657	
		50	31.216	36.67	32.114	Rod-particles randomly organised t-plate type brushite
		100	66.631	16.762	16.607	
		200	1.3211	49.602	49.077	Well-defined rods

4.4 Conclusions and Future Work

Various calcium orthophosphates have been effectively synthesised by using the hydrothermal injection reactor designed by the Dunne group. It was possible to obtain three different calcium orthophosphates when varying the synthetic conditions: temperature, Ca/P ratio, phosphate precursor and pH. The minerals obtained were brushite, monetite and hydroxyapatite. The XRD and FTIR of the samples suggest a preferred synthesis of the hydrated compound, brushite, at lower temperatures. Monetite obtention on the other hand, is enhanced at higher temperatures. Finally, the formation of HAP is closely related to the Ca/P ratio of the precursors employed. Hydroxyapatite exhibits a specific ratio of calcium to phosphate equal to 1.67. This compound was only encountered at that ratio or higher of calcium to phosphate. Nonetheless, the samples showed the presence two or more species regardless of the conditions employed. Although XRD and FTIR are sufficient to recognise the presence of the different minerals, they are qualitative techniques. Rietveld refinements with preferential orientation correction of the XRD patterns was carried out to quantitively demonstrate the presence of the different calcium orthophosphates.

Due to the number of samples obtained, driven by the number of synthetic conditions that were tuned for the different reactions, extracting trends is extremely challenging by comparison of the different XRD patterns or the Rietveld refinement. The statistical technique Principal Component Analysis was carried out to plot the presence of the different phosphates in relation to their synthetic conditions. The XRD patterns were subjected to this analysis. From PCA it can be established that the position of the XRD patterns for the different phosphates accounts for 76% of the total variability of the XRD patterns. Brushite pattern was the most redundant for the information load, as it is obtained for the largest number of synthetic conditions. Secondly, HAP features are the ones that give the maximum variability of the XRD patterns, defined as PC1. When observing the PCA plot this compound's presence is restricted to Ca/P $\geq$ 1.67. Intermediate temperatures are required for its synthesis (50 – 100°C). Finally, the synthesis of monetite is preferred when the synthesis is carried out at higher temperatures and higher ratios. From this analysis, PCA has proven to be a powerful tool for the analysis of large sets of XRD patterns in order to reveal the relationship between the

different synthetic conditions and the samples that can be yielded. The optimum synthetic conditions for the formation of the different calcium orthophosphates were described.

From the SEM images it is highlighted that brushite shows poorly defined particles, apparently formed from non-oriented platelets creating networks within the structure. Monetite is shown to form more directional structures intermediate between plates and rods. Finally, hydroxyapatite shows the more defined shapes for the calcium orthophosphates exhibiting some whisker- and rod-like particles, perfectly evidenced by the anisotropic behaviour of its XRD peak intensities.

Although a great number of conditions were attempted, once the optimum conditions for the formation of the different calcium orthophosphates have been proved, more variability can be introduced in the system. The injection of the phosphate precursor to the pre-heated solution of calcium can be attempted to test how the system behaves when the availability of the calcium is greater when the phosphates is injected, increasing the saturation of calcium in solution at the first stages of nucleation. Secondly, different precursors of calcium and phosphate can be introduced in the system in order to identify how the different nature of the precursors interplay with the phosphate selection when they get formed. Thirdly, HAP can be obtained at a second step. The formation of HAP from the reaction of calcium carbonate with phosphate sources such as phosphoric acid reacting with a calcium carbonate colloid has been reported.[88] Additionally the reaction of solid calcium carbonate with different phosphates such as ammonium dihydrogen phosphate has been also published.[89] Therefore, the different polymorphs of calcium carbonate can react with phosphates to yield apatites. It might serve as a great test to prove how the system evolved in these processes in nature. There is extensive research on the doping of phosphate materials for biomedical applications,[90] *e.g. in vivo* observation of the bones by replacing calcium with rare earth metals. It can be tested in the reactor, by choosing the best conditions for the formation of these new materials and later testing their properties.

4.5 References

1 J. Mahamid, A. Sharir, L. Addadi and S. Weiner, *Proc. Natl. Acad. Sci. U. S. A.*, 2008, **105**, 12748–12753.
2 S. Boonrungsiman, E. Gentleman, R. Carzaniga, N. D. Evans, D. W. McComb, A. E. Porter and M. M. Stevens, *Proc. Natl. Acad. Sci. U. S. A.*, 2012, **109**, 14170–14175.
3 M. Kerschnitzki, A. Akiva, A. Ben Shoham, Y. Asscher, W. Wagermaier, P. Fratzl, L. Addadi and S. Weiner, *J. Struct. Biol.*, 2016, **195**, 82–92.
4 R. Gelli, F. Ridi and P. Baglioni, *Adv. Colloid Interface Sci.*, 2019, **269**, 219–235.
5 S. V. Dorozhkin and M. Epple, *Angew. Chemie Int. Ed.*, 2002, **41**, 3130–3146.
6 K. Pajor, L. Pajchel and J. Kolmas, *Materials (Basel).*, 2019, **12**, 2683.
7 L. Wang and G. H. Nancollas, *Chem. Rev.*, 2008, **108**, 4628–4669.
8 P. Bodier-Houllé, P. Steuer, J.-C. Voegel and F. J. G. Cuisinier, *Acta Crystallogr. Sect. D Biol. Crystallogr.*, 1998, **54**, 1377–1381.
9 W. J. E. M. Habraken, J. Tao, L. J. Brylka, H. Friedrich, L. Bertinetti, A. S. Schenk, A. Verch, V. Dmitrovic, P. H. H. Bomans, P. M. Frederik, J. Laven, P. van der Schoot, B. Aichmayer, G. de With, J. J. DeYoreo and N. A. J. M. Sommerdijk, *Nat. Commun.*, 2013, **4**, 1507.
10 X. Y. Liu and S. W. Lim, *J. Am. Chem. Soc.*, 2003, **125**, 888–895.
11 S. Jiang, Y. Chen, H. Pan, Y. J. Zhang and R. Tang, *Phys. Chem. Chem. Phys.*, 2013, **15**, 12530–12533.
12 S. Jiang, H. Pan, Y. Chen, X. Xu and R. Tang, *Faraday Discuss.*, 2015, **179**, 451–461.
13 J. F. Banfield, S. A. Welch, H. Zhang, T. T. Ebert and R. L. Penn, *Science*, 2000, **289**, 751–754.
14 H. Cölfen and S. Mann, *Angew. Chemie - Int. Ed.*, 2003, **42**, 2350–2365.
15 A. Lotsari, A. K. Rajasekharan, M. Halvarsson and M. Andersson, *Nat. Commun.*, 2018, **9**, 4170.
16 S. V. Dorozhkin, *Prog. Biomater.*, 2016, **5**, 9–70.
17 D. Gebauer, *Science*, 2008, **120**, 1819–1823.
18 G. De With and N. A. J. M. Sommerdijk, *Science*, 2009, **587**, 2007–2010.
19 M. Faatz, F. Gröhn and G. Wegner, *Adv. Mater.*, 2004, **16**, 996–1000.
20 L. Addadi, S. Raz and S. Weiner, *Adv. Mater.*, 2003, **15**, 959–970.
21 S. V. Dorozhkin, *Acta Biomater.*, 2010, **6**, 4457–4475.
22 G. Mancardi, C. E. Hernandez Tamargo, D. Di Tommaso and N. H. De Leeuw, *J. Mater. Chem. B*, 2017, **5**, 7274–7284.
23 E. D. Eanes, in *Calcium Phosphates in Biological and Industrial Systems*, Springer US, Boston, MA, 1998, vol. 8, pp. 21–39.
24 G. Treboux, P. Layrolle, N. Kanzaki, K. Onuma and A. Ito, *J. Phys. Chem. A*, 2000, **104**, 5111–5114.
25 A. Dey, P. H. H. Bomans, F. A. Müller, J. Will, P. M. Frederik, G. De With and N. A. J. M. Sommerdijk, *Nat. Mater.*, 2010, **9**, 1010–1014.
26 M. L. Watson and R. A. Robinson, *Am. J. Anat.*, 1953, **93**, 25–59.
27 S. V. Dorozhkin, *Int. J. Mater. Chem.*, 2012, **2**, 19–46.
28 A. J. Hoeher, S. T. Mergelsberg, O. J. Borkiewicz and F. M. Michel, *Cryst. Growth Des.*, 2021, **21**, 3736–3745.
29 N. C. Blumenthal, F. Betts and A. S. Posner, *Calcif. Tissue Res.*, 1977, **23**, 245–250.
30 W. Kibalczyc, J. Christoffersen, M. R. Christoffersen, A. Zielenkiewicz and W. Zielenkiewicz, *J. Cryst. Growth*, 1990, **106**, 355–366.
31 J. D. Termine and A. S. Posner, *Arch. Biochem. Biophys.*, 1970, **140**, 307–317.
32 N. C. Blumenthal, A. S. Posner and J. M. Holmes, *Mater. Res. Bull.*, 1972, **7**, 1181–1189.
33 O. Bertran, L. J. Del Valle, G. Revilla-López, M. Rivas, G. Chaves, M. T. Casas, J. Casanovas, P. Turon, J. Puiggalí and C. Alemán, *Chem. - A Eur. J.*, 2015, **21**, 2537–2546.
34 J. Christoffersen, M. R. Christoffersen, W. Kibalczyc and F. A. Andersen, *J. Cryst. Growth*, 1989, **94**, 767–777.
35 M. S. A. Johnsson and G. H. Nancollas, *Crit. Rev. Oral Biol. Med.*, 1992, **3**, 61–82.
36 D. Haverty, S. A. M. Tofail, K. T. Stanton and J. B. McMonagle, *Phys. Rev. B*, 2005, **71**, 094103.
37 M. I. Kay, R. A. Young and A. S. Posner, *Nature*, 1964, **204**, 1050–1052.

38 H. El Briak-BenAbdeslam, M. P. Ginebra, M. Vert and P. Boudeville, *Acta Biomater.*, 2008, **4**, 378–386.
39 I. Grigoraviciute-Puroniene, Y. Tanaka, V. Vegelyte, Y. Nishimoto, K. Ishikawa and A. Kareiva, *Ceram. Int.*, 2019, **45**, 15620–15623.
40 M. Markovic, B. O. Fowler and M. S. Tung, *J. Res. Natl. Inst. Stand. Technol.*, 2004, **109**, 553.
41 A. Bigi, E. Boanini and K. Rubini, *J. Solid State Chem.*, 2004, **177**, 3092–3098.
42 K. Sasaki, K. Toshiyuki, K. Ideta, H. Miki, T. Hirajima, J. Miyawaki, M. Murayama and I. Dabo, *J. Environ. Chem. Eng.*, 2016, **4**, 1092–1101.
43 Y. Sun, G. Guo, D. Tao and Z. Wang, *J. Phys. Chem. Solids*, 2007, **68**, 373–377.
44 J. Coreño A., O. Coreño A., J. J. Cruz R. and C. Rodríguez C., *Opt. Mater. (Amst).*, 2005, **27**, 1281–1285.
45 L. Y. Cao, C. B. Zhang and J. F. Huang, *Ceram. Int.*, 2005, **31**, 1041–1044.
46 M. Yoshimura and K. Byrappa, *J. Mater. Sci.*, 2008, **43**, 2085–2103.
47 F. Chen, Y.-J. Zhu, K.-W. Wang and K.-L. Zhao, *CrystEngComm*, 2011, **13**, 1858–1863.
48 D. K. Lee, J. Y. Park, M. R. Kim and D.-J. Jang, *CrystEngComm*, 2011, **13**, 5455.
49 E. Lester, S. V. Y. Tang, A. Khlobystov, V. L. Rose, L. Buttery and C. J. Roberts, *CrystEngComm*, 2013, **15**, 3256.
50 M.-G. Ma, Y.-J. Zhu and J. Chang, *Mater. Lett.*, 2008, **62**, 1642–1645.
51 L. X. Yang, J. J. Yin, L. L. Wang, G. X. Xing, P. Yin and Q. W. Liu, *Ceram. Int.*, 2012, **38**, 495–502.
52 A. Aminian, M. Solati-Hashjin, A. Samadikuchaksaraei, F. Bakhshi, F. Gorjipour, A. Farzadi, F. Moztarzadeh and M. Schmücker, *Ceram. Int.*, 2011, **37**, 1219–1229.
53 M. Sadat-Shojai, M. T. Khorasani and A. Jamshidi, *J. Cryst. Growth*, 2012, **361**, 73–84.
54 K. Lin, Y. Zhou, Y. Zhou, H. Qu, F. Chen, Y. Zhu and J. Chang, *J. Mater. Chem.*, 2011, **21**, 16558–16565.
55 R. Zhu, R. Yu, J. Yao, D. Wang and J. Ke, *J. Alloys Compd.*, 2008, **457**, 555–559.
56 D. Gopi, S. Ramya, D. Rajeswari, P. Karthikeyan and L. Kavitha, *Colloids Surfaces A Physicochem. Eng. Asp.*, 2014, **451**, 172–180.
57 Y. Zhu, L. Xu, C. Liu, C. Zhang and N. Wu, *AIP Adv.*, 2018, **8**, 085221.
58 J. Liu, X. Ye, H. Wang, M. Zhu, B. Wang and H. Yan, *Ceram. Int.*, 2003, **29**, 629–633.
59 H. Zhang and B. W. Darvell, *Acta Biomater.*, 2011, **7**, 2960–2968.
60 J. S. Earl, D. J. Wood and S. J. Milne, *J. Phys. Conf. Ser.*, 2006, **26**, 268–271.
61 H. Zhang and B. W. Darvell, *J. Am. Ceram. Soc.*, 2011, **94**, 2007–2013.
62 B. Viswanath and N. Ravishankar, *Biomaterials*, 2008, **29**, 4855–4863.
63 M. Yoshimura, P. Sujaridworakun, F. Koh, T. Fujiwara, D. Pongkao and A. Ahniyaz, *Mater. Sci. Eng. C*, 2004, **24**, 521–525.
64 X. Guo, P. Xiao, J. Liu and Z. Shen, *J. Am. Ceram. Soc.*, 2005, **88**, 1026–1029.
65 S. C. J. Loo, Y. E. Siew, S. Ho, F. Y. C. Boey and J. Ma, *J. Mater. Sci. Mater. Med.*, 2008, **19**, 1389–1397.
66 N. A. Curry and D. W. Jones, *J. Chem. Soc. A Inorganic, Phys. Theor.*, 1971, 3725.
67 A. A. Mirtchi, J. Lemaitre and N. Terao, *Biomaterials*, 1989, **10**, 475–480.
68 A. A. Mirtchi, J. Lemaître and E. Hunting, *Biomaterials*, 1989, **10**, 634–638.
69 A. A. Mirtchi, J. Lemaître and E. Munting, *Biomaterials*, 1991, **12**, 505–510.
70 F. Tamimi, Z. Sheikh and J. Barralet, *Acta Biomater.*, 2012, **8**, 474–487.
71 F. Tamimi, J. Torres, C. Kathan, R. Baca, C. Clemente, L. Blanco and E. L. Cabarcos, *J. Biomed. Mater. Res. Part A*, 2008, **87A**, 980–985.
72 J. Aberg, H. Brisby, H. B. Henriksson, A. Lindahl, P. Thomsen and H. Engqvist, *J. Biomed. Mater. Res. Part B Appl. Biomater.*, 2010, **93B**, 436–441.
73 A. C. Tas and S. B. Bhaduri, *J. Am. Ceram. Soc.*, 2004, **87**, 2195–2200.
74 M. Hamdan Alkhraisat, C. Moseke, L. Blanco, J. E. Barralet, E. Lopez-Carbacos and U. Gbureck, *Biomaterials*, 2008, **29**, 4691–4697.
75 S. Graulis, D. Chateigner, R. T. Downs, A. F. T. Yokochi, M. Quirós, L. Lutterotti, E. Manakova, J. Butkus, P. Moeck and A. Le Bail, *J. Appl. Crystallogr.*, 2009, **42**, 726–729.
76 L. I. Ardanova, E. I. Get'man, S. N. Loboda, V. V. Prisedsky, T. V. Tkachenko, V. I. Marchenko, V. P. Antonovich, N. A. Chivireva, K. A. Chebishev and A. S. Lyashenko, *Inorg. Chem.*, 2010, **49**, 10687–10693.
77 M. Espanol, J. Portillo, J.-M. Manero and M.-P. Ginebra, *CrystEngComm*, 2010, **12**, 3318.
78 C. I. Sainz-Díaz, A. Villacampa and F. Otálora, *Am. Mineral.*, 2004, **89**, 307–313.

79 M. Catti, G. Ferraris and S. A. Mason, *Acta Crystallogr. Sect. B Struct. Crystallogr. Cryst. Chem.*, 1980, **36**, 254–259.
80 A. C. Larson and R. B. Von Dreele, *Los Alamos Natl. Lab. Rep.*, 2000.
81 B. H. Toby, *J. Appl. Crystallogr.*, 2001, **34**, 210–213.
82 L. Tortet, J. R. Gavarri, G. Nihoul and A. J. Dianoux, *J. Solid State Chem.*, 1997, **132**, 6–16.
83 J. Chen, J. Liu, H. Deng, S. Yao and Y. Wang, *Ceram. Int.*, 2020, **46**, 2185–2193.
84 R. N. Panda, M. F. Hsieh, R. J. Chung and T. S. Chin, *J. Phys. Chem. Solids*, 2003, **64**, 193–199.
85 M. A. Miller, M. R. Kendall, M. K. Jain, P. R. Larson, A. S. Madden and A. C. Tas, *J. Am. Ceram. Soc.*, 2012, **95**, 2178–2188.
86 B. Jokić, M. Mitrić, V. Radmilović, S. Drmanić, R. Petrović and D. Janaćković, *Ceram. Int.*, 2011, **37**, 167–173.
87 K. Suchanek, A. Bartkowiak, M. Perzanowski and M. Marszałek, *Sci. Rep.*, 2018, **8**, 15408.
88 M. Sawada, K. Sridhar, Y. Kanda and S. Yamanaka, *Sci. Rep.*, 2021, **11**, 11546.
89 D. Pham Minh, N. Lyczko, H. Sebei, A. Nzihou and P. Sharrock, *Mater. Sci. Eng. B*, 2012, **177**, 1080–1089.
90 I. A. Neacsu, A. E. Stoica, B. S. Vasile and E. Andronescu, *Nanomaterials*, 2019, **9**, 239.
91 B. Lafuente, T. D. R, H. Yang and S. N, *The power of databases: the RRUFF project*, Mineralogical Crystallography, Berlin, Germany, 2015.
92 J. Xu, I. S. Butler and D. F. R. Gilson, *Spectrochim. Acta Part A Mol. Biomol. Spectrosc.*, 1999, **55**, 2801–2809.
93 S. Koutsopoulos, *J. Biomed. Mater. Res.*, 2002, **62**, 600–612.

Chapter 5. Hydrothermal Injection for the Phase-Controlled Synthesis of Calcium Carbonate

5.1 Introduction

Calcium carbonate ($CaCO_3$) is a naturally occurring material studied widely due to its importance in geological processes and its medical and industrial applications. The huge flexibility of this material lies, in part, in its polymorphism — the ability of the substance to form solids with different crystal structures — and consequently the different properties and behaviours that they exhibit. Calcium carbonate can be found in three different anhydrous ploymorphs:[1,2] calcite, aragonite and vaterite in decreasing order of stability;[3] as well as hydrated versions such as ikaite ($CaCO_3 \cdot 6H_2O$), which is naturally found in polar areas (only stable at lower temperatures than 5 °C),[4] and monohydrocalcite ($CaCO_3 \cdot H_2O$) [5–7] that is formed in Mg-rich environments.[8] Vaterite is known to be the least thermodynamically stable anhydrous polymorph,[9] appearing as a metastable conformation. Calcite, on the other hand, is the thermodynamically favoured structure.[10] Aragonite formation is not as well-known as for calcite, but it plays huge role in biomineralisation.[11–15]

In addition to the crystalline phases, amorphous calcium carbonate (ACC) is also known. Even though it is not strictly classed as a polymorph it has been reported to be critical in geological and biological processes.[11,16–20] The crystal structures, and selected crystallographic data of the anhydrous $CaCO_3$ polymorphs, calcite, vaterite, and aragonite are given below in Figure 5.1 and Table 5.1.

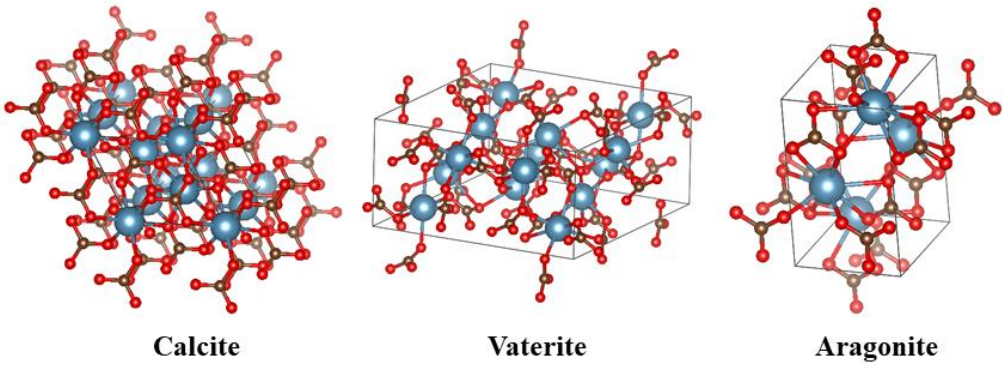

Figure 5.1. Calcium carbonate anhydrous phases structure models (calcite, vaterite and aragonite).

Table 5.1.Selected crystallographic data of the polymorphs.[21–23]

Polymorph	Calcite	Vaterite	Aragonite
Space Group	$R\bar{3}c$	$C2/c$	$Pmcn$
Lattice Parameter a(Å)	4.98760	12.17000	4.96183
Lattice Parameter b (Å)	4.98760	7.12000	7.96914
Lattice Parameter c (Å)	17.05750	9.47000	5.74285
Unit-cell Volume ($Å^3$)	367.476219	722.025649	227.081102

Calcium carbonate mineralisation occurs in geological environments. From that perspective, it is studied as a geomineralisation component, with applications including use as a trapping material for uranium in groundwaters[24] to CO_2 sequestration under supercritical conditions in natural mineralisation processes.[25,26] In addition, the study of stromatolites (Ca-Mg carbonates) precipitated from the transformation of atmospheric CO_2 shows that this material played a huge role in the formation of the current atmosphere increasing the oxygen content to the present levels.[27]

Calcium carbonate is not only produced massively in geological transformations but in biochemical processes. It has been found to be a key component in specific biological structures and functions: *e.g.* diatom shells, spicules,[19,28] larval shell formation,[11] or bone regeneration.[29] The exquisite interplay of morphology and function found in calcium carbonate biominerals led to an explosion of research over the past several decades in an effort to achieve even a fraction of the precision and control found in natural systems. These efforts have resulted in significant advancements in biomimetic crystal engineering and associated technological advancements.

Due to its abundance and its properties, calcium carbonate, in the form of limestone, has been used extensively throughout human history as a building material. More recently, the addition of calcite to Portland cement, has shown an enrichment in its properties by altering the distribution of lime, alumina and sulphate in the structure.[30] Other industrial fields in which calcium carbonate is used, among others, are plastic, rubbers, paper making and drug delivery.[31]

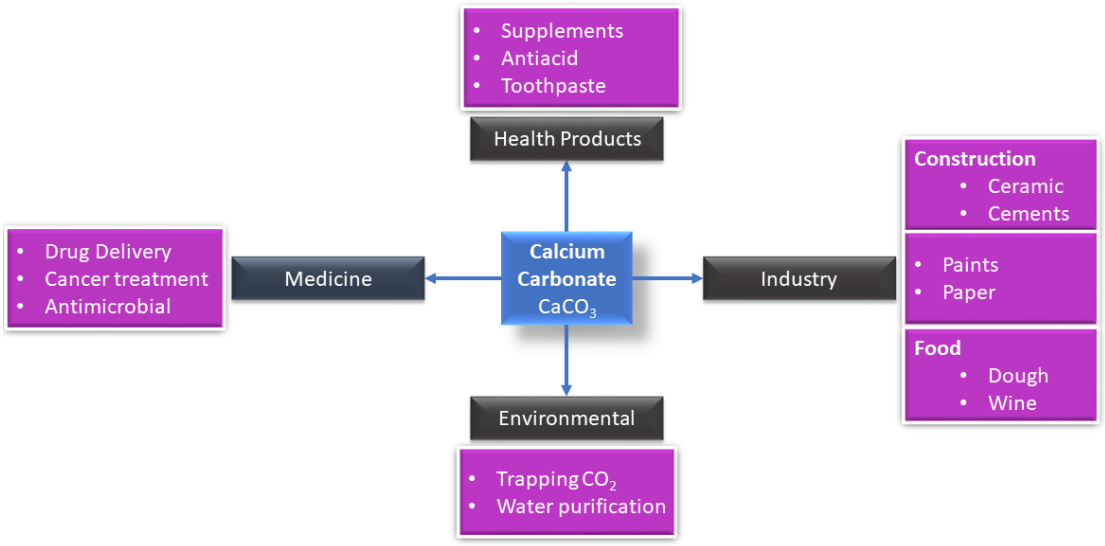

Figure 5.2. Applications of $CaCO_3$ in various fields

Most of the processes and applications highlighted above are strongly dependent on the $CaCO_3$ properties, which are determined by the phase present in the structure.[31] Thus, during recent years, researchers have focused on replicating the capability of mineralisation and biomineralisation processes to control the polymorph selection of these carbonates at the nanoscale and beyond, and taking advantage of their properties.[32–34] They work not only as a model for phase control, but to orientational growth such as in sea urchin teeth.[35] As the understanding of calcium carbonate formation and biomineralisation increases, the higher the scope to design and develop carbonate based materials for specific applications,[1] such as in medicine employed as a targeted container of drugs, which requires the high solubility of vaterite *versus* the rest of the more stable polymorphs (calcite and aragonite)[36] or tumour treatment using rare earth doped $CaCO_3$.[37] The polymorph selection therefore will influence the applicability of the carbonates synthetised.

5.1.1 Nucleation and Growth of Calcium Carbonate

To understand this phase selection and the conditions required to yield each polymorph of this material some models are needed to understand its nucleation and growth. These models go from more simplistic way of understanding it (LaMer model that comprises the Classic Nucleation Theory) to more specific and complicated explanations to unveil how solids are obtained (*e.g.*, $CaCO_3$ amorphous prenucleation

precursors). Calcium carbonate nucleation and growth has been reported to be an illustrative example of non-classical nucleation and growth. Therefore, each stage prior to the formation of calcium carbonate crystalline polymorphs needs to be acknowledged.

5.1.1.1 Non-Classical Nucleation

As previously explained, from the classical view, nucleation occurs when the supersaturated system needs to relieve the ion concentration by precipitating it into solid state where the cluster has a thermodynamically determined critical size.[38] That simplistic point of view has gradually evolved to non-classical descriptions, which allow for the formation of stable oligomeric or polymeric clusters, prior to the solid nucleation, which drive the solid precipitation from solution.[39,40] It is worth mentioning that these clusters can be seen in both under- and over-saturated conditions. These "pre-nucleation clusters" often exhibit well-defined structural features, which are closely related to crystal structures adopted by the material in the solid state, though the clusters themselves strictly speaking remain as solutes. As a result, it has been suggested that the nature of the pre-nucleation clusters formed can exert a significant influence on the particular polymorph formed in these multistructural systems.

In the case of calcium carbonate, it is suggested that these pre-nucleation clusters lead to the formation of solid amorphous calcium carbonate (ACC).[41] It is conceived as an amorphous material comprised of a Ca-rich framework with water and carbonate ions in its pores with only short range local order up to 1.5 nm, which may form spherical particles with sizes ranging from 50-200 nm.[42,43] There is strong evidence that multiple phases of ACC exist, each leading to a different crystalline phase, and it is suggested that they are formed by different stable pre-nucleation clusters.[44,45] These different prenucleation clusters have a low, but important, degree of order shown by variations in the binding strength between the carbonate and calcium ions in different conformations.[46] Determination of the binding strength is based on the constant titration of the carbonates in the structure with dilute NaOH. This binding strength is therefore pH dependent. At lower pH, the binding strength is larger, so that it is obtaining calcite at those conditions. At intermediate pH both calcite and vaterite are formed with no aragonite traces. At higher pH, *i.e.* lower binding

strength, vaterite is formed with only traces of calcite.[47] This model was studied for a really narrow pH range (due to the low amount of carbonate at pH lower than 9 and precipitation of the hydroxide at pH higher than 10), however even within this narrow range great changes in the obtained phase were observed. These different conformations modelled as prenucleation clusters for calcium carbonate are represented in Figure 5.3. No mechanism of growth or aggregation has been described yet although the stoichiometry and the possible conformations has been effectively proposed.

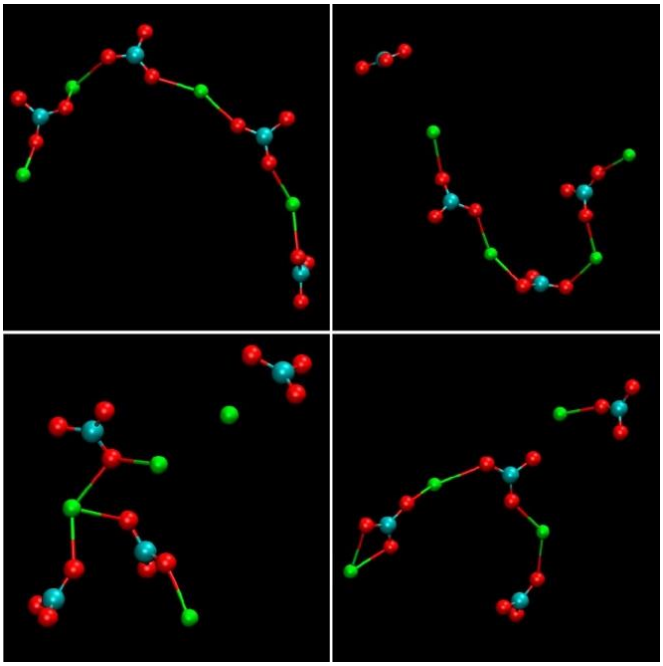

Figure 5.3. Four stable clusters simulated by Gebauer *et al.*[48] after 1 ns at conditions of $C_{Ca^{2+}}$ = 0.4 mM , $C_{HCO_3^-}$ = 10 mM and pH = 10. The colours of the atoms are assigned as calcium (green), carbon (blue) and oxygen (red).

5.1.1.2 Post-Nucleation: Amorphous Calcium Carbonate (ACC)

Later, these prenucleation clusters evolve to solid-state amorphous phases with atomic scale order related to one of the three structures. These pre-crystalline phases are often called ACC-I and ACC-II.[47] It has been concluded by pH-variation in the absence of additives for ACC nucleation that those amorphous phases have structural order in low range, corresponding to proto-calcite ACC (pc-ACC) and proto-vaterite ACC (pv-ACC), which promote the formation of either calcite or vaterite depending on the respective amorphous phase. The short-range order and crystallisation is closely related to level of hydration of the structures,[49,50] even though the whole mechanism

remains unclear. The content of water can vary,[51,52] but it has been concluded that the main stoichiometric composition is $CaCO_3 \cdot H_2O$.[53–55] This close interaction of the water molecules with the calcium carbonate framework leads to the understanding of the aragonite formation. Proto-aragonite ACC (pa-ACC) has been found to appear, in larger amounts, above 50 °C at pH = 9.80, additive free solution. The dipole-dipole interaction of the carbonate end with at pa-ACC formation has been suggested as a key component for facilitating the kinetic pathway for its mineralisation, driven by the heating of pv-ACC and later crystallisation at high temperatures.[56]

5.1.1.3 Crystallisation: Calcite, Vaterite and Aragonite

ACC is highly unstable and transforms very fast (less than 2 min. at room temperature).[10] It crystallises into any of the crystalline polymorphs through the amorphous clusters, which are highly dependent on external factors such as temperature, pressure, ion activity, pH,… The formation of solid and well-structured calcium carbonate polymorphs is not limited to the thermodynamically driven transformation of ACC but can also arise from the interconversion of each polymorph. Since the 1970s vaterite was established as the precursor of the calcite phase calcium carbonate found in sediments.[57] The transformation from ACC to vaterite has been reported by cryo-TEM studies, and has been shown to proceed by a solid-state transformation, where ACC aggregates into larger particles and gets dehydrated yielding classical spherical, randomly oriented, spheres related to vaterite.[58,59] Nonetheless, many reports on this topic assert that this process consists of the dissolution of the amorphous phase, followed by vaterite formation.[60] More recent research has shown that the phase crystallisation is pH-dependent. Neutral pH promotes the transformation of ACC to calcite, but basic pH promotes the generation of calcite *via* intermediate vaterite step. In basic conditions it starts with the dissolution of the amorphous phase that promotes spherulitic growth of vaterite.[61,62]

Spherulitic growth consists of the nucleation of particles with structural relation on an already nucleated core surface. This process is described in Figure 5.4. This non-classical growth requires great saturation of the system. Spherulitic growth in calcium carbonate systems takes place when there exists a great difference of solubility between the amorphous phase and the crystalline phase. This type of growth is not exclusive for vaterite, but also calcite[62] and aragonite.[63]

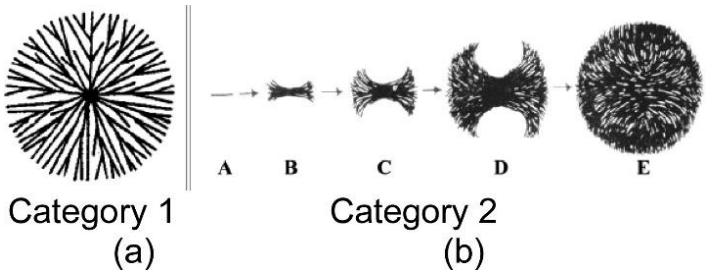

Figure 5.4. Spherulitic growth. Category 1 (a) correspond to multidirectional attachment of the particles on the core (spheres). Category 2 (b) directional attachment of the particles leaving two "eyes" in both directions (dumbbells).[64]

The kinetics of vaterite to calcite transformation have been shown to be temperature dependent. It is a surface related process slower than the spherulitic growth (6h *versus* minutes at room temperature). It is reported to be a dissolution-recrystallisation process driven by the dissolution of vaterite in the solution, reprecipitating into calcite.[10] However, calcite can be formed directly from the amorphous phase, at neutral pH and high-supersaturations, in spherulitic form.[62,64] A summary of all the processes followed for the non-classical nucleation of calcium carbonate are shown in Figure 5.5.

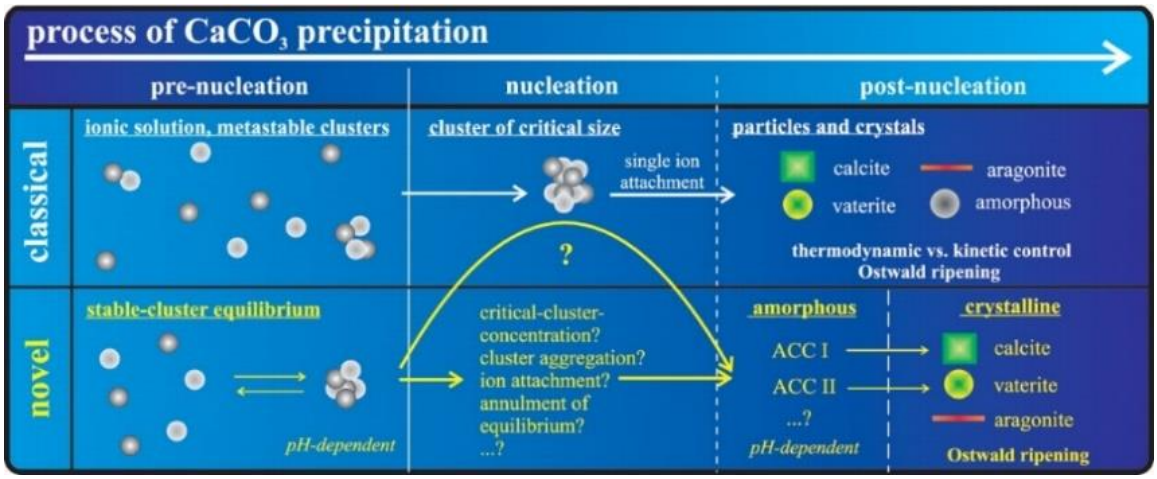

Figure 5.5. Schematic comparison of the classic nucleation theory and multiple-step theory suggested for calcium carbonate.[47]

The factors that influence the formation of calcite from ACC or vaterite in a pure system (in absence of additives) are two: the low-range ordered precursors (explained above) and the solubility of ACC. As it has been previously explained, basic media promotes vaterite formation over calcite. While neutral and acid promotes direct transformation of ACC into calcite. The second factor is explained by the pH at

which each phase is formed. At high pH ACC is more soluble, promoting the dissolution and recrystallisation process in vaterite, not only transforming into it, rising the saturation in solution of the amorphous phase. For calcite, acid media prevent the dissolution of the ACC, transforming into calcite directly.[48,65,66] The mechanism of aragonite formation remains unclear despite the huge body of work on $CaCO_3$ systems.

5.2 Experimental

5.2.1 Synthesis Methods

For the controlled synthesis of the different calcium carbonate polymorphs the hydrothermal injection reactor was employed. The standard procedure shown in Chapter 2 was followed to carry out these experiments.

The source used for calcium precursor is $Ca(NO_3)_2$ 1.5 M with constant concentration for every reaction, injecting a total of 2.5 mL into the reactor chamber. In the reactor 5 mL of either sodium carbonate (Na_2CO_3) or sodium bicarbonate ($NaHCO_3$) were pipetted in. The ratios chosen to study the influence of the concentration (defined as $R = moles_{CO_3^{2-}} / moles_{Ca^{2+}}$) on the reaction were 0.5, 1, 1.5 and 2 that corresponds to 0.375, 0.75, 1.125 and 1.5 M solutions of the carbonate source respectively. The total volume in the reactor after injection is 7.5 mL. The temperatures chosen for the synthesis were room temperature (25), 50, 100 and 200 °C.

The overall equations for the reactions are:

$$Ca(NO_3)_2 + Na_2CO_3 \rightarrow CaCO_3 \text{ (calcite, vaterite and/or aragonite)} \quad (5.1)$$

$$Ca(NO_3)_2 + NaHCO_3 \rightarrow CaCO_3 \text{ (calcite, vaterite and/or aragonite)} \quad (5.2)$$

The standard injection procedure consists of: Firstly, the HPLC pump is filled with the metal solution, getting rid of the cleaning water from the system. Secondly, 5 mL of the carbonate precursor either carbonate or bicarbonate are pipetted in the reactor. A magnetic stirrer is introduced, and the tube gets assembled to the reactor and sealed. Finally, the heating jacket is placed around the reactor tube. All the system is finally positioned in the middle of the stirring plate. The stirring rate is set to 600 rpm.

The temperature controller is set to heat up to the desired temperature. Once the temperature is reached, the heating is maintained for 5 minutes, in order to stabilize the temperature and pressure. Then, 2.5 mL are injected from the HPLC pump. The reaction proceeds for 10 minutes at that temperature before cooling down by turning

off the heating jacket. At room temperature the reaction product is filtrated and washed and then dried at 75°C in the oven overnight.

By varying the reaction ratios, carbonate precursor, and injection temperature, a total number of 35 reactions were successful in obtaining a final product. Details are given in Table 5.3 in the results section.

5.3 Characterisation Methods

5.3.1 X-Ray Diffraction (XRD)

X-ray diffraction patterns were obtained using a Bruker D2 Phaser. The source employed was Cu K_α = 1.5418 Å. A zero-background holder was used for the measurements.

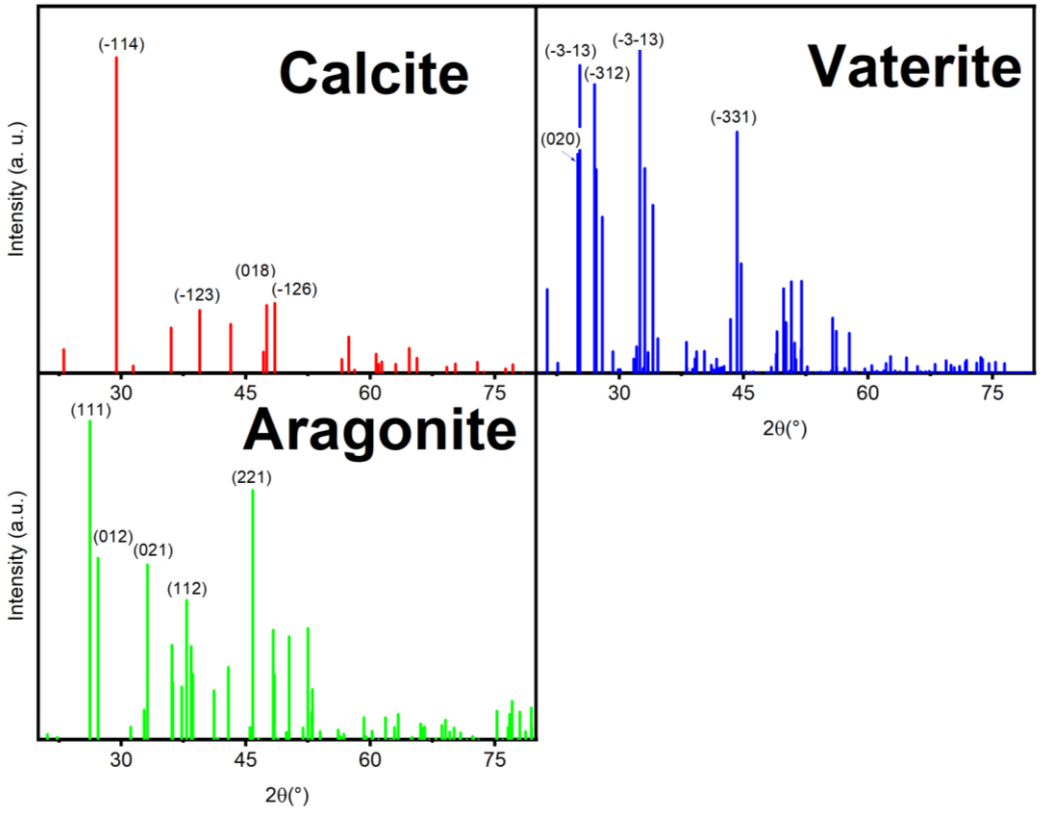

Figure 5.6. XRD patterns of the three $CaCO_3$ polymorphs.[67]

The calculated X-ray diffraction patterns are shown in Figure 5.6 They are used to analyse and assign the peaks observed in the samples' patterns.

5.3.2 Fourier-Transformed Infrared Spectroscopy (FTIR)

Infrared spectra were recorded using a Perkin Elmer ATR-FTIR spectrometer with ATR single reflection diamond accessory from Specac. Spectra were collected from 4000 to 200 cm^{-1}.

5.3.3 Raman Spectroscopy

Raman spectra were recorded using a Renishaw Raman Microscope with 785nm laser, three lenses and automated xyz stage. The measurement ranged from 100 to 1300 cm^{-1} with an exposure time of 10 seconds for 50 cycles. The reported active IR and Raman bands for the different polymorphs are shown in Table 5.2.

Table 5.2. IR/Raman band assignment.[68–74]

Frequency (cm^{-1})	IR/Raman active	Assignment	Phase
105	Raman	Lattice Mode	Vaterite
150-155	Raman	Lattice Mode	Calcite
180	Raman	Lattice Mode	Aragonite
206	Raman	Lattice mode	Aragonite
265	Raman	Lattice Mode	Vaterite
278	Raman	Lattice Mode	Calcite
300	Raman	Lattice Mode	Vaterite
700	IR	In plane bending	(Rod-shaped) Aragonite
703	Raman	Asymmetric bending mode (v_4)	Aragonite
712-714	IR	In plane bending (v_4)	Calcite + Aragonite
711-715	Raman	Asymmetric bending mode (v_4)	Calcite
746	IR	Asymmetric Stretching (v_4)	Vaterite
749	Raman	Asymmetric Stretching (v_4)	Vaterite
854	IR	Carb. Out of plane bending (v_2)	Aragonite
874	IR	Carb. Out of plane bending (v_2)	Calcite + Vaterite
1074	Raman	Symm. Carb Stretching (v_1)	Vaterite
1084	IR	Symm. Carb. Stretching (v_1)	Calcite
1085	IR/Raman	Symm. Carb. Stretching (v_1)	Aragonite
1086	Raman	Symm. Carb. Stretching (v_1)	Calcite
1088	IR	Symm. Carb Stretching (v_1)	Vaterite
1090	Raman	Symm. Carb Stretching (v_1)	Vaterite

5.3.4 Scanning Electron Microscopy (SEM)

SEM images were obtained by using a Zeiss Ultra TEM microscope running at 5.00 kV with *in Lens* detection. All samples were prepared and deposited onto a carbon tab over an aluminium stub and coated with a thin gold/palladium film.

5.4 Results and Discussions

5.4.1 XRD, Raman and IR from selected samples

XRD patterns, Raman and IR spectra were obtained for all the synthesised samples. Due to the large amount of data obtained, only four representative samples, which contain varying amounts of each polymorph will be discussed in detail to highlight relevant qualitative features of data obtained through each characterisation technique. These samples are named as AS103, AS104, AS105 and AS106, prepared at a CO_3^{2-}:Ca^{2+} ratio, R = 1, using Na_2CO_3 as the carbonate source and temperatures from 25 °C to 200 °C.

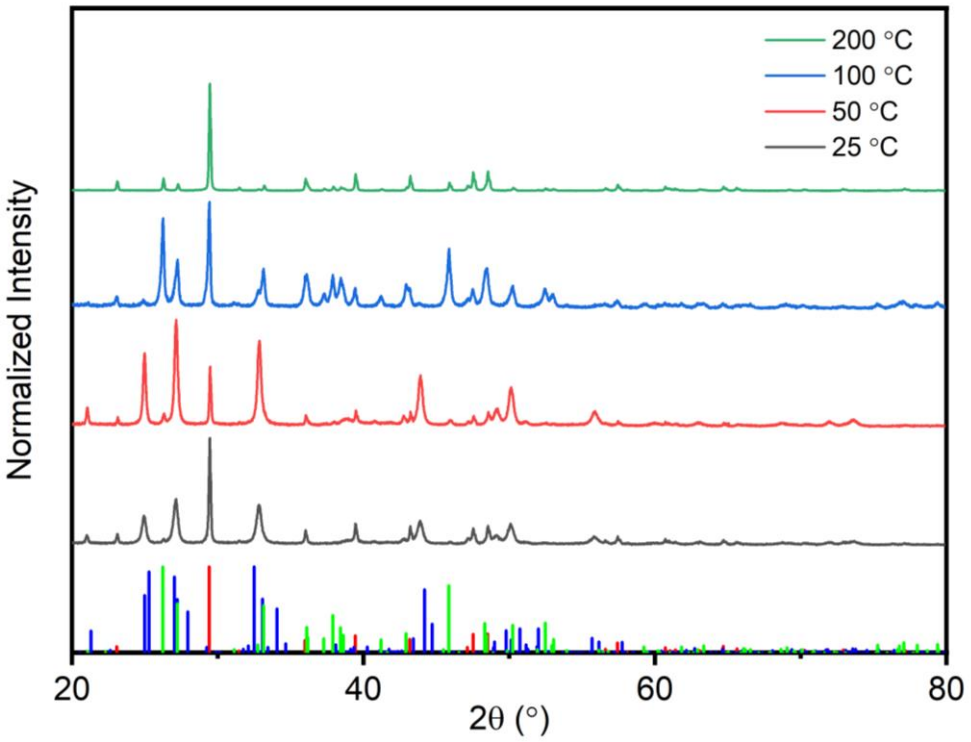

Figure 5.7. Powder XRD patterns from samples AS103 (25 °C) to AS106 (200 °C) - prepared at a CO_3^{2-}/Ca^{2+} ratio, R = 1, Na_2CO_3 as precursor. The vertical lines below represent the XRD model for each polymorph: red-calcite, blue-vaterite and green-aragonite. Data have been normalised and offset for clarity.

The XRD patterns of the selected samples are shown in Figure 5.7. It can be seen that each pattern is comprised of peaks corresponding to each of the anhydrous polymorphic phases: calcite, vaterite, and aragonite (the predicted patterns of which are denoted by the vertical lines) in different proportions. AS103, prepared by injection of 2.5 mL of a 1.5 M calcium nitrate solution into 5 mL of the 0.75 M sodium carbonate

solution at room temperature, 25 °C, shows a significant proportion of highly crystalline calcite, as evidenced by the sharp peak at 29.4° 2θ, as well as a high amount of vaterite, which exhibits peaks at 24.9 and 27.1° 2θ, the broadness of which is indicative of lower crystallinity, with only slight traces of aragonite. At a higher synthetic temperature (50 °C), AS104 shows a higher proportion of vaterite, with some calcite and only traces of aragonite. Further increasing the reaction temperature to 100 °C results in a sample which is dominated by aragonite (major peaks at 26.2 and 27.2°2θ) and calcite, with only a slight contribution from vaterite. At the highest reaction temperature of 200 °C, the product AS106 is predominantly calcite with traces of aragonite. Extensively every XRD pattern obtained is shown in the Appendix section (Figure A. 4 and Figure A. 5).

The infrared spectra of these samples are shown in Figure 5.8 ranging from 1250 cm^{-1} to 500 cm^{-1}. In each spectrum the most intense absorption bands are observed at 854 cm^{-1} and 874 cm^{-1}, which are assigned to the out-of-plane bending of carbonates in aragonite and calcite/vaterite, respectively. Additional bands are observed at 1088 cm^{-1} and 746 cm^{-1} in samples AS103 and AS104 prepared at 25°C and 50°C. They are attributed to the symmetric and asymmetric carbonate stretches of vaterite. Bands at 1084 cm^{-1} and 700 cm^{-1} are present in samples AS105 and AS106, prepared at 100 °C and 200 °C, assigned to the asymmetric stretching and in-plane bending of aragonite carbonates. It is worth pointing out that sample AS106, which by XRD shows almost exclusively calcite, with only small amounts of aragonite, in IR shows almost equal intensities of the major bending mode bands of aragonite and calcite at 854 cm^{-1} and 874 cm^{-1}, suggesting that this spectroscopic technique can be more highly sensitive to the presence of aragonite.

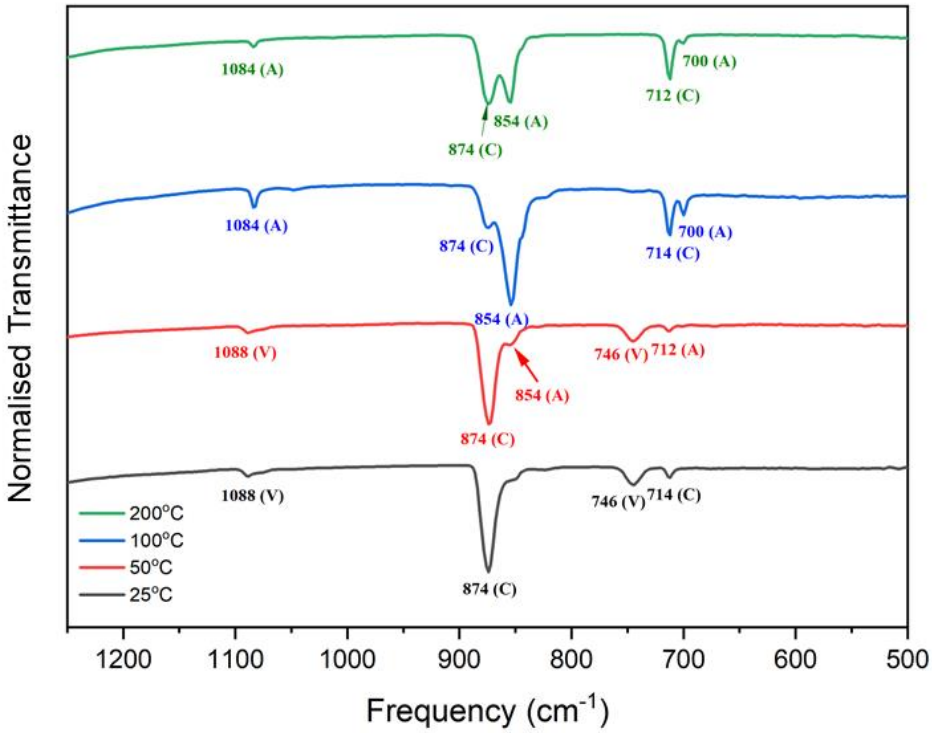

Figure 5.8. IR spectra from AS103 (25ºC) to AS106 (200ºC) - prepared at a CO_3^{2-}/Ca^{2+} ratio, R = 1, Na_2CO_3 as precursor. Each peak is assigned to its frequency (cm^{-1}) and the corresponding polymorph is highlighted as: (C) calcite, (V) vaterite and (A) aragonite. Data have been normalised and offset for clarity.

The Raman spectra of the samples are shown in Figure 5.9 (a). The carbonate stretching region is highlighted at the right of the figure (Figure 5.9 (b)). The symmetric stretch of calcite carbonate is observed at 1086 cm^{-1}, with aragonite appearing at 1085 cm^{-1}. Bands assigned to vaterite appear at 1074 cm^{-1} and 1091 cm^{-1}. Similar trends can thus be observed from the Raman spectra, as were seen in both XRD patterns and IR spectra: samples prepared at 25 °C and 50°C, AS103 and AS104, are a mix of calcite and vaterite, sample AS105, prepared by injection at 100 °C is predominantly aragonite, while AS106, prepared at 200 °C is mostly calcite. The literature assignments of all IR and Raman active bands observed are given in Table 5.2. Every Raman and IR spectrum measured is shown in the Appendix section (Raman in Figure A. 6 and Figure A. 7; and FT-IR in Figure A. 8 and Figure A. 9).

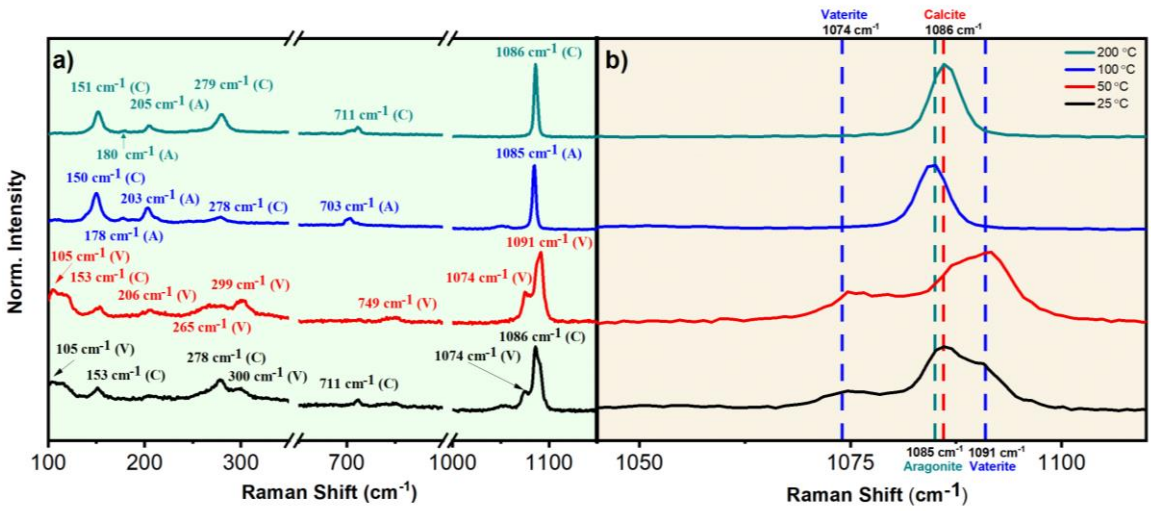

Figure 5.9. a) Raman spectra from AS103 (25ºC) to AS106 (200ºC) - prepared at a CO_3^{2-}/Ca^{2+} ratio, R = 1, Na_2CO_3 as precursor. Each peak measured as Raman shift is shown in cm^{-1} and its corresponding polymorph is highlighted as: (C) calcite, (V) vaterite and (A) aragonite. b) Main Raman features from 1045 to 1125 cm^{-1}. Data have been normalised and offset for clarity.

As a summary of all the techniques at higher synthesis temperatures calcite is the predominant structure, as expected, being the most stable calcium carbonate polymorph. Nonetheless, at intermediate to higher temperatures (100-200 °C) aragonite coexists as a metastable polymorph with the already mentioned calcite. When approaching lower temperatures aragonite decreases as vaterite appears. This transformation suggests a strong correlation between the polymorph selection and temperature in the reactor. The alternated appearance of each polymorph is due to the selection of each one depending on the synthesis conditions, where higher ratios and intermediate temperatures yields aragonite and lower temperatures and ratios forms vaterite.

From IR (Figure 5.8) and Raman (Figure 5.9), the trend highlighted from XRD (Figure 5.7*)* can be corroborated. This analysis allowed the identification of the different polymorphs present at the sample, nevertheless, for quantification, analysis techniques must be carried out. The extrapolation from a calibration line, for example, from IR, Raman and XRD intensities have been used before,[75] even though Rietveld refinement has been found in this research to be a perfect method to quantify numerically the presence of each polymorph.

5.4.2 Rietveld Refinement

Calcium carbonate has shown from the X-ray measurements (Figure 5.7) to have simple and well-resolved patterns, therefore, Rietveld refinement quantification is suitable for this compound. Examples of Rietveld refinements fits are shown in Figure 5.10. The refinement parameters are tabulated in the Appendix section (Table A. 5.).

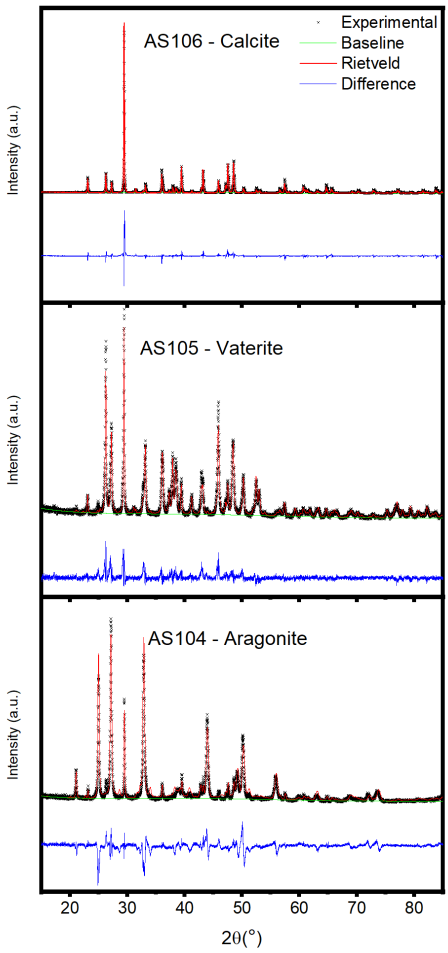

Figure 5.10. Rietveld refinement obtained of the samples AS104, AS105 and AS106 by GSAS.[78] The principal polymorph in the sample is highlighted. The red-line is the calculated refinement for the experimental scattering. The green line is the baseline and the blue graph underneath shows the difference between the calculated and the experimental pattern.

Figure 5.10 shows GSAS/EXPGUI[78] software interface. It evidences how accurate the refinement to the experimental data is. The disparity between the data and the calculated pattern is minimal, represented by the blue line below the graph and, numerically, by the R_p value calculated in Table 5.3 ($R_p < 0.15$ is considered a good

fit). The phase percentage wasn't calculated for samples where only one polymorph is present (calcite in all cases) noted as NC in Table 5.3. The data obtained can be plotted in relation to the experimental parameters in order to observe some trend between the polymorph formation and synthesis conditions.

Table 5.3. Phase percentage calculated by Rietveld refinement. Samples in bold are those used as exemplars throughout this chapter. The goodness of fitting as well as the refined parameters are included in Table A.5 at the Appendix section.

CO_3^{2-} **Source**	**Ratio** (CO_3^{2-}/Ca^{2+})	**T (ºC)**	***Calcite***	***Vaterite***	***Aragonite***
Bicarbonate	0.5	50	67.54	24.9	7.56
		100	100	0	0
		200	83.79	12.99	3.21
	1	25	85.88	13.72	0.4
		50	93.27	6.73	0.01
		100	85.82	8.15	6.03
		200	99.97	0	0.03
	1.5	25	64.1	34.49	1.41
		100	71.33	11.34	17.34
		200	100	0	0
	2	50	29.95	70.03	0.01
		100	64.2	6.68	29.12
		200	36.89	0	63.11
Carbonate	0.5	25	17.83	79.82	2.36
		50	9.72	83.76	6.52
		100	97.73	0	2.27
		200	63.71	0	36.29
	1	**25**	**26.29**	**72.29**	**1.42**
		50	**7.88**	**78.19**	**13.94**
		100	**24.78**	**2.41**	**72.81**
		200	**77.2**	**0**	**22.8**
	1.5	25	51.59	48.41	0
		50	85.73	14.27	0
		100	59.56	0	40.44
		200	93.6	0	6.4
	2	25	55.07	42.24	2.7
		50	81.16	18.84	0
		100	45.43	6.64	47.93
		200	78.25	0	21.75

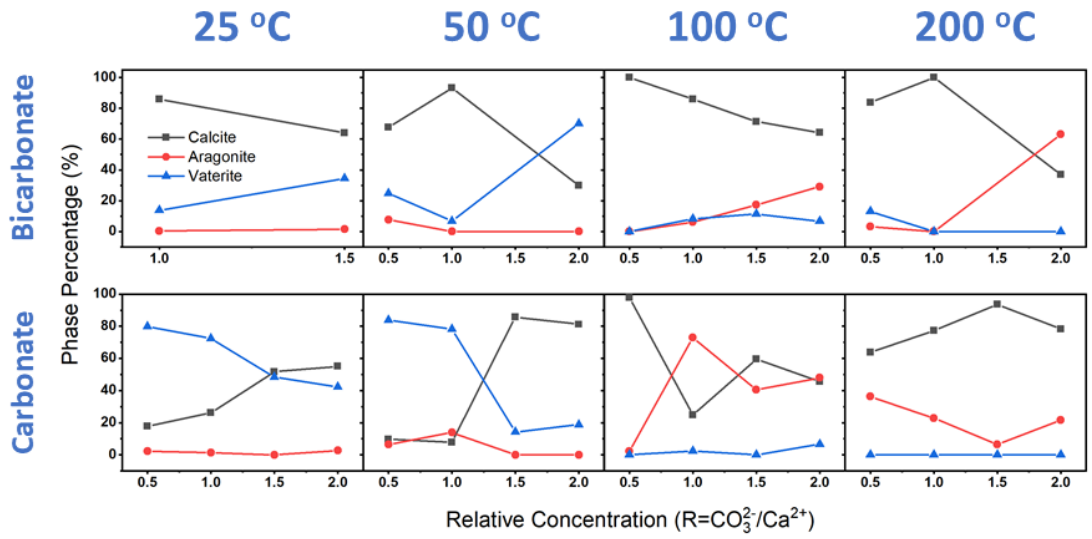

Figure 5.11. Phase percentage calculation by Rietveld refinement.

From Figure 5.11 completely different trends can be observed from using sodium carbonate (top) and sodium bicarbonate (bottom) as precursor.

Regarding to the use of the carbonate as a precursor at lower ratio and lower-intermediate temperatures (25 and 50 °C) vaterite is predominant over the rest of the polymorphs. At R = 2 it gets switched with higher calcite content on both of them. When the reaction temperature is increased (100 °C) calcite is the major component at R=0.5 with no appearance of the other polymorphs. When R gets higher there's and alternating predominance between aragonite and calcite, with little or no vaterite in any case. Finally, at 200 °C a mix between aragonite and calcite (40:60 % respectively) is seen at lower ratios, with almost only calcite at R=1.5.

When bicarbonate is used as the carbonate ion precursor the result is radically different. For the lowest temperature (25°C) calcite is predominant. At mid-lower temperature (50°C) and lower ratios there is a mix phase between calcite (around 70 %) and vaterite (around 25%). At ratio R = 1 calcite is predominant in the sample, but at R = 2 vaterite is predominant over calcite. So, it can be concluded that by using bicarbonate, low temperatures and increasing the saturation calcite and vaterite presence gets switched. A similar behaviour is seen at the highest temperature (200 °C), but in this case with calcite and aragonite.

Looking at both precursors, vaterite is only yielded at lower temperatures, while aragonite is yielded at intermediate temperatures. Even though, vaterite is predominant at lower carbonate ratios for carbonate as a precursor, while it is mainly formed at R =2 at 50°C when using bicarbonate in the reaction. A similar trend is seen for aragonite at 200°C. At intermediate ratios, for both precursors there is always a mix between aragonite and calcite.

The variables affecting the polymorph selection is rather large. The presence of the three crystals structures of calcium carbonate in different percentages will depend on magnitudes such as temperature, calcium to carbonate ratio, saturation, precursor, … Therefore, multiple plotting arises combining all of the factors and how they interplay to each other. Nonetheless, it is very difficult to generate an idea of how they play a role in the polymorph selection. For that mean the dimensionality of the data load needs to be reduced by Principal Component Analysis (PCA) of the XRD, FTIR and Raman data collected. The PCA analysis from the XRD patterns is shown below (Figure 5.12). The percent of variance expressed by the different components is given in Table 5.4.

Table 5.4. Percentage of variance represented by the three main components for XRD patterns PCA analysis.

Principal Component	Percentage of variance (%)	Cumulative (%)
1	58.37	58.37
2	19.23	77.60
3	13.43	91.03

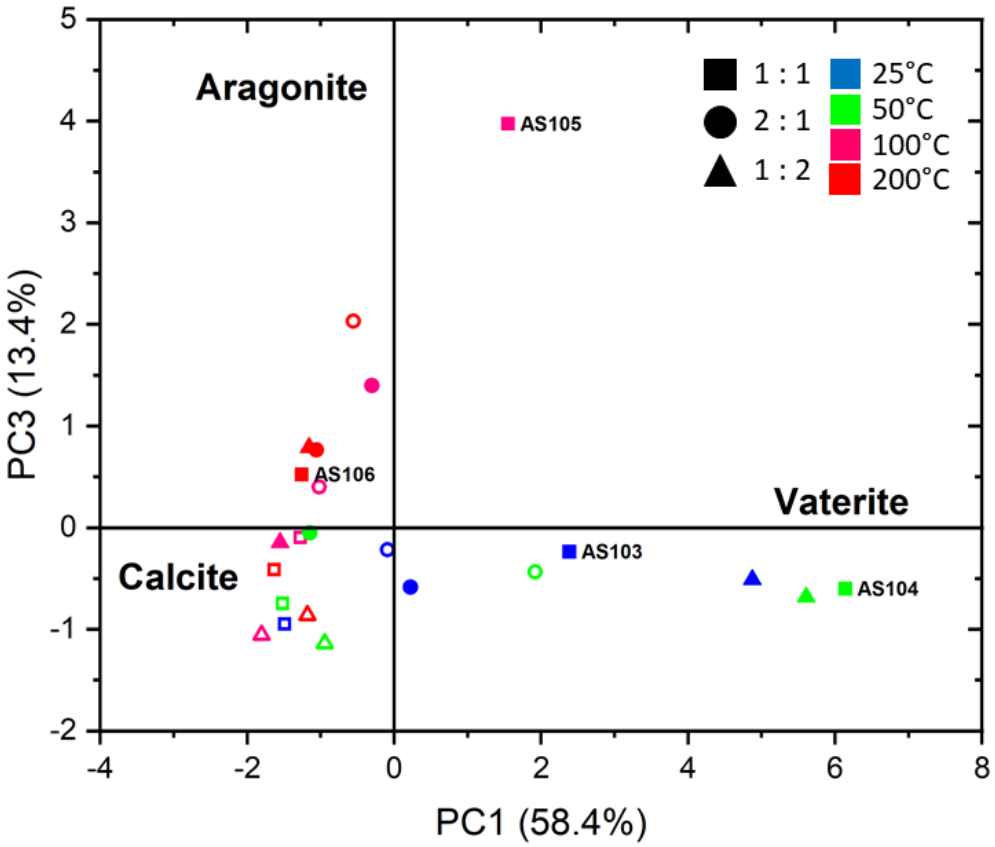

Figure 5.12. PCA from XRD patterns from carbonate and bicarbonate as a CO_3^{2-} precursor. The empty symbols represent the use of bicarbonate as the precursor, the filled symbols are the samples obtained by using carbonate as the precursor.

Figure 5.12 shows that samples are well distributed, representative of the presence of the three different polymorphs in different percentages. The total variability plotted in Figure 5.12 is 71.8%. It is calculated as a combination of the variability composed by PC1 and PC2, as shown in Table 5.4.

Even though they get fairly clustered on each of the extremes, they don't represent accurately the small differences in polymorph composition. It must be remembered that PCA is a mathematical analysis with not physical explanation.

The total percentage of variability, although it is a decent value, can be improved. The resting variability not presented can be caused by the incapability of the method to discern small peaks with the background, where only when the peaks are much more intense than the baseline is recognised as a main component. Another factor that can play a role reducing the variability shown by the 2D plotting is the peak shape and shifting. Variations in the peak positioning and changes in the morphology

of the peak can be viewed as variations by PCA as well, reducing the percentage of variability represented by the polymorphs.

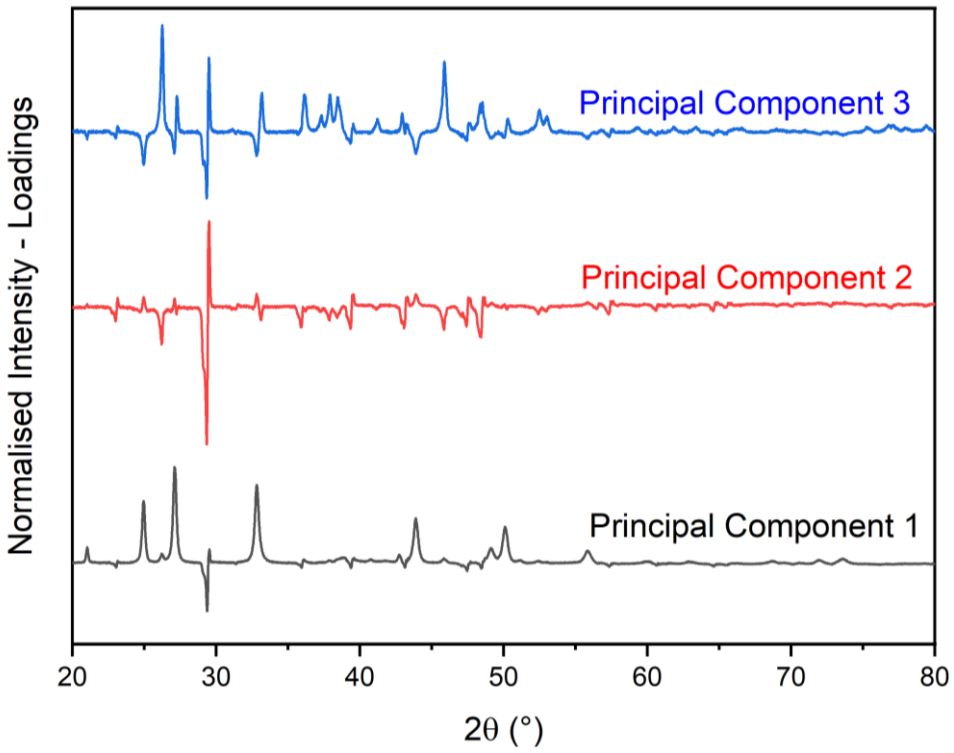

Figure 5.13. Plot of the loadings of the PCs for the PCA analysis of the normalised XRD patterns.

When looking at the loadings in Figure 5.13 the real physical meaning of each PC can be analysed. PC1 is the compound that gives the most variability to the sample (58.37%) which will be either vaterite or aragonite. As calcite is present in every pattern it is treated as redundant information. The loadings show a positive value for peak positions at 27, 33 and 25° 2θ in order of intensity. Those three main features are characteristic features for vaterite, corresponding to the (-121), (-3-21) and (-3-11), respectively. Therefore, PC1 corresponds to the variability given by vaterite. The samples that show vaterite features will be represented along the *x*–axis. Secondly, PC2 and PC3 show a similar value for the percentage of variance expressed. It can be acknowledged that PC2 corresponds to shifting in the peak position for calcite. The main peak for PC2 has a derivative-shape or -/+ kind of peak, showing a local minimum and local maximum next to each other. As shown in Chapter 4, it is usually related to a change in the position towards either higher or lower angles. That main

shifting corresponds to the most intense peak at 29° 2θ, corresponding to the (-114) orientation for calcite.

Finally, PC3 is related to aragonite as shown by the peak at 26° 2θ that is the (111) plane for aragonite. Therefore, PC3 will be plotted at the *y* – axis. The relative position of the samples to the coordinate axis are closely linked to the percentages obtained by Rietveld refinement. AS104 which is analysed by Rietveld as 83.76% of vaterite is plotted further in the *x* – axis. On the other hand, AS105 that has a higher presence of aragonite is plotted at higher numbers in the *y* – axis. It can be concluded that the poor separation of the samples along the axis is reflected at the low difference between the PC2 and PC3, where PC2 is a shifting effect of the peaks, while PC3 shows aragonite variability. Due to their similar value, it can be concluded that shape effects are close to pattern positioning, which leads to a poor selectivity of shape-to-polymorph difference. To avoid these effects, the Pair Distribution Function (PDF) was calculated for the XRD patterns of the carbonates.

5.4.3 Conversion to the Pair Distribution Function (PDF)

The pair distribution function (PDF) can be obtained from the XRD patterns. The PDF diagram of a compound tells the weighted interatomic distances, where the maxima correlate to the interatomic distance and the intensity is related to the number of atom pairs at that given distance. Therefore, a description of the intermolecular surroundings in the crystals can be obtained from the PDF.

PCA has been widely used for different techniques, including Raman and IR. The reliability of PCA on these techniques is therefore, already proven. XRD patterns on the other hand, have rarely been subjected to PCA. A powder XRD pattern is defined by three main variables: peak positions, relative peak intensities, and peak shapes. The peak position is a function of the underlying unit cell of the compound, *i.e.* the d-spacing, which is inherent to a given crystal structure. The peak intensity results from the identity of the scattering atoms and their spatial relationship. Thirdly, peak shape arises from broadening due to incomplete destructive interference, *i.e.* small crystal domain sizes, as well as crystal strain. In an ideal, infinite crystal the peaks would occur at exact Bragg angles, with intensities directly determined by the crystal structure, and would have zero width. In reality peak positions can shift slightly

with strain, and peak intensity and shape can be altered by crystal size, shape, and strain effects — XRD data are susceptible to external macroscopic effects. While Rietveld refinement is capable of overcoming these limitations, thanks to non-uniform corrections introduced when calculating the percentages, PCA, as a statistical method, is effectively "blind" to the physical significance of these effects. By obtaining the pair distribution function the influence of these external macroscopic effects can be limited as it is only dependent on the identity and relative position of atoms in the structure — the phase. Thus, by transforming XRD data to PDFs the phase composition becomes the dominant influence and then can be more readily distinguished by PCA.

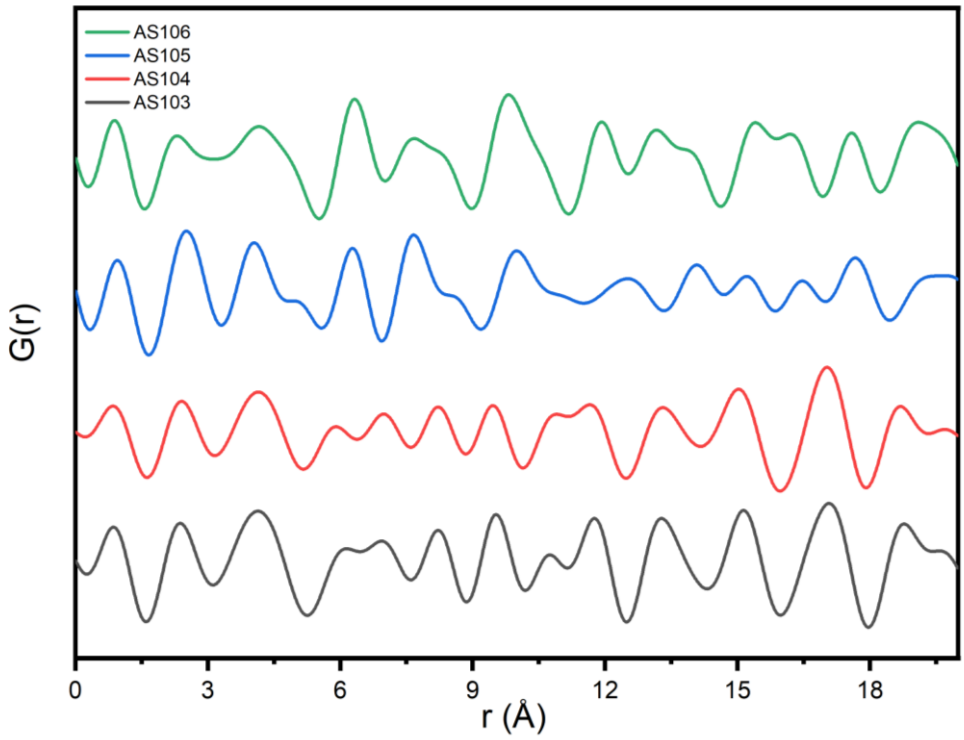

Figure 5.14. PDFs from samples AS103-106.

The PDF of the four samples already studied for XRD, IR and Raman are shown in Figure 5.14. All PDF conversions were performed using PDFgetX2.[79]

5.4.4 PCA of PDF calculations

The PCA representation from the calculated PDFs is presented below (Figure 5.15) and the calculated variability in Table 5.5.

Table 5.5. Percentage of variance represented by the three main components for the PCA analysis of the PDF analysis of the XRD patterns for calcium carbonate.

Principal Component	Percentage of variance (%)	Cumulative (%)
1	61.86	61.86
2	28.77	90.63
3	4.94	95.57

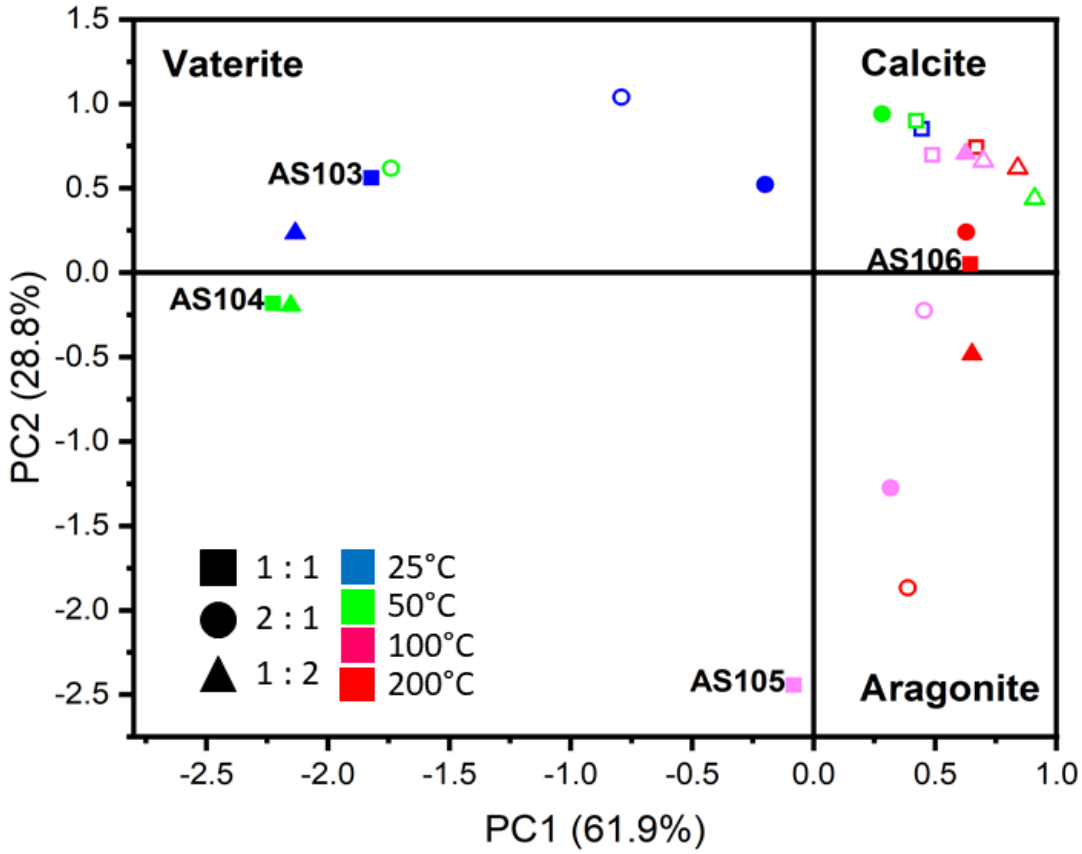

Figure 5.15. PCA of the PDF analysis of the XRD patterns for the calcium carbonate samples. The empty symbols represent the use of bicarbonate as the precursor, the filled symbols are for carbonate as precursor.

The limit of accuracy for real space measurements for the data acquired in Figure 5.14 resides in a Q_{max} = 55 A^{-1}. Although this approach can lead to errors in the interpretation of the structure of the polymorphs due to a large and unrealistic Q employed, the target of this analysis is not obtaining a structural description of the material but to show characteristic features for the relative disposition of the atoms

within the structure. PCA by statistical means will minimise the effects due to inaccuracies, only analysing the features related to the polymorph. The effective use of this approach is proven by the good representation of the different polymorphs obtained depending on the synthesis conditions shown for the PCA in Figure 5.15.

The loading patterns for the different PCs are plotted in Figure 5.16.

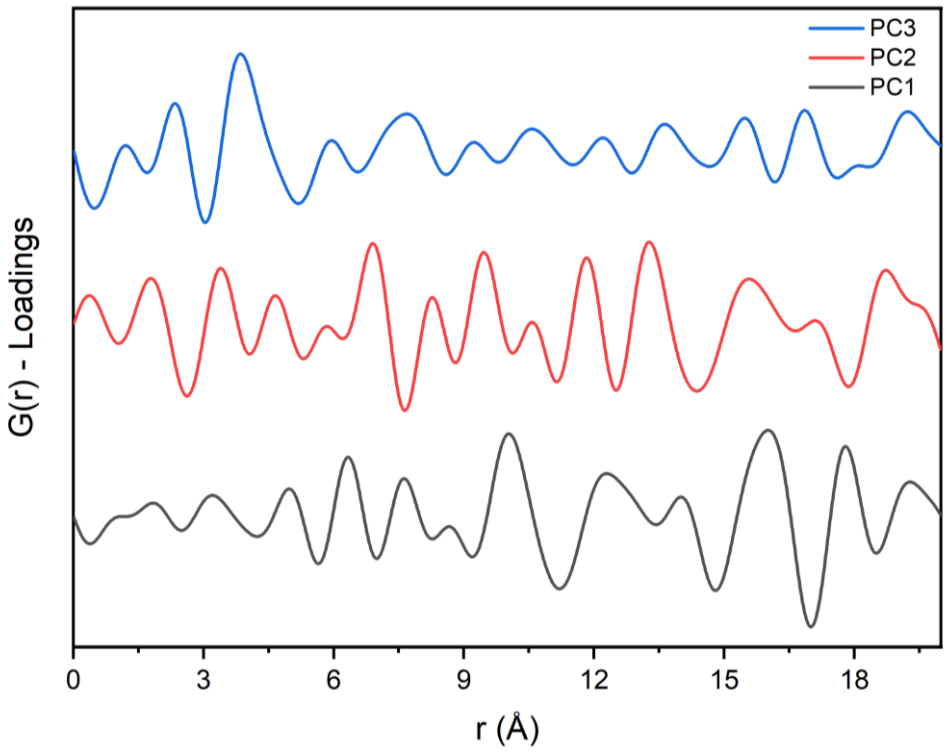

Figure 5.16. Plot of the loadings of the PCs for the PCA analysis of the PDF obtained from the XRD patterns.

By comparing the PCA above to the one obtained straight from the XRD patterns a better position-phase percentage relationship can be obtained. Therefore, by using the calculated PDFs the plotting is really improved. The difference between PC2 and PC3 is larger than when using XRD and there is a reduction of the shape effects to less than 5% for PC>2. T The loadings of the PDF is plotted in Figure 5.16. The use of PDF analysis is then justified for this analysis once the representation has a real physical meaning when comparing with the Rietveld is calculated. The total variability plotted in this sample is 90.7% which shows a great improvement compared to the normalised XRD PCA. The sample distribution shows that vaterite can be directly related to PC1 and aragonite to PC2. The comparison of the loadings with the

corresponding extreme sample with the highest content of that component is plotted in Figure 5.17. It is observed that the PCs describe the specular image of the samples. This explains why the plots are represented along the negative values of the axis of the PCs.

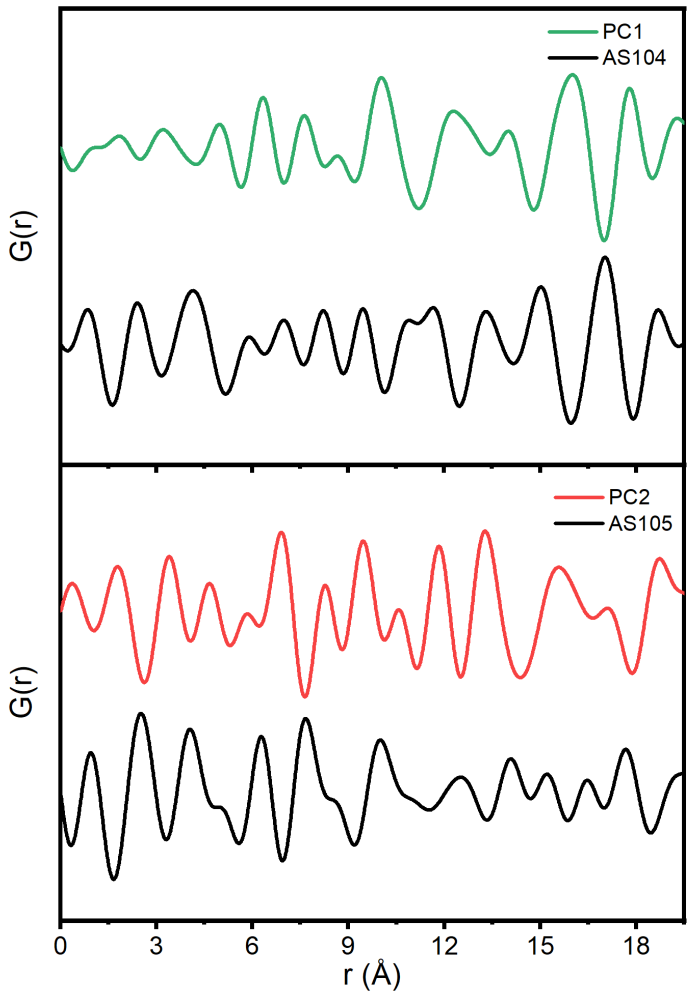

Figure 5.17. Direct comparison of the PCs with the corresponding extreme samples.

Analysing the PCA distribution, in conjunction with the results from Rietveld refinement, it can be concluded that calcite is the most common phase. Most of the samples in the calcite region are 100 and 200°C. Nonetheless, it is not a general rule as some 25 and 50°C samples are in the calcite region or close to it. More interestingly, for vaterite only low and mid-low temperature samples gets clustered in the vaterite region. In the aragonite region, there are only mid-high and high temperature samples. Therefore, there is a clear trend of obtaining vaterite at lower temperatures and aragonite at higher temperatures as seen for XRD. When analysing the ratio that yields

the greatest number of extreme samples, at 1:1 with only a 50°C difference in the synthesis temperature there is a jump between obtaining AS104 (50 °C), clearly vaterite based, to AS105 (100°C) aragonite based. On the other hand, the samples with 1:2 ratio (R=0.5) are the samples with less aragonite content. Therefore, it can be concluded, that lower carbonate saturation ratios don't promote aragonite crystallisation.

Finally, focusing on the effect of precursor choice on polymorph selection, carbonate shows to be pushing the crystallisation to higher vaterite and aragonite phase percentages. Thus, for obtaining greater phase selection, carbonate must be chosen. There are very few samples between the vaterite and aragonite region. The polymorph selection between both is corroborated by PCA. When vaterite is formed, aragonite is minimal or inexistent, which would suggest that there's a polymorph selection between vaterite and aragonite. It can be either because at the conditions of aragonite formation vaterite is unstable, or vaterite is formed at early stages but evolves into aragonite at those conditions.

5.4.5 PCA of Raman

Table 5.6. Percentage of variance represented by the three main components for Raman PCA analysis.

Principal Component	Percentage of variance (%)	Cumulative (%)
1	93.65	93.65
2	2.93	96.58
3	1.14	97.72

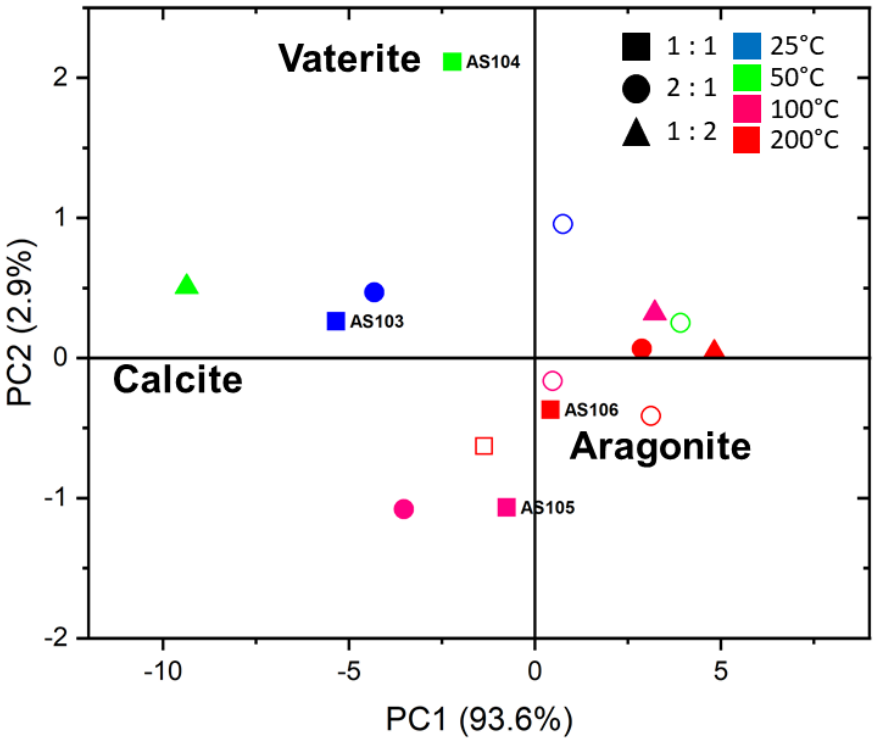

Figure 5.18. Principal Component Analysis of Raman spectra from selected calcium carbonate samples. The empty symbols represent the use of bicarbonate as the carbonate precursor, filled symbols are the carbonate as precursor samples. Due to the clustering selected samples were plotted.

The plotting of the PCA of the Raman spectra can be seen in Figure 5.18. From Table 5.6. PC1 represents the 93.65% of the variability of the samples. On the other hand, PC2 is much smaller, which contributes with a 2.93% of the total variability. Therefore, the total number represented by the plotting is 96.5%. Nonetheless, the difference between the two main components can be seen at Figure 5.19.

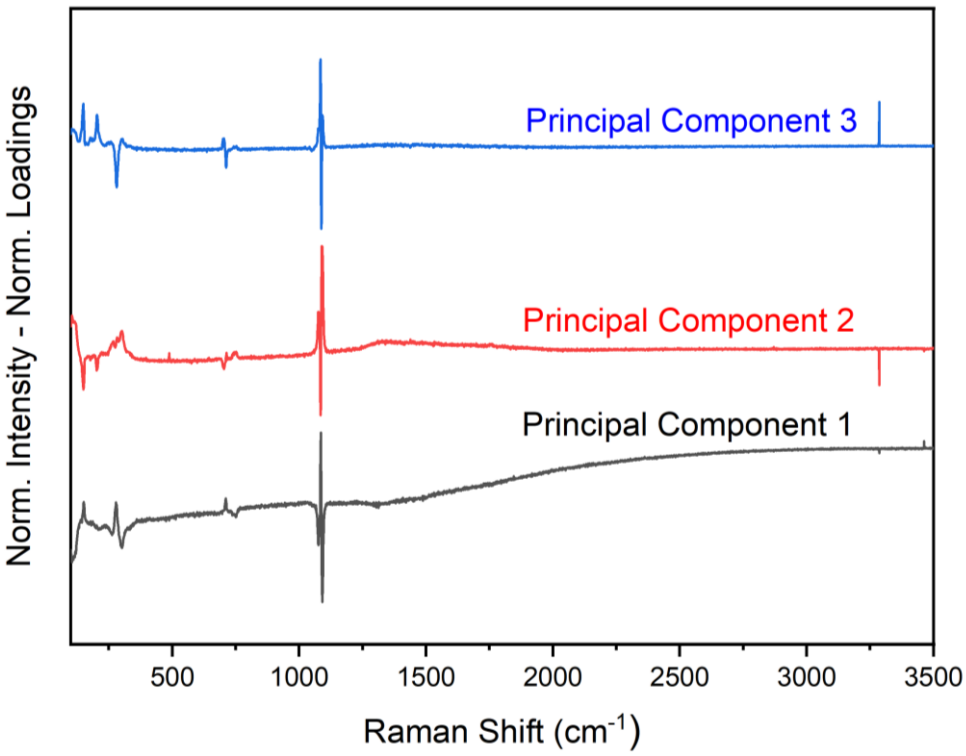

Figure 5.19. Plot of the loadings of the PCs for the PCA analysis of the Raman spectra.

The main features that are observed for PC1 are the main peak around 1086 cm^{-1} and smaller peaks at around 278 and 710 cm^{-1} which are related to various modes for calcite. For PC2, the peaks are centred at around 1088 and 300 cm^{-1} which are related to carbonyl stretching and lattice modes for vaterite. PC3 implies a low variability for the pattern, with a combination of vaterite and calcite features. Therefore, the polymorphs feature that are most commonly seen is aragonite. This would imply that Raman preferable shows more intense and defined peaks for aragonite than for the rest of the polymorphs of calcium carbonate, as it has been already discussed.

The use of PCA analysis for Raman spectra is an extensive practice, widely used for recognition of several substances[80,81] but barely used for polymorphic minerals.[82–84] The main limitation arrives from the selectivity of Raman showing greater sensitivity to the features for the polymorphs in the order of aragonite > calcite > vaterite. It shows the requirement of knowing the interaction of the phase of the material with the spectroscopic technique.

The selection rule of the different bonds corresponding to different atomic arrangements and the spectroscopic technique will be further understood when looking at the PCA analysis of the FTIR.

5.4.6 PCA of FTIR

Table 5.7. Percentage of variance represented by the three main components for FTIR PCA analysis.

Principal Component	Percentage of variance (%)	Cumulative (%)
1	57.38	57.38
2	20.52	77.90
3	1.27	79.17

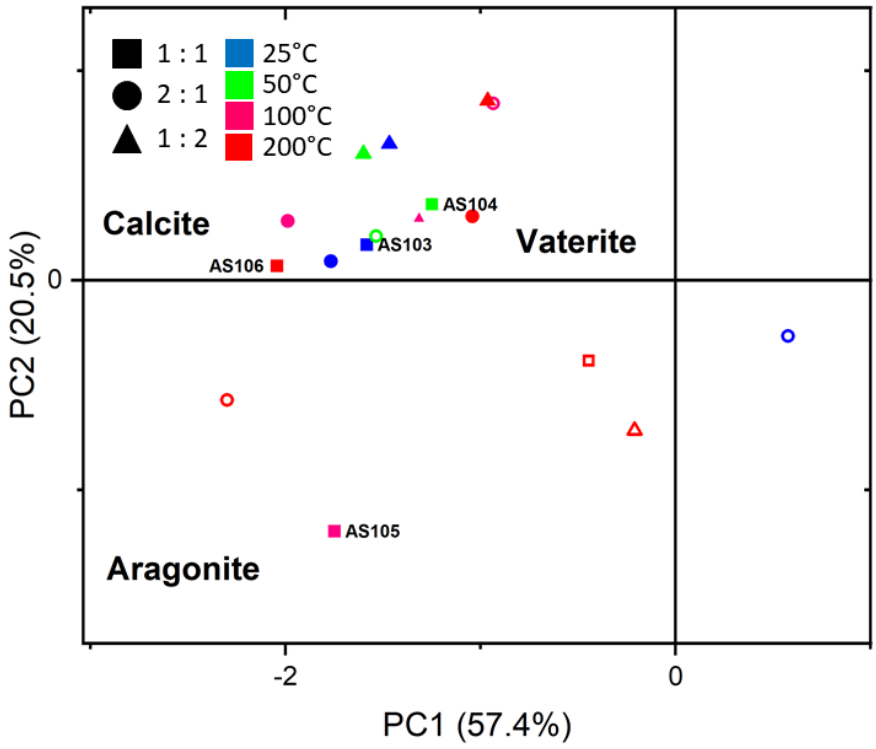

Figure 5.20. Principal Component Analysis of FTIR spectra from selected calcium carbonate samples. The empty symbols represent the use of bicarbonate as the carbonate precursor, filled symbols are the carbonate as precursor samples.

The main Principal Component obtained from the PCA of the FTIR spectra (PC1) expresses 57.38% of the total variance of the spectra analysed, where PC2 entails the 20.5% of the variability. The total percentage of variance shown by Figure 5.20 is 77.9%. When looking at the plotting of the PCA the disposition of the samples

in the graph is improved when compared to the analysis of Raman spectra. Nonetheless, it is worse than the PCA for normalised XRD patterns which reaches values of 90% when using the Pair Distribution Function of the patterns. Expressing the variation of the pattern is not sufficient. When observing the relative position of the samples with the coordinate axis, the percentage difference doesn't fully correspond with the values obtained from the PCs. The sample AS104 which contains the highest amount of vaterite is close to AS103 which is almost pure calcite. To assign the PCs to the corresponding polymorph expressed by them, the plot of the loadings can be observed. The different loadings used for the PCA are shown in Figure 5.21.

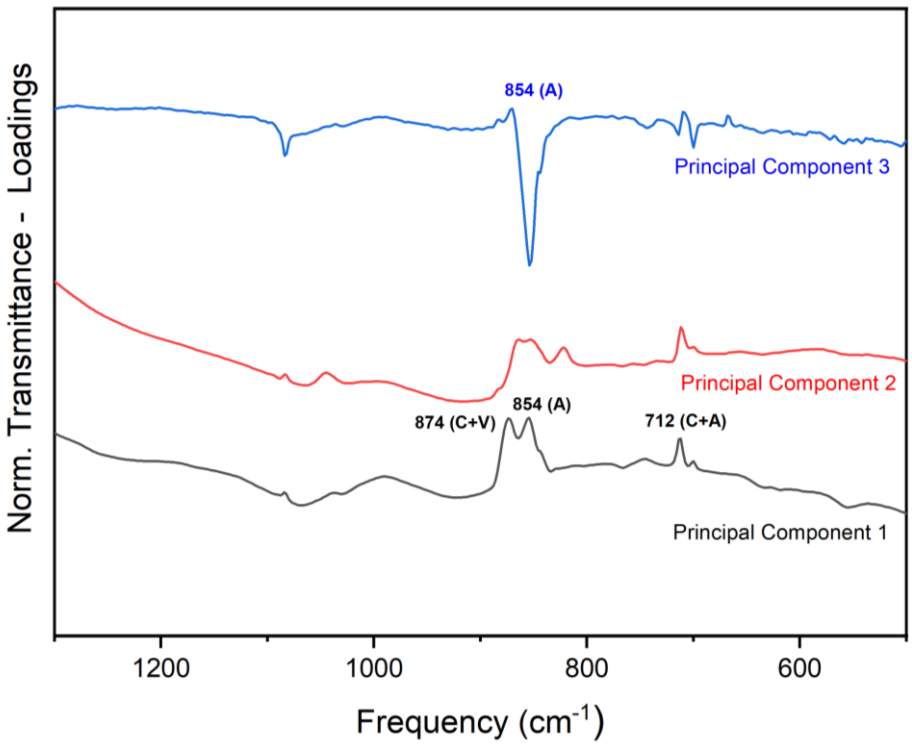

Figure 5.21. Plot of the loadings of the PCs for the PCA analysis of the FTIR spectra.

When observing Figure 5.21, PC1 and PC2 are observed to have similar features. The three most intense peaks are highlighted. The peaks shown correspond to all the three polymorphs in different intensities and iterations. Therefore, although PC1 has a higher calcite component, it doesn't fully express the polymorph content in the sample, as vaterite and aragonite play some part in the spectra as well. Similarly, with PC2, which expresses in a better way the features for vaterite, although is not specific enough to be directly correlated. Therefore, although FTIR expresses in a

better way than Raman the variability in the samples features, its analysis is not sufficiently specific to be assigned to any polymorph.

5.4.7 SEM from the extreme samples

From the previous Rietveld refinement calculations it is concluded that AS103 and AS104 are predominantly vaterite based, AS105 aragonite and AS106 calcite. Therefore, different shapes are expected from these three samples.

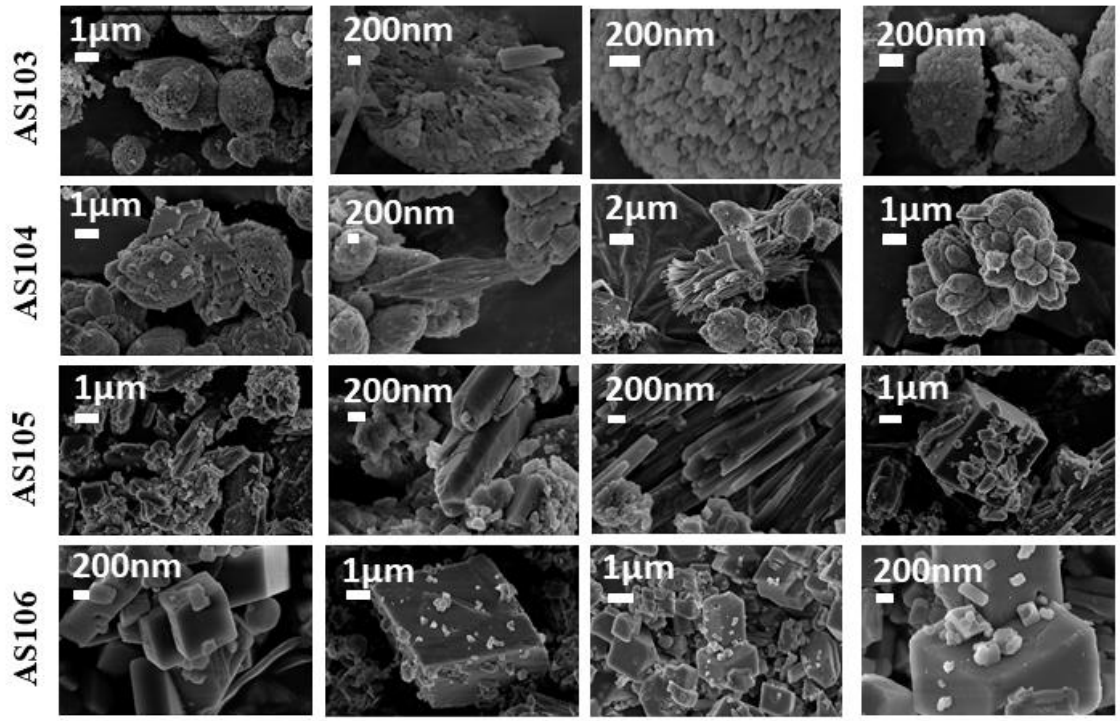

Figure 5.22. Corresponding SEM images from AS103 to AS106.

The SEM images show how the particle shape is strongly correlated to the predominant polymorph in the particle. For AS103 where vaterite is the main structure present, spherulitic nanoparticles are seen. Similar particles are present in AS104. Even though, in AS104 aragonite rods are interconnected to those spheres breaking the sphere-like shape. Calcite rhombohedra and aragonite rods coexists in AS105. In AS106 only calcite rhombohedra exist. These SEM images corroborate the phase percentage calculation and suggests some kind of interconnection between vaterite and aragonite polymorph selection. That interconnecting trend was previously suggested by the phase percentage graphs and was clearly highlighted by the PCA results.

5.5 Conclusions and Future Work

$CaCO_3$ has been successfully synthesised from two different carbonate sources, using the newly developed hydrothermal injection reactor. The relationship of the reaction temperature, relative concentration of the precursors, carbonate source employed and the polymorph selection have previously been highlighted. Few synthetic studies have been performed on the calcium carbonate system under hydrothermal conditions, as in this thesis. Importantly it has been shown that under these hydrothermal injection conditions different polymorphs may be obtained, despite the expectation that only calcite would form at higher temperatures, due to its thermodynamic stability. Phase percentage calculations on samples prepared in this work shows that this assumption cannot be taken as an imperative in every condition. It was found here that aragonite presence increases at higher CO_3^{2-}:Ca^{2+} ratios, even at the highest synthetic temperature of 200 °C. This proves that this compound is promoted at higher saturation ratios.

The synthesis at temperatures over the standard conditions reaches to unexpected results. Polymorph stability is then more closely linked to the carbonate saturation in solution than it was previously thought, influencing on thermodynamic properties of the crystal structures. It is crucial for mineralisation understanding of $CaCO_3$ at extreme conditions, where not only calcite is yielded. The next step for this approach would be to obtain the pure versions of each polymorph by extrapolating the optimal conditions the PCA representation of the synthetic landscape explored, varying temperature and saturation, as well, as with different precursors. Shape control has been easily reached with clear correlation between different techniques and synthesis conditions.

Principal component analysis (PCA) has been successfully employed for XRD diffraction patterns, that has been very rarely previously used.[85] It is a useful tool for obtaining trends and managing a huge dataset. By plotting the PCA graph the relationship between polymorph formation and condition of synthesis can be easily tracked. PDF correction has been needed to avoid clustering caused by the complexities of real XRD patterns and giving a better percentage of variability representation by these PCs. The main limitation for this technique is that clear sharp

peaks are needed for the calculations to discern the variability between the polymorphs present in the system. Nevertheless, by testing the system with many different ratios a map of polymorph formation and synthesis conditions (temperature, pressure and ratios) can be created. The PCA pattern has shown, as major conclusions, that carbonate precursor and 1:1 ratio is the best in order to obtain various different phase percentages with the minimal temperature variation. It not only has a scientific importance, but an industrial impact, as the calcium carbonate properties are closely related to the polymorph synthesised. Therefore, when a polymorph composition is needed, by just looking at the graph, the perfect conditions can be chosen.

Looking specifically at the statistical analysis of the different characterisation techniques it can be concluded that Principal Component Analysis of the XRD not only expresses the variability of the patterns in a greater way, but it is specific for each polymorph. Although PCA has been extensively employed for Raman and FTIR spectra, more so than XRD, these reported results shows that it carries some limitations that need to be considered when analysing different polymorphs of the same compound. When observing the Raman spectra of calcium carbonate, aragonite can be clearly distinguished as well as calcite, nonetheless, vaterite shows rather low intensity peaks which are difficult to be analysed by PCA. This lower intensity makes the differentiation for PCA analysis of the polymorphic features from the background of the measurement more difficult. For FTIR, although the intensity of the peaks is sufficient to discern one polymorph from the others, the position of the peaks is very similar, causing a greater coalescence of the samples in the PCA plot. Therefore, the PCA of the XRD patterns and in particular that one performed on the PDF has been proven to be a more precise methodology to qualitatively plot large amounts of datasets of different polymorphs.

Furthermore, from the Rietveld phase calculation and the SEM images, some relationship between aragonite and vaterite polymorph selection can be suggested where they switch on appearance depending on the conditions, showing a strong dependence on each other. There are no samples at the fourth corner of PCA where vaterite and aragonite would coexist, proving the polymorph selection between both. Therefore, the synthesis conditions for each one is extremely opposite.

Finally, for future approaches, some work on changing the component order (carbonate injected and calcium already in the reactor) has been started, as this is expected to change the saturation relationship in the early nucleation stages.

5.6 References

1 Y. Boyjoo, V. K. Pareek and J. Liu, *J. Mater. Chem. A*, 2014, **2**, 14270–14288.
2 M. Ni and B. D. Ratner, *Surf. Interface Anal.*, 2008, **40**, 1356–1361.
3 L. N. Plummer and E. Busenberg, *Geochim. Cosmochim. Acta*, 1982, **46**, 1011–1040.
4 G. S. Dieckmann, G. Nehrke, S. Papadimitriou, J. Göttlicher, R. Steininger, H. Kennedy, D. Wolf-Gladrow and D. N. Thomas, *Geophys. Res. Lett.*, 2008, **35**, 35–37.
5 K. Dahl and B. Buchardt, *J. Sediment. Res.*, 2006, **76**, 460–471.
6 G. F. Taylor, *Am. Mineral.*, 1975, **60**, 690–697.
7 R. Fischbeck and G. Müller, *Contrib. to Mineral. Petrol.*, 1971, **33**, 87–92.
8 J. D. Rodriguez-Blanco, S. Shaw, P. Bots, T. Roncal-Herrero and L. G. Benning, *Geochim. Cosmochim. Acta*, 2014, **127**, 204–220.
9 J. P. Andreassen, *J. Cryst. Growth*, 2005, **274**, 256–264.
10 J. D. Rodriguez-Blanco, S. Shaw and L. G. Benning, *Nanoscale*, 2011, **3**, 265–271.
11 I. M. Weiss, N. Tuross, L. Addadi and S. Weiner, *J. Exp. Zool.*, 2002, **293**, 478–491.
12 C. Y. Sun, M. A. Marcus, M. J. Frazier, A. J. Giuffre, T. Mass and P. U. P. A. Gilbert, *ACS Nano*, 2017, **11**, 6612–6622.
13 H. Liao, H. Mutvei, M. Sjöström, L. Hammarström and J. Li, *Biomaterials*, 2000, **21**, 457–468.
14 J. P. Gattuso, M. Frankignoulle, I. Bourge, S. Romaine and R. W. Buddemeier, *Glob. Planet. Change*, 1998, **18**, 37–46.
15 E. C. Shaw, S. R. Phinn, B. Tilbrook and A. Steven, *Limnol. Oceanogr.*, 2015, **60**, 777–788.
16 D. Evans, P. B. Webb, K. Penkman, R. Kröger and N. Allison, *Cryst. Growth Des.*, 2019, **19**, 4300–4313.
17 M. E. Hodson, L. G. Benning, B. Demarchi, K. E. H. Penkman, J. D. Rodriguez-Blanco, P. F. Schofield and E. A. A. Versteegh, *Geochem. Trans.*, , DOI:10.1186/s12932-015-0019-z.
18 A. Gal, S. Weiner and L. Addadi, *J. Am. Chem. Soc.*, 2010, **132**, 13208–13211.
19 P. U. P. A. Gilbert, T. Z. Forbes, A. Navrotsky, C. E. Killian and A. V. Radha, *Proc. Natl. Acad. Sci.*, 2010, **107**, 16438–16443.
20 J. Aizenberg, G. Lambert, S. Weiner and L. Addadi, *J. Am. Chem. Soc.*, 2002, **124**, 32–39.
21 N. Ishizawa, H. Setoguchi and K. Yanagisawa, *Sci. Rep.*, 2013, **3**, 9–11.
22 E. Mugnaioli, I. Andrusenko, T. Schüler, N. Loges, R. E. Dinnebier, M. Panthöfer, W. Tremel and U. Kolb, *Angew. Chemie*, 2012, **124**, 7148–7152.
23 B. Pokroy, A. N. Fitch and E. Zolotoyabko, *Cryst. Growth Des.*, 2007, **7**, 1580–1583.
24 Y. Suzuki, H. Mukai, T. Ishimura, T. D. Yokoyama, S. Sakata, T. Hirata, T. Iwatsuki and T. Mizuno, *Sci. Rep.*, 2016, **6**, 2–7.
25 T. Xu, J. A. Apps and K. Pruess, *Chem. Geol.*, 2005, **217**, 295–318.
26 Kharaka YK Campbell P Thorden JJ Thomas PB Cole DR Hovorka SD, *Geochim Cosmochim Acta*, 2010, **74**, A511–A511.
27 T. Bosak, A. H. Knoll and A. P. Petroff, *Annu. Rev. Earth Planet. Sci.*, 2013, **41**, 21–44.
28 H. A. Lowenstam and D. P. Abbott, *Science*, 1975, **188**, 363–365.
29 K. Fujihara, M. Kotaki and S. Ramakrishna, *Biomaterials*, 2005, **26**, 4139–4147.
30 T. Matschei, B. Lothenbach and F. P. Glasser, *Cem. Concr. Res.*, 2007, **37**, 551–558.
31 G. Hadiko, Y. S. Han, M. Fuji and M. Takahashi, *Mater. Lett.*, 2005, **59**, 2519–2522.
32 C. Yang, J. Zhang, W. Li, S. Shang and C. Guo, *Cryst. Res. Technol.*, 2017, **52**, 1–7.
33 J. Jia, Q. Liu, T. Yang, L. Wang and G. Ma, *J. Mater. Chem. B*, 2017, **5**, 1611–1623.
34 B. Rugabirwa, D. Murindababisha, Y. Li, Y. Hong, Y. Su, H. Wang and J. Li, *ACS Sustain. Chem. Eng.*, 2019, **7**, 6251–6258.
35 C. E. Killian, R. A. Metzler, Y. U. T. Gong, I. C. Olson, J. Aizenberg, Y. Politi, F. H. Wilt, A. Scholl, A. Young, A. Doran, M. Kunz, N. Tamura, S. N. Coppersmith and P. U. P. A. Gilbert, *J. Am. Chem. Soc.*, 2009, **131**, 18404–18409.

36 B. V. Parakhonskiy, A. Haase and R. Antolini, *Angew. Chemie - Int. Ed.*, 2012, **51**, 1195–1197.
37 C. C. Yang, W. Y. Wang, F. H. Lin and C. H. Hou, *Int. J. Mol. Sci.*, 2109, **20**(5), 1148.
38 V. K. LaMer and R. H. Dinegar, *J. Am. Chem. Soc.*, 1950, **72**, 4847–4854.
39 A. Navrotsky, *Proc. Natl. Acad. Sci.*, 2004, **101**, 12096–12101.
40 D. Horn and J. Rieger, *Angew. Chemie - Int. Ed.*, 2001, **40**, 4330–4361.
41 M. Faatz, F. Gröhn and G. Wegner, *Adv. Mater.*, 2004, **16**, 996–1000.
42 J. D. Rodriguez-Blanco, S. Shaw and L. G. Benning, *Mineral. Mag.*, 2008, **72**, 283–286.
43 A. L. Goodwin, F. M. Michel, B. L. Phillips, D. A. Keen, M. T. Dove and R. J. Reeder, *Chem. Mater.*, 2010, **22**, 3197–3205.
44 C. G. Sinn, R. Dimova and M. Antonietti, *Macromolecules*, 2004, **37**, 3444–3450.
45 D. Quigley and P. M. Rodger, *J. Chem. Phys.*, 2018, **128**, 221101
46 G. Scatchard, *Ann. N. Y. Acad. Sci.*, 1949, **51**, 660–672.
47 D. Gebauer, *Science*, 2008, **120**, 1819–1823.
48 R. Demichelis, P. Raiteri, J. D. Gale, D. Quigley and D. Gebauer, *Nat. Commun.*, 2011, **2**, 1–8.
49 A. V. Radha and A. Navrotsky, *Cryst. Growth Des.*, 2015, **15**, 70–78.
50 J. Ihli, W. C. Wong, E. H. Noel, Y. Y. Kim, A. N. Kulak, H. K. Christenson, M. J. Duer and F. C. Meldrum, *Nat. Commun.*, 2014, **5**, 1–10.
51 J. W. Morse, R. S. Arvidson and A. Lüttge, *Chem. Rev.*, 2007, **107**, 342–381.
52 Z. Zou, W. J. E. M. Habraken, G. Matveeva, A. C. S. Jensen, L. Bertinetti, M. A. Hood, C. Sun, P. U. P. A. Gilbert, I. Polishchuk, B. Pokroy, J. Mahamid, Y. Politi, S. Weiner, P. Werner, S. Bette, R. Dinnebier, U. Kolb, E. Zolotoyabko and P. Fratzl, *Science (80-.).*, 2019, **363**, 396–400.
53 J. H. E. Cartwright, A. G. Checa, J. D. Gale, D. Gebauer and C. I. Sainz-Díaz, *Angew. Chemie*, 2012, **124**, 12126–12137.
54 M. Farhadi Khouzani, D. M. Chevrier, P. Güttlein, K. Hauser, P. Zhang, N. Hedin and D. Gebauer, *CrystEngComm*, 2015, **17**, 4842–4849.
55 R. Innocenti Malini, Y. G. Bushuev, S. A. Hall, C. L. Freeman, P. M. Rodger and J. H. Harding, *CrystEngComm*, 2015, **18**, 92–101.
56 M. Farhadi-Khouzani, D. M. Chevrier, P. Zhang, N. Hedin and D. Gebauer, *Angew. Chemie - Int. Ed.*, 2016, **55**, 8117–8120.
57 D. L. G. Rowlands and R. K. Webster, *Nat. Phys. Sci.*, 1971, **229**, 158–158.
58 E. M. Pouget, P. H. H. Bomans, A. Dey, P. M. Frederik, G. de With and N. A. J. M. Sommerdijk, *J. Am. Chem. Soc.*, 2010, **132**, 11560–11565.
59 E. M. Pouget, P. H. H. Bomans, J. A. C. M. Goos, P. M. Frederik, G. de With and N. A. J. M. Sommerdijk, *Science*, 2009, **323**, 1455–1458.
60 Q. Shen, H. Wei, Y. Zhou, Y. Huang, H. Yang, D. Wang and D. Xu, *J. Phys. Chem. B*, 2006, **110**, 2994–3000.
61 P. Bots, L. G. Benning, J. D. Rodriguez-Blanco, T. Roncal-Herrero and S. Shaw, *Cryst. Growth Des.*, 2012, **12**, 3806–3814.
62 J. D. Rodriguez-Blanco, S. Shaw, P. Bots, T. Roncal-Herrero and L. G. Benning, *J. Alloys Compd.*, 2012, **536**, S477–S479.
63 K. K. Sand, J. D. Rodriguez-Blanco, E. Makovicky, L. G. Benning and S. L. S. Stipp, *Cryst. Growth Des.*, 2012, **12**, 842–853.
64 R. Beck and J. P. Andreassen, *Cryst. Growth Des.*, 2010, **10**, 2934–2947.
65 P. Raiteri, R. Demichelis, J. D. Gale, M. Kellermeier, D. Gebauer, D. Quigley, L. B. Wright and T. R. Walsh, *Faraday Discuss.*, 2012, **159**, 61–85.
66 D. Gebauer, M. Kellermeier, J. D. Gale, L. Bergström and H. Cölfen, *Chem. Soc. Rev.*, 2014, **43**, 2348–2371.
67 Crystallography Open Database, http://www.crystallography.net/cod/.
68 U. Wehrmeister, A. L. Soldati, D. E. Jacob, T. Häger and W. Hofmeister, *J. Raman Spectrosc.*, 2010, **41**, 193–201.
69 C. Gabrielli, R. Jaouhari, S. Joiret and G. Maurin, *J. Raman Spectrosc.*, 2000, **31**, 497–501.
70 C. Paper, N. Buzgar, U. Alexandru, I. Cuza, R. Database, R. S. View and N. Buzgar, *Geol. Tomul LV.*, 2009, **2**, 97–112.
71 G. Behrens and R. Ubic, *Spectrosc. Lett.*, 2006, **28**, 983–995.
72 L. Dupont, F. Portemer and M. Figlarz, *J. Mater. Chem.*, 1997, **7**, 797–800.

73 H. Guo, Z. Qin, P. Qian, P. Yu, S. Cui and W. Wang, *Adv. Powder Technol.*, 2011, **22**, 777–783.
74 C. Shivkumara, P. Singh, A. Gupta and M. S. Hegde, *Mater. Res. Bull.*, 2006, **41**, 1455–1460.
75 C. G. Kontoyannis and N. V. Vagenas, *Analyst*, 2000, **125**, 251–255.
76 G. Malmros and J. O. Thomas, *J. Appl. Crystallogr.*, 1977, **10**, 7–11.
77 H. M. Rietveld, *Aust. J. Phys.*, 1988, **41**, 113–116.
78 B. H. Toby, *J. Appl. Crystallogr.*, 2001, **34**, 210–213.
79 X. Qiu, J. W. Thompson and S. J. L. Billinge, *J. Appl. Crystallogr.*, 2004, **37**, 678–678.
80 C. Frausto-Reyes, C. Medina-Gutiérrez, R. Sato-Berrú and L. R. Sahagún, *Spectrochim. Acta - Part A Mol. Biomol. Spectrosc.*, 2005, **61**, 2657–2662.
81 K. Sivashanmugan, K. Squire, A. Tan, Y. Zhao, J. A. Kraai, G. L. Rorrer and A. X. Wang, *ACS Sensors*, 2019, **4**, 1109–1117.
82 A. G. Ilie, M. Scarisoareanu, I. Morjan, E. Dutu, M. Badiceanu and I. Mihailescu, *Appl. Surf. Sci.*, 2017, **417**, 93–103.
83 X. He, Y. Liu, S. Huang, Y. Liu, X. Pu and T. Xu, *RSC Adv.*, 2018, **8**, 23348–23352.
84 G. M. Sarabia and B. Sharma, *Analyst*, 2021, **146**, 6288–6296.
85 C. Collins, M. S. Dyer, M. J. Pitcher, G. F. S. Whitehead, M. Zanella, P. Mandal, J. B. Claridge, G. R. Darling and M. J. Rosseinsky, *Nature*, 2017, **546**, 280–284.

Chapter 6. Conclusions and Future Work

6.1 Conclusions and Future Work

Hydrothermal synthesis has been effectively employed for the synthesis of several materials: silicates, phosphates, and carbonates. It shows the versatility of this synthetic method, capable of yielding such different minerals following similar reaction methodologies. The synthesis of the silicates was carried by the used of standard "batch" hydrothermal synthesis. The hydrothermal injection reactor was employed for the synthesis of the phosphates and carbonates.

Firstly, for the synthesis of zircon-type silicates the optimum conditions for the synthesis of pure zircon ($ZrSiO_4$) and stetindite ($CeSiO_4$) have been reported in this thesis. The common ground for the mineralisation of the pure compounds was achieved at acidic conditions (pH = 1), longer reaction times than 1 day and lower temperatures than 200°C. From the zircon XRD pattern analysed an anisotropic behaviour of the peak shape was acknowledged. That differentiator feature was never seen for the samples of pure stetindite. When observing the TEM images zircon showed a directional growth evidenced by platelets and sharp-looking rods. Stetindite, on the other hand, only exhibited spherical-looking crystals. The different behaviour was justified by the presence of structural water in along the tunnels allocated in the (001) direction. The presence of these water molecules was supported by FTIR spectra water bands for zircon. In order to obtain a better idea of the effect water in these two materials DSC-TGA measurements of the different sample need to be carried in order to corroborate the presence of structural water at the silicate structure and what is the temperature require to extract it. From this methodology it may be estimated if the water belongs to the structure or is only superficially bonded. By XRD analysis of the resultant samples could show if the anisotropic behaviour of zircon is persistent or cease after the water removal from the lattice. Therefore, the mechanism by which the water affects the growth of the zircon particles could be established.

The formation of mixed silicates, $Ce_xZr_{1-x}SiO_4$, was attempted following the same optimum reaction conditions for zircon and stetindite. It was found that only $Ce_{0.2}Zr_{0.8}SiO_4$ could be yielded as an intermediate silicate. This presence of cerium atoms in a mainly zirconium silicate was justified by the higher stability of zircon *versus* the corresponding oxides, zirconia (ZrO_2) and silica (SiO_2). On the other hand, stetindite is

known to be metastable to the oxides, therefore the introduction of an additional metal in the reaction will destabilise the formation of the silicate only yielding the oxides, ceria (CeO_2) and SiO_2, or not accommodating the metal and forming pure stetindite. Similar behaviour has been reported for the $(Zr,Pu)SiO_4$ system. Understanding the ability of zircon to accommodate other metals in the structure is essential as it has been proposed as a promising repository for SNF due to the chemical and thermal stability. As well, it is highly used in geochronology studies for dating rocks where it is capable to store different metals within its structure for an extended period of time. Therefore, more synthetic conditions are required to understand the loading capacity of zircon. The presence of actinides and lanthanides in the reaction can be a promising future outlook to understand the most effective way for them to be stored in the zircon structure. Finally, the conditions proposed can be attempted to the synthesis of other metal silicates and compounds that appear in similar environments, such as SNF repositories as the window of stability must be similar due to be formed in similar conditions. Other silicates could be synthesised such as the never acknowledged either in nature or synthetically $PbSiO_4$ or more complicated silicate containing minerals such as cuprosklodowskite, $Cu[(UO_2)_2(SiO_3OH)_2]\cdot 6H_2O$.

As the optimum conditions for obtaining zircon and stetindite were unveiled, the synthesis of another silicate, thorite ($ThSiO_4$), was carried out. The best version of pure thorite was similarly achieved at pH = 1. The temperature was slightly higher than the optimal 150°C to avoid the presence of water in the structure. The XRD pattern for that sample was subjected to Le Bail refinement to obtain the cell parameters of the material. From comparison of the pattern with the model an evident peak shifting to lower angles is observed. This was reflected by a bigger unit cell than the reported values. In order to obtain a precise pattern of the samples high-energy X-Ray and neutron diffraction will be carried for the thorite sample. Measurement of the diffraction pattern under high-pressure in order to unveil a potential structural transition from thorite to huttonite at those extreme conditions. Furthermore, the sample is proposed to be sent for SEM imaging and FTIR measurements to recognise the morphology of the particle yielded as well as to gain more knowledge about the presence of structural water to compare with the other silicates in this project.

Although coffinite was not obtained pure, some promising results were obtained for the synthetic conditions attempted. The synthesis at pH = 1, 150°C and 3 days of reaction showed similar peaks to the ones reported for coffinite. More attempts need to be carried out to obtain pure coffinite, as well as additional parameters in the reaction need to be tweaked. It is supported by the idea of the easy formation of UO_2 directly from reaction and the metastability of coffinite *versus* the oxides. Therefore the optimum stability conditions must be narrower than for the silicates attempted. The use of a reducing agent that hinders the oxidation of uranium in solution, such as hydrazine has been proposed in the group along with the use of different uranium precursors such as uranium (IV) triflates in order to promote the stabilisation of the required U(IV).

Secondly, calcium phosphate was synthesised by using the newly-designed hydrothermal injection reactor at different conditions (temperature, Ca/P ratio, …). The samples were characterised by XRD and FTIR in order to deduce the components present in the samples synthetised. To obtain the exact concentration of the minerals in the structure, Rietveld refinement was carried against the XRD patterns. Due to the large number of samples obtained and the different synthetic conditions that intervene in the outcome of the reactions, Principal Component Analysis of the XRD patterns was conducted. These refinements were capable of showing the relationship of the compounds obtained and the optimal conditions for their synthesis in a visual and simple way. Brushite was acknowledged to be the phosphate mineral present at the largest number of samples. Monetite was obtained preferentially for temperatures higher than 50°C. HAP required a Ca/P ratio larger than 1.67 and it was successfully obtained at intermediate temperatures (50 and 100°C). PCA simplified the obtention of trends for such a large dataset of reactions. The use of the reactor also permitted to obtain a large number of samples in a shorter time than for the batch reaction. The mapping of the correlation of conditions *vs.* the selection of compound synthesised was readily more accessible by this technique. It goes in contrast with the classic methodology (as followed for the silicates) where several reactions are carried out and later analysed to obtain the optimal synthetic conditions. Regarding the phosphates, a large dataset of samples was obtained by the synthesis in the injection reactor at every condition. The optimum conditions for the synthesis of the target compound were then stabilised by PCA of the XRD graphically. It is less time-consuming and as precise as analysing each X-ray

diffraction pattern individually. PCA correlates the different variables making it easier to show the different trends of samples synthesis. This procedure is therefore a great candidate to screen the most advantageous conditions for the synthesis of any material. It needs to be considered that PCA is a statistical approach with no physical meaning that require of a numerical analysis, such as Rietveld refinement, to corroborate the trend shown by the graph.

Thirdly, similarly to the calcium orthophosphates, calcium carbonate was synthesised by the hydrothermal injection reactor. The main different lies on the fact that calcium carbonate exhibits different polymorphs rather than different compounds as the orthophosphate when the conditions are modified. Calcite, vaterite and aragonite were synthesised at ratios for different conditions. The samples were analysed by XRD, FTIR and Raman. Additionally, to obtain the percentages of the different polymorphs present in the sample, Rietveld refinement was performed for the diffraction patterns. Again, due to the large number of samples synthesised by this technique PCA was required to obtain the correlation of the polymorph selection with the synthetic conditions. The process of analysis of the samples was extremely simplified by PCA. Although the PCA of the XRD patterns precisely represented the variability of the patterns, and therefore the relative position of the polymorph content along the two axes, it was remarkably improved when applying PCA to the Pair Distribution Function (PDF) calculated from the patterns. The improvement was justified as PDF is a more specific representation of the atomic position of the atoms in the unit cell discriminating against other features that might appear in XRD patterns. XRD is influenced in a greater way by some external macroscopic effects relative to the measurement or the sample itself: such as background effect, shape broadening by crystal size or shifting of the peak position due to strain. Therefore, the representation of the variability by the PCA of the PDF increased from 77.6% by the use of only the XRD patterns to 90.63%. From the graphs it was shown that calcite is the pattern that is obtained in a larger number of samples as it is the thermodynamically more stable structure for calcium carbonate. Vaterite was obtained at milder temperatures and aragonite is more influenced by the carbonate to calcium ratio employed for the synthesis. Additionally, it was proven that using sodium carbonate as the precursor yields the largest differences in polymorph content of the two precursors attempted. The carbonate to calcium ratio 1:1 promotes the most prominent differences. Additional variables can be

introduced for the synthesis, such as pH control and/or changing the precursor injected. As well, it could be compared to the "batch reactions" to prove how effective is the injection reactor controlling the polymorph formed. The PCA analysis of the Raman and FTIR compared to the one exhibited by XRD showed less precise representation of the polymorph content by the variability expressed by their spectra. Raman has been proven to show preferentially the features for aragonite, while FTIR is more specific for vaterite presence. Therefore, it is ratified that when analysing the polymorph composition by PCA, XRD is the best candidate.

Additionally, in these complicated nucleation processes where the different polymorphs are correlated and there's a continuous evolution from prenucleation clusters to crystalline materials, *in situ* measurements could be carried out. Real-time diffraction tracking of the carbonates evolution is proposed as a great candidate. As well, in situ Raman measurements in the reactor can be carried on testing the features along the reaction. It would show the nucleation and growth pathways of carbonates and the polymorph selection. At the same time Raman or IR tracking combined with the known principal components in real time could achieve a representation of the polymorph content at different times. It is a process that can be carried out industrially to effectively test the outliers form the target composition calculated by PCA.

Among the multiple results, this thesis has shown some conclusions which establish a novel procedure for the easy plotting and analysis of the XRD pattern data by PCA. Although it is a mere statistical approximation, when it is coupled with a physical meaning, like polymorph composition determined by Rietveld Refinement, it has been shown to be a very powerful technique to understand the processes followed by the material synthetised. To understand the novelty of this technique previous literature can be acknowledged and compared to our work. PCA has arisen as a powerful technique for the analysis of multicomponent systems by various techniques: FTIR,[1,2] Raman,[3–5] X-ray absorption,[6] among many others. Nonetheless PCA usually drives to complicated systems to be analysed, the requirement of using various complementary techniques to understand the results and low selectivity of the peaks in the case of powder-XRD.[7] The results obtained in Chapter 4 show that PCA was capable of describing the relationship between the synthetic conditions and the phosphate formed from the analysis of the XRD patterns. Although PCA has been previously performed for the analysis of the composition of

phosphates,[8] to the best of our knowledge it has never been employed for the correlation of the phosphate formation conditions and the XRD patterns. This serves as a great approach in order to predict and design a targeted synthesis where a certain composition is required. By an already trained matrix, the conditions for the synthesis of a specific material can be acknowledged. As well it serves as a great analytical technique to recognise the composition from the XRD without any further complicated analysis,[9] just by introducing the pattern in the matrix the different components are discriminated and plotted in reference with the rest of the already analysed samples within seconds.

Secondly, the main limitation for the use of PCA for the XRD patterns, as already mentioned, is the inability to discriminate overlapping peaks and high background in respect to the peaks from the material. In Chapter 5 those limitations are overcome by employing the PDF of the XRD patterns as the subject of the principal component analysis. By obtaining a structural description of the atoms in the crystal a better description is achieved by PCA. This approach has been successfully performed already for various materials,[10,11] nonetheless the novelty resides on the description of the polymorphic content expressed for calcium carbonate by tracking the optimum synthetic conditions by the novel hydrothermal injection reactor tracking feature. As the conditions of synthesis could be tracked there is a direct correlation of the polymorphic content with the conditions of synthesis. This could describe the processes followed for the formation of each material and describe the trends of preferential formation related to the conditions of synthesis. This is critical for the industrial application of these materials. Each polymorph will exhibit different characteristics that can be industrially explored. By this analysis, just by looking at the map of components the optimal synthetic conditions can be extrapolated in an easy and understandable way. Additionally, it is the first time, to the best of our knowledge, that PCA shows such a great selectivity for the plotting of the PDFs obtained from a low-energy source X-ray diffractometer, proving it to be accessible to a larger number of researchers. Finally, PCA showed the greater sensitivity when analysing diffraction patterns rather than spectroscopic methods. It describes in a greater way the polymorphic relationship between samples when plotting the PCA. Raman scattering and FTIR suffer an evident limitation by preferentially describing rather one or the other polymorph, while in this thesis it is shown that XRD is the most optimal technique to obtain this description.

In terms of publications, which manuscripts are already being written, the ones chosen are the following:

- Chapter 3: “Mild Hydrothermal synthesis of Zircon-type silicates ($MSiO_4$) as analogues to radioactive species”.

  There’s already planned work on obtaining coffinite by the conditions tested in this chapter as well as the potential formation of $PbSiO_4$ with some promising results. So depending on the outcome of those experiments rather one or two publications could be extracted from this chapter.
- Chapter 4: “Principal Component Analysis for the Hydrothermal Injection Synthesis of Calcium Orthophosphates”.

  It will contain a full description of the synthesis of the calcium orthophosphates (brushite, monetite and hydroxyapatite) as described in the chapter. As well, the corresponding PCA analysis to obtain the trends for the synthetic conditions.
- Chapter 5: “Hydrothermal Injection for the Phase-Controlled Synthesis of Calcium Carbonate and its polymorphic mapping by Principal Component Analysis (PCA)”.

  In this publication a full description of the calcium carbonate synthesis will be included by the novel reactor. As well the analysis by PCA of the results by PDF and comparison to the XRD, Raman and FTIR to show the advantages of using the structural description rather than the other techniques.

6.2 References

1 S. Suresh, S. Karthikeyan and K. Jayamoorthy, *J. Sci. Adv. Mater. Devices*, 2016, **1**, 343–350.
2 T. Dou, B. Zhou, S. Hu and P. Zhang, *Polymer (Guildf).*, 2021, **236**, 124318.
3 A. G. Ilie, M. Scarisoareanu, I. Morjan, E. Dutu, M. Badiceanu and I. Mihailescu, *Appl. Surf. Sci.*, 2017, **417**, 93–103.
4 K. Sivashanmugan, K. Squire, A. Tan, Y. Zhao, J. A. Kraai, G. L. Rorrer and A. X. Wang, *ACS Sensors*, 2019, **4**, 1109–1117.
5 J. Lim, J. Nam, H. Shin, J. Park, H. Song, M. Kang, K. Lim and Y. Choi, *Anal. Chem.*, 2019, **91**, 5677–5684.
6 G. A. Horrocks, E. J. Braham, Y. Liang, L. R. De Jesus, J. Jude, J. M. Velázquez, D. Prendergast and S. Banerjee, *J. Phys. Chem. C*, 2016, **120**, 23922–23932.
7 J. S. Clemente, S. Beauchemin, Y. Thibault, T. MacKinnon and D. Smith, *ACS Omega*, 2018, **3**, 6931–6944.
8 M. Kleine-Boymann, M. Rohnke, A. Henss, K. Peppler, J. Sann and J. Janek, *Appl. Surf. Sci.*, 2014, **309**, 27–32.
9 J. M. Cole, X. Cheng and M. C. Payne, *Inorg. Chem.*, 2016, **55**, 10870–10880.
10 K. W. Chapman, S. H. Lapidus and P. J. Chupas, *J. Appl. Crystallogr.*, 2015, **48**, 1619–1626.
11 X. Mu, L. Chen, R. Mikut, H. Hahn and C. Kübel, *Acta Mater.*, 2021, **212**, 116932.

Appendices

Appendix A Hydrothermal Injection Synthesis of Calcium Orthophosphates

Raman

All the Raman spectra can be compared to the reported using the data provided by the RRUF™ Project.[91]

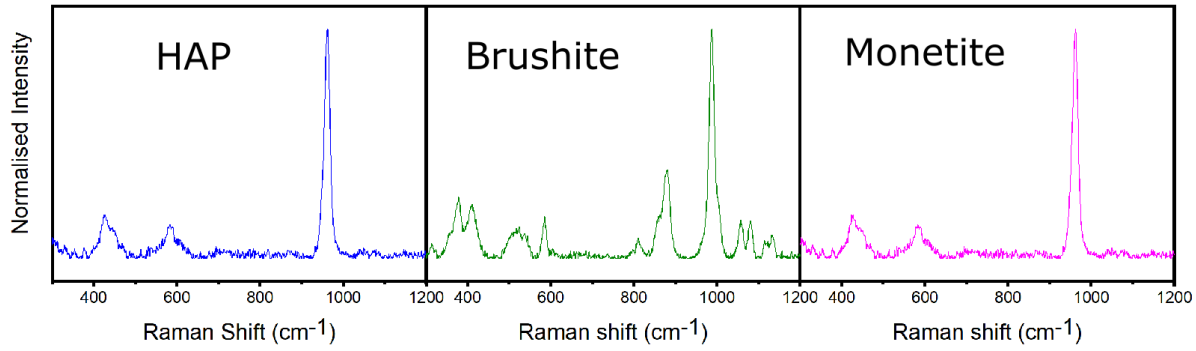

Figure A. 1. Model Raman spectra for the calcium orthophosphates.

Raman spectra were obtained using a Renishaw Raman Microscope with a 785 nm laser. The measurement ranged from 300 to 1300 cm^{-1} with an exposure time of 10 seconds for 50 cycles.

All the Raman active modes for brushite, monetite and HAP and the corresponding assignments are summarised in Table A. 1, Table A. 2, and Table A. 3, respectively.

Table A. 1. Raman shifts and assignments for brushite.[92] The intensity of the peaks is expressed as (w) weak, (m) medium, (s) strong, (vs) very strong and (br) broad.

Raman Shift (cm-1)	Assignment
1119 (w)	O-H in-plane bending
1083 (m)	O-H in-plane bending
1060 (m)	PO stretching
998 (vs)	PO stretching
880 (m)	P-O(H) stretching
784 (w, br)	Water libration
588 (m)	Water libration
525 (m)	PO bending
414 (m)	PO bending
383 (m)	Water translation
323 (w)	PO bending

Table A. 2. Raman shifts and assignments for monetite.[92] The intensity of the peaks is expressed as (m) medium, (s) strong and (vs) very strong.

Raman Shift (cm^{-1})	Assignment
1133 (m)	PO stretching (ν_3)
1095 (m)	PO stretching (ν_3)
988 (vs)	PO stretching (ν_1)
901 (s)	P-O(H) stretching (ν_3)
591 (m)	PO bending (ν_4)
562 (m)	PO bending (ν_4)
420 (m)	PO bending (ν_2)
395 (m)	PO bending (ν_2)

Table A. 3. Raman shifts and assignments for HAP.[93] The intensity of the peaks is expressed as (vw) very weak, (w) weak, (m) medium, (vs) very strong.

Raman Shift (cm^{-1})	Assignment
1076 (w)	PO asymmetric stretching (ν_3)
1054 (w)	PO asymmetric stretching (ν_3)
1046 (m)	PO asymmetric stretching (ν_3)
1030 (w)	PO asymmetric stretching (ν_3)
961 (vs)	PO Symmetric stretching (ν_1)
620 (vw)	PO bending mode (ν_4)
610 (w)	PO bending mode (ν_4)
594 (m)	PO bending mode (ν_4)
582 (w)	PO bending mode (ν_4)
447 (m)	PO bending mode (ν_2)
433 (w)	PO bending mode (ν_2)

The corresponding Raman spectra recorded for the samples are shown below in Figure A. 6 and Figure A. 7.

Ca/P = 0.5 – $(NH_4)_2HPO_4$ phosphate precursor

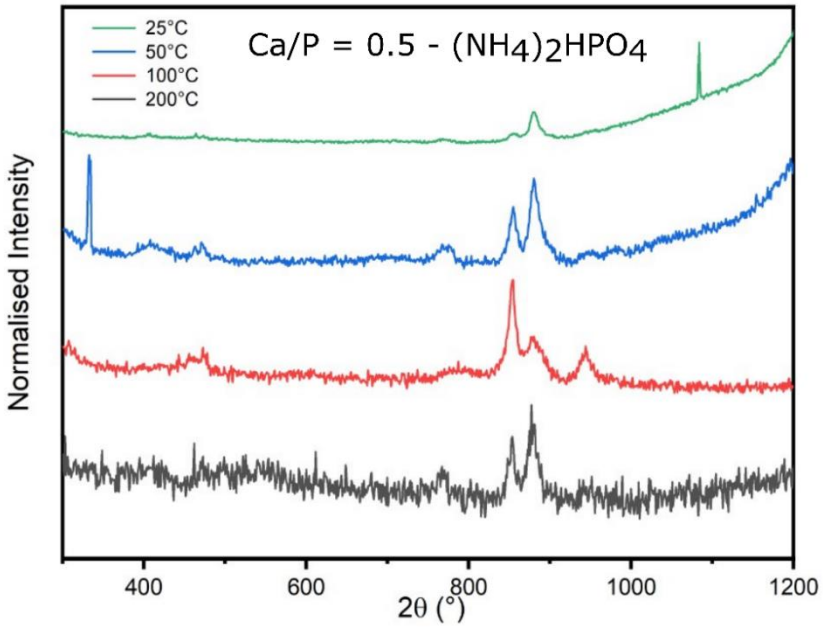

Figure A. 2. Raman spectra for Ca/P ratio 0.5 using $(NH_4)_2HPO_4$ as the phosphate precursor in the reaction.

Ca/P = 1.67 - $Na_2HPO_4 \cdot 7H_2O$ phosphate precursor buffered pH = 10

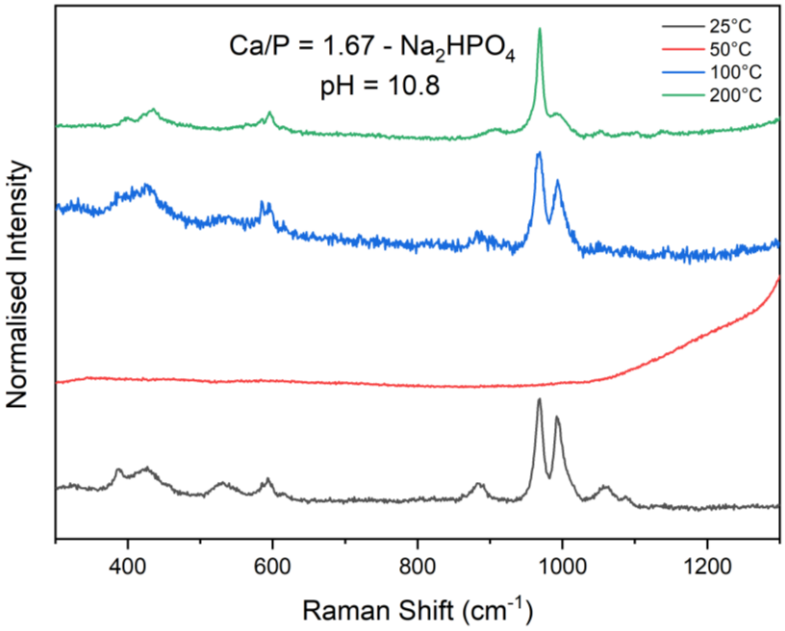

Figure A. 3. Raman spectra for Ca/P ratio 1.67 using Na_2HPO_4 as the phosphate precursor in the reaction, buffered to pH = 10.8.

Appendix B Hydrothermal Injection for the Phase-Controlled Synthesis of Calcium Carbonate

XRD

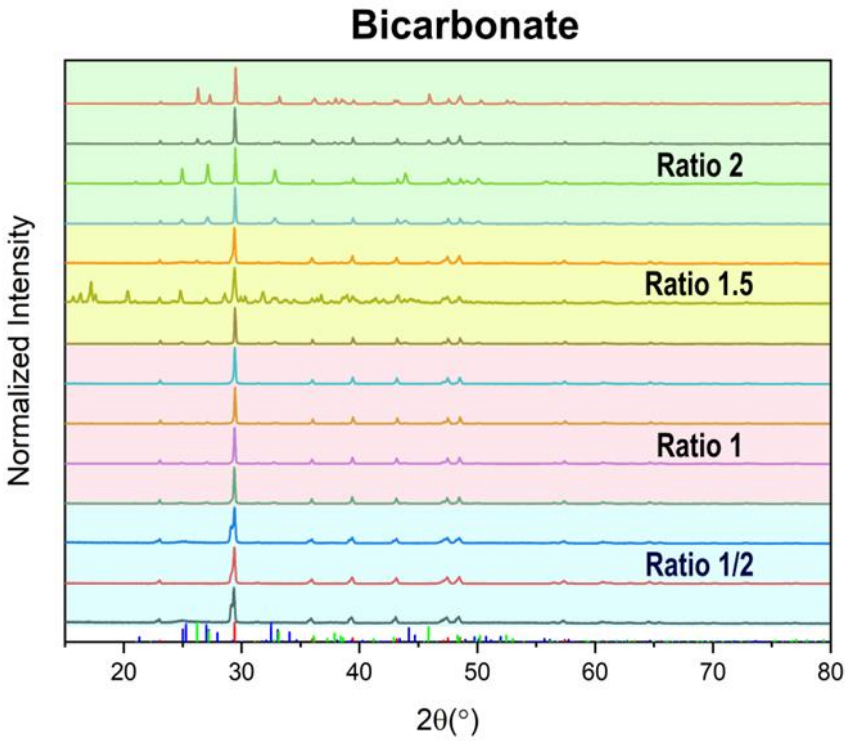

Figure A. 4. Powder XRD patterns of the samples used for principal component analysis. Bicarbonate was used as precursor in the vessel and calcium was injected through the HPLC. The ratio is written as CO_3^{2-}/Ca^{2+}. The vertical lines below represent the XRD model for each polymorph: red-calcite, blue-vaterite and green-aragonite.

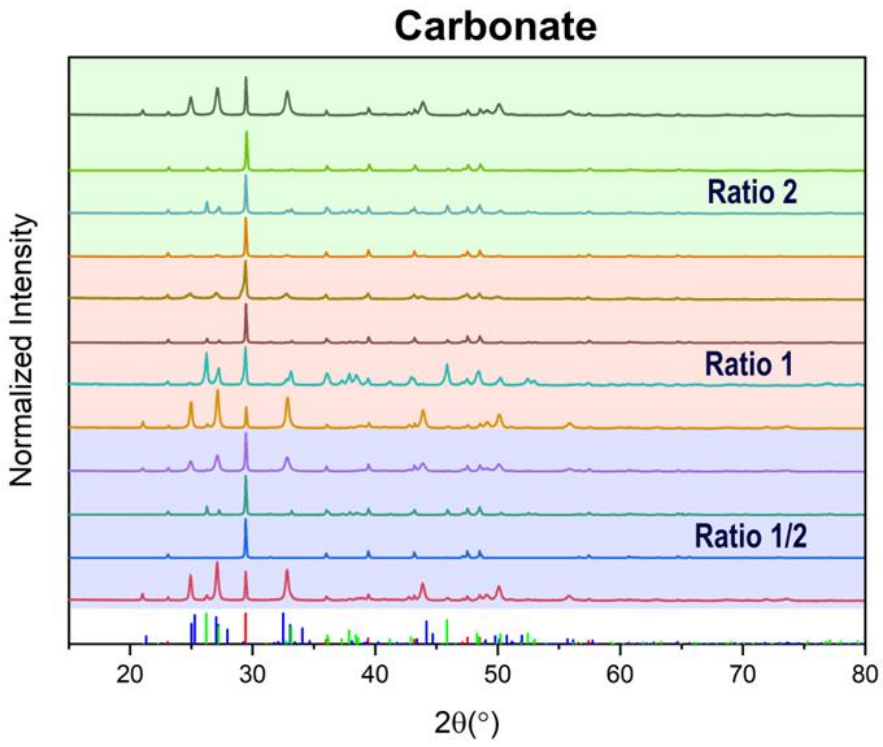

Figure A. 5. Powder XRD patterns of the samples used for principal component analysis. Bicarbonate was used as precursor in the vessel and calcium was injected through the HPLC. The ratio is written as CO_3^{2-}/Ca^{2+}. The vertical lines below represent the XRD model for each polymorph: red-calcite, blue-vaterite and green-aragonite.

Raman

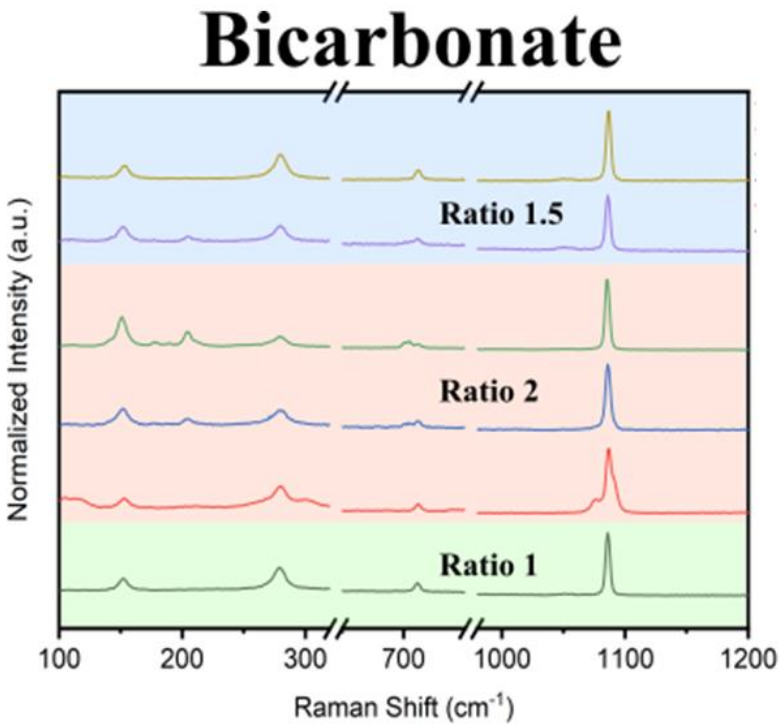

Figure A. 6. Raman spectra obtained for bicarbonate as a CO_3^{2-} precursor.

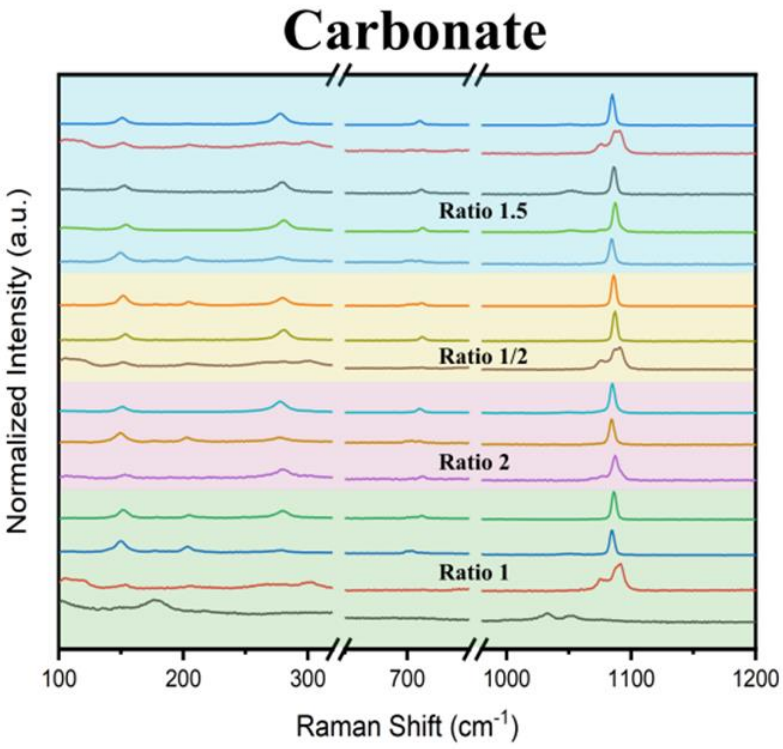

Figure A. 7. Raman spectra obtained for carbonate as a CO_3^{2-} precursor.

FTIR

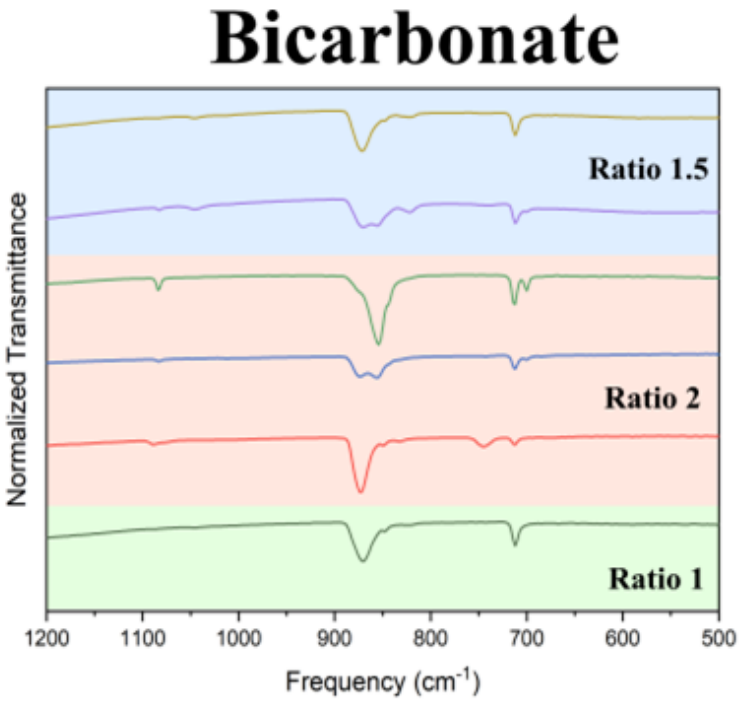

Figure A. 8. FT-IR spectra from bicarbonate as a source of CO_3^{2-} .

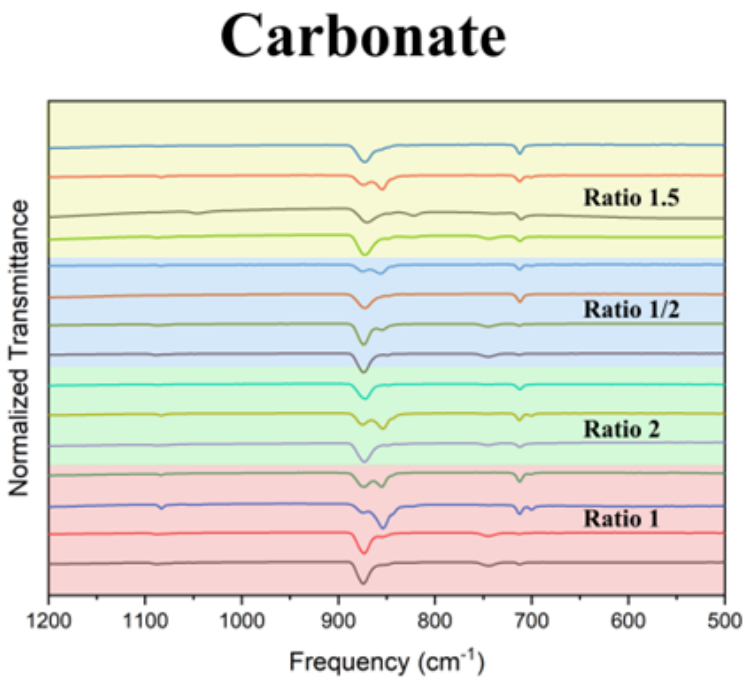

Figure A. 9. FT-IR spectra from carbonate as a source of CO_3^{2-} .

Reactor Profiles

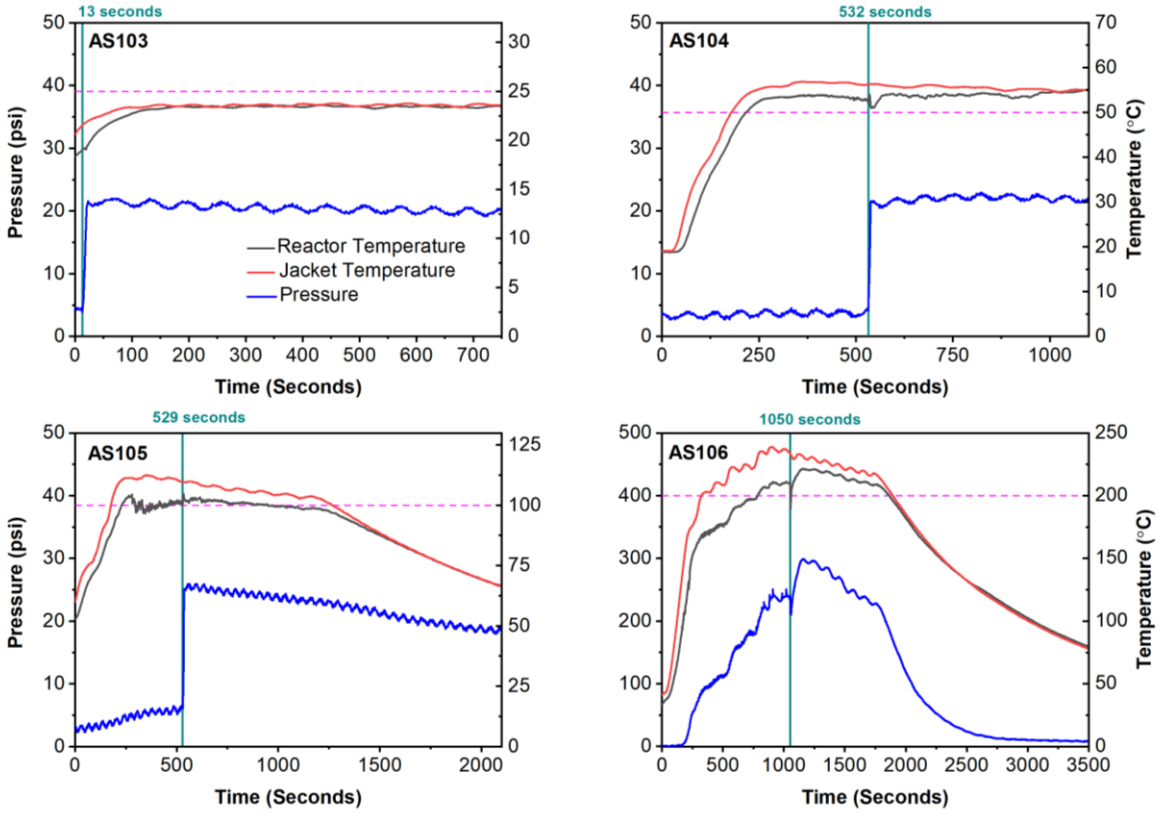

Figure A. 10. Reactor profiles for samples AS103-106 showing the reactor and heating jacket temperature on the right axis and the pressure for the reactor vessel at the left axis. The cyan blue vertical solid line shows the injection point, and the dashed pink line is aligned to the target temperature.

Appendix C Rietveld Refinement Parameters

Chapter 3. Calcium Orthophosphates

Table A. 4. Synthesis conditions and sample coding used for the hydrothermal injection samples of calcium orthophosphates.

PO_4^{3-} Source	Ca/P Ratio	T (ºC)	Sample name
$(NH_4)_2HPO_4$	0.5	25	FD001
		50	FD002
		100	FD003
		200	FD004
	1.5	25	FD005
		50	FD006
		100	FD007
		200	FD008
	1.67	25	FD009
		50	FD010
		100	FD011
	3	25	FD012
		50	FD013
		100	FD014
		200	FD015
Na_2HPO_4	1.67	25	FD016
		50	FD021
		100	FD022
		200	FD023
	1.67 (pH 10.8)	25	FD025
		50	FD026
		100	FD027
		200	FD028
	3	25	FD029
		50	FD030
		100	FD031
		200	FD032

Table A. 5. Rietveld Refinement parameters for the hydrothermal injection samples of calcium orthophosphates.

Sample name	R_{wp} = 0.1488	R_p = 0.1195	$R\chi^2$ = 9.036	Brushite	Monetite	Hydroxyapatite
FD001	Unit Cell Parameters (Å)			6.37 (a), 15.20 (b), 5.82 (c)	6.92 (a), 6.63 (b), 6.99 (c)	9.40 (a), 18.99 (b), 6.86 (c)
	Unit Cell Angles (°)			90.00 (α), 118.52 (β), 90.00 (γ)	96.52 (α), 104.02 (β), 88.20 (γ)	90.00 (α), 90.00 (β), 119.20 (γ)
FD002	R_{wp} = 0.1193	R_p = 0.0943	$R\chi^2$ = 6.463	Brushite	Monetite	Hydroxyapatite
	Unit Cell Parameters (Å)			6.37 (a), 15.20 (b), 5.82 (c)	6.92 (a), 6.62 (b), 6.94 (c)	9.43 (a), 18.84 (b), 6.88 (c)
	Unit Cell Angles (°)			90.00 (α), 118.51 (β), 90.00 (γ)	96.15 (α), 103.90(β), 88.32 (γ)	90.00 (α), 90.00 (β), 119.91 (γ)
FD003	R_{wp} = 0.1733	R_p = 0.1412	$R\chi^2$ = 14.26	Brushite	Monetite	Hydroxyapatite
	Unit Cell Parameters (Å)			6.37 (a), 15.19 (b), 5.82 (c)	6.90 (a), 6.63 (b), 6.98 (c)	9.46 (a), 18.88 (b), 6.87 (c)
	Unit Cell Angles (°)			90.00 (α), 118.52 (β), 90.00 (γ)	96.26 (α), 103.90 (β), 88.42 (γ)	90.00 (α), 90.00 (β), 120.00 (γ)
FD004	R_{wp} = 0.1635	R_p = 0.1345	$R\chi^2$ = 12.24	Brushite	Monetite	Hydroxyapatite
	Unit Cell Parameters (Å)			6.38 (a), 15.20 (b), 5.82 (c)	6.93 (a), 6.59 (b), 7.01 (c)	9.41 (a), 18.90 (b), 6.87 (c)
	Unit Cell Angles (°)			90.00 (α), 118.53 (β), 90.00 (γ)	98.25 (α), 103.81 (β), 89.00 (γ)	90.00 (α), 90.00 (β), 119.64 (γ)
FD005	R_{wp} = 0.1730	R_p = 0.1404	$R\chi^2$ = 13.71	Brushite	Monetite	Hydroxyapatite
	Unit Cell Parameters (Å)			6.36 (a), 15.17 (b), 5.81 (c)	6.91 (a), 6.63 (b), 6.89 (c)	9.43 (a), 18.98 (b), 6.87 (c)
	Unit Cell Angles (°)			90.00 (α), 118.53 (β), 90.00 (γ)	94.82 (α), 103.14 (β), 89.40 (γ)	90.00 (α), 90.00 (β), 119.70 (γ)
FD006	R_{wp} = 0.1693	R_p = 0.1326	$R\chi^2$ = 11.37	Brushite	Monetite	Hydroxyapatite
	Unit Cell Parameters (Å)			6.37 (a), 15.18 (b), 5.81 (c)	6.92 (a), 6.66 (b), 6.95 (c)	9.43 (a), 18.98 (b), 6.87 (c)
	Unit Cell Angles (°)			90.00 (α), 118.51 (β), 90.00 (γ)	97.04(α), 103.08 (β), 88.16 (γ)	90.00 (α), 90.00 (β), 120.25 (γ)
FD007	R_{wp} = 0.1556	R_p = 0.1282	$R\chi^2$ = 9.343	Brushite	Monetite	Hydroxyapatite
	Unit Cell Parameters (Å)			6.40 (a), 15.20 (b), 5.86 (c)	6.91 (a), 6.61 (b), 6.98 (c)	9.46 (a), 18.94 (b), 6.87 (c)
	Unit Cell Angles (°)			90.00 (α), 119.02 (β), 90.00 (γ)	96.44(α), 104.03 (β), 88.21 (γ)	90.00 (α), 90.00 (β), 120.23 (γ)
FD008	R_{wp} = 0.1653	R_p = 0.1284	$R\chi^2$ = 9.301	Brushite	Monetite	Hydroxyapatite
	Unit Cell Parameters (Å)			6.40 (a), 15.13 (b), 5.83 (c)	6.90 (a), 6.62 (b), 6.97 (c)	9.42 (a), 18.86 (b), 6.88 (c)
	Unit Cell Angles (°)			90.00 (α), 119.11 (β), 90.00 (γ)	96.21(α), 103.95(β), 88.40 (γ)	90.00 (α), 90.00 (β), 119.70 (γ)
FD009	R_{wp} = 0.1771	R_p = 0.1404	$R\chi^2$ = 12.72	Brushite	Monetite	Hydroxyapatite
	Unit Cell Parameters (Å)			6.37 (a), 15.20 (b), 5.82 (c)	6.90 (a), 6.61 (b), 6.97 (c)	9.40 (a), 18.88 (b), 6.86 (c)
	Unit Cell Angles (°)			90.00 (α), 118.50 (β), 90.00 (γ)	95.89 (α), 103.92(β), 88.71 (γ)	90.00 (α), 90.00 (β), 119.48 (γ)

FD010	R_{wp} = 0.1290	R_p = 0.1014	$R\chi^2$ = 6.261	Brushite	Monetite	Hydroxyapatite
	Unit Cell Parameters (Å)			6.32 (a), 16.70 (b), 5.73 (c)	6.91 (a), 6.64 (b), 7.00 (c)	9.40 (a), 18.87 (b), 6.86 (c)
	Unit Cell Angles (°)			90.00 (α), 116.95 (β), 90.00 (γ)	96.28 (α), 103.93(β), 88.44 (γ)	90.00 (α), 90.00 (β), 119.34 (γ)
FD011	R_{wp} = 0.1873	R_p = 0.1455	$R\chi^2$ = 14.33	Brushite	Monetite	Hydroxyapatite
	Unit Cell Parameters (Å)			6.37 (a), 15.19 (b), 5.83 (c)	6.91 (a), 6.64 (b), 6.99 (c)	9.49 (a), 18.96 (b), 6.86 (c)
	Unit Cell Angles (°)			90.00 (α), 118.48 (β), 90.00 (γ)	96.29 (α), 103.96 (β), 88.41 (γ)	90.00 (α), 90.00 (β), 120.23 (γ)
FD012	R_{wp} = 0.1678	R_p = 0.1328	$R\chi^2$ = 10.94	Brushite	Monetite	Hydroxyapatite
	Unit Cell Parameters (Å)			6.48 (a), 15.16 (b), 5.92 (c)	6.91 (a), 6.63 (b), 6.99 (c)	9.40 (a), 18.85 (b), 6.87 (c)
	Unit Cell Angles (°)			90.00 (α), 119.87(β), 90.00 (γ)	96.21 (α), 103.96 (β), 88.40 (γ)	90.00 (α), 90.00 (β), 119.42 (γ)
FD013	R_{wp} = 0.1848	R_p = 0.1398	$R\chi^2$ = 13.67	Brushite	Monetite	Hydroxyapatite
	Unit Cell Parameters (Å)			6.37 (a), 15.17 (b), 5.81 (c)	6.90 (a), 6.61 (b), 6.94 (c)	9.43 (a), 18.79 (b), 6.85 (c)
	Unit Cell Angles (°)			90.00 (α), 118.52 (β), 90.00 (γ)	94.87 (α), 103.37 (β), 88.55 (γ)	90.00 (α), 90.00 (β), 119.04 (γ)
FD014	R_{wp} = 0.1550	R_p = 0.1309	$R\chi^2$ = 10.50	Brushite	Monetite	Hydroxyapatite
	Unit Cell Parameters (Å)			6.37 (a), 15.20 (b), 5.82 (c)	6.90 (a), 6.63 (b), 6.98 (c)	9.39 (a), 18.92 (b), 6.87 (c)
	Unit Cell Angles (°)			90.00 (α), 118.52 (β), 90.00 (γ)	96.25 (α), 103.99 (β), 88.44 (γ)	90.00 (α), 90.00 (β), 119.32 (γ)
FD015	R_{wp} = 0.1710	R_p = 0.1341	$R\chi^2$ = 11.72	Brushite	Monetite	Hydroxyapatite
	Unit Cell Parameters (Å)			6.37 (a), 15.19 (b), 5.82 (c)	6.94 (a), 6.62 (b), 7.00 (c)	9.51 (a), 19.05 (b), 6.87 (c)
	Unit Cell Angles (°)			90.00 (α), 118.50 (β), 90.00 (γ)	96.66 (α), 103.85 (β), 87.95 (γ)	90.00 (α), 90.00 (β), 119.90 (γ)
FD016	R_{wp} = 0.1371	R_p = 0.1105	$R\chi^2$ = 6.91	Brushite	Monetite	Hydroxyapatite
	Unit Cell Parameters (Å)			6.58 (a), 15.20 (b), 6.00 (c)	6.91 (a), 6.63 (b), 6.98 (c)	9.42 (a), 18.87 (b), 6.88 (c)
	Unit Cell Angles (°)			90.00 (α), 121.56 (β), 90.00 (γ)	96.21 (α), 103.97 (β), 88.38 (γ)	90.00 (α), 90.00 (β), 119.80 (γ)
FD021	R_{wp} = 0.1441	R_p = 0.1181	$R\chi^2$ = 12.57	Brushite	Monetite	Hydroxyapatite
	Unit Cell Parameters (Å)			6.37 (a), 15.20 (b), 5.82 (c)	6.92 (a), 6.64 (b), 6.97 (c)	9.49 (a), 19.04 (b), 6.86 (c)
	Unit Cell Angles (°)			90.00 (α), 118.51 (β), 90.00 (γ)	96.94 (α), 102.33 (β), 88.91 (γ)	90.00 (α), 90.00 (β), 120.86 (γ)
FD022	R_{wp} = 0.1773	R_p = 0.1324	$R\chi^2$ = 13.43	Brushite	Monetite	Hydroxyapatite
	Unit Cell Parameters (Å)			6.37 (a), 15.20 (b), 5.82 (c)	6.93 (a), 6.63 (b), 6.99 (c)	9.43 (a), 19.26 (b), 6.84 (c)

Unit Cell Angles (°)	90.00 (α), 118.49 (β), 90.00 (γ)	96.15 (α), 103.94 (β), 88.29 (γ)	90.00 (α), 90.00 (β), 120.68 (γ)

FD023	R_{wp} = 0.1509	R_p = 0.1267	$R\chi^2$ = 11.47	Brushite	Monetite	Hydroxyapatite
	Unit Cell Parameters (Å)			6.37 (a), 15.18 (b), 5.81 (c)	6.90 (a), 6.64 (b), 6.99 (c)	9.44 (a), 18.77 (b), 6.87 (c)
	Unit Cell Angles (°)			90.00 (α), 118.52 (β), 90.00 (γ)	96.24 (α), 103.99 (β), 88.42 (γ)	90.00 (α), 90.00 (β), 119.18 (γ)
FD025	R_{wp} = 0.1749	R_p = 0.1386	$R\chi^2$ = 11.72	Brushite	Monetite	Hydroxyapatite
	Unit Cell Parameters (Å)			6.36 (a), 15.17 (b), 5.80 (c)	6.90 (a), 6.62 (b), 6.98 (c)	9.42 (a), 18.83 (b), 6.85 (c)
	Unit Cell Angles (°)			90.00 (α), 118.53 (β), 90.00 (γ)	96.36 (α), 104.04 (β), 88.45 (γ)	90.00 (α), 90.00 (β), 119.22 (γ)
FD026	R_{wp} = 0.1843	R_p = 0.1453	$R\chi^2$ = 13.57	Brushite	Monetite	Hydroxyapatite
	Unit Cell Parameters (Å)			6.37 (a), 15.19 (b), 5.82 (c)	6.93 (a), 6.62 (b), 7.00 (c)	9.65 (a), 19.21 (b), 6.85 (c)
	Unit Cell Angles (°)			90.00 (α), 118.49(β), 90.00 (γ)	96.38 (α), 104.13 (β), 88.15 (γ)	90.00 (α), 90.00 (β), 121.41(γ)
FD027	R_{wp} = 0.1816	R_p = 0.1510	$R\chi^2$ = 13.86	Brushite	Monetite	Hydroxyapatite
	Unit Cell Parameters (Å)			6.37 (a), 15.18 (b), 5.81 (c)	6.90 (a), 6.63 (b), 6.98 (c)	9.40 (a), 18.89 (b), 6.85 (c)
	Unit Cell Angles (°)			90.00 (α), 118.55(β), 90.00 (γ)	96.22 (α), 104.01 (β), 88.45 (γ)	90.00 (α), 90.00 (β), 119.34 (γ)
FD028	R_{wp} = 0.1639	R_p = 0.1366	$R\chi^2$ = 11.92	Brushite	Monetite	Hydroxyapatite
	Unit Cell Parameters (Å)			6.83(a), 14.36 (b), 7.49 (c)	6.91 (a), 6.64 (b), 7.00 (c)	9.43 (a), 18.90 (b), 6.87 (c)
	Unit Cell Angles (°)			90.00 (α), 126.05 (β), 90.00 (γ)	96.21 (α), 104.00 (β), 88.38 (γ)	90.00 (α), 90.00 (β), 119.64 (γ)
FD029	R_{wp} = 0.1554	R_p = 0.1256	$R\chi^2$ = 7.03	Brushite	Monetite	Hydroxyapatite
	Unit Cell Parameters (Å)			6.37(a), 15.19(b), 5.82 (c)	7.08 (a), 6.53 (b), 7.20 (c)	9.40 (a), 19.00 (b), 6.88 (c)
	Unit Cell Angles (°)			90.00 (α), 118.50 (β), 90.00 (γ)	96.39 (α), 100.00 (β), 85.57 (γ)	90.00 (α), 90.00 (β), 119.64 (γ)
FD030	R_{wp} = 0.1730	R_p = 0.1455	$R\chi^2$ = 10.02	Brushite	Monetite	Hydroxyapatite
	Unit Cell Parameters (Å)			6.37(a), 15.21(b), 5.81 (c)	7.00 (a), 6.76 (b), 7.00 (c)	9.54 (a), 19.22 (b), 6.84 (c)
	Unit Cell Angles (°)			90.00 (α), 118.57 (β), 90.00 (γ)	100.44 (α), 100.80 (β), 89.89 (γ)	90.00 (α), 90.00 (β), 121.24(γ)
FD031	R_{wp} = 0.1707	R_p = 0.1397	$R\chi^2$ = 10.78	Brushite	Monetite	Hydroxyapatite
	Unit Cell Parameters (Å)			6.37(a), 15.19(b), 5.81 (c)	6.89 (a), 6.62 (b), 6.98 (c)	9.43(a), 18.80 (b), 6.86 (c)
	Unit Cell Angles (°)			90.00 (α), 118.53 (β),	96.21 (α), 103.94 (β), 88.44(γ)	90.00 (α), 90.00 (β), 119.16 (γ)

				90.00 (γ)		
FD032	R_{wp} = 0.2041	R_p = 0.1609	$R\chi^2$ = 7.45	Brushite	Monetite	Hydroxyapatite
	Unit Cell Parameters (Å)			6.39(a), 14.54(b), 5.85 (c)	6.90 (a), 6.62 (b), 6.98 (c)	9.41(a), 18.87 (b), 6.88 (c)
	Unit Cell Angles (°)			90.00 (α), 119.15 β), 90.00 (γ)	96.23 (α), 103.95 (β), 88.38 (γ)	90.00 (α), 90.00 (β), 119.49 (γ)

Chapter 4. Calcium Carbonate

Table A. 6. Synthesis conditions and sample coding used for the hydrothermal injection samples of calcium carbonate.

CO_3^{2-} **Source**	**Ratio** (CO_3^{2-}/Ca^{2+})	**Sample name**	**T (ºC)**
Bicarbonate	0.5	AS126	50
		AS127	100
		AS128	200
	1	AS095	25
		AS096	50
		AS097	100
		AS098	200
	1.5	AS153	25
		AS155	100
		AS156	200
	2	AS122	50
		AS123	100
		AS124	200
Carbonate	0.5	AS133	25
		AS134	50
		AS135	100
		AS136	200
	1	**AS103**	**25**
		AS104	**50**
		AS105	**100**
		AS106	**200**
	1.5	AS157	25
		AS158	50
		AS159	100
		AS160	200
	2	AS129	25
		AS130	50
		AS131	100
		AS132	200

Table A. 7. Rietveld Refinement parameters for the hydrothermal injection samples of calcium carbonate.

AS095	R_{wp} = 0.1918	R_p = 0.1474	$R\chi^2$ = 4.31	Calcite	Aragonite	Vaterite
	Unit Cell Parameters (Å)			4.99 (a), 4.99 (b), 17.09 (c)	4.95 (a), 7.97 (b), 5.80 (c)	12.20 (a), 7.17 (b), 9.38 (c)
	Unit Cell Angles (°)			90.00 (α), 90.00 (β), 120.00 (γ)	90.00 (α), 90.00 (β), 90.00 (γ)	90.00 (α), 117.93 (β), 90.00 (γ)
AS096	R_{wp} = 0.1935	R_p = 0.1650	$R\chi^2$ = 6.55	Calcite	Aragonite	Vaterite
	Unit Cell Parameters (Å)			4.99 (a), 4.99 (b), 17.07 (c)	4.99 (a), 7.97 (b), 5.80 (c)	12.25 (a), 7.17 (b), 9.35 (c)
	Unit Cell Angles (°)			90.00 (α), 90.00 (β), 120.00 (γ)	90.00 (α), 90.00 (β), 90.00 (γ)	90.00 (α), 118.07 (β), 90.00 (γ)
AS098	R_{wp} = 0.1709	R_p = 0.1341	$R\chi^2$ = 3.35	Calcite	Aragonite	Vaterite
	Unit Cell Parameters (Å)			4.99 (a), 4.99 (b), 17.07 (c)	4.96 (a), 7.97 (b), 5.74 (c)	12.17 (a), 7.12 (b), 9.47 (c)
	Unit Cell Angles (°)			90.00 (α), 90.00 (β), 120.00 (γ)	90.00 (α), 90.00 (β), 90.00 (γ)	90.00 (α), 118.37 (β), 90.00 (γ)
AS103	R_{wp} = 0.1510	R_p = 0.1208	$R\chi^2$ = 3.19	Calcite	Aragonite	Vaterite
	Unit Cell Parameters (Å)			4.99 (a), 4.99 (b), 17.05 (c)	4.95 (a), 7.95 (b), 5.75 (c)	12.33 (a), 7.16 (b), 9.42 (c)
	Unit Cell Angles (°)			90.00 (α), 90.00 (β), 120.00 (γ)	90.00 (α), 90.00 (β), 90.00 (γ)	90.00 (α), 116.09 (β), 90.00 (γ)
AS104	R_{wp} = 0.1896	R_p = 0.1586	$R\chi^2$ = 6.37	Calcite	Aragonite	Vaterite
	Unit Cell Parameters (Å)			4.98 (a), 4.98 (b), 17.04 (c)	4.93 (a), 7.91 (b), 5.75 (c)	12.37 (a), 7.13 (b), 9.39 (c)
	Unit Cell Angles (°)			90.00 (α), 90.00 (β), 120.00 (γ)	90.00 (α), 90.00 (β), 90.00 (γ)	90.00 (α), 115.81 (β), 90.00 (γ)
AS105	R_{wp} = 0.1500	R_p = 0.1154	$R\chi^2$ = 12.72	Calcite	Aragonite	Vaterite
	Unit Cell Parameters (Å)			4.99 (a), 4.99 (b), 17.07 (c)	4.62 (a), 7.97 (b), 5.75 (c)	12.17 (a), 7.17 (b), 9.44 (c)
	Unit Cell Angles (°)			90.00 (α), 90.00 (β), 120.00 (γ)	90.00 (α), 90.00 (β), 90.00 (γ)	90.00 (α), 118.33 (β), 90.00 (γ)
AS106	R_{wp} = 0.2173	R_p = 0.1727	$R\chi^2$ = 13.81	Calcite	Aragonite	Vaterite
	Unit Cell Parameters (Å)			4.99 (a), 4.99 (b), 17.06 (c)	4.96 (a), 7.97 (b), 5.74 (c)	12.17 (a), 7.12 (b), 9.47 (c)
	Unit Cell Angles (°)			90.00 (α), 90.00 (β), 120.00 (γ)	90.00 (α), 90.00 (β), 90.00 (γ)	90.00 (α), 118.37 (β), 90.00 (γ)
AS122	R_{wp} = 0.2036	R_p = 0.1577	$R\chi^2$ = 6.38	Calcite	Aragonite	Vaterite
	Unit Cell Parameters (Å)			4.99 (a), 4.99 (b), 17.05 (c)	4.84 (a), 7.95 (b), 5.82 (c)	12.33 (a), 7.14 (b), 9.41 (c)
	Unit Cell Angles (°)			90.00 (α), 90.00 (β), 120.00 (γ)	90.00 (α), 90.00 (β), 90.00 (γ)	90.00 (α), 116.16 (β), 90.00 (γ)
AS123	R_{wp} = 0.1958	R_p = 0.1473	$R\chi^2$ = 5.19	Calcite	Aragonite	Vaterite
	Unit Cell Parameters (Å)			4.99 (a), 4.99 (b), 17.07 (c)	4.96 (a), 7.96 (b), 5.75 (c)	12.57 (a), 7.16 (b), 9.56 (c)
	Unit Cell Angles (°)			90.00 (α), 90.00 (β), 120.00 (γ)	90.00 (α), 90.00 (β), 90.00 (γ)	90.00 (α), 116.95 (β), 90.00 (γ)

AS124	R_{wp} = 0.2097	R_p = 0.1648	$R\chi^2$ = 6.35	Calcite	Aragonite	Vaterite
	Unit Cell Parameters (Å)			4.99 (a), 4.99 (b), 17.06 (c)	4.96 (a), 7.97 (b), 5.74 (c)	12.17 (a), 7.12 (b), 9.47 (c)
	Unit Cell Angles (°)			90.00 (α), 90.00 (β), 120.00 (γ)	90.00 (α), 90.00 (β), 90.00 (γ)	90.00 (α), 118.37 (β), 90.00 (γ)
AS126	R_{wp} = 0.1666	R_p = 0.1309	$R\chi^2$ = 2.34	Calcite	Aragonite	Vaterite
	Unit Cell Parameters (Å)			4.99 (a), 4.99 (b), 17.06 (c)	4.97 (a), 7.97 (b), 5.74 (c)	12.24 (a), 7.12 (b), 9.56 (c)
	Unit Cell Angles (°)			90.00 (α), 90.00 (β), 120.00 (γ)	90.00 (α), 90.00 (β), 90.00 (γ)	90.00 (α), 118.99 (β), 90.00 (γ)
AS128	R_{wp} = 0.2167	R_p = 0.1656	$R\chi^2$ = 3.98	Calcite	Aragonite	Vaterite
	Unit Cell Parameters (Å)			5.00 (a), 5.00 (b), 17.09 (c)	4.97 (a), 7.98 (b), 5.75 (c)	12.35 (a), 7.07 (b), 9.73 (c)
	Unit Cell Angles (°)			90.00 (α), 90.00 (β), 120.00 (γ)	90.00 (α), 90.00 (β), 90.00 (γ)	90.00 (α), 119.76 (β), 90.00 (γ)
AS129	R_{wp} = 0.2000	R_p = 0.1560	$R\chi^2$ = 3.39	Calcite	Aragonite	Vaterite
	Unit Cell Parameters (Å)			4.99 (a), 4.99 (b), 17.06 (c)	4.96 (a), 7.95 (b), 5.76 (c)	12.16 (a), 7.15 (b), 9.42 (c)
	Unit Cell Angles (°)			90.00 (α), 90.00 (β), 120.00 (γ)	90.00 (α), 90.00 (β), 90.00 (γ)	90.00 (α), 118.12 (β), 90.00 (γ)
AS130	R_{wp} = 0.1565	R_p = 0.1217	$R\chi^2$ = 3.91	Calcite	Aragonite	Vaterite
	Unit Cell Parameters (Å)			4.99 (a), 4.99 (b), 17.06 (c)	4.95 (a), 7.95 (b), 5.77 (c)	12.36 (a), 7.09 (b), 9.36 (c)
	Unit Cell Angles (°)			90.00 (α), 90.00 (β), 120.00 (γ)	90.00 (α), 90.00 (β), 90.00 (γ)	90.00 (α), 115.57 (β), 90.00 (γ)
AS131	R_{wp} = 0.1774	R_p = 0.1369	$R\chi^2$ = 3.54	Calcite	Aragonite	Vaterite
	Unit Cell Parameters (Å)			4.99 (a), 4.99 (b), 17.06 (c)	4.96 (a), 7.97 (b), 5.74 (c)	12.19 (a), 7.13 (b), 9.45 (c)
	Unit Cell Angles (°)			90.00 (α), 90.00 (β), 120.00 (γ)	90.00 (α), 90.00 (β), 90.00 (γ)	90.00 (α), 118.26 (β), 90.00 (γ)
AS132	R_{wp} = 0.1907	R_p = 0.1526	$R\chi^2$ = 5.25	Calcite	Aragonite	Vaterite
	Unit Cell Parameters (Å)			4.99 (a), 4.99 (b), 17.05 (c)	4.96 (a), 7.97 (b), 5.74 (c)	12.17 (a), 7.12 (b), 9.47 (c)
	Unit Cell Angles (°)			90.00 (α), 90.00 (β), 120.00 (γ)	90.00 (α), 90.00 (β), 90.00 (γ)	90.00 (α), 118.36 (β), 90.00 (γ)
AS133	R_{wp} = 0.1883	R_p = 0.1493	$R\chi^2$ = 5.03	Calcite	Aragonite	Vaterite
	Unit Cell Parameters (Å)			4.99 (a), 4.99 (b), 17.06 (c)	4.96 (a), 7.95 (b), 5.75 (c)	12.27 (a), 7.11 (b), 9.35 (c)
	Unit Cell Angles (°)			90.00 (α), 90.00 (β), 120.00 (γ)	90.00 (α), 90.00 (β), 90.00 (γ)	90.00 (α), 115.79 (β), 90.00 (γ)
AS134	R_{wp} = 0.2294	R_p = 0.1699	$R\chi^2$ = 7.95	Calcite	Aragonite	Vaterite
	Unit Cell Parameters (Å)			4.99 (a), 4.99 (b), 17.06 (c)	4.96 (a), 7.97 (b), 5.75 (c)	12.37 (a), 7.11 (b), 9.38 (c)
	Unit Cell Angles (°)			90.00 (α), 90.00 (β), 120.00 (γ)	90.00 (α), 90.00 (β), 90.00 (γ)	90.00 (α), 115.88 (β), 90.00 (γ)

AS135	R_{wp} = 0.1791	R_p = 0.1413	$R\chi^2$ = 4.56	Calcite	Aragonite	Vaterite
	Unit Cell Parameters (Å)			4.99 (a), 4.99 (b), 17.06 (c)	4.96 (a), 7.96 (b), 5.74 (c)	12.17 (a), 7.12 (b), 9.47 (c)
	Unit Cell Angles (°)			90.00 (α), 90.00 (β), 120.00 (γ)	90.00 (α), 90.00 (β), 90.00 (γ)	90.00 (α), 118.37 (β), 90.00 (γ)
AS136	R_{wp} = 0.1778	R_p = 0.1388	$R\chi^2$ = 4.25	Calcite	Aragonite	Vaterite
	Unit Cell Parameters (Å)			4.99 (a), 4.99 (b), 17.06 (c)	4.90 (a), 7.89 (b), 5.87 (c)	12.25 (a), 7.15 (b), 9.50 (c)
	Unit Cell Angles (°)			90.00 (α), 90.00 (β), 120.00 (γ)	90.00 (α), 90.00 (β), 90.00 (γ)	90.00 (α), 116.90 (β), 90.00 (γ)
AS153	R_{wp} = 0.2226	R_p = 0.1582	$R\chi^2$ = 7.14	Calcite	Aragonite	Vaterite
	Unit Cell Parameters (Å)			4.99 (a), 4.99 (b), 17.06 (c)	4.90 (a), 7.89 (b), 5.87 (c)	12.25 (a), 7.11 (b), 9.36 (c)
	Unit Cell Angles (°)			90.00 (α), 90.00 (β), 120.00 (γ)	90.00 (α), 90.00 (β), 90.00 (γ)	90.00 (α), 116.90 (β), 90.00 (γ)
AS155	R_{wp} = 0.1869	R_p = 0.1377	$R\chi^2$ = 3.32	Calcite	Aragonite	Vaterite
	Unit Cell Parameters (Å)			4.99 (a), 4.99 (b), 17.06 (c)	4.96 (a), 7.97 (b), 5.75 (c)	12.17 (a), 7.12 (b), 9.49 (c)
	Unit Cell Angles (°)			90.00 (α), 90.00 (β), 120.00 (γ)	90.00 (α), 90.00 (β), 90.00 (γ)	90.00 (α), 118.42 (β), 90.00 (γ)
AS156	R_{wp} = 0.2375	R_p = 0.1893	$R\chi^2$ = 7.71	Calcite	Aragonite	Vaterite
	Unit Cell Parameters (Å)			4.99 (a), 4.99 (b), 17.06 (c)	4.96 (a), 7.97 (b), 5.75 (c)	12.17 (a), 7.12 (b), 9.49 (c)
	Unit Cell Angles (°)			90.00 (α), 90.00 (β), 120.00 (γ)	90.00 (α), 90.00 (β), 90.00 (γ)	90.00 (α), 118.42 (β), 90.00 (γ)
AS157	R_{wp} = 0.1741	R_p = 0.1337	$R\chi^2$ = 3.76	Calcite	Aragonite	Vaterite
	Unit Cell Parameters (Å)			4.99 (a), 4.99 (b), 17.06 (c)	4.95 (a), 7.96 (b), 5.76 (c)	12.33 (a), 7.11 (b), 9.38 (c)
	Unit Cell Angles (°)			90.00 (α), 90.00 (β), 120.00 (γ)	90.00 (α), 90.00 (β), 90.00 (γ)	90.00 (α), 116.27(β), 90.00 (γ)
AS158	R_{wp} = 0.1627	R_p = 0.1252	$R\chi^2$ = 2.37	Calcite	Aragonite	Vaterite
	Unit Cell Parameters (Å)			4.99 (a), 4.99 (b), 17.08 (c)	4.95 (a), 7.94 (b), 5.82 (c)	12.32 (a), 7.04 (b), 9.55 (c)
	Unit Cell Angles (°)			90.00 (α), 90.00 (β), 120.00 (γ)	90.00 (α), 90.00 (β), 90.00 (γ)	90.00 (α), 119.28 (β), 90.00 (γ)
AS159	R_{wp} = 0.2149	R_p = 0.1707	$R\chi^2$ = 6.79	Calcite	Aragonite	Vaterite
	Unit Cell Parameters (Å)			4.99 (a), 4.99 (b), 17.04 (c)	4.96 (a), 7.97 (b), 5.74 (c)	12.17 (a), 7.12 (b), 9.48 (c)
	Unit Cell Angles (°)			90.00 (α), 90.00 (β), 120.00 (γ)	90.00 (α), 90.00 (β), 90.00 (γ)	90.00 (α), 118.41 (β), 90.00 (γ)
AS160	R_{wp} = 0.1841	R_p = 0.1427	$R\chi^2$ = 5.00	Calcite	Aragonite	Vaterite
	Unit Cell Parameters (Å)			4.99 (a), 4.99 (b), 17.06 (c)	4.96 (a), 7.97 (b), 5.74 (c)	12.17 (a), 7.12 (b), 9.47 (c)
	Unit Cell Angles (°)			90.00 (α), 90.00 (β), 120.00 (γ)	90.00 (α), 90.00 (β), 90.00 (γ)	90.00 (α), 118.37 (β), 90.00 (γ)

List of Conferences and Publications

i. 2022 N. García Doménech, F. Purcell-Milton, A. Sanz Arjona, M. L. Casasín García, M. Ward, M. B. Cabré, A. Rafferty, K. McKelvey, P. Dunne and Y. K. Gun'ko, *Nanomaterials*, 2022, **12**, 473

ii. 2021 "Mild Hydrothermal synthesis of Zircon-type silicates ($MSiO_4$) as analogues to radioactive species" - at the 72nd Irish Chemistry research Colloquium, University of Limerick, Ireland. *Oral Presentation*

iii. 2021 "How to write a lab report – A hands-on approach to improving chemistry undergraduate writing skills" – at Eurovariety, Ljubljana, Slovenia. *Co-oral presentation*

iv. 2021 "Mild Hydrothermal synthesis of Zircon-type silicates ($MSiO_4$) as analogues to radioactive species - at the 15th International Conference of Materials Chemistry (MC15), Dublin, Ireland. *Poster presentation*

v. 2021 "Mild Hydrothermal Synthesis of Zircon-type Silicates ($MSiO_4$)" – at the RSC Materials Chemistry Division poster Symposium. *Poster presentation*

vi. 2021 "Hydrothermal Injection for Phase-Controlled $CaCO_3$ Synthesis" – at the RSC Materials Chemistry Division poster Symposium. *Poster presentation*

vii. 2018 "PhD Flash Presentation" – at the TCD School of Chemistry Careers in Chemistry. *Oral Presentation*